THERMAL-HYDRAULIC BEHAVIOUR OF THE BRUCE A MODERATOR

A STUDY OF THE THERMAL-HYDRAULIC BEHAVIOUR OF THE BRUCE A CANDU MODERATOR USING A SMALL-SCALE MODEL

By JAMES M. V. STRACK, B.Eng.Mgt., M.A.Sc.

A Thesis
Submitted to the School of Graduate Studies
in Partial Fulfillment of the Requirements for the Degree
Doctor of Philosophy

McMaster University

DOCTOR OF PHILOSOPHY (2019) MCMASTER UNIVERSITY
(Engineering Physics) Hamilton, Ontario, Canada

Title: A Study of the Thermal-Hydraulic Behaviour of the Bruce A CANDU Moderator Using a Small-Scale Model

Author: James Michael Vincent Strack, B.Eng.Mgt., M.A.Sc.
(McMaster University)

Supervisor: Dr. D. R. Novog

Number of Pages: xxxii, 173

Abstract

The prediction of the moderator temperature distribution in a CANDU reactor is important in establishing its ability to act as an emergency heat sink for certain beyond design basis accidents. This analysis typically relies on computational models which are benchmarked against experimental data from small-scale test facilities. These small-scale models prioritize the matching of the Archimedes number (*Ar*) of the full-scale reactor, which represents the ratio of buoyancy forces to inertial forces. Concerns regarding similarity between the reactor and small-scale facilities may exist due to a large difference in scale, as well as geometric simplifications made due to practical limitations.

This study examined the behaviour within an approximately 1/16 scale facility representative of the Bruce A calandria vessel, which features a unique inlet and outlet configuration. Experimental measurements were obtained for a range of power and flow conditions. Unsteady RANS simulations of the small-scale facility were also performed using the realizable k-ε model. Goals of the study included the assessment of the unique moderator inlet on the flow patterns inside the calandria vessel and how well existing CFD modelling approaches replicated these features.

The observed flow and temperature distributions in the scale facility did not appear highly sensitive to changes in *Ar*. For all tested conditions, a large front-to-back recirculation pattern resulted from the asymmetric inlet arrangement. Peak

temperatures consistently occurred toward the front of the vessel where inertial flows were assisted by buoyancy induced flows.

Under steady-state conditions, unsteady and three-dimensional behaviour was observed within the vessel. Temperature fluctuations near the upper rear end of the vessel arose from the unstable interaction between cool downward flow from the inlets and upward buoyant flow from the tube bank. In the peak temperature regions, flow direction was relatively consistent in the upward direction.

The simulations tended to overpredict the peak temperatures within the vessel by approximately 0.5 – 3.8 ºC. This behaviour was attributed to the model tending to underpredict the upward velocities entering the base of the tube bank in the peak temperature regions. As *Ar* increased and buoyancy effects became more significant in determining the local velocities, agreement between the predicted and measured velocities was improved.

The similarity between the small-scale model and the full-size reactor was also assessed through comparisons to existing simulations of the full-size calandria. There was qualitative similarity between the two geometries, albeit at lower *Ar* for the small-scale facility. This suggested that buoyancy effects were more significant in the small-scale facility compared to the full-size calandria. This was attributed to the use of surface heating (as opposed to volumetric heating in the reactor), and relatively high surface heat fluxes caused by a reduced number of tube bank elements.

Acknowledgements

This project was funded by the CANDU Owners Group (COG) and the Natural Sciences and Engineering Research Council of Canada (NSERC) as part of the Collaborative Research and Development (CRD) program. The author would also like to acknowledge the financial assistance of the Ontario Graduate Scholarship and investments made in instrumentation at McMaster University by the University Network of Excellence in Nuclear Engineering (UNENE).

I owe sincere thanks to my supervisor Dr. D. R. Novog for providing this research opportunity and for his technical guidance, support, and patience over the past five-plus years that this project has been underway. I also would like to thank the members of my supervisory committee, Dr. J. Cotton and Dr. D. Jackson, for providing valuable feedback and questions throughout the project.

The computer modelling work would not have been possible without the assistance of Dr. A. Rashkovan. Thank you for help with the mesh and guidance in setting up the runs in STAR-CCM+. I also owe thanks for Dr. J. C. Luxat for providing additional computational resources which made the transient simulations possible.

Many others have helped over the years to bring this experiment from an idea on paper to reality. Thanks to Jim and Clea in the machine shop for their construction help and practical design guidance. Thanks also go to past summer students Kendall, Brian, Phil, Steven, and Malcolm for their construction help.

I am indebted to all of my lab mates for help and moral support over the years. Ken, thanks for coming back to help us with the early prototypes. Chris, thank for your assistance with the headers and help with manning the experiments during those long LDV runs. Thanks also to Garik for help and moral support around B119, those memories of being elbow deep in a rusty heat exchanger will live on forever.

Last but certainly not least, thank you to my family for their love and support which has allowed me to get where I am today. Words cannot express my gratitude for all that you have done for me.

Table of Contents

List of Figures

List of Tables

List of All Abbreviations and Symbols

Symbols

A_i	inlet cross-sectional area [m^2]
C_P	specific heat capacity at constant pressure [$kJ \cdot kg^{-1} \cdot K^{-1}$]
d_t	calandria tube diameter [m]
D	vessel diameter [m]
e_i	error in quantity i
F_S	factor of safety, in the context of grid convergence index
F	focal length, in the context of LDV measurement probe [mm]
g	gravitational acceleration [$m \cdot s^{-2}$]
h	height [m]
k	thermal conductivity [$W \cdot m^{-1} \cdot K^{-1}$]
k	turbulent kinetic energy, in the context of turbulence models [$m^2 \cdot s^{-2}$]
L	vessel length [m]
$\dot{m}$	mass flow rate [$kg \cdot s^{-1}$]
n	index of refraction, in the context of LDV beam crossing distance
N_t	number of tube rows
p	pitch [m]
P	pressure [Pa]
P_e	electric power [kW]
q	thermal energy [kJ]
q''	heat flux [$kJ \cdot m^{-2}$]
q'''	volumetric heat [$kJ \cdot m^{-3}$]
$\dot{q}$	thermal power [kW]

Q	volumetric flow rate [$m^3 \cdot s^{-1}$]
r	radius [m]
r_{ij}	refinement ratio, in the context of grid convergence index
RA	running average
s_T	temperature standard deviation [ºC]
t	time [s]
T	temperature [ºC]
u_i	velocity component in direction *i* [$m \cdot s^{-1}$]
u	velocity component in *x* direction [$m \cdot s^{-1}$]
U_i	inlet velocity [$m \cdot s^{-1}$]
v	velocity component in *y* direction [$m \cdot s^{-1}$]
$\vec{v}$	velocity [$m \cdot s^{-1}$]
V	velocity [$m \cdot s^{-1}$]
V_l	local velocity within porous medium [$m \cdot s^{-1}$]
V_m	velocity upstream of tube bank [$m \cdot s^{-1}$]
w	velocity component in *z* direction [$m \cdot s^{-1}$]

Greek Letters

α	exponential smoothing factor
β	coefficient of thermal expansion [K^{-1}]
γ	porosity
δ_i	relative error in quantity *i* between simulation and measurement
ε	turbulence dissipation rate [$m^2 \cdot s^{-3}$]
ϵ_{ij}	relative error between quantities *i* and *j* in the context of GCI
θ_i	nozzle rotation angle, in the context of test section geometry [º]
θ	3D velocity direction component angle [º]
κ	LDV beam crossing half-angle [º]
λ	wavelength of light [mm]
μ	dynamic viscosity [$kg \cdot m^{-1} \cdot s^{-1}$]
ν	kinematic viscosity [$m^2 \cdot s^{-1}$]

ρ	density [$kg \cdot m^{-3}$]
σ	measurement uncertainty
τ	thermocouple response time constant [s]
ϕ	3D velocity direction component angle [º]
ω	specific dissipation rate, in the context of turbulence models [s^{-1}]

Abbreviations

2D	two-dimensional
3D	three-dimensional
AC	alternating current
AECL	Atomic Energy of Canada Limited
BD	buoyancy dominated
CANDU	Canada Deuterium Uranium
CHF	critical heat flux
CFD	computational fluid dynamics
COG	CANDU Owners Group
CT	calandria tube
DC	direct current
ECC	emergency core cooling
emf	electromotive force
GCI	grid convergence index
IAPWS	International Association for the Properties of Water and Steam
ID	inner diameter
JMD	jet momentum dominated
KAERI	Korean Atomic Energy Research Institute
LDV	laser Doppler velocimetry
LIF	laser induced fluorescence
LOCA	loss-of-coolant accident
LLOCA	large-break loss-of-coolant accident
MCT	moderator circulation test, specifically the facility at KAERI

MTF	moderator test facility, specifically the facility at AECL
OD	outer diameter
PHWR	pressurized heavy water reactor
PID	proportional-integral-derivative, in context of flow rate controller
PIV	particle image velocimetry
PLC	pressure loss coefficient
PT	pressure tube
PVC	polyvinyl chloride
RANS	Reynolds-averaged Navier-Stokes
RMS	root mean square
RNG	Reynolds normalization group
RTD	resistive temperature device
SBO	station blackout
SPEL	Sheridan Park Engineering Laboratory
SST	shear stress transport, specifically *k-ω* SST turbulence model
VFD	variable frequency drive

Dimensionless Numbers

Ar	Archimedes number
C	Courant number
Gr	Grashof number
P^*	dimensionless pressure
Pr	Prandtl number
q^*	dimensionless heat source
q^*_{av}	volume averaged dimensionless heat source
Re	Reynolds number
Ri	Richardson number
t^*	dimensionless time
T^*	dimensionless temperature
V^*	dimensionless velocity

Declaration of Academic Achievement

The work presented in this thesis was primarily supervised by Dr. D. R. Novog who was regularly consulted for guidance throughout this project since October 2013 and acted as a liaison to the CANDU Owners Group. He also provided technical feedback and editing assistance with the initial drafts of this dissertation. The author's supervisory committee consisting of Dr. J. Cotton and Dr. D. Jackson also provided valuable suggestions and guidance throughout this project.

The experimental facility used in this study was designed and constructed by the author as part of a project funded by the CANDU Owners Group (COG), who provided the top-level design requirements and final approval. The detail design and specification of the test section, flow loop, and instrumentation was performed by the author under the supervision of Dr. D. R. Novog. Dr. K. Leung assisted with the specification of the flow controllers and the commissioning of an early isothermal prototype of the facility.

The design and construction of the heaters were performed by Stern Laboratories. Manufacturing of the test vessel and end shields were performed by J. Cleaver who suggested several practical design modifications. The flow headers were designed and constructed as part of a M.A.Sc. project by C. W. Hollingshead. Several undergraduate research assistants also aided with the fabrication of test section components under the supervision of the author: the unheated tube bank elements were fabricated by K. Boniface, the inlet nozzles were fabricated by P. Pastolero, and B. McCrindle assisted the author with flow loop assembly. Assembly of the

test section, commissioning of the flow loop, and development of the experimental procedures were performed by the author.

Execution of the presented experiments and all temperature measurements were performed by the author. Velocity measurements were performed by the author with assistance from C. W. Hollingshead. Processing and analysis of all experimental results were performed by the author.

The turbulence model selection and computational meshes used in the CFD studies were developed and refined by Dr. A. Rashkovan, who also provided valuable guidance and feedback in setting up the simulations presented in this thesis. The boundary and initial conditions were modified by the author to match the experimental conditions tested. The time-step and mesh size sensitivity studies were performed by the author. All post processing and analysis of the simulation results were performed by the author.

Chapter 1

Introduction

1.1 Background

In the core of a CANDU pressurized heavy water reactor (PHWR), fuel and coolant are located within an array of horizontal fuel channels surrounded by low pressure and temperature heavy water moderator in the calandria vessel. In a fuel channel, high temperature and high-pressure coolant is located within a pressure tube (PT) which is surrounded by a calandria tube (CT); annulus gas (CO_2) and spring spacers separate the two tubes. Under normal operating conditions, heat is deposited into the moderator from several sources (including thermalization of neutrons, absorption of gamma rays, and heat loss from fuel channels); about 5% of the reactor power is deposited into the moderator, which is circulated and cooled in heat exchangers to prevent boiling [1].

The configuration of moderator inlets and outlets differs between the various CANDU stations as the reactor design evolved through the years:

- In the Pickering A reactor design, the majority of the moderator flow enters the calandria at twelve upward facing fan shaped diffusers located along the walls the calandria vessel. The remainder of the flow enters through spray clusters located at the top of the calandria vessel.

- The Bruce A reactor design does not feature spray clusters or fan shaped diffusers. This reactor design originally used sixteen enriched uranium booster rods as a reactivity control mechanism; these were cooled in the moderator water circuit by heavy water flowing vertically upwards past these assemblies before entering the top of the calandria vessel. An additional six booster bypass inlets at the top of the calandria vessel are also present. This configuration is shown in Figure 1-2 and Figure 1-3.
- In the Pickering B, Bruce B, and CANDU-6 reactor designs, the moderator enters the calandria through eight upward facing fan-shaped nozzles directed at the calandria walls as shown in Figure 1-1. The Darlington reactor design is similar to Bruce B but has 12 nozzles; an additional four upward facing nozzles are included at a higher elevation.

In all of the aforementioned calandria designs, the moderator water leaves the calandria at the bottom of the vessel at locations which vary between designs.

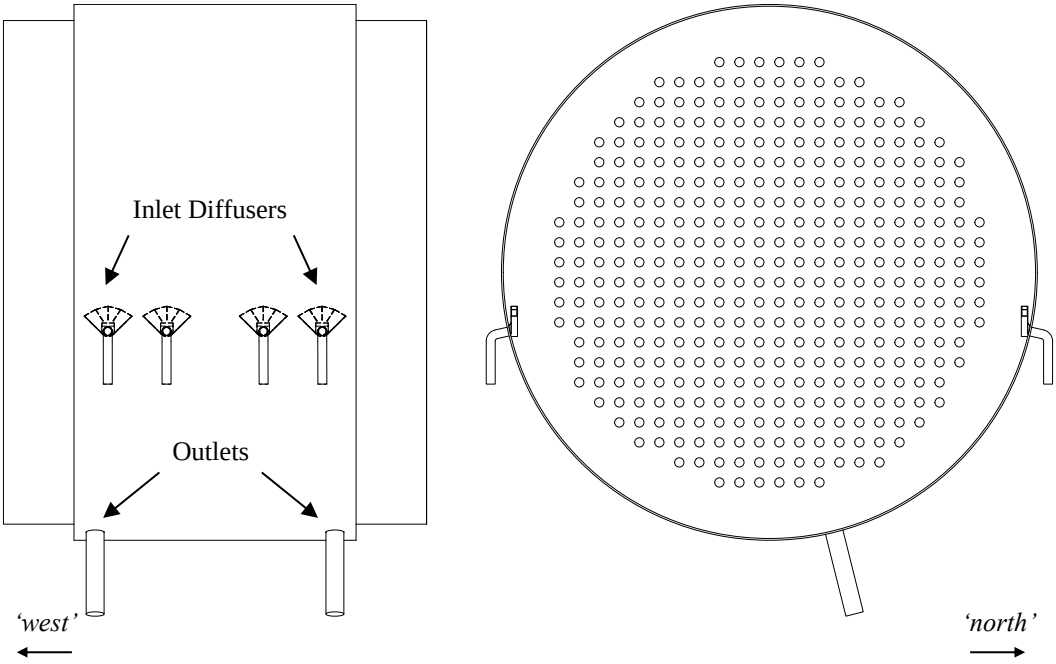

Figure 1-1: Moderator inlet and outlet configuration for a typical CANDU calandria vessel (Pickering B, Bruce B, CANDU-6)

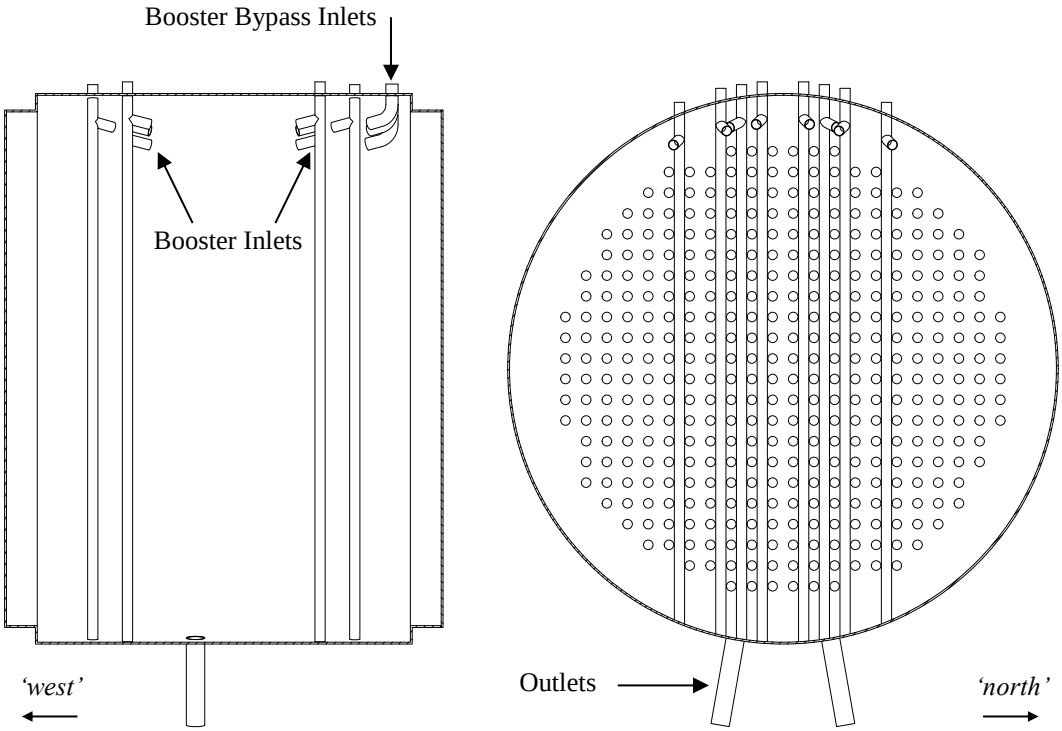

Figure 1-2: Moderator inlet and outlet configuration for a typical Bruce A CANDU calandria vessel ('south' and 'east' elevations)

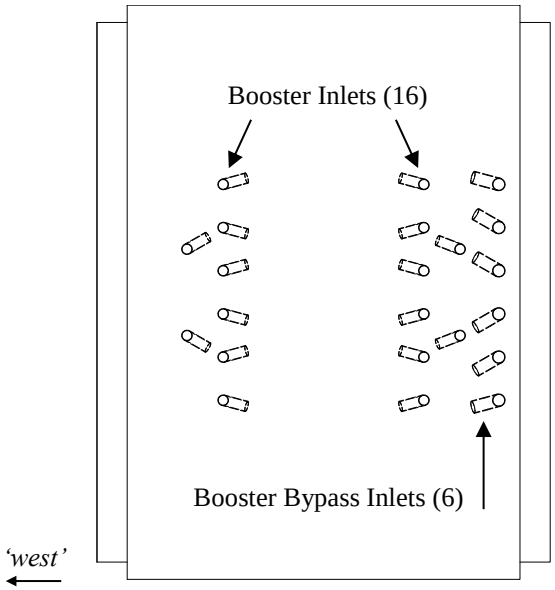

Figure 1-3: Moderator inlet and outlet configuration for a typical Bruce A CANDU calandria vessel (top-down view)

An important feature of CANDU is that it allows for alternative cooling of the fuel and pressure boundaries in the event of the low-likelihood limiting Large Break LOCA (LLOCA) or for events involving multiple failures such as station blackouts (SBOs). In a postulated LLOCA, the Emergency Core Cooling (ECC) actuates automatically to supply water directly to the fuel channels within a very short time after the event initiates (generally less than 60 seconds), such that fuel and fuel channel failures are precluded except in the most limiting analyses.

During a postulated LOCA with coincident loss of ECC, or during a postulated low-probability limiting LLOCA scenario, the elevated fuel temperatures will transfer heat to the pressure tube through radiation. Pressure tube ballooning/sag and contact with the calandria tube may occur depending on the power, pressure and temperatures experienced during the transient as shown in Figure 1-4. If contact occurs between the pressure tube and calandria tube, a significant increase in the heat removed by the moderator is possible, enabling the moderator to act as an alternate heat sink. Thus, an effective decay heat removal configuration is established, so long as the moderator remains within the calandria and the calandria tube does not experience extensive periods beyond the critical heat flux (CHF) [2].

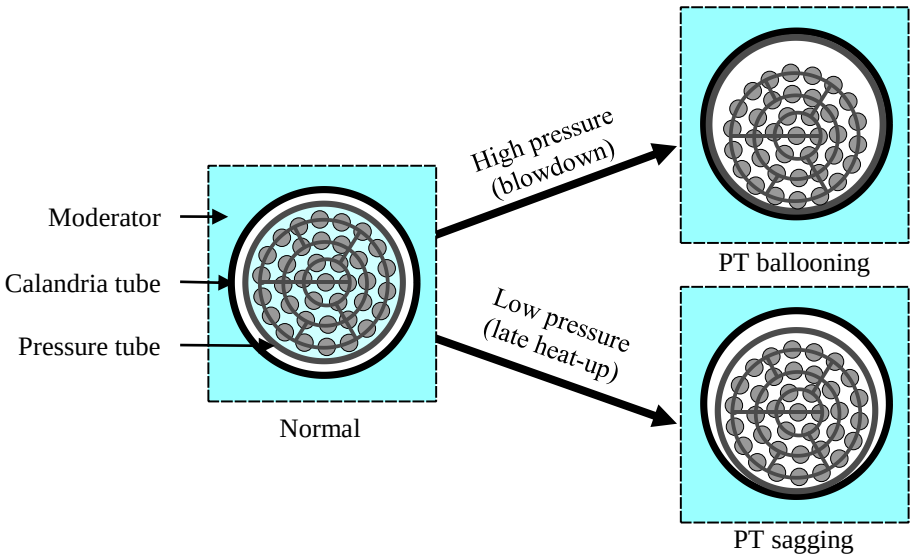

Figure 1-4: Mechanisms for establishing PT/CT contact following a LLOCA

Numerous experimental investigations have been performed to study the boiling heat transfer on the outer surface of the calandria tube following PT-CT contact, including work reported in references [3], [4], [5], [6], and [7]. These investigations reported that the mode of boiling on the calandria tube surface (nucleate boiling, patchy film boiling, entire surface film boiling) was a function of the water temperature and PT contact temperature, with the PT contact temperature reported to be a function of the heating rate and PT pressure [4]. These experiments formed the basis of the 'contact boiling curve' which defines the conditions under which fuel channel integrity is maintained. For a certain PT-CT contact temperature, the fuel channel integrity would be maintained provided that the local moderator temperature falls below the contact boiling curve (i.e. – the moderator is sufficiently subcooled) [7]. In a LOCA scenario with loss of ECC, PT-CT contact is predicted to occur within the first 30 seconds; due to the large volume of the moderator, the temperature distribution (and thus available subcooling) would not have largely changed from regular operating conditions [8]. The temperature distribution in the moderator during regular operating conditions is thus an important safety consideration, in addition to how it evolves in the short period after the LOCA is initiated.

Performing *in situ* moderator temperature measurements in operating CANDU reactors presents numerous difficulties. Austman *et al.* [9] summarized these issues as instrument calibration errors arising from radiation effects on the temperature sensors and difficulties in gaining physical access to the moderator through the vessels and shielding. Radiation effects on the temperature sensors include direct heating by gamma rays, transmutation of sensor materials arising from neutron absorption, and induced voltages in the measurement leads. Accessing the interior of the calandria is also problematic; measurement entry locations would be limited to reactivity mechanism penetrations in the calandria, requiring removal of a reactivity mechanism or use of a spare mechanism penetration if available. The number of available measurement locations at a particular time would be limited to

prevent impairment of systems using these penetrations. Additionally, the available penetrations may not coincide with location where moderator subcooling may be low and hence the usefulness of the measurements may be questioned. Installation and removal of measurement probes would also require a maintenance outage, providing further logistical complications. While some studies have provided limited *in situ* measurements from operating CANDU plants, such as Austman *et al*. [9] and Sion [10], the bulk of the effort in CANDU moderator temperature analysis has focussed on the development, verification, and use of computer modelling tools.

Circulating flows inside the CANDU calandria vessel are difficult to model due to the complex geometry, flow patterns and numerous interacting phenomena. There are combined effects of forced and natural convection in additional to flow across a bank of tubes. Due to the interaction of the inlet jets with the curvature of the calandria vessel, flows from the inlets may enter the tube bank at various angles to the tube bank lattice. Flows inside the vessel span a large range of velocity magnitudes and turbulence levels and in many regions of the core buoyant forces are of similar magnitude to inertial forces. Nevertheless, computer modelling is used to determine the local subcooling and the uncertainties in these predictions must be quantified.

For licensing purposes in the Canadian nuclear industry, a specialized computational fluid dynamics (CFD) code MODTURC_CLAS is used to make predictions of the moderator flow and temperature distributions [11]. Computer modelling tools used for licensing purposes are subject to verification and validation. This process includes tests to determine the tool's accuracy, how well its conceptual models reflect the physical phenomena present in the real system, as well as the range of design parameters which can be applied [12]. In the 1990s and 2000s, extensive experimental programs were undertaken to generate benchmark data for moderator circulation flows for these purposes. These investigations

included several separate effects tests (pressure loss data within a tube bank for flow at various angles, jet development along a curved surface, inlet nozzle velocity profiles) as well as integral tests using a scaled moderator test facility. The moderator test facility (MTF) was created at Atomic Energy of Canada Limited (AECL) as a 1/4 scale mock-up of a CANDU-9 reactor core with 480 electric heaters representing 480 fuel channels [13]. Important non-dimensional numbers were identified to ensure that the test conditions covered those expected in the full-sized reactors. Additionally, the MTF was also reconfigured for moderator inlet conditions representative of Darlington, Bruce B, and Pickering B to generate benchmark data for these reactors [11]. These data were used to validate MODTURC_CLAS and to assess its accuracy in predicting moderator subcooling.

Moderator inlet configurations representative of the four units at Bruce A were not part of the integral tests performed at the MTF; at that time these reactors were in long-term shutdown with no plans to bring them back online. In the past decade, however, the units at Bruce A have been returned to service. The MTF facility no longer exists and thus Bruce A tests at 1/4 scale can no longer be performed. The need for additional experimental benchmark data provided the initial motivation behind the creation of the experimental apparatus used in this study. This facility is described in detail in Chapter 3.

The new facility was constructed at a smaller scale than the previous MTF (approximately 1/16 scale compared to 1/4 scale). At this smaller scale it was not practical to replicate all geometric features within the calandria and certain simplifications were made. For example, the 1/16 scale test section contained a reduced number of tube bank elements (120 tubes in the mock-up compared to 480 calandria tubes in the full-scale reactor), with only the central tube elements heated in order to mimic the higher power levels in the central core region.

1.2 Study Objectives and Scope

This work was funded by the CANDU Owners Group (COG) in order to design and construct a new experimental facility capable of obtaining data experimental relevant to the Bruce A reactors. Of particular importance was assessment of the impacts of the different moderator inlet configuration in the Bruce A calandria on the flow patterns inside the calandria vessel and how well the phenomena included in the CFD models can replicate these changes. While the facility has been constructed, the test data completed, and the report sent to COG, this thesis aims to analyze this data further to assess the importance of scaling between this facility, the MTF, and the full-scale reactors. This includes examination of issues arising from geometric simplifications made for practical reasons (such a reduced number of tube bank elements) as well as issues that arise from a large difference in scale between the model and the facility. The literature review recalls the scaling approach used for the construction of previous 1/4 scale facilities and highlights issues that could arise from further reducing the scale.

The experimental facility consists of an approximately 1/16 scale model of a Bruce A calandria vessel. Since at the outset it was known that scaling issues at this size may be subtle, a wide range of power and flow conditions were included in the test plan in order to study which conditions best represent the full-scale reactor conditions. The present work also includes extensive CFD predictions of the 1/16 scale facility behaviour and compares the temperature and velocity fields to the measurements. The simulations of the small-scale facility are also compared against existing simulations of moderator flow in the full-scale Bruce A calandria to assess similarity between the two facilities.

The experimental measurements obtained in the facility have wider applicability to the nuclear safety analysis field. The literature review examines recent numerical and experimental studies of CANDU moderator flows, showing that recent studies suggested that the flow behaviour is three-dimensional, asymmetric, and unsteady.

However, the modelling approaches have typically relied on time-averaged benchmark data from earlier two-dimensional test facilities due to the lack of published data from the three-dimensional test facilities. While the specific geometry in the small-scale model differs from a typical CANDU-6 vessel, it replicates several phenomena common to both, including three-dimensional flow through a tube bank, interaction of inlet jets with a tube bank at a variety of angles, and the interaction of cool inlet jets with buoyant flows in the tube bank leading to unsteady features.

Therefore, the experimental measurements that are collected will also provide valuable benchmark data from a three-dimensional CANDU calandria-like vessel. These data can be used in future studies for the validation of selected modelling approaches to capture three-dimensional effects. Additionally, the numerical studies conducted as part of this work will demonstrate the effectiveness of current commercially available CFD tools at predicting conditions in a CANDU calandria like vessel over a wide range of combined power and flow conditions.

1.3 Organization

Chapter 2 presents a review of previous experimental and numerical modelling of CANDU moderator inlet flows, with an emphasis on studies representative of normal operating conditions in the reactor. Descriptions of the various small-scale models used to generate benchmark data for the validation of numerical models are provided. Additionally, various numerical studies of moderator flows are reviewed along with the findings relevant to the present work.

Chapter 3 presents a detailed description of the experimental facilities and measurement techniques that were used for the current study, along with an overview of the measurement uncertainties. The range of power and flow conditions that were included in the testing plan are introduced.

Chapter 4 presents details regarding the numerical modelling of the current facility. Unsteady RANS simulations of steady-state conditions within the experimental facility were conducted in order to capture the fluctuating behaviour observed in the temperature measurements. Details regarding the computational mesh are provided along with a study of mesh size and time-step size sensitivity.

Chapter 5 presents the results of the experimental and numerical studies. First, the time-averaged behaviour is presented, with the time-averaged temperature maps gathered at various conditions compared to the simulation results. The transient behaviour is also examined, comparing the maximum observed temperatures in the experiments and simulations for similar conditions. The dependence of local temperature fluctuations on local velocity fluctuations is presented, with level of fluctuations appearing to depend on the local interaction between buoyant flows and the inlet jet inertial flows. The effects of increasing buoyancy significance relative to inlet inertia on the temperature distribution within the vessel is discussed. Comparisons between temperature distributions in the small-scale facility and the full-size Bruce A calandria vessel are also presented.

Chapter 6 presents the conclusions of the present work and discusses suggestions for future work in this area of study.

Chapter 2

Literature Review

2.1 Experimental Studies

2.1.1 In-Core Temperature Measurements

As discussed in section 1.1, the performance of *in situ* moderator temperature measurements presents several practical difficulties. As a result, few instances of in-core moderator temperature measurements have been reported in open literature.

Austman *et al*. reported of the first in-core moderator temperature measurement attempts which were made at the Bruce A Generating Station (Unit 2) [9]. Temperature probes were sealed within a horizontal flux monitor tube, with the moderator circulating around the tube; the probes were not in direct contact with the moderator. The tests ultimately failed due to radiation heating of the flux monitor tube, which resulted in erroneously high temperature readings [9].

Sion performed in-core moderator temperature measurements at the Bruce A Generating Station (Unit 3) operating at 88% full power [10]. The purpose of the experiment was to generate practical benchmark data for the validation of MODCIR, an early tool for the simulation of CANDU moderator flows [10]. Additionally, the study would examine the feasibility of in-core temperature

measurements of the moderator given concerns about radiation effects on the temperature sensors (radiation heating, transmutation, and induced emf) [9].

The measurements were collected using a specialized vertical temperature profile probe which was inserted into the calandria in place of a single shut-off rod. The probe consisted of 15 measuring stations located at 50 cm intervals, with each measurement station consisting of two differently sized K-type thermocouples and a nickel resistive temperature device (RTD). The measurement probe was perforated to allow contact between the temperature probes and the moderator fluid at each measuring station. The probe was located in a region nearest predicted by MODCIR to contain the maximum temperatures in the calandria vessel [14]. Temperatures were seen to increase with vertical position along the probe, suggesting that buoyancy effects were dominant at the selected location. The study showed that in-core temperature measurements with K-type thermocouples were feasible with probes in direct contact with the moderator fluid, but that nickel RTD elements showed significant gamma heating effects.

Two similar temperature probes were installed in unit 5 at the Pickering Generating Station (Pickering B) prior to station commissioning [9]. Following the results of the tests at the Bruce A generating station, the probes used at Pickering B excluded RTD sensors and were located in a shutoff rod penetration and a viewing port. Measurement uncertainty was improved to ±1.4ºC. To the knowledge of the author, the data from these tests were not publicly published in literature.

Table 2-1: Summary of relevant parameters from small-scale integral test facilities as compared to a full scale CANDU-6 calandria

	CANDU-6 (Full Scale)	SPEL	Stern Laboratories	MTF (AECL)	MCT KAERI 1/40	MCT KAERI 1/8	MCT KAERI 1/4	2D MCT
Working fluid	heavy water	salt water	light water	light water	light water	light water	light water	air
Reference power [kW]	1×10^5	10	100	1090	1.839	214.6	1566	N/A
Reference flow rate [kg/s]	1019	0.94	2.4	22.9	0.042	0.863	22.3	0.21
$T_{outlet} - T_{inlet}$ [°C]	23	2.5	9.9	11.4	10	15	17	N/A
Total inlet area [m^2]	4.56×10^{-1}	3.78×10^{-3}	2.44×10^{-3}	2.80×10^{-2}	1.50×10^{-4}	1.88×10^{-3}	2.87×10^{-2}	2.28×10^{-2}
Mean inlet velocity [m/s]	2.04	0.25	1.00	0.82	0.29	0.46	0.81	19
Tank diameter [mm]	7600	740	2000	2115	180	980	1900	1900
Tank length [mm]	6000	254	200	1486	200	200	1500	1230
Tube diameter [mm]	131	38	33	33	18	18	33	32
Tube pitch [mm]	286	75	71	71	37	37	72	70.4
Number of tubes	380	52	440	480	12	380	380	380
Archimedes number (Ar)	0.21	0.092	0.10	0.10	0.21	0.21	0.21	N/A
Dimensionless heat (q^*_{av})	0.013	0.025	0.0076	0.011	0.0053	0.012	0.013	0.012
References	[23]	[15] [16] [19] [20]	[21] [22]	[11] [13] [72]	[23] [26]	[23] [41]	[23] [73]	[30] [31]

2.1.2 Integral Testing Facilities

Several experimental studies have been conducted using small-scale models of the CANDU calandria vessel at a variety of sizes and varying levels of geometric similarity to the full-scale reactor. Earlier studies generally focussed on a simplified two-dimensional geometry by limiting extents in the axial direction, or simplifying the geometry by reducing the number of elements in the tube bank. Generally, all testing facilities tended to maintain the same tube pitch to diameter ratio as CANDU to provide a similar porosity in the tube bank region of the vessel.

The key parameters from various facilities used for these experiments are summarized in Table 2-1; reference values are also included from a CANDU-6 reactor. All of the listed facilities were used to study conditions in a CANDU calandria featuring inlet flow directed upwards along the curved calandria walls, similar to the Pickering B, Bruce B, and CANDU-6 designs. The AECL MTF facility was additionally configured for Darlington and CANDU-9 configurations. None of the listed small-scale models featured inlet configurations representative of the Bruce A calandria vessel.

A key parameter in designing a test facility was matching the ratio of buoyancy forces to inlet inertial forces to conditions, also known as the Archimedes number *Ar*[1]. Later facilities also identified the dimensionless heat source q^* as a scaling parameter. Details regarding the scaling methodology are discussed in section 2.3 on page 31.

[1] The quantity referred to as the Archimedes (*Ar*) number by the Canadian nuclear industry differs from the usual definition. *Ar* is usually defined to represent a ratio of buoyancy forces to viscous forces ($Ar = gD^3(\rho - \rho_0)/(\nu^2\rho_0)$) and is analogous to the Grashof (*Gr*) number. In existing literature sources regarding CANDU moderator flow studies, the *Ar* is typically defined as a ratio of buoyancy to inertial forces ($Ar = g\beta\Delta TD/U_i^2$). The latter definition is closer to the Richardson (*Ri*) number but is calculated using bulk parameters such as calandria vessel diameter, inlet-to-outlet temperature rise, and inlet velocity. For consistency with the existing literature in this field this study uses the latter definition for *Ar*. Further discussion of the scaling parameters follows in section 2.3.

2.1.2.1 Sheridan Park Engineering Laboratory (SPEL) Facility

Experimental investigations were performed in 1983 by Koroyannakis *et al.* at Sheridan Park Engineering Laboratory (SPEL) using a small-scale 'calandria-like vessel' [15]. This facility was not a perfectly scaled model of a CANDU calandria, but contained several features similar to a typical CANDU calandria with upward facing, fan shaped inlet diffusers (similar to Pickering B). The facility consisted of a transparent acrylic cylindrical tank 740 mm in diameter and 254 mm in length. The tube bank array consisted of 52 copper tubes, each 32 mm in diameter and arranged in a 75 mm square array pitch, yielding a similar pitch-to-diameter ratio as used in CANDU. This facility was unique in that heat was generated in the working fluid volumetrically; the copper tube elements acted as electrodes and the working fluid – a mixture of water and sodium chloride – acted as an electrolyte [16]. Temperature measurements were made using fluoroptic temperature probes and flow patterns were visualized using chemical tracer techniques. Results from the SPEL experiments were also later used as benchmark data for several numerical studies, including studies reported in references [16], [17], [18], [19], and [20].

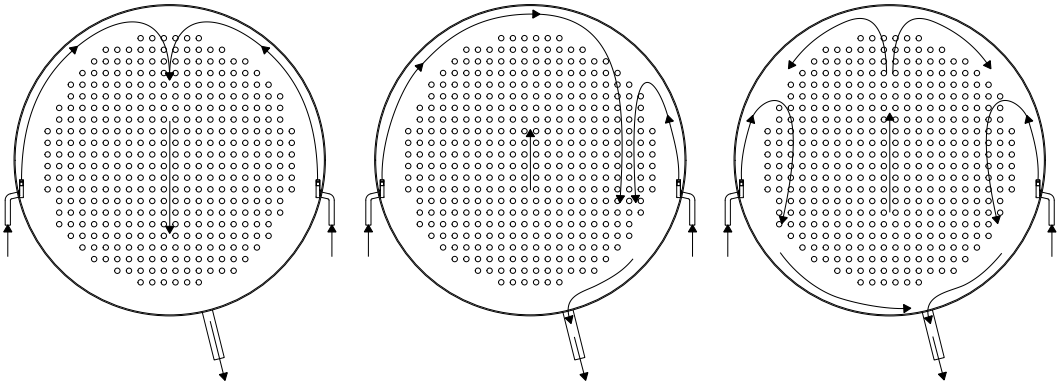

a) JMD b) Mixed c) BD

Figure 2-1: Typical flow pattern types observed in SPEL experiments, including inlet jet momentum dominated (JMD), mixed type, and buoyancy dominated (BD)

Three distinct circulation patterns were observed in the SPEL experiments which depended on the heat generation rate and inlet flow rate as depicted in Figure 2-1. For the isothermal case with no or low heat generation, the 'inlet jet momentum dominated' (JMD) pattern was observed. In this case, inlet jets from the nozzles flow upward along the curved walls of the calandria vessel, meeting at the top where a downward secondary jet is formed at their impingement point. Maintaining the same flow rate, at intermediate power levels the 'mixed' flow pattern was observed. In this case, the presence of upward buoyant flows induced by temperature gradients in the tube bank caused the impingement point of the inlet jets to be shifted to one side of the vessel. At higher powers, the 'buoyancy dominated' (BD) flow pattern was observed. In these cases, the relatively higher strength of the buoyancy flows prevented the inlet jets from either side of the vessel from interacting with each other.

2.1.2.2 Stern Laboratories (SL) 2D Test Facility

In the late 1980s, an experimental facility was built at Stern Laboratories (SL) in order to generate experimental data for the validation of the CFD tool MODTURC_CLAS. Details of regarding the experimental facility were provided by Huget *et al.* [21]. It was constructed of a transparent polycarbonate cylindrical vessel which was 2000 mm in diameter (approximately 1/4 the diameter of a CANDU calandria) and 200 mm in depth, acting effectively as a two-dimensional slice of a calandria vessel. The facility contained 440 tube heaters which were 33 mm in diameter and arranged in a square lattice at a 71 mm pitch, and also contained two upward facing inlet nozzles. The heaters were described as operable as DC resistance heaters, or as AC electrodes for volumetric heating similar to the SPEL experiment [21]. Heating loads of up to 150 kW and mass flow rates of up to 4 kg/s were possible. Velocity measurements were made using laser Doppler velocimetry (LDV); additional flow visualization was performed with a dye tracer technique using a pH indicator. Temperatures were measured using thermocouples.

Isothermal experiments showed a similar JMD flow pattern as previously observed in the SPEL experiments. For equal flow rates from each nozzle the flow pattern was symmetric about the vertical axis, with the impingement point of the two jets at the top of the vessel; the impingement point was observed to fluctuate a small amount over time in a range of 0 to 10º from the vertical [21]. The position of the impingement point could also be altered continuously by introducing a flow imbalance to the two inlet nozzles [21].

Heated tests were performed at a power level of 100 kW (with the heaters in DC mode) and a mass flow rate of 2.4 kg/s (corresponding to an inlet jet velocity of 1 m/s), and an outlet temperature of 65ºC; these conditions correspond to an Archimedes number of 0.10 and were reported as representative of those in a CANDU calandria [22]. For symmetrical inlet flow, an asymmetric flow pattern similar to the 'mixed' pattern identified in the SPEL experiments was observed, with the impingement point of the nozzles shifted approximately 50º off of vertical. It was also noted that the peak temperature within the flow field was 72ºC and that the average temperature was above the outlet temperature [22]. This implied that mixed or non-symmetric flow patterns are present in a CANDU calandria even with symmetrical inlet and outlet geometries. A test for the same inlet flow and power conditions was conducted with the addition of a vertical dividing wall at the centre of the vessel. With enforced symmetry, lower temperatures were observed and the peak temperature was 67ºC. This result implied that enforced symmetry had a favourable effect on moderator subcooling [22].

2.1.2.3 AECL Moderator Test Facility (MTF)

The moderator test facility (MTF) was constructed at AECL Chalk River Labs as a 1/4 scale, three-dimensional experimental model of a CANDU-9 calandria vessel with 480 electric heaters representing 480 fuel channels [13]. Additionally, the MTF was also reconfigured for moderator inlet conditions representative of Darlington, Bruce B, and Pickering B to generate benchmark data for these reactors

[11]. Temperatures in the MTF were measured using thermocouples and 3D velocity measurements were made using a submersible laser Doppler velocimetry probe.

The scaling methodology used for the design of the MTF identified the Archimedes number *Ar* (representing the ratio of buoyancy to inertial forces) and the dimensionless heat source q^* as the key scaling parameters. This scaling methodology has been used in the design of subsequent small-scale test facilities and is described in detail in section 2.3 on page 31.

Limited temperature and velocity measurements from CANDU-9 relevant tests in the MTF and comparisons to predictions from MODTURC_CLAS were reported by Carlucci *et al.* [13]. In the CANDU-9 design, moderator flow entered the calandria through downward facing fan-shaped nozzles located along the vessel walls and exited through four outlet ports located at the top. In this configuration, the inlet jets would flow downwards along the calandria walls and recirculate upward through the tube bank, assisting buoyant flows in the tube bank. Under steady-state and nominal flow and power conditions, upward flows were measured throughout the tube bank. The temperature field was noted to largely be two-dimensional and increasing from the bottom to the top of the core [13].

The test plan for configurations relevant to Pickering B and Bruce B included several steady-state conditions (isothermal, 50% power, 100% power), flow imbalance tests, sensitivity tests to examine the transition between JMD and BD flow patterns, and transient-tests to simulate power rundowns [11]. To the knowledge of the author, the experimental results relevant to the Pickering B, Bruce B, and Darlington reactors have not been published in literature and are available only in unpublished industry reports.

2.1.2.4 KAERI Moderator Circulation Test (MCT) Facility

The Korean Atomic Energy Research Institute (KAERI) undertook an experimental research program to study moderator circulation in CANDU-6 calandria vessels in support of the development of CFD tools to be used for reactor licensing purposes in Korea [23]. The research program included the construction of a 1/4 scale facility; the scaling methodology was described by Rhee *et al*. [24] and followed the approach taken earlier by Khartabil *et al*. The facility contained 380 electric heaters with a cosine axial power profile and two radial power zones. Velocity measurements were made using particle image velocimetry (PIV) and temperature measurements were made using thermocouples [23]. Laser induced fluorescence (LIF) measurements of temperature fields were planned but not yet reported for the 1/4 scale facility.

Two smaller facilities at approximately 1/40 scale and 1/8 scale were also constructed. These facilities were not intended to be accurate scale models but were intended to provide a test bed to explore potential difficulties that would be encountered with using PIV and LIF measurement techniques in the 1/4 scale facility [25]. In the typical measurement arrangement for PIV, a planar laser sheet is used to illuminate tracer particles in the flow. Similarly, LIF measurements rely on the excitation of a fluorescent tracer dye in the flow field. Opaque objects in the path of the laser sheet would cause shadows, limiting the regions where measurements would be possible. Kim *et al.* [26] and Im *et al.* [27] reported on difficulties with PIV and LIF measurements in the shadow regions in the tube bank during isothermal testing. These difficulties led to the development of customized tube bank elements which contained internal light-sheet optics, allowing the laser-sheet to be emitted from the tube itself [28] [29].

Im *et al*. [27] reported PIV measurements of the velocity field in a plane corresponding to the region above the tube bank, near the impingement point of two inlet jets under isothermal and heated conditions for the 1/4 scale MCT. They

reported that for isothermal conditions and balanced flow rates from the nozzles, the impingement point was observed to fluctuate in position over time and was centered occur at the top of the vessel; the position could be biased to the left or right by introducing a left-right flow imbalance. These observations matched those made earlier by Huget *et al.* [21]. Heated tests were also performed corresponding to Ar = 0.06, 0.08, 0.12, and 0.16. The addition of heat was observed to cause the impingement point to shift off center to the left or right, with the bias related to Ar; a larger Ar value (i.e. – greater relative importance of buoyancy effects to inlet inertial effects) yielded a larger shift in the impingement point position. The impingement point position was observed to be more stable at higher values of Ar [27]. This asymmetric flow pattern corresponded to the 'mixed' flow pattern as reported in earlier experiments.

Repeat measurements were also performed for multiple combinations of power input and flow corresponding to Ar = 0.08 and found that the level of bias in the impingement point after the addition of heat was comparable in each case [27]. This result confirmed that for this given flow configuration, the Archimedes number was capable of predicting the flow condition in the moderator vessel.

The direction of the bias after the addition of heat was shown to be influenced by small left/right flow imbalances in the flow before heat was added. For example, if a small inlet flow balance was adjusted to shift the impingement point to favour one direction under isothermal conditions, the addition of heat caused the impingement point to shift further in the favoured direction. Hysteresis was also observed in the flow pattern; following the addition of heat, a large opposite flow imbalance was required to shift the impingement point in the other direction. This was in contrast to isothermal conditions where the bias of the impingement point could be adjusted continuously by altering the left/right flow balance [27]. These results suggested that the introduction of buoyant flows had a stabilizing effect on the flow distribution in the vessel.

2.1.2.5 2D MCT (Air)

Atkins *et al*. [30] described a simplified version of the 1/4 scale MCT which was constructed at the University of Witwatersrand. The primary focus of the facility was to study mixed convection heat transfer in a CANDU-6 calandria vessel under LOCA conditions following PT-CT contact which differs from the objectives of the work presented in this thesis. However, a description of the facility is provided for reference.

The facility used ambient temperature air as the working fluid as opposed to water and simplified inlet geometry. The inlets consisted of two slot jets (19 mm by 600 mm each) in place of the eight fan-shaped diffuser nozzles, simplifying the flow behaviour as more two-dimensional [30]. The vessel contained up to 380 unheated PVC tubes. To represent regions where PT-CT contact had occurred, a limited number of tube elements had a 340 mm long section replaced with a heated glass tube; the heated section would represent the section of calandria tube with an elevated surface heat flux following the PT-CT contact. Tube surface temperatures were monitored using thermocouples. Atkins *et al.* justified their use of air as the working fluid noting that the Prandtl number *Pr* of air was similar to water vapour and that mixed convective heat transfer in air could be comparable to film boiling heat transfer in water as a result [30].

Kim *et al*. performed measurements of the secondary jet generated by the interaction of the two inlet jets under isothermal conditions in this facility and compared the results to measurements from the KAERI MCT using water at comparable values for inlet jet *Re* number over a range of $10\,000 < Re < 50\,000$ [31]. The results showed that the peak velocity of the secondary jet was roughly 50% of the mean exit velocity of the inlet nozzle, located near the first row of tubes in the tube bank. The secondary jet velocity was also observed to decay to approximately 10–15% of the inlet jet velocity at the centre of the vessel, with the result being independent of *Re* [31].

2.1.3 Tube Bank Pressure Drop Experiments

As described in section 2.2.1, the industry standard code MODTURC_CLAS used a porous medium approach to modelling the tube bank in the calandria vessel. The porosity γ is defined as the ratio of the fluid occupied volume to the total volume. A typical CANDU calandria features calandria tubes arranged in a square lattice with a pitch-to-diameter ratio of 13/6, which corresponds to a porosity of approximately 0.83:

$$\gamma = \frac{L\times\left(\left(\frac{13}{6}d_t\right)^2 - \frac{\pi d_t^2}{4}\right)}{L\times\left(\frac{13}{6}d_t\right)^2} = 1 - \frac{9\pi}{169} \approx 0.83 \tag{2.1}$$

The local velocity in the porous medium V_l can be related to the velocity upstream of the tube bank V_m by [32]:

$$V_m = \gamma V_l \tag{2.2}$$

Several experiments were performed to develop correlations for the frictional pressure drop within the calandria tube bank to be used in the porous medium model. Additionally, this data was also used by several researchers to benchmark the ability of various turbulence models to predict the pressure drop in the calandria tube bank in later numerical studies which resolved each tube bank element. These numerical studies are discussed in section 2.2.4.

The correlation for the pressure loss coefficient (PLC), which equals the pressure drop divided by the product of the number of tube rows N_t and the dynamic head, is shown Equation 2.3 [32]. The Reynolds number *Re* used the tube diameter d_t as the reference length and the velocity upstream of the tube bank V_m as the reference velocity.

$$PLC = \frac{\Delta P}{N_t \rho \frac{V_m^2}{2}} = a \times Re^b \tag{2.3}$$

$$Re = \frac{V_m d_t}{\nu} = \frac{\gamma V_l d_t}{\nu} \tag{2.4}$$

Table 2-2: Coefficients for the pressure loss coefficient correlation shown in Equation 2.3

Source	Direction	*a*	*b*	Range
Hadaller et al. [32]	90º / 45º	4.54	-0.172	2000 < Re < 9000
Khartabil et al. [11]	90º	9.52	-0.258	5000 < Re < 50 000
Khartabil et al. [11]	60º	6.09	-0.231	5000 < Re < 50 000
Khartabil et al. [11]	30º	2.33	-0.218	5000 < Re < 50 000

The SL facility was used by Hadaller *et al.* to develop a correlation for frictional pressure drop in the tube bank for aligned and staggered configurations [32]. For the in-line tube bank configuration, a rectangular channel was inserted into the vessel spanning the height of the vessel (24 tube rows) and encompassing four tube columns; for the staggered tube bank configuration, the test apparatus was rotated 45º. Flow with a uniform flow profile entered the top of the channel and exited at the bottom. Hadaller *et al.* reported that a single correlation for PLC fit the in-line and staggered tube bank configurations well.

Khartabil *et al.* later performed additional tests at higher *Re* (5000 < *Re* < 50 000) for flow at 90º (in-line), at 60º, and at 30º to the tube bank. They reported agreement within ± 3% with the correlation from Hadaller *et al.* for *Re* < 10 000 for flow at 90º, but reported that the PLC decreased with decreasing flow angle [11].

2.2 Numerical Studies

2.2.1 Background

The wide range of geometrical dimensions and the flow structures of various length scales in the calandria vessel of CANDU reactors necessitate a high-fidelity grid and large computational resources in the numerical computations. Until relatively recently it was not feasible to model the geometry of all 380 – 480 tubes located in the calandria. In the past many numerical studies modelled the tube bank matrix as a porous medium in order to reduce computational requirements. Using this

strategy, the bank of calandria tubes is modelled as a continuous region with an added frictional pressure drop. As discussed in section 2.1.3, experimental work was undertaken to develop correlations for frictional pressure loss in the calandria tube bank and is shown in Equation 2.3. Additionally, the Boussinesq approximation is often employed, in which the fluid volume is assumed to be incompressible with a constant density aside from small variations in the buoyancy term in the momentum conservation equation (further details are provided in section 2.3).

The former utility Ontario Hydro was involved in the early development of simulation tools used to study moderator circulation. MODCIR (short for MODerator CIRculation code) was an early code which used a porous medium approach and did not include turbulence modelling; reported examples of results were calculated on a mesh of 4000 – 6000 nodes [33]. Later development on MODCIR let to its successor MODTURC (short for MODerator TUrbulent Circulation code), which employed k-ε turbulence modelling and typically solved problems on a mesh of approximately 10 000 nodes [21]. In 1990, the successor to MODTURC was developed jointly between Ontario Hydro and Advanced Scientific Computing in order to develop MODTURC_CLAS (short for MODerator TUrbulent Circulation, Co-Located Advanced Solution). MODTURC_CLAS improved upon MODTURC with enhancements such as allowing non-orthogonal meshes, improving the efficiency of the numerical solvers, and more accurate discretization schemes [21]. Validation of MODTURC_CLAS was performed using experimental benchmark data, such as the work previously described in sections 2.1.1, 2.1.2.2, 2.1.2.3, and 2.1.3. For moderator safety analysis related to licensing purposes in the Canadian nuclear industry, MODTURC_CLAS currently remains as an industry standard tool.

Outside of the safety analysis performed for licensing purposes in the Canadian nuclear industry, other studies have employed commercial CFD packages using a

porous medium approach to modelling the tube bank geometry. Drawbacks of the porous medium approach include the inability to predict local flow effects around individual tubes, such as the generation of turbulence in the wake regions of the tube elements [34]. More recently, advances in computational power have allowed larger mesh sizes to be feasible, allowing the entire tube bank geometry to be resolved.

A list of selected numerical studies of moderator flow in the calandria is presented in Table 2-3. The majority of the reported studies have focussed on the typical moderator inlet arrangement common to the Pickering B, Bruce B, and CANDU-6 reactors. There is consensus among studies that the three distinct flow patterns are possible: jet momentum dominated (JMD), buoyancy dominated (BD), and mixed type as introduced in section 2.1.2.1. The flow pattern has been shown to depend on the *Ar* by many, including Carlucci and Cheung [35] and Mehdi Zadeh *et al.* [36]. Recent studies have also suggested that the flow pattern is unsteady with time (Sarchami et al. [37], Mehdi Zadeh et al. [36]) and asymmetric in all three dimensions (Sarchami et al [37]).

Table 2-3: Summary of selected modelling studies of full calandria behaviour (CANDU and small-scale facilities)

Reference	Inlet Geometry	2D/3D	Tube Bank Model	Code	Turbulence Model	Mesh Size	Time Step	*Ar*	Notes
Carlucci [75]	Typical CANDU	2D	porous	TEACH	high Re k-ε	1020	steady	0 – 0.35	Imposed symmetry plane
Sion [10]	Bruce A	3D	porous	MODCIR	laminar	not reported	steady	0.20	Reported single temperature profile
Huget *et al.* [22]	SL MTF	2D	porous	MODTURC_CLAS	standard k-ε	2205	steady	0.10	Validation against 2D facility
De *et al.* [8]	CANDU-6	3D	porous	PHOENICS2	standard k-ε	9180	steady	0.21	Quasi-steady state solution
Carlucci *et al.* [13]	AECL MTF	3D	porous	MODTURC_CLAS	standard k-ε	135 792	steady	not reported	CANDU-9 configuration
Yoon *et al.* [74]	CANDU-6	3D	porous	CFX-4.4	standard k-ε	19 504	steady	0.21	Grid independence not achieved
Kim *et al.* [19]	CANDU-6	3D	resolved	FLUENT	standard k-ε	830 000	steady	0.21	
Sarchami [40]	Bruce B	3D	resolved	FLUENT	RNG k-ε	3.2M	0.01s	0.10	
Sarchami [40]	AECL MTF	3D	resolved	FLUENT	RNG k-ε	3.2M	0.01s	0.10	Volumetric and surface heating comparisons
Seo *et al.* [41]	KAERI MCT	3D	resolved	CFX-V13	k-ε, k-ω	4.2M	steady	isothermal	1/8 scale facility
Mehdi Zadeh *et al.* [36]	CANDU-6	2D	resolved	Code_Saturne	standard k-ε	3.5M	0.01 s	0 – 0.35	Did not use Boussinesq
Mehdi Zadeh *et al.* [47]	CANDU-6	3D	resolved	Code_Saturne	standard k-ε	30M	steady	0.01, 0.05, 0.12	Did not use Boussinesq
Kim *et al.* [31]	KAERI MCT	2D	resolved	CFX-V15	k-ω *SST*	892 500	N/A	isothermal	1/4 scale facility

2.2.2 Temperature Fluctuations

Sarchami *et al.* [38] performed simulations to investigate temperature fluctuations that were observed in the AECL MTF 1/4 scale facility. The three-dimensional, transient simulations were performed with FLUENT V12 on an unstructured tetrahedral mesh with 3.2 million elements and used the RNG k-ε turbulence model. The length of the simulated transient was 150 s, with a timestep size of 0.01 s.

Sarchami *et al.* [38] reported that fluctuations were characterised by amplitude and frequency and depended on the local conditions in the vessel. Large amplitude fluctuations were associated with interactions at the boundaries between cold inlet flows and hot buoyant flows (e.g. – near the top of the calandria tube bank, near the secondary inlet jet penetration). Small amplitude fluctuations were associated with regions with low temperature gradients in the central and lower parts of the vessel. High frequency fluctuations were associated with high velocities in regions where wall jet flows interact at the top of the vessel and low frequency fluctuations were associated with low velocity regions lower in the core. Simulations of the full-size calandria using volumetric heating were later reported and exhibited comparable characteristics [37].

Medhi Zadeh *et al*. [36] noted cyclical behaviour occurring on time scales of approximately 60 minutes in a reported experimental temperature record from the AECL MTF.[2] They performed 2D transient simulations of a CANDU-6 calandria over a range of *Ar* and a transient length of 5000 s. Simulations were performed using Code_Saturne on 3.5 million element mesh with a timestep of 0.01 s and employed the standard k-ε turbulence model. Temperature and velocity results were reported for a probe located at the centre of the tube bank and the dominant frequency of behaviour at this location was mapped to *Ar*. The results showed that

[2] Full experimental results from the AECL MTF have not been published in literature. However, a single long time-scale temperature record from the experimental data was reproduced and reported by Sarchami [40].

the amplitude and frequency of fluctuations was very low for $Ar < 0.01$ (momentum dominated) and for $Ar > 0.12$ (buoyancy dominated). For conditions in the mixed region, the dominant frequency for temperature peaked at a value of 0.003 Hz for $Ar = 0.07$. The secondary inlet jet was also observed to fluctuate in position over time with a similar frequency between approximately 5º off vertical and approximately 45º. On this time scale (i.e. – on the scale of 300 – 500 s), temperatures were seen to vary over a range of 37ºC. The lower temperatures at the centre of the vessel were associated with high fluid velocities, associated with movement of the secondary inlet jet to the top of the vessel, resulting in greater cooling. These results demonstrated that long time-scale fluctuations may exist for the expected 'mixed' flow conditions in the calandria which would necessitate long simulation or experimental measurement durations.

2.2.3 Surface Heating Compared to Volumetric Heating

Within a CANDU calandria, heat is deposited in the moderator through neutron thermalization and gamma ray heating from fission products. This heat source is volumetrically distributed throughout the moderator, with the local volumetric heat generation rate related to the local fuel channel power. These conditions are difficult to replicate in an experimental setting. With the exception of the tests in the SPEL facility, the reported small-scale experimental results as shown in section 2.1.2 have used tube elements with heated surfaces to represent calandria tubes.

In order to examine the effects of using surface heating over a volumetric heat source, Sarchami *et al*. [39] performed simulations AECL MTF (with Bruce B representative inlets) using both heating methods. The numerical approach was the same as the study reported in their previous studies in [38] with further details reported by Sarchami in reference [40]. Sarchami *et al*. [39] noted high tube surface temperatures as expected for the surface heating case as a result of a surface heat flux at the tube surfaces; this is in contrast to the volumetric heat source case where the heat generation is distributed more evenly throughout the fluid domain. This

resulted in larger temperature gradients and higher overall maximum temperatures in the surface heating case. This suggested that buoyancy forces were more significant for the surface heating case.

Sarchami *et al* [39]. also observed temperature and velocity fields on several planes, including axial planes corresponding to the inlet jets. Both cases showed the asymmetric 'mixed' flow pattern as shown in Figure 2-1, however the impingement point where the inlet jets interacted was pushed further to the side. This behaviour was consistent with more significant buoyancy effects caused by larger temperature gradients within the vessel.

2.2.4 Turbulence Model Comparisons

Seo *et al*. [41] performed 3D simulations of the 1/8 scale KAERI MCT under isothermal conditions using CFX V13 with using both standard k-ε and k-ω models. The results of the simulation were compared to PIV measurements made in the corresponding experimental facility. Comparisons to PIV measurements were limited to the near-wall regions of the vessel and regions near the top of the tube bank due to laser access considerations (see section 2.1.2.4). In these regions, the k-ω model was reported to more accurately describe the qualitative flow field which was attributed to the model ability to accurately predict the wall boundary layer flows.

Conversely, Kim *et al*. [31] performed isothermal simulations of the flow inside the 2D 1/4 scale MCT facility (described in section 2.1.2.5) using CFX V15 and employing the k-ω SST model. This experimental facility used air as a working fluid. Simulations results were compared to hot-wire anemometry velocity measurements from the experimental facility. They reported that with the default model parameters, the k-ω SST underpredicted the dissipation of the secondary jet in the tube bank. This resulted in overpredicted velocities down the centerline of

the tube bank. Kim *et al*. [31] were able to improve agreement with the experimental data by tuning the turbulence model parameters.

The tube bank pressure drop experiments performed by Hadaller *et al*. [32] have been used in several studies to benchmark the ability of various turbulence models to predict flow around the calandria tubes. Teyssedou *et al.* [42] performed 2D simulations using Code_Saturne to compare the performance of the standard k-ε, realizable k-ε, k-ε RNG, and k-ω models. They reported that for the staggered tube bank configuration, all models were able to predict the pressure drop within ±30%, with the k-ω model overpredicting the pressure drop while the k-ε models underpredicted the pressure drop. All models were reported to perform poorly for the in-line configuration, underpredicting the pressure drop by 40 – 70%.

Kim *et al*. [43] performed 2D and 3D simulations of the in-line tube bank experiments using COMSOL, CFX, and OpenFOAM to compare the performance of the performance of the standard k-ε, standard k-ω, k-ω SST, and Spalart-Allmaras turbulence models. For the 2D experiments, they reported the similar poor performance of all models at predicting the pressure drop that was noted by Teyssedou *et al* [42]. Better performance was noted in the 3D simulations, with the k-ε model best predicting the pressure drop; the pressure drop was underpredicted within 1 – 16% with better agreement at higher *Re*. The Spalart-Allmaras model was noted to perform well at low *Re*, predicting the pressure drop within 5%, but performed poorly at higher *Re*, overpredicting the pressure drop by 47%. Given that flow within the calandria tube bank was expected to be turbulent, the k-ε model was recommended.

2.2.5 Bruce A Specific Studies

To the knowledge of the author, few studies have been presented in literature with regards to the specific inlet configuration for the Bruce A calandria vessel. As discussed in section 2.1.1, MODCIR was used to predict the temperature fields in

the Bruce A unit 3 calandria vessel prior to the in-core temperature measurements reported by Sion [10] in order to select a location of interest where the temperature probe would be installed. The measurements were also compared to predictions made using MODCIR, with the predicted temperatures falling within 3 – 5ºC of the measurements, compared to a measurement uncertainty of ± 2ºC. MODCIR tended to underpredict temperatures near the top of the core and overpredict temperatures near the bottom of the core [10]. The experimental results from this study were later used by Vuong *et al.* in a validation exercise for MODTURC_CLAS [14]. The results of this validation study have not been published in literature.

In parallel with the present study on the small-scale facility used for this study, numerical simulations of the full-scale Bruce A calandria vessel were performed by Ashgriz and Behzad [44]. Unsteady RANS simulations of the Bruce A calandria vessel were performed under isothermal and 88% full power conditions using STAR-CCM+ on a 20 million element mesh using the realizable k-ε turbulence model. Comparisons between results of these simulations and simulations of the small-scale facility are presented in Chapter 5 section 5.5.

2.3 Test Facility Scaling Approach

2.3.1 Scaling Considerations

As introduced in section 1.1, flow behaviour in the CANDU calandria vessel is complex and three-dimensional, with combined effects of forced and natural circulation and flow through a tube bank. Within the vessel there exist numerous interacting phenomena at various velocity and length scales which complicate the design of a small-scale test facility while maintaining similitude to the full-scale case.

First, considering a fully buoyancy driven case, a key similarity parameter is the Grashof number (Gr), describing the ratio of buoyancy forces to viscous forces:

$$Gr_L = \frac{g\beta\Delta T L^3}{\nu^2} \tag{2.5}$$

In this case, it can be seen that *Gr* depends on the cube of the length scale *L*. Next, considering the scaling of a purely momentum driven case (i.e. – no heat generation), a key similarity parameter is the Reynolds number (*Re*), describing the ratio of inertial forces to viscous forces. For a selected length scale *L* and reference velocity U_0, *Re* is given by equation 2.6 and depends linearly on *L*:

$$Re_L = \frac{U_0 L}{\nu} \tag{2.6}$$

In the case of flow within the CANDU moderator, both buoyancy and inertial effects are important, leading to a practical difficulty while maintaining both *Re* and *Gr* similarity (i.e. – buoyancy and inertial effects scale differently with a reduction in the length scale *L*). For a 1/4 reduction in scale, the reference temperature difference ΔT would need to be 64 times larger in order to maintain a similar *Gr* given a similar working fluid viscosity. With a typical CANDU moderator having an inlet to outlet temperature rise on the order of 30ºC, matching *Gr* in a small-scale model becomes unrealistic for any sizeable reduction in scale.

In studies of mixed convective flows, the Richardson number (*Ri*) can be used to describe the relative importance of buoyancy and inertial effects:

$$Ri = \frac{Gr}{Re^2} = \frac{g\beta\Delta T L}{U_0} \tag{2.7}$$

The expression in Equation 2.7 assumes that a single length scale *L* is adequate in describing the behaviour in the system. However, there exist various important length scales within the calandria, with varying significance to momentum and buoyancy:

- *Tube bank height:* For a given temperature difference, the height of the heated region of the tube bank influences the temperature gradient responsible for driving buoyancy forces.
- *Tube bank spacing (minimum cross section):* the size of the gap between tube bank elements would influence the maximum velocity (and in turn, flow momentum) within the tube bank.
- *Tube bank bypass area:* the spacing between the edge of the tube bank and vessel wall influences the relative amount of flow which bypasses the tube bank, impacting the level of interaction between inlet jet flow and buoyant flow.
- *Inlet jet hydraulic diameter:* For a given volumetric flow rate, the hydraulic diameter of the inlet jets influences the inlet jet momentum entering the vessel.

Similarly, the selection of a reference velocity and temperature difference to represent the vessel internal momentum and buoyancy effects can be problematic, since the internal temperatures and velocities of the full-scale CANDU reactor are not inherently known. The maximum velocity entering the tube bank, for example, could be used to represent flow momentum. However, this velocity depends on the inlet jet development before interaction with the tube bank, as well as interaction with rising buoyant flow above the tube bank.

From the above discussion, it can be seen that maintaining similarity between a full-sized CANDU calandria vessel and a scaled facility is difficult due in part to competing length scale requirements for buoyancy and momentum effects. Nonetheless, scale-models have historically played a key role in the study of CANDU moderator flows. The approach taken to design the AECL MTF at 1/4 scale is reviewed below in section 2.3.2.

2.3.2 AECL MTF Scaling Methodology

The scaling procedure that was used for the design of the 1/4 scale MTF constructed at Atomic Energy of Canada Limited (AECL) was described by Khartabil *et al*. and is summarized below [11]. The moderator is assumed to be incompressible with constant fluid properties, aside from density variations which drive buoyancy forces (Boussinesq approximation). For this case, the conservation equations for mass, momentum, and energy are:

$$\nabla \cdot V = 0 \tag{2.8}$$

$$\frac{\partial V}{\partial t} + (V \cdot \nabla)V = -\frac{1}{\rho_{ref}}\nabla P + \frac{\mu}{\rho_{ref}}\nabla^2 V + g\left(\frac{\rho - \rho_{ref}}{\rho_{ref}}\right) \tag{2.9}$$

$$\frac{\partial T}{\partial t} + (V \cdot \nabla)T = \frac{k}{\rho_{ref} C_P}\nabla^2 T + \frac{q'''}{\rho_{ref} C_P} \tag{2.10}$$

The equations above are made dimensionless by defining these dimensionless parameters:

$$V^* = \frac{V}{U_i} \qquad T^* = \frac{T - T_{ref}}{\Delta T} \qquad P^* = \frac{P}{\rho_{ref} U_i^2}$$

$$t^* = \frac{t U_i}{D} \qquad \nabla^* = \frac{D}{\nabla} \qquad q^* = \frac{q'''(x,y,z,t) D}{\rho_{ref} C_P U_i \Delta T}$$

$$Re = \frac{\rho_{ref} U_i D}{\mu} \qquad Pr = \frac{\mu C_P}{k} \qquad Ar = \frac{|g| \beta \Delta T D}{U_i^2}$$

Here, the calandria diameter is taken as the reference diameter D, the reference velocity is taken as the average inlet velocity U_i, and the temperature difference is evaluated as the temperature rise between the inlet and outlet $\Delta T = (T_{out} - T_{in})$. The volumetric thermal expansion coefficient β is also introduced:

$$\beta = -\frac{1}{\rho}\left(\frac{\partial \rho}{\partial T}\right)_P \approx -\left(\frac{\rho - \rho_{ref}}{\rho_{ref} \Delta \mathrm{T}}\right) \tag{2.11}$$

The mass, momentum, and energy equations in Equations 2.8 through 2.10 are rewritten as:

$$\nabla^* \cdot V^* = 0 \tag{2.12}$$

$$\frac{\partial V^*}{\partial t^*} + (V^* \cdot \nabla^*)V^* = -\nabla^* P^* + \frac{1}{Re}(\nabla^*)^2 V^* - Ar\frac{g}{|g|}T^* \tag{2.13}$$

$$\frac{\partial T^*}{\partial t^*} + (V^* \cdot \nabla^*)T^* = \frac{1}{RePr}(\nabla^*)^2 T^* + q^* \tag{2.14}$$

Khartabil *et al.* [11] pointed out that the solution to Equations 2.12 through 2.14 would depend on the Reynolds number *Re* (ratio of inertial forces to viscous forces in the fluid), the Prandtl number *Pr* (ratio of momentum diffusivity to thermal diffusivity), the Archimedes number *Ar* (ratio of buoyancy forces to inertial forces)[3], and the dimensionless heat source q^* [11]. Similarity between the full-size and the scaled facility exists provided that geometric similarity, dimensionless boundary conditions, and that the parameters *Re*, *RePr*, *Ar*, and q^* are maintained. However, there exist practical limitations which preclude maintaining similarity for both *Ar* and *Re*, as previously introduced in section 2.4.1. Considering the definition described above for the facility *Re* using the vessel diameter as the reference length:

$$\left(\frac{\rho_{ref} U_i D}{\mu}\right)_{MTF} = \left(\frac{\rho_{ref} U_i D}{\mu}\right)_{CANDU}$$

$$\frac{U_{i_{MTF}}}{U_{i_{CANDU}}} = \left(\frac{D_{CANDU}}{D_{MTF}}\right)\left(\frac{\rho_{CANDU}}{\rho_{MTF}}\right)\left(\frac{\mu_{MTF}}{\mu_{CANDU}}\right) \tag{2.15}$$

Equation 2.15 states that in order to maintain *Re* similarity, the inlet velocity increases proportionally with the facility diameter decrease (e.g. – the inlet velocity

[3] As indicated in note 1 on page 14, this differs from the conventional definition of the Archimedes number. The definition listed above is more in-line with the Richardson number ($Ri = Gr/Re^2$) and is used in this discussion for consistency with existing CANDU moderator flow literature sources.

would increase by a factor of four for a 1/4 scale facility). Next, considering *Ar* equivalence and substituting the result from Equation 2.15 yields:

$$\left(\frac{|g|\beta\Delta TD}{U_i^2}\right)_{MTF} = \left(\frac{|g|\beta\Delta TD}{U_i^2}\right)_{CANDU}$$

$$\frac{\Delta T_{MTF}}{\Delta T_{CANDU}} = \left(\frac{U_{i_{MTF}}}{U_{i_{CANDU}}}\right)^2 \left(\frac{D_{CANDU}}{D_{MTF}}\right)\left(\frac{\beta_{CANDU}}{\beta_{MTF}}\right)$$

$$\frac{\Delta T_{MTF}}{\Delta T_{CANDU}} = \left(\frac{D_{CANDU}}{D_{MTF}}\right)^3 \left(\frac{\rho_{CANDU}}{\rho_{MTF}}\right)^2 \left(\frac{\mu_{MTF}}{\mu_{CANDU}}\right)^2 \left(\frac{\beta_{CANDU}}{\beta_{MTF}}\right) \qquad (2.16)$$

The result in Equation 2.16 shows that to maintain both *Re* and *Ar* when scaling the facility, the temperature difference between the inlet and outlet increases cubically with the diameter decrease (e.g. – ΔT would increase by a factor of 64 for a 1/4 scale facility). This constraint is not workable at 1/4 scale; for a typical CANDU moderator ΔT on the order of 30ºC [14], this would result in a scaled facility ΔT of nearly 2000ºC. Instead, Khartabil *et al.* [11] relaxed the requirement on *Re* similarity between the full-size reactor and the scaled facility. The approach taken was to maintain *Ar* and q^* similarity, select a ΔT and facility size such that energy input was feasible given power supply constraints, and ensure that *Re* was high enough to ensure turbulent flow throughout the facility. It was argued that while relative contributions from the momentum diffusion term from Equation 2.13 and the energy diffusion term from Equation 2.14 would not be matched in the scaled facility, the contribution of these terms to the overall system was negligible for large enough values of *Re* [11].

As discussed in section 2.1.2.4, a 1/4 scale facility representative of a CANDU-6 calandria was constructed at the Korean Atomic Energy Research Institute (KAERI). As reported by Kim and Rhee [23], the facility was designed using a similar scaling procedure to that described by Khartabil *et al*. Rhee *et al*. revisited the scaling procedure and argued that it would be difficult to ensure that flow would

be turbulent throughout the entire volume under steady and transient conditions without first performing CFD analyses for both geometries [45].

2.4 Discussion

2.4.1 Scaling Parameters

As discussed in section 2.3, Both *Ar* and *Re* similarity cannot feasibly be maintained in the small-scale facility, with the inlet *Re* being lower in the small-scale model. The approach taken in designing a small-scale test facility for calandria flows emphasized the importance of maintaining the Archimedes number *Ar*. This parameter is intended to represent the overall relative importance of buoyancy forces and inertial forces:

$$Ar = \frac{|g|\beta\Delta T D}{U_i^2} = \frac{|g|\beta q D}{C_P \rho A_i U_i^3} \tag{2.17}$$

The inertial forces term in this expression depends solely on the average inlet velocity U_i. Due to the importance of the interaction between the inertial flows entering the tube bank (driven by the inlet jets) and buoyant flows in the tube bank, a more representative velocity could be the velocity of jets entering the top of the calandria tube bank.

For the CANDU-6 inlet arrangement for example, this could correspond to the velocity of the secondary jet formed at the top of the vessel at the impingement point of a pair of inlet jets. However, since this velocity is not easily determined, the average inlet velocity (determined from the flow area of the nozzle and volumetric flow rate) is a more practical term. Studies by Kim *et al.* [31] have suggested that the peak velocity of the secondary jet scales reasonably well with inlet velocity for 10 000 < Re < 50 000, and behaviour was expected to be similar to the full-scale CANDU-6 (inlet *Re* = 550 000). Thus, for the 1/4 scale case, the use of inlet velocity in *Ar* may be reasonable in terms of representing the inertia of

the secondary jet entering the tube bank. At smaller scales, the inlet *Re* could be much lower. Hence there is a need to study if the assumption related to the similarity of the inlet average velocity and the impingement velocity applies at such a small scale.

For the Bruce A configuration, the inlets consist of circular jets angled 14º downward from the horizontal, positioned above the tube bank. In this arrangement, the inlet jets do not travel upward along the curved calandria walls before entering the tube bank, but do propagate through the fluid volume above the tube bank. A previous study by Abdel-Rahmen *et al.* [46] using circular jets in the range of 1400 < Re < 19 400 found that for lower Re, the centreline velocity decayed faster and the potential core was shorter. Similar to the CANDU-6 case mentioned above, should the inlet *Re* in the small-scale facility be too low, the centerline velocity of the inlet jets could decay over a shorter relative distance before interacting with the buoyant flow in the tube bank, an effect not captured by the Archimedes number. For the small-scale experiments in this work, reducing the inlet flow rate below nominal conditions may be required in order to reach larger values of *Ar*. Therefore, consideration of the impacts of low inlet *Re* may be required.

Next, the buoyancy term in *Ar* depends only on the total amount of applied heat in the vessel. However, locally induced buoyancy forces would depend on local temperature gradients. If the local heat distribution in the moderator is not maintained between the scale facility and the reactor, this could result in an over- or under-representation of buoyancy effects not captured by *Ar*.

The average q^* for the calandria vessel is often quoted in studies when comparing scaled facilities and is calculated using the vessel average volumetric heat generation rate:

$$q^*_{av} = \frac{q'''_{av} D}{\rho C_P U_i \Delta T} = \frac{4q}{\pi D^2 L} \frac{D}{\rho C_P U_i \Delta T} \tag{2.18}$$

Applying a heat balance to the system, the total heat generation rate can be represented as $q = \rho U_i A_i C_P \Delta T$, where A_i represents the total inlet flow area. Equation 2.18 can thus be simplified as:

$$q^*_{av} = \frac{4A_i}{\pi DL} \tag{2.19}$$

Equation 2.19 depends only on calandria vessel geometry parameters, namely the total inlet flow area A_i, vessel diameter D and vessel length L. If geometric similarity is maintained between the full-sized reactor and the scaled facility (i.e. – equivalent number of inlets, same relative physical size and location of inlets, same relative vessel diameter and length), then q^*_{av} for the scaled facility will be the same as the full-scale calandria. However, unless the local heat distribution in the scaled model is similar to that of the full-scale reactor, local q^* equivalence would not be maintained. This is particularly important for the present study where the number of heated rods is smaller than the actual case which results in much higher surface heat fluxes even with acceptable *Ar* and q^*_{av} scaling.

As discussed in section 2.2.3, the use of surface heating in the test facility as opposed to a volumetric heat source would impact the local heat distribution, since in this case heat is transferred only through the surface area of the heated tube elements rather than being distributed more evenly through the fluid volume. Thus, the use of surface heating would result in the local q^* equivalence not being maintained, even if q^*_{av} is equivalent. As evidenced by the numerical study by Sarchami *et al.* [39], the larger temperature gradients associated with surface heating could result in larger buoyancy forces which could have an observable impact on the flow distribution within the test vessel. For the 1/16 scale facility in this study, the number of tubes will also be reduced causing a reduction in the available heated surface area. This will result in higher local heat fluxes which would result in a larger distortion of q^*. This would also resort in an over-

representation of local buoyancy forces in the small-scale facility for a given Archimedes number.

Due to these factors, it is difficult to determine which power and flow conditions in the small-scale facility best correspond to nominal conditions in the full scale calandria vessel using *Ar* alone. This necessitates the study of a wide range of power and flow conditions in the small-scale model to observe how the temperature and velocity fields change with the increasing relative significant of buoyancy forces in the vessel. Multiple power and flow combinations for similar *Ar* should also be studied to evaluate its effectiveness at predicting the flow fields within the vessel. Additionally, comparisons should be made between results from the small-scale model and the full-scale facility in order to explore the level of similarity between the two facilities.

2.4.2 Modelling and Benchmarking Calandria Flow

As shown in Table 2-3, numerical studies of CANDU moderator flow have grown increasingly complex as computational resources have advanced. Earlier studies were limited to two-dimensional time averaged conditions and used a porous medium approach to model resistances in the tube bank to allow for coarser meshes; the porous medium relied on experimentally derived correlations for the frictional pressure drop in the tube bank. More recent studies model three-dimensional unsteady flow in the vessel and resolve flow around the individual tube elements.

The studies presented in section 2.2.4 highlighted the sensitivity of the selected turbulence model on prediction of flow in the tube bank. The work of Teyssedou *et al.* [42] and Kim *et al.* [43] showed that the predicted pressure drop across a tube bank is sensitive to the selected turbulence model. Since the pressure and velocity fields are linked, incorrectly predicted pressure fields in tube bank would result in the tube bank flow being predicted incorrectly. The isothermal flow studies of Kim et al. [31] also highlighted this issue where the parameters of the k-ω SST

turbulence model had to be tuned in order for the predicted flow field to correspond to the experimental results.

The results of numerical studies need to be verified against experimental results to ensure that physical phenomena are being adequately represented. The modelling approaches in the selected numerical studies have typically been benchmarked against the reported results from facilities where flow is predominately two-dimensional (including the SPEL experiments and the Stern Laboratories experiments). However, results from studies by Sarchami *et al.* [37] and Mehdi Zadeh *et al.* [47] have suggested that flows in the calandria are three-dimensional and asymmetric. Due to the proprietary nature of the tests performed at the 3D MTF facility at AECL, benchmark data from this facility is not readily available. While a new 1/4 scale facility has been constructed at KAERI, only limited test results under heated conditions have been published in literature to date. As a result, few numerical studies published in literature have been able to use benchmark data from a three-dimensional test facility.

To address this, the present work includes the collection of experimental temperature and velocity data in a three-dimensional calandria-like facility. Temperature profile measurements are collected within the tube bank at several vertical and axial locations and three-dimensional velocity measurements were made using laser Doppler velocimetry (LDV). Additionally, three-dimensional, unsteady simulations of behaviour in the facility are conducted using a commercial computational fluid dynamics (CFD) package. Similar to recent numerical studies, turbulence is modelled using a k-ε model and the individual tube bank elements are resolved by the computational mesh. Experimental results and simulations are compared to assess the ability of the selected approach to model the physical system.

Chapter 3

Experimental Details

This chapter provides a detailed description of the facilities used to perform the experiments in this study. A new experimental facility was designed, constructed and commissioned as part of this work in order to perform the proposed experiments. Full standard operating procedures are provided in Appendix A.

The facility consisted of a moderator vessel test section connected to an instrumented flow loop operating at atmospheric pressure with inlet temperatures controlled via an external heat exchanger. The test vessel was approximately 1/16 linear scale as compared to the full-scale reactors. The test section utilized a 508 mm (20 inch) diameter stainless steel cylindrical vessel with polycarbonate end plates containing a total of 120 tubes. The outer two tubes of the array (68 total) were unheated acetal rods while the centrally located tubes (52 total) featured a cosine axial heat flux profile. Additionally, a polycarbonate window was included at the top of the vessel for visual and laser access. Temperatures inside the tube bank were measured using movable thermocouple assemblies which entered the vessel through the curved side walls. Inlet and outlet flow geometries were configured to model those of the Bruce A reactors.

The total flow through the loop was monitored by magnetic flow meters while the inlet and outlet temperatures were measured using thermocouples. An external heat

exchanger loop was used to reject heat from the facility to the university chilled water supply. Water quality was ensured by passing the fluid through a 50 μm particle filter.

A summary of the important design values is provided in Table 3-1 as compared to the dimensions of the Bruce A stations as well as conditions for the 1/4 scale OPG-MTF tests conducted in the 1990s. It should be noted that the flow and power configuration in the table represents estimated reference values; in actuality a range of condition were tested to ensure broad coverage of buoyancy and momentum phenomena.

Table 3-1: Comparison of key facility dimensions and reference test conditions

	Bruce A Station	AECL MTF Tests	Bruce A Test Configuration
Vessel D [m]	8.0	2.0	0.508
Vessel L [m]	6.0	1.5	0.508
Vessel L/D	0.75	0.75	1.0
Volume [m^3]	263	4.10	0.085
Calandria Tube Diameter [m]	0.13	0.033	0.013
Tube pitch [m]	0.282	0.072	0.029
Pitch/diameter	2.167	2.167	2.167
Total number of tubes	480	480	120
Unheated tubes	N/A	N/A	68
Tube columns	24	24	12
Wall to tube clearance [m]	0.70	0.16	0.078
Clearance/pitch	2.47	2.26	2.68
Nozzle flow area [m^2]	0.32	0.028	2.5×10^{-4}
Mass flow [kg/s]	850	22.9	0.50
Heat load to moderator [kW]	118 000	1200	40
Power per heater tube [kW]	N/A	2.5	0.77
Inlet to outlet ΔT [°C]	33.5	11.3	19.1
Transit time [s]	279	161	154
Volume to flow rate [m^3/kg·s]	0.310	0.179	0.171

Table 3-2: McMaster 'Bruce A' test section as-built dimensions

	McMaster MTF (as built)	Method of Measurement
Vessel ID, front face/back face [in]	19.26 ± 0.03	Average of eight measurements at the front/back
Vessel L, inside length [in]	19.74 ± 0.06	Average of four repeat measurements of length at differing azimuthal locations along the outside of the tank
Unheated rod diameter, at centre [in]	0.5325 ± 0.0005	Average of all unheated rod diameter measurements
Heater rod diameter, at centre [in]	0.5284 ± 0.0008	Average of all heater rod diameter measurements
Tube pitch [in]	1.144 ± 0.006	Average of all pitch measurements
Wall to tube clearance [in]	1.12 ± 0.01	Calculated from measured vessel inner diameter and measured tube bank height

3.1 Test Section

3.1.1 Heated Assemblies

The test section used customized 13.4 ± 0.05 mm (0.528 ± 0.002 in) diameter heater rods manufactured by Stern Laboratories. An overview of these heaters is shown in Figure 3-1. These heater rods featured a double helix element design which allows for all electrical connections to be made at the rear of the test section. This reduced visual obstructions at the front face of the test sections, allowing for improved visual and laser access for flow measurements. The heaters also featured a cosine axial heat flux profile $F(z)$ as defined by Equation 3.1:

$$F(z) = 0.7785 + 0.6215 \times \cos\left(2 \times \frac{2.2255z}{L} - 2.2255\right) \qquad (3.1)$$

Here, z is the position along the heated length of the heater and L is the total heated length, both in metres. This corresponds to a peak to average heat flux of 1.4 and a minimum to average heat flux of 0.4.

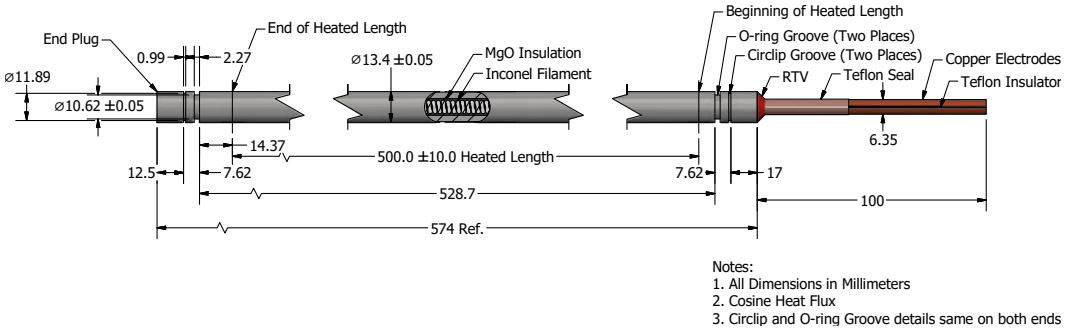

Figure 3-1: Test section heater design, adapted from [48]

Table 3-3: Heated assembly specifications

Parameter	Design specification	Measured value / test condition
Operating pressure (max) [MPa]	1.0	N/A
Nominal power [kW]	1.0	Test dependent
Nominal voltage [V]	20	Test dependent
Nominal current [A]	50	Test dependent
Maximum linear power [kW/m]	2.8	N/A
Average surface heat flux [kW/m^2]	47.5	Test dependent
Outside diameter [mm]	13.40 ± 0.05	13.42 ±0.02[4]
Straightness over 1.0 m [mm]	≤ 1.26	N/A
Heated length [mm]	500 ± 10	N/A
Filament resistance (25°C) [Ω]	0.392 ± 0.020	0.378 ± 0.010[5]

Relevant dimensions are shown in Figure 3-2 and Table 3-4. The heated rods were sealed to the vessel end shields via O-rings located at groove locations D and E. Retaining rings were installed at locations B and G.

[4] Mean and 2-standard deviation over all heater diameters measured
[5] Mean and 2-standard deviation of all resistances for all heaters

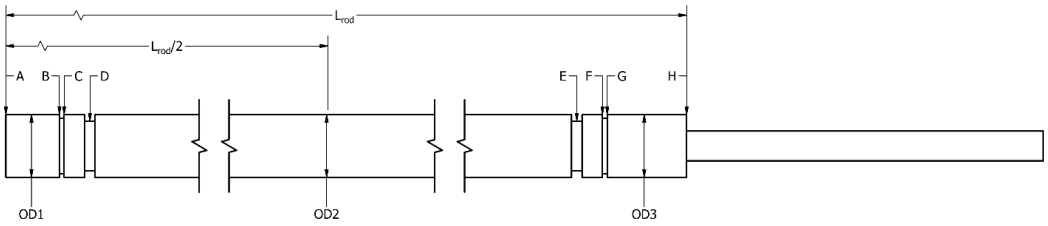

Figure 3-2: Geometric overview of heated and unheated assemblies

Table 3-4: Heated assembly dimensions (mean and 2-sigma deviation over all samples)

Parameter	Dimension [in]	Comment
OD_1	0.5284 ± 0.0007	Heater outer diameter, front end
OD_2	0.5284 ± 0.0008	Heater outer diameter, middle
OD_3	0.5289 ± 0.0007	Heater outer diameter, electrode end
L_{rod}	22.596 ± 0.048	Heater overall length

3.1.2 Unheated Assemblies

The outer two rows of the tube bank in the test section consisted of unheated rods. The unheated rods were manufactured from acetal plastic and had a diameter of 13.5 ± 0.1 mm (0.533 ± 0.005 in). Acetal plastic was selected for its low thermal conductivity and compatibility with the temperature range in the experiments. The dimensions of the unheated rods were matched to the heated rod dimensions as close as practically possible.

The geometry of the assemblies was comparable to the heated assemblies as shown in Figure 3-2 with relevant dimensions shown in Table 3-5. The rods were sealed to the vessel end shields via O-rings located at groove locations D and E. Retaining rings were installed at locations B and G.

Table 3-5: Unheated assembly dimensions (mean and 2-sigma deviation over all samples)

Parameter	Dimension [in]	Description
OD_1	0.5264 ± 0.0025	Acetal rod outer diameter, front end
OD_2	0.5325 ± 0.0005	Acetal rod outer diameter, middle
OD_3	0.5278 ± 0.0014	Acetal rod outer diameter, rear end
L_{rod}	22.533 ± 0.006	Acetal rod overall length

3.1.3 Test Vessel

An overview of the test section design is shown in Figure 3-3. Detailed drawings follow in Figure 3-4 through Figure 3-8; relevant dimensions are shown in Table 3-6. In the Bruce A reactor design, moderator flow enters the calandria vessel through sixteen 'booster' inlets and six 'booster bypass' inlets at the top of the calandria vessel. In the test section, all 22 inlets and their relative positioning in the vessel were replicated to the greatest extent practicable. As with the Bruce A stations, the 'booster' inlets were positioned symmetrically in the axial direction while the 'booster-bypass' inlets were located at the 'east' end of the vessel. Details regarding the inlet and outlet configuration are provided in section 3.1.4.

Visual access was provided to the tube bank through polycarbonate end shields, allowing for laser Doppler velocimetry (LDV) measurements. Sixteen movable, sheathed thermocouple probes entered the vessel horizontally from the north and south sides of the vessel. Details regarding the thermocouple probes are provided in section 3.2.3.

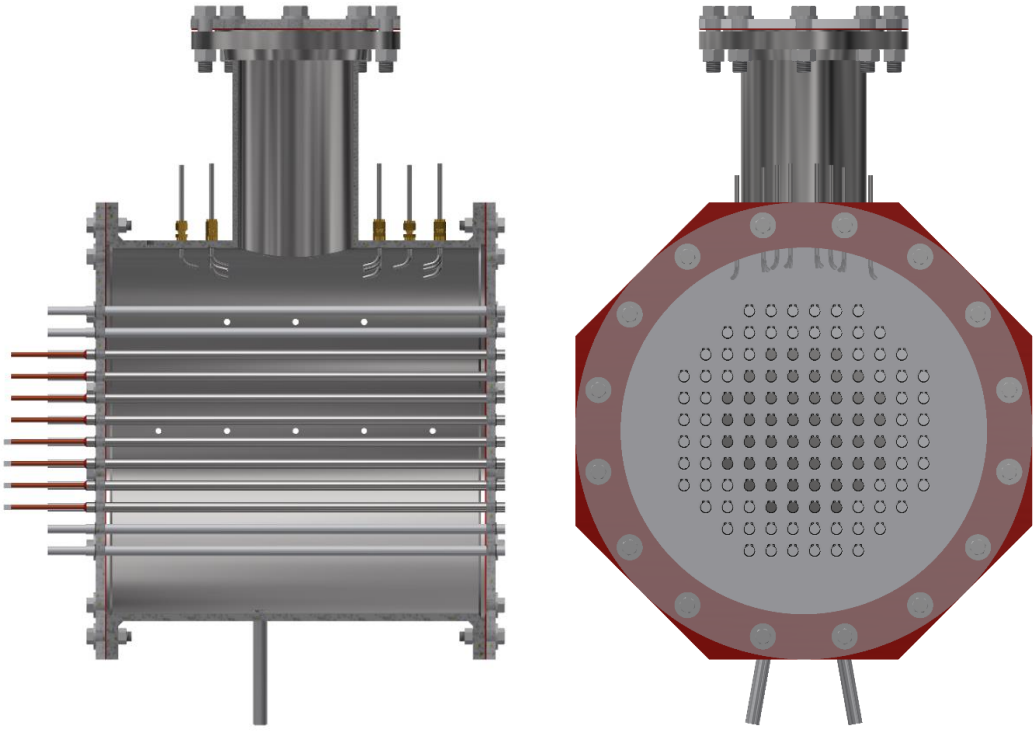

Figure 3-3: 'Bruce A' test section overview

The important end-shield dimensions are shown in Figure 3-8 and Table 3-6, with the most critical dimensions being the hole to hole spacing (tube pitch) and the co-linearity of the tube holes in the vertical and horizontal locations (since it affects tube alignment and horizontal alignment). The average tube pitch p_1 was confirmed from the overall tube bank height (dimensions h_3 and h_5) and tube hole diameter d_3. The distances between bore holes (dimensions s_2 and s_3) were also measured at 20 locations. The measured distance between the tube bank and the vessel wall was calculated from measurements of the distance between the tube bank and the end-shield bolt-hole circle (dimensions h_4 and h_6) and the distance between the bolt hole circle and the vessel inner wall (dimension s_1 in Figure 3-4).

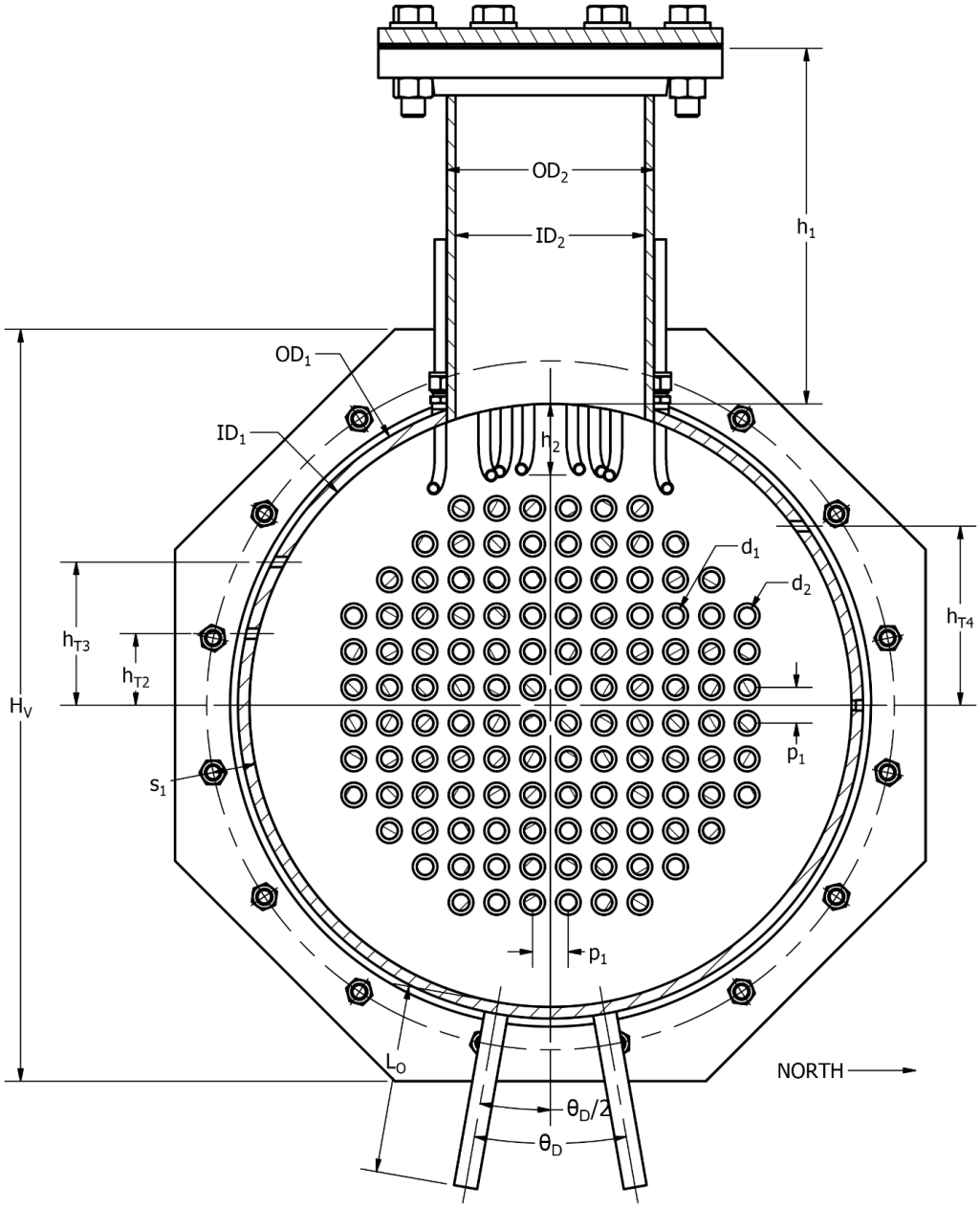

Figure 3-4: 'Bruce A' test section, vessel cross-section

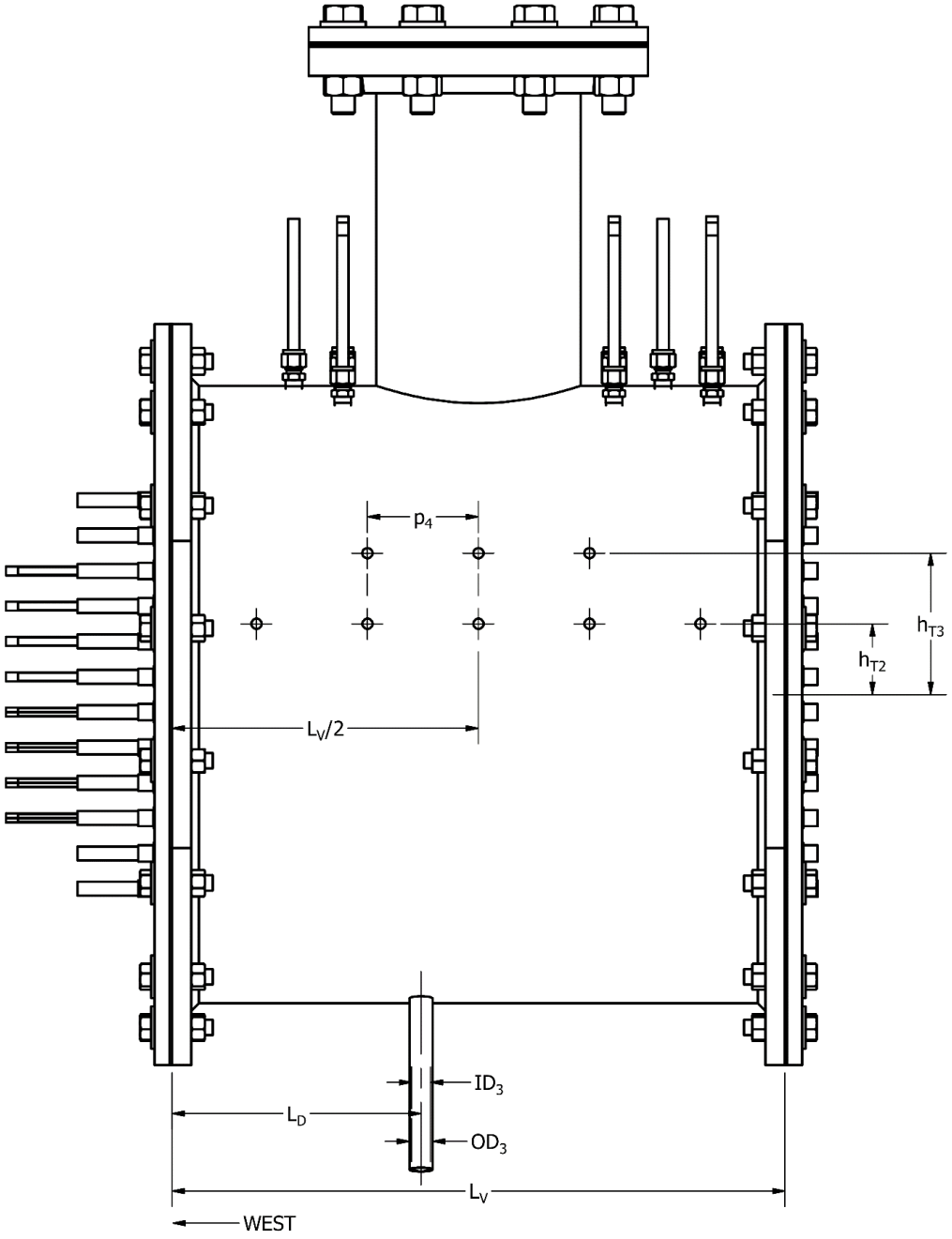

Figure 3-5: 'Bruce A' test section, vessel south side

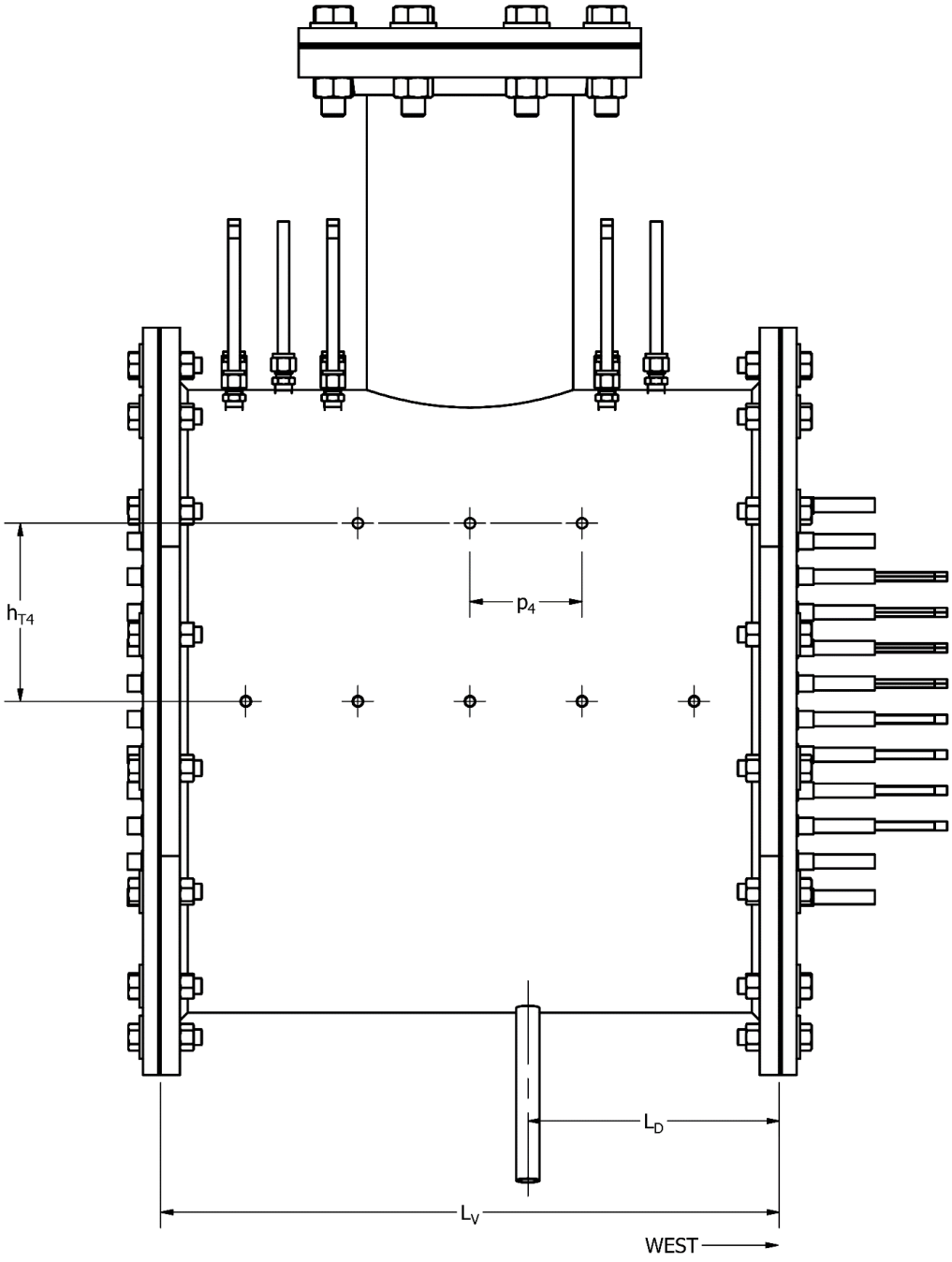

Figure 3-6: 'Bruce A' test section, vessel north side

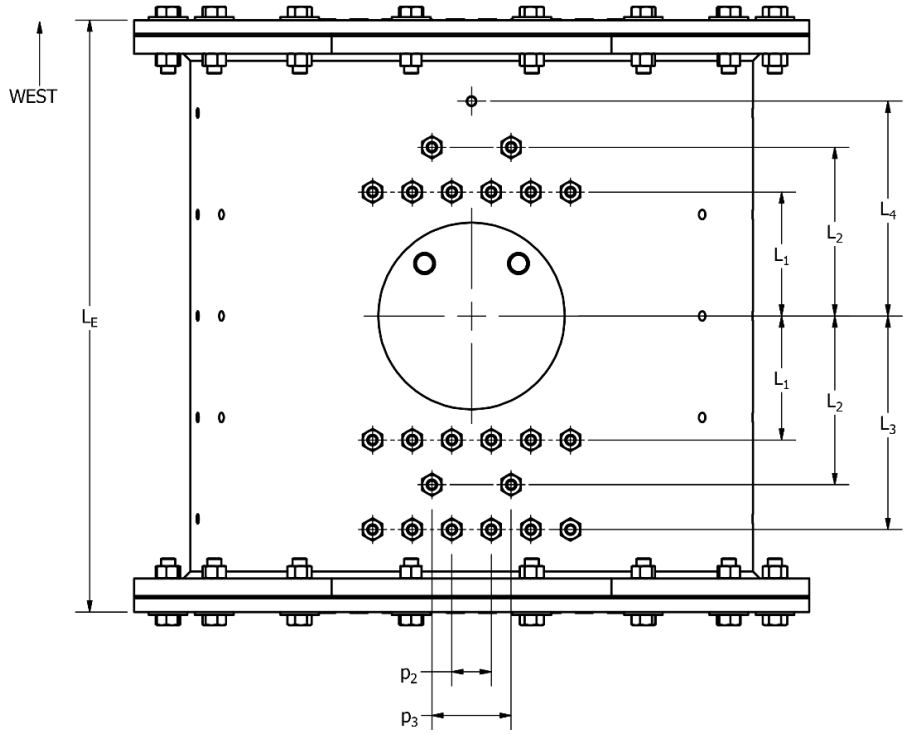

Figure 3-7: 'Bruce A' test section, vessel top view (inlet position detail)

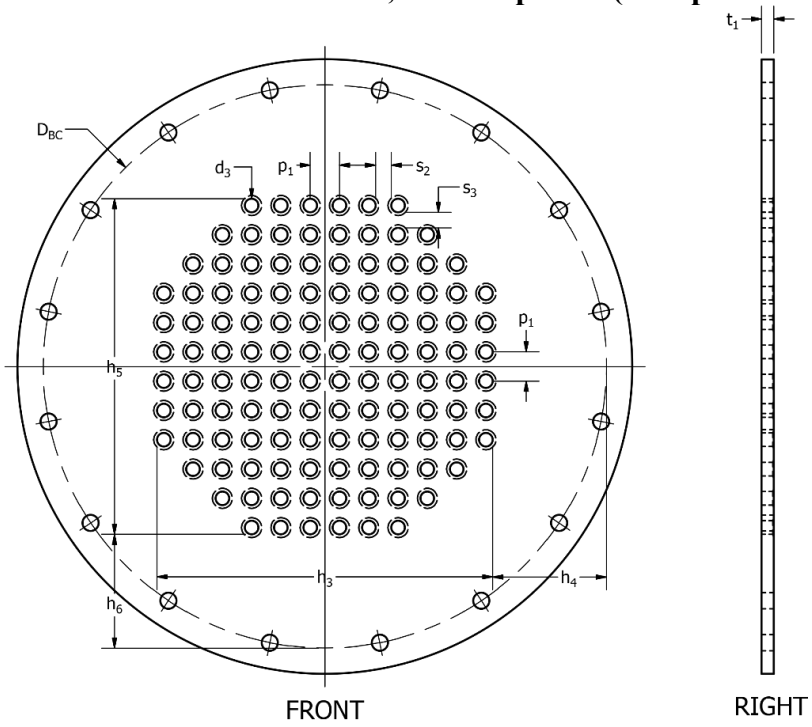

Figure 3-8: 'Bruce A' test section, end shield

Table 3-6: 'Bruce A' test section, relevant dimensions[6]

Parameter	Value	Comment
D_{BC} [in]	22.006 ± 0.009	End-shield bolt hole circle diameter
d_1 [in]	0.5284 ± 0.0008	Heated assembly, rod outer diameter at axial centre
d_2 [in]	0.5325 ± 0.0005	Unheated assembly, rod outer diameter at axial centre
d_3 [in]	0.534 ± 0.005	End shield bore diameter for rod assemblies
H_V [in]	23.96 ± 0.05	Vessel flange height
h_1 [in]	11.35 ± 0.05	Laser access window height
h_2 [in]	1.102 ± 0.005	Inlet installation height (vessel wall to nozzle base)[7]
h_3 [in]	13.123 ± 0.004	Tube bank height (horizontal direction)
h_4 [in]	4.442 ± 0.010	Distance from tube bank to bolt hole circle (horizontal direction)
h_5 [in]	13.124 ± 0.003	Tube bank height (vertical direction)
h_6 [in]	4.441 ± 0.009	Distance from tube bank to bolt hole circle (vertical direction)
h_{T1} [in]	0.00	Thermocouple plane 1 height above vessel centre
h_{T2} [in]	2.29	Thermocouple plane 2 height above vessel centre
h_{T3} [in]	4.58	Thermocouple plane 3 height above vessel centre
h_{T4} [in]	5.72	Thermocouple plane 4 height above vessel centre
ID_1 [in]	19.26 ± 0.03	Vessel inner diameter
ID_2 [in]	6.09 ± 0.01	Laser access window port inner diameter
ID_3 [in]	0.619 ± 0.004	Outlet inner diameter
L_1 [in]	4.399 ± 0.008	Axial distance from vessel centre to 'booster' inlets row 1
L_2 [in]	5.986 ± 0.005	Axial distance from vessel centre to 'booster' inlets row 2
L_3 [in]	7.576 ± 0.013	Axial distance from vessel centre to 'booster bypass' inlets
L_4 [in]	7.714 ± 0.007	Axial distance from vessel centre to pressure transmitter
L_D	8.332 ± 0.019	Distance from vessel west end to outlets
L_E	21.15 ± 0.08	End-shield to end-shield distance[8]
L_O	5.73 ± 0.07	Outlet length to first bend[9]
L_V	19.74 ± 0.06	Vessel overall length
p_1 [in]	1.144 ± 0.006	Tube-bank pitch
p_2 [in]	1.407 ± 0.009	Spacing between inlet nozzles
p_3 [in]	2.810 ± 0.007	Spacing between 'booster' inlet nozzles in row 2
p_4 [in]	3.654 ± 0.002	Horizontal spacing between in-vessel thermocouples
OD_1 [in]	19.99 ± 0.05	Vessel outer diameter
OD_2 [in]	6.55 ± 0.12	Laser access window port outer diameter

[6] Uncertainties represent 2-standard deviations
[7] Distance is measured with nozzle installed at zero-degree rotation (i.e. nozzle is installed at a fixed height in a feedthrough fitting prior to being rotated to 15 or 30 degrees off centre)
[8] Includes end-shield and gasket thicknesses
[9] Includes entrance length of compression fitting at connection to flow loop (0.96 inches)

Parameter	Value	Comment
OD_3 [in]	0.7458 ± 0.0004	Outlet outer diameter
s_1 [in]	1.12 ± 0.01	Distance from end shield bolt hole circle to vessel inside wall
s_2 [in]	0.611 ± 0.005	Spacing between bore holes in end-shields (horizontal direction)
s_3 [in]	0.610 ± 0.005	Spacing between bore holes in end-shields (vertical direction)
t_1 [in]	0.489 ± 0.006	End-shield thickness
θ_D [º]	19.6 ± 2.3	Angle between outlets

3.1.4 Inlet and Outlet Configuration

The inlets consisted of bent stainless steel tubing and were located near the top of the vessel and direct flow towards the center-plane and at an angle downwards from the horizontal. The nozzles were rotated clockwise or counter-clockwise with respect to the flow entrance axis. Details are shown in Figure 3-9 through Figure 3-11 with dimensions provided in Table 3-7.

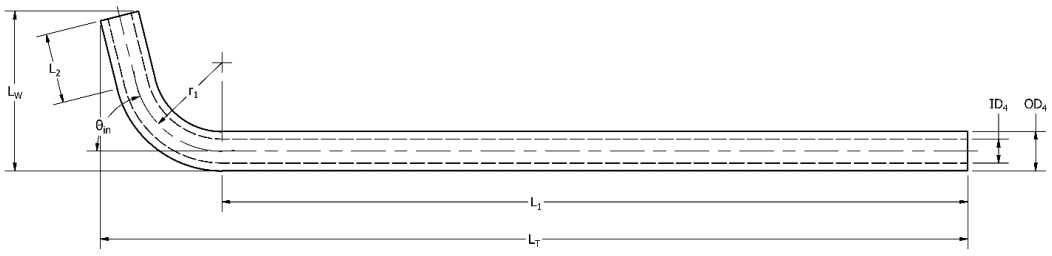

Figure 3-9: 'Bruce A' test section, individual nozzle detail

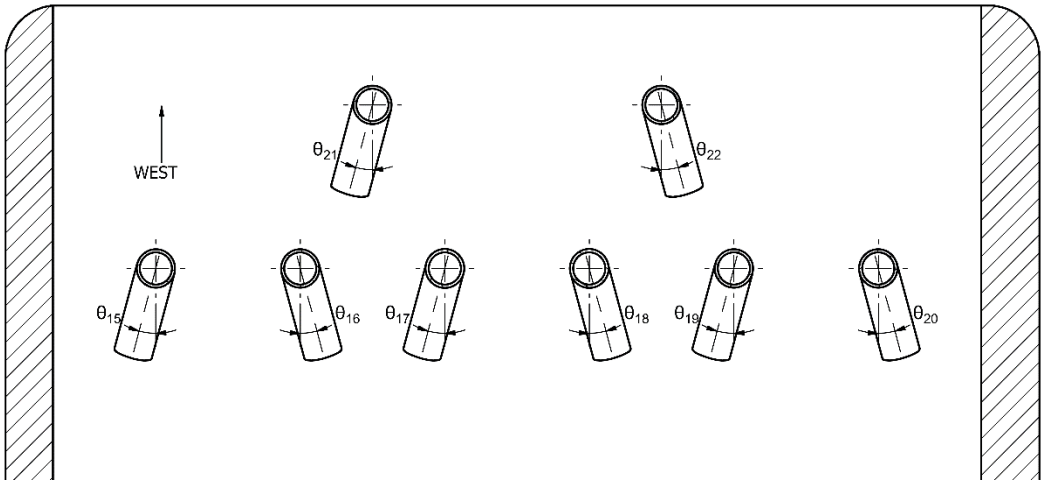

Figure 3-10: 'Bruce A test section' west end nozzle rotation detail (top view)

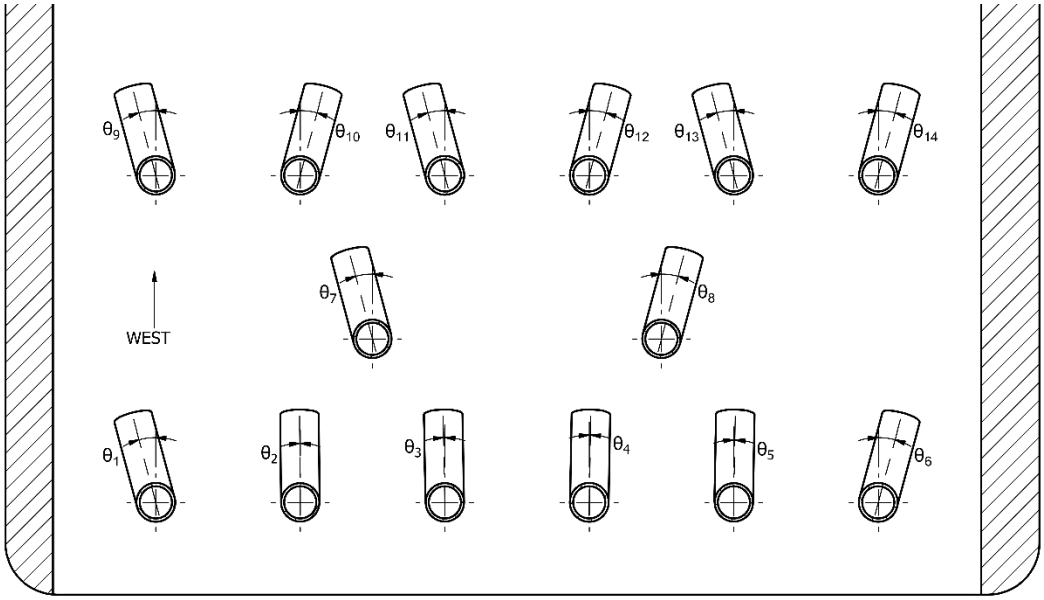

Figure 3-11: 'Bruce A test section' east end nozzle rotation detail (top view)

Table 3-7: 'Bruce A' inlet nozzles relevant dimensions

Parameter	Value	Comment
ID_4 [in]	0.1486 ± 0.0015	Inlet tube inner diameter
L_1 [in]	4.750	Inlet tube entrance length (before bend)
L_2 [in]	0.445	Inlet tube exit length (after bend)
L_T [in]	5.51 ± 0.02	Nozzle overall length (entrance to exit)
L_W [in]	1.00 ± 0.03	Nozzle overall width (entrance to exit)
OD_4 [in]	0.2500 ± 0.0006	Inlet tube outer diameter
r_1 [in]	0.56	Inlet tube bend radius
θ_{in} [°]	76 ± 5	Inlet tube bend angle
θ_1 [°]	15 ± 5	Nozzle 1 rotation angle (counter-clockwise)
θ_2 [°]	0 ± 5	Nozzle 2 rotation angle (counter-clockwise)
θ_3 [°]	0 ± 5	Nozzle 3 rotation angle (counter-clockwise)
θ_4 [°]	0 ± 5	Nozzle 4 rotation angle (clockwise)
θ_5 [°]	0 ± 5	Nozzle 5 rotation angle (clockwise)
θ_6 [°]	15 ± 5	Nozzle 6 rotation angle (clockwise)
θ_7 [°]	15 ± 5	Nozzle 7 rotation angle (counter-clockwise)
θ_8 [°]	15 ± 5	Nozzle 8 rotation angle (clockwise)
θ_9 [°]	15 ± 5	Nozzle 9 rotation angle (counter-clockwise)
θ_{10} [°]	15 ± 5	Nozzle 10 rotation angle (clockwise)
θ_{11} [°]	15 ± 5	Nozzle 11 rotation angle (counter-clockwise)
θ_{12} [°]	15 ± 5	Nozzle 12 rotation angle (clockwise)
θ_{13} [°]	15 ± 5	Nozzle 13 rotation angle (counter-clockwise)
θ_{14} [°]	15 ± 5	Nozzle 14 rotation angle (clockwise)
θ_{15} [°]	15 ± 5	Nozzle 15 rotation angle (clockwise)
θ_{16} [°]	15 ± 5	Nozzle 16 rotation angle (counter-clockwise)
θ_{17} [°]	15 ± 5	Nozzle 17 rotation angle (clockwise)
θ_{18} [°]	15 ± 5	Nozzle 18 rotation angle (counter-clockwise)
θ_{19} [°]	15 ± 5	Nozzle 19 rotation angle (clockwise)
θ_{20} [°]	15 ± 5	Nozzle 20 rotation angle (counter-clockwise)
θ_{21} [°]	15 ± 5	Nozzle 21 rotation angle (clockwise)
θ_{22} [°]	15 ± 5	Nozzle 22 rotation angle (counter-clockwise)

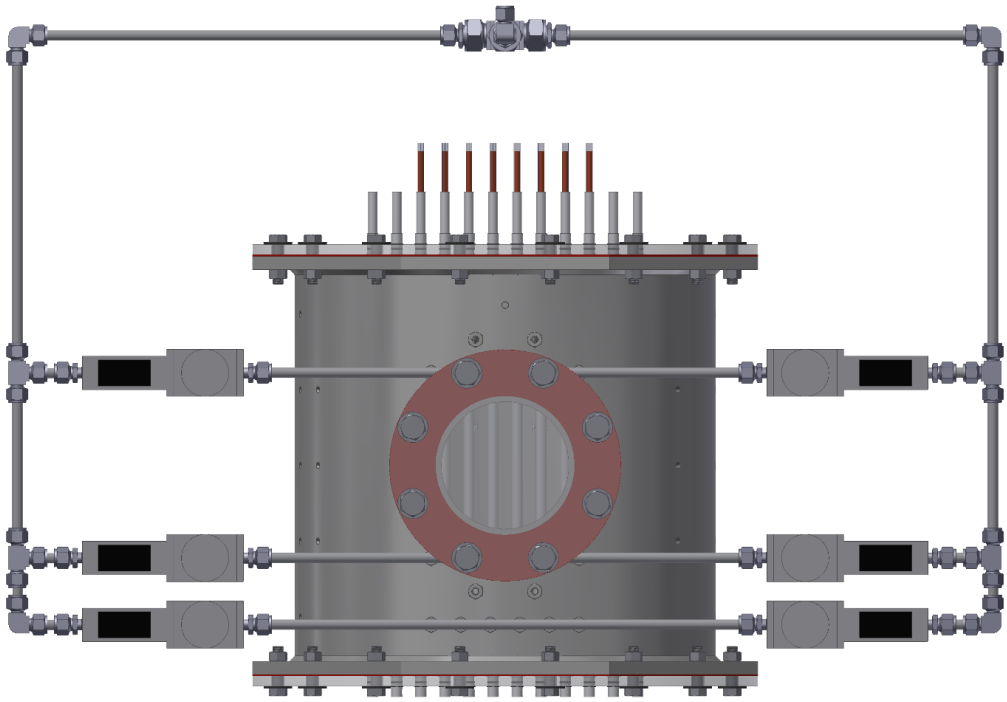

Figure 3-12: 'Bruce A' inlet header and mass flow controller arrangement

The inlet manifolds consisted of stainless-steel tubing with welded tube stubs. Connections were made between the header manifolds and the inlet nozzles using flexible tubing. Identical length flexible hose was used for all stub to inlet nozzle spans to minimize the nozzle to nozzle flow differences. Details are shown in Figure 3-13 and Figure 3-14 with dimensions shown in Table 3-8.

The inlets were fed from three separate header manifolds: one header for the 'booster bypass' inlets (six total) and the 'booster' inlets split evenly between two headers (eight per header). The flow rate at each entrance was monitored and controlled with a mass flow controller to ensure balanced and stable flow. Details regarding the mass flow controllers are provided in section 3.2.1. The general flow controller and inlet manifold arrangement is shown in Figure 3-12.

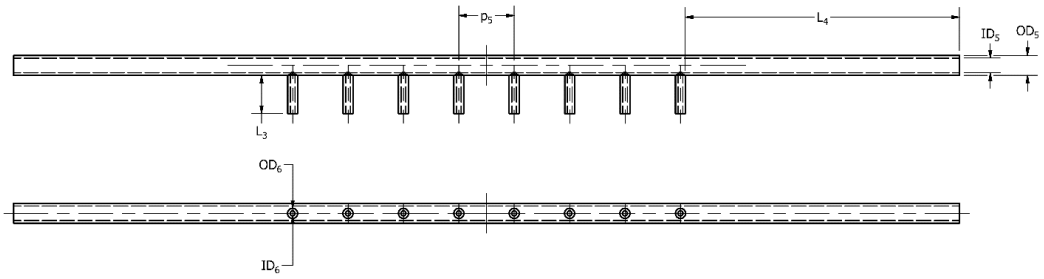

Figure 3-13: 'Bruce A booster' inlet manifold

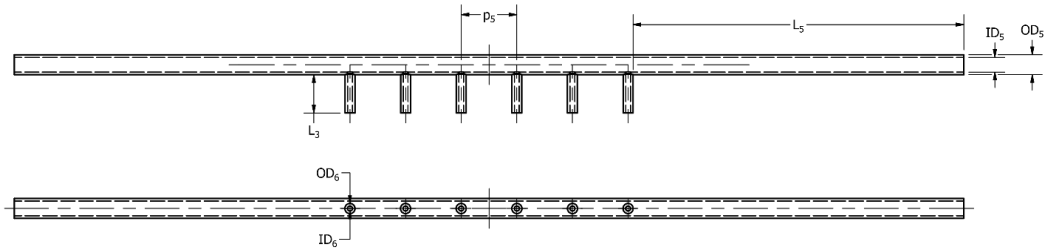

Figure 3-14: 'Bruce A booster bypass' inlet manifold

Table 3-8: 'Bruce A' test section inlet manifold dimensions (mean and 2-sigma deviation over all samples)

Parameter	Value	Comment
ID_5 [in]	0.3784 ± 0.0025	Header manifold inner diameter
ID_6 [in]	0.1315 ± 0.0049	Header stub inner diameter
L_3 [in]	0.901 ± 0.021	Header stub length
L_4 [in]	6.96 ± 0.04	'Booster' header manifold entrance length
L_5 [in]	8.38 ± 0.03	'Booster bypass' header manifold entrance length
OD_5 [in]	0.5009 ± 0.0022	Header manifold outer diameter
OD_6 [in]	0.2491 ± 0.0007	Header stub outer diameter
p_5 [in]	1.407 ± 0.024	Header stub spacing

The relative positioning of the outlets from the Bruce A reactors was maintained (offset towards the 'western' end of the vessel). Positioning of the outlets is detailed in section 3.1.3.

3.2 Description of Flow Loop and Instrumentation

An overview of the primary flow loop is shown in Figure 3-15. A 120 L reservoir tank supplied water through 38 mm PVC piping (NPS 1.5 SCH 80) to a 2.4 kW (3

hp) pump controlled via a variable frequency drive (VFD). The pump discharged to 25 mm piping (NPS 1 SCH 40) where flow passed through a 50 μm particle filter. Test section inlet flow rate and temperature were measured upstream of the flow branching to each inlet flow controller. Test section outlet flow rates and temperatures were measured separately at each drain. The flow was recombined and returned to the reservoir through 25 mm PVC pipe (NPS 1 SCH 40).

Heat removal from the reservoir was achieved via connection to a secondary heat exchanger loop. A second drain on the reservoir fed a 1.5 kW (2 hp) pump via 19 mm (0.75 inch) rubber hose. The pump discharge flowed via 25 mm OD (1 inch) stainless steel tubing through the tube side of a shell-and-tube heat exchanger before returning the reservoir. The shell side of the heat exchanger was supplied by the university chilled water supply at 4 – 8 ºC.

For higher power test conditions, additional cooling was provided by an immersed cooling coil in the reservoir. The coil was constructed of 13 mm (0.5 inch) OD copper tubing with a total length of 15 metres (20 turns at a bend radius of approximately 114 mm) and was supplied by municipal cold tap water.

During the experiments conducted for these tests, a practical limiting factor for test section power was determined by the heat removal capabilities of these two cooling systems. Under steady state conditions, the test section outlet temperatures were required to be maintained below 65ºC as this was the upper working temperature limits of the PVC piping in the primary flow loop. For the nominal flow condition of 30 L/min, it was observed that the maximum test section power was approximately 40 kW.

Table 3-9: Flow loop operating characteristics

Parameter	Specification
Working fluid	Water
Nominal flow rate	30 L/min
Maximum flow rate	36 L/min

Parameter	Specification
Temperature range	10 – 65 ºC
Maximum heat removal (at nominal flow rate)	40 kW

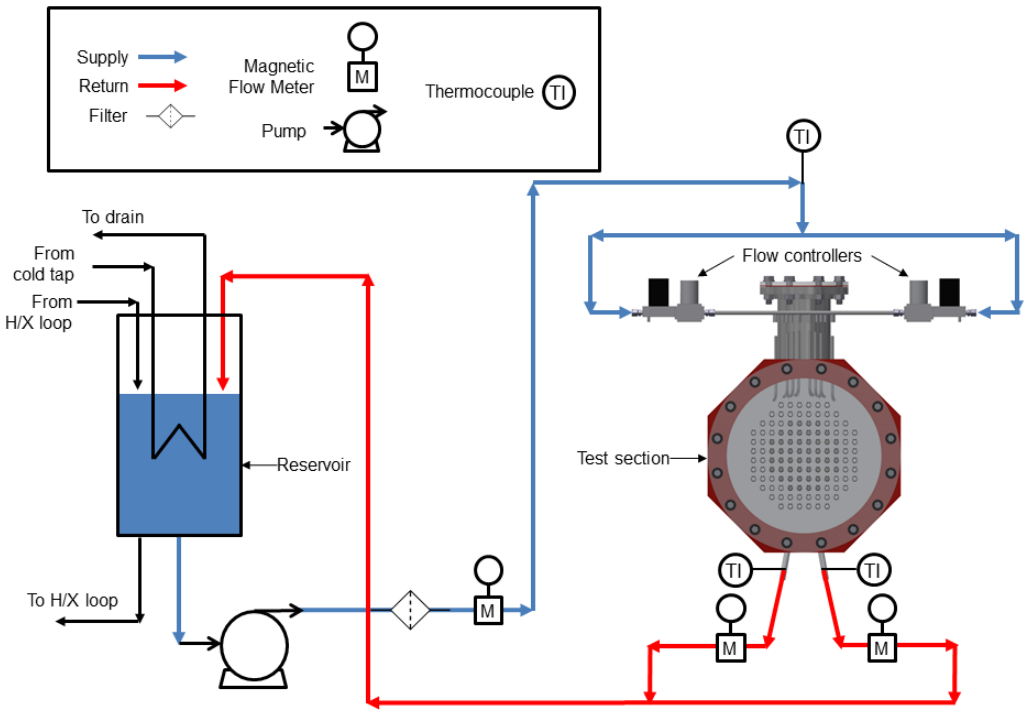

Figure 3-15: Overview of flow loop and test section configuration

3.2.1 Inlet Mass Flow Controllers

The flow to each side of the three separate inlet manifolds was separately controlled and monitored using six Alicat model LCR-5LPM-D-100PSIG liquid flow controllers as shown in Figure 3-12 (two controllers per header). Relevant specifications for the flow controllers are reproduced in Table 3-10. The flow controllers were operated via RS-232 with the flow rate, flow set point, pressure and water temperature of each controller logged at a sampling rate of 10 Hz.

Table 3-10: Alicat LCR flow controller specifications [49]

Parameter	Specification
Flow range	5 L/min
Accuracy at calibration conditions after tare	± 2% full scale
Repeatability	± 2% full scale
Zero and span shift	± 0.02% full scale/ °C / atm
Operating range / turndown ratio	2% to 100% full scale (50:1 turndown)
Typical response time	100 ms
Maximum serial refresh rate	20 S/s
Temperature accuracy	± 1.5°C

3.2.2 Process Flow Rate Measurement

In addition to the flow rate measurements provided from the mass flow controllers, the total inlet and outlet flow rates were measured using three Rosemount 8732E magnetic flowmeter processors with Rosemount 8711 sensors. The inlet flow rate was measured by a single flow meter downstream of the primary loop pump and water filter (before branching for the header manifolds) while the outlet flow rates were measured separately, immediately prior to recombination and entry into the reservoir tank. Relevant specifications are reproduced in Table 3-11. The inlet and outlet flow meters were respectively configured with 36 L/min and 18 L/min flow ranges and output a linear analog current signal in the range of 4-20 mA.

Table 3-11: Rosemount 8732E magnetic flow meter with 8711 sensor specifications

Parameter	Specification
Flow range	30 ft/s
Flow tube diameter	1.0 in
Ambient temperature range	-25°C to 65°C
Stated system accuracy	< 0.5%
Accuracy at calibration	< 0.0125%
Repeatability	± 0.1% of reading
Stability	± 0.1% per six months
Temperature drift	± 0.25% over temperature range

3.2.3 Temperature Measurements

The test section internal temperatures were monitored using Omega TMTSS-125G-12 sheathed thermocouple probes. These probes entered the vessel horizontally at locations shown in Figure 3-16. Temperatures were measured at a spacing equal to ½ of the tube bank pitch (14.5 mm) such that measurement locations corresponded to locations centred directly above a tube bank element or centered within the subchannel between tube bank columns. At each measurement location, data was collected at a rate of 10 Hz over a period of 300 seconds.

Table 3-12: Thermocouple feedthrough locations (*y* and *z* coordinates)

ID	*y* [mm]	*z* [mm]	ID	*y* [mm]	*z* [mm]
TCM1-00	58.1	73.3	TCM1-07	116.2	347.8
TCM1-01	58.1	164.7	TCM1-08	0.0	73.3
TCM1-02	58.1	256.2	TCM1-09	0.0	164.7
TCM1-03	58.1	347.6	TCM1-10	0.0	256.2
TCM1-04	58.1	439.1	TCM1-11	0.0	347.6
TCM1-05	116.2	164.7	TCM1-12	0.0	439.1
TCM1-06	116.2	256.2			

The repeatability of temperature measurements was evaluated by comparing temperature data collected for comparable conditions collected over several experimental tests, as described in Appendix E section E.3. Repeated temperature measurements were typically within ± 0.1 ºC – 0.7 ºC, depending on the positional uncertainty and local temperature gradients.

The inlet and outlet bulk flow temperatures as well as ambient room temperature were monitored using Omega TMTSS-062U-6 thermocouple probes. The inlet flow was monitored at the first branch point show at the top of Figure 3-12. The temperature at each outlet was separately monitored at the base of each drain (at location L_O from the vessel wall as shown in Figure 3-4). Additionally, the temperature at the entrance to each flow manifold was monitored by the mass flow controllers; these instruments are described in section 3.2.1.

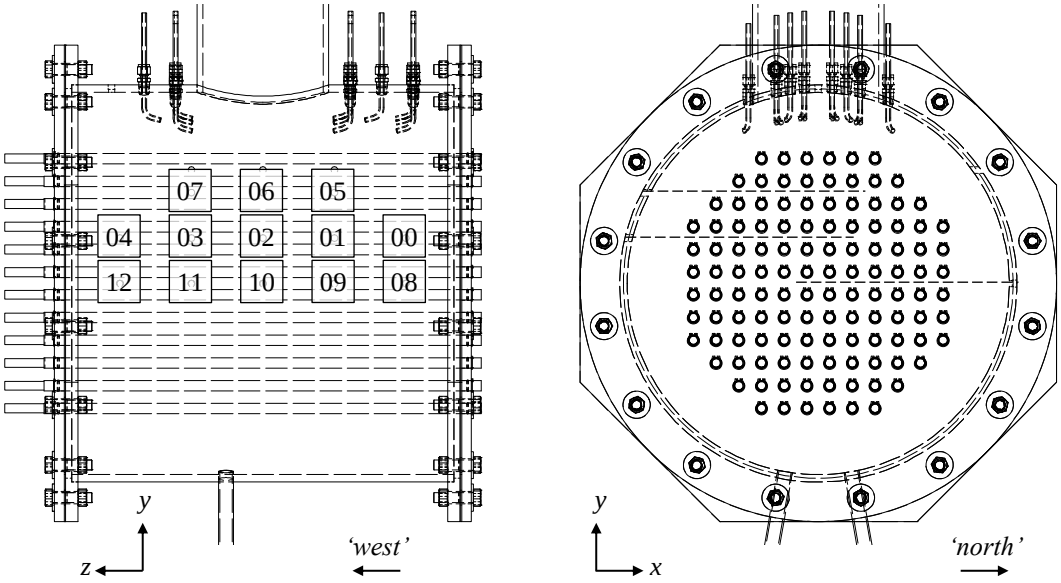

Figure 3-16: Location of thermocouple feedthrough fittings (left) and lines traversed by thermocouples (right).

All thermocouples used were type T and specified to meet special limits of error. The manufacturer specified accuracy was the greater of 0.5ºC or 0.4%; for the temperature range in the experiments this corresponded to ±0.5 ºC. The thermocouple response times – defined as the time to reach 63.2% of the final value following a step change – were provided by the manufacturer and are included in Table 3-13.

Table 3-13: Omega thermocouple probe specifications [50] [51]

Parameter	TMTSS-125G-12	TMTSS-062U-6
Calibration	Type T	Type T
Temperature range	-250 – 350 ºC	-250 – 350 ºC
Tip configuration	Grounded	Ungrounded
Tip diameter	3.18 mm (0.125 in)	1.59 mm (0.0625 in)
Response time[10]	0.34 s	0.28 s
Accuracy	±0.5ºC	±0.5ºC

[10] The response time τ is defined as the amount of time required to reach 63.2% of an instantaneous temperature change [51].

The thermocouples and thermocouple measurement hardware used in the experiment were calibrated in-house against a high-precision resistive temperature detector (RTD) probe (Omega DP251 precision RTD thermometer with PRP-3 probe). This reference system was specified to have 0.025°C accuracy over a range of -50°C to 250°C [52]. Details of the calibration procedure and calibration data are included in Appendix B.

3.3 Description of Power Supply and Instrumentation

3.3.1 DC Power Supply

A TopCon programmable DC power supply was used to power the heated assemblies. The unit consisted of four TCP32.100.480S units arranged in a parallel configuration to provide a maximum power output of 128 kW. Relevant output specifications are shown in Table 3-14.

Table 3-14: DC power supply output specifications [53]

Parameter	Specification
Voltage range	0 – 100 V
Current range	0 – 1600 A
Transient response time	2 ms
Stability	0.05% full scale
Temperature coefficient	0.03% full scale / °C
Output ripple (300 Hz)	1.1 V_{pp}
Output noise (40 kHz – 1 MHz)	1.5 V_{pp}

The 52 heated assemblies were arranged in a 4 × 13 configuration with 13 strings in parallel and four heaters in series per string. Current was conducted through dual 373.7 kcmil stranded copper cables from the power supply to power distribution bus bars. Each string of heaters was connected to the bus bars through AWG 6 wiring.

3.3.2 Test Section Power Measurement

The DC current supplied and the DC voltage drop across the test section heaters were separately measured; the electrical power delivered to the heaters was calculated as the product of these measurements. The voltage drop was measured directly between the positive and negative bus bars (0 – 100 V range) was measured using a Watanabe WAP-DS-99A-3 isolation transmitter. The current was measured indirectly as a voltage drop across a calibrated shunt resistor (Canadian Shunt Industries model # 90000-1143). The shunt was specified to have a resistance of 25.0 μΩ ± 0.1% (50 mV voltage drop for an applied current of 2000 A). The voltage drop across the shunt was measured using a Watanabe WAP-DS-16A-3 isolation transmitter. Relevant specifications for the isolation transmitters are provided in Table 3-15.

Table 3-15: Voltage transmitter specifications [54]

Parameter	WAP-DS-99A-3	WAP-DS-16A-3
Input range	0 – 100 V	0 – 50 mV
Output range	4 – 20 mA	4 – 20 mA
Response time	2 ms	2 ms
Accuracy	± 0.1% full scale	± 0.1% full scale
Temperature coefficient	± 0.015% full scale/ºC	± 0.015% full scale/ºC

Both isolation transmitters were calibrated in-house against a high precision multimeter (Agilent 34401A 6.5-digit digital multimeter). Details of the calibration procedure and calibration data are included in Appendix B.

The test section heat balance was determined by comparing the measured heat load (from the mass flow rate and inlet/outlet temperature rise) to the measured electrical power at various power levels. In all cases it was found to be less than 3%, with the discrepancy attributed to the measurement uncertainties. Details of these measurements are provided in Appendix E section E.1.

3.4 Data Acquisition System

Analog measurements were logged using a National Instruments cDAQ-9178 modular data acquisition system. Current measurements (4 – 20 mA signals from magnetic flow meters and voltage transmitters) were logged using two NI 9203 modules while thermocouple measurements were logged using NI 9214 modules (process temperatures and test section internal temperatures). Relevant specifications for the analog to digital hardware are provided in Table 3-16.

Table 3-16: Analog to digital data logging specifications [55]

NI 9203 (current module)	
Current range	0 – 21.5 mA
Maximum gain error	± 0.18% of reading
Maximum offset error	± 0.06% of range
Offset drift	63 nA/°C
Gain drift	± 14 ppm/°C
ADC resolution	16 bit
Conversion time	5 µs
Sampling rate	25 kS/s (all channels used)

NI 9214 (high accuracy thermocouple module, high speed mode)	
Voltage range	± 78.125 mV
Maximum gain error	± 0.16% of reading
Maximum offset error	± 0.03% of range
Sensitivity	0.10 °C
Measurement accuracy (Type T)	0.88 °C typical 1.77 °C maximum
ADC resolution	24 bit
Conversion time	735 µs
Sampling rate	68 S/s (all channels used)

3.5 Velocity Measurements

Laser Doppler velocimetry (LDV) was used to obtain point velocity measurements inside the test section. A three channel LDV system supplied by TSI Inc. consisting of an Innova 70C laser, Fiberlight beam splitter, PDM1000 photodetector module,

and FSA 3500 signal processor was used with a TR360-250 5-beam measurement transceiver. Additional background information on the LDV system implementation used in the experiments is provided in Appendix C.

The TR360 transceiver contains both transmitting and receiving optics and allows for the collection of three-dimensional velocity measurements with a single probe. In order to facilitate the collection of point measurements within defined planes inside the vessel, the LDV measurement probe was mounted to a programmable 3-axis traverse mechanism. The traverse mechanism was controlled by stepper motors capable of moving the measurement probe in increments of 0.0125 mm in the horizonal directions (x and z) and 0.00625 mm increments in the vertical direction (y).

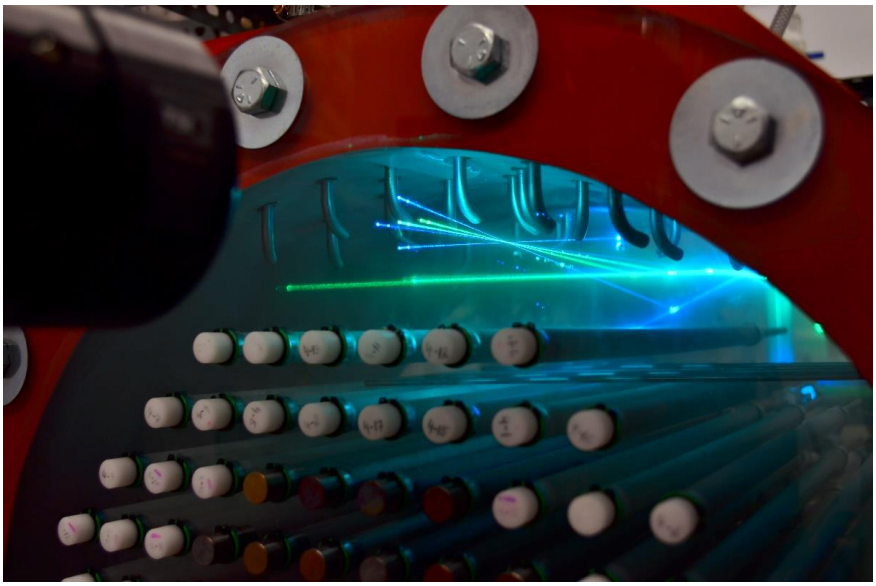

Figure 3-17: Arrangement of the LDV measurement probe for velocity measurements within the test section. The measurement volume is located at the intersection of the five visible beams of light

In these experiments, the beam from the measurement probe passed through multiple materials with differing indices of refraction (air, polycarbonate, and water), which impacted the location of the beam crossing within the test section.

This necessitated a correction to the beam crossing depth position as recorded by the traversing mechanism. This position correction function is shown in Equation 3.2 and is discussed further in section C.3.

$$z_{water} = z_{traverse} \frac{\tan \kappa_{air}}{\tan \kappa_{water}} \tag{3.2}$$

$$\kappa_{water} = \sin^{-1}\left(\frac{n_{air}}{n_{water}} (\sin \kappa_{air})\right) \tag{3.3}$$

Table 3-17: Specifications for the TSI TR360-250 transceiver [56]

Parameter	514.5 nm	488 nm	476.5 nm
Probe beam diameter [mm]	1.8	1.8	1.8
Probe beam spacing [mm]	25.0	50.0	25.0
Lens focal distance [mm]	250.0	250.0	250.0
Beam crossing half angle κ [º]	2.74	5.49	2.74
Measurement volume diameter [μm]	104	99	97
Measurement volume length [μm]	2.1	1.0	2.0

As described in Appendix C, LDV measurements rely on the collection of light deflected by particles flowing through the measurement volume. The flow was seeded with Sphericel hollow glass spheres 10 μm in diameter. Concentrated suspensions were prepared and added to the reservoir tank as needed to maintain acceptable LDV data rates.

3.5.1 Velocity Measurement Limitations

Owing to space and visual accessibility constraints, velocity measurements were limited to the region of the fluid volume accessible through the front plate of the test section. Velocity measurements were not possible from the rear of the vessel due to visual obstructions caused by the heater electrical connections. The traversing mechanism used to position the LDV measurement probe also had a limited range of motion in the *y* direction; as such it was also not possible to collect measurements along the full vertical height of the test section (-245 mm < *y* < -245 mm).

The LDV measurement probe had a focal distance of 250 mm in air. Considering the thickness of the end shield and allowing for clearance between the probe and tube elements, the traversing mechanism was capable of approximately 220 mm of travel in the axial direction of the test section while keeping the LDV measurement volume within the fluid volume. Applying Equation 3.2, this corresponded to a maximum measurement depth of approximately 290 mm in the axial direction inwards from the front plate. For heated cases, unsteady temperature gradients (and hence, unsteady variations in the index of refraction) also limited measurement data rates at higher depths in the test section. This effect is discussed further in Appendix section F.1.

3.6 Experimental Uncertainties

In order to estimate the uncertainties in the measured experimental data, the error propagation equation shown in Equation 3.5 was used to propagate the individual sources of error for each measurement component [57].

$$y = f(x_0, x_1, x_2, \dots, x_n) \tag{3.4}$$

$$\sigma_y^2 \cong \sum \sigma_i^2 \left(\frac{\partial y}{\partial x_i}\right)^2 \tag{3.5}$$

Note that Equation 3.5 assumed that co-variance terms were insignificant by assuming that variables were un-correlated. A summary of the measurement uncertainties is shown in Table 3-18. Additional discussion around the individual sources of error that were considered for each measurement is provided in Appendix D.

Table 3-18: Typical measurement uncertainties

Measurement	Uncertainty sources	Typical uncertainty value
Thermocouple temperature measurements	- RTD calibration - Standard deviation in measured data for averaged measurements	Larger of: σ_T = ± 0.50 °C or $\sigma_T = \frac{1}{N-1}\sqrt{(\bar{T} - T_i)^2}$

Measurement	Uncertainty sources	Typical uncertainty value
Inlet flow rate measurement	- Flow meter system accuracy - Data acquisition gain and offset error	$\frac{\sigma_Q}{Q}$ = ± 0.6%
Heat load	- Measured temperature rise from inlet to outlet - Inlet flow rate uncertainty	$\sigma_{\dot{q}}$ = ± 1400 W (Q = 30 L/min)
Electrical power	- Heater and shunt voltage transmitter calibration - Shunt resistance uncertainty	$\frac{\sigma_{P_e}}{P_e}$ = ± 0.4%
Thermocouple tip position	- Probe tip diameter - Probe straightness	σ_{x_i} = ± 3 mm
Velocity measurement position	- Manual location of beam crossing at z = 0 - Local variation of water refractive index	σ_x = ± 0.1 mm σ_y = ± 0.1 mm σ_z = ± 0.1 mm + 0.3%
Average velocity	- Statistical uncertainty from sample count n over measurement period	$\frac{\sigma_{u_i}}{u_i} = \frac{1}{\sqrt{n}}$

3.7 Test Matrix

A test matrix indicating the ranges of examined flow rate and power conditions that were included in the testing plan is provided in Table 3-19. Due to uncertainties in the scaling parameters and other simplifications made when designing the small-scale test facility, a range of inlet flow rate and power conditions were included in the test plan. This was done to ensure broad coverage of buoyancy conditions.

Table 3-19: Test matrix for the range of examined flow rate and test section power conditions

	8 L/min	15 L/min	24 L/min	30 L/min
0 kW	N/A	N/A	velocities only	velocities only
9 kW	N/A	temperatures only	N/A	N/A
10 kW	N/A	N/A	N/A	velocities and temperatures
12 kW	temperatures only	N/A	N/A	N/A
20 kW	N/A	N/A	velocities and temperatures	velocities and temperatures
40 kW	N/A	N/A	N/A	velocities and temperatures

At the reference 30 L/min inlet flow rate, several power levels were tested (40 kW, 20 kW, and 10 kW). An additional case examined decreasing the inlet flow rate by 20% (24 L/min at 20 kW). Two cases at lower power and flow rates were selected to further examine the *Ar* scaling parameter. A case with 9 kW input power at 15 L/min inlet flow was selected as this would correspond to $Ar \approx 0.010$, similar to the 40 kW at 30 L/min case. Finally, a case with 12 kW input power at 8 L/min inlet flow was selected to examine a case with higher buoyancy effects, corresponding to $Ar \approx 0.10$.

3.8 Summary

This chapter described the facilities used to perform the experiments described in this text. The facility consisted of an approximately $1/16^{th}$ scale model of a Bruce A calandria vessel connected to an instrumented flow loop.

The test section consisted of a stainless-steel vessel 508 mm in diameter and length. The vessel contained 120 horizontal tubes approximately 13 mm in diameter configured in the same pitch-to-diameter ratio as the calandria tubes in a CANDU calandria. The central 52 tube elements were heated with a cosine power profile. Vessel inlets and outlets were configured to closely model those of a Bruce A reactor. Power was supplied to the test section by a programmable DC power supply capable of delivering up to 128 kW.

The flow loop was constructed of PVC tubing and operated at atmospheric pressure. Water flow was driven by a 3 hp pump at rates up to 36 L/min. Cooling was provided by connection to a shell-and-tube heat exchanger connected to a chilled water supply, capable of removing up to 40 kW of heat. Flow rates to the inlets were controlled using six Alicat flow controllers, each consisting of a flow meter, electronically controlled valve, and PID controller. Process flow rates were monitored by Rosemount 8732E magnetic flowmeter processors with Rosemount 8711 sensors. Process temperatures and test section internal temperatures were

measured using K-type thermocouples. Analog measurements were monitored using NI 9214 thermocouple modules and NI 9203 current modules.

Velocity measurements were obtained using LDV performed with a three-dimensional TSI TR360 transceiver. The measurement probe was mounted to a three-axis traversing mechanism to allow for mapping of velocities in specified measurement planes.

Chapter 4

Modelling Details

This chapter presents a description of the computational model used in this study along with the results of a time-step size and grid size study. Results from the modelling studies and comparisons to the experimental results follow in Chapter 5.

4.1 Model Description

The numerical results were obtained using the commercial CFD code STAR-CCM+ version 11.02. All of the computations were performed on a computer system containing 64 processors (2 GHz x86-64 CPU) with 128 GB of memory running under Linux (CentOS 5.5, kernel version 2.6.18).

4.1.1 Computational Mesh

The simulations for this study were performed using a computational mesh developed by Dr. A. Rashkovan, which was previously used for studies reported in [58]. The geometry of the experimental vessel was constructed in the STAR-CCM+ modeller. All geometric features of the vessel, the inlet nozzles, and outlet pipe dimensions were accurately represented while the thermocouples were not modelled. The mesh was built using the trimmed cell meshing tool in STAR-CCM+ with prism layers applied at the boundaries of the tube elements and vessel walls. Three computational meshes were used for this study with base dimensions of

4 mm, 6 mm, and 8 mm for the 'fine', 'medium', and 'coarse' grids, respectively. Other dimensions in the mesh were set relative to the base size. The total number of cells for each size were 20.0 million cells for the fine grid, 8.70 million cells for the medium grid, and 5.21 million cells for the coarse grid. Examples of the mesh at various locations within the vessel are shown in Figure 4-1, Figure 4-2, and Figure 4-3; the grid density in the regions near the tube bank elements was approximately twice as fine as the region near the vessel walls.

In this study, turbulence was accounted for using the realizable k-ε model [59]. With the chosen meshing strategy, not all of the walls were meshed fine enough for the low $y+$ wall treatment to be employed throughout the domain. Hence, the so called 'all $y+$' wall treatment was set in all the simulations. The all $y+$ wall treatment is a hybrid treatment that attempts to emulate the high $y+$ wall treatment for coarse meshes and the low $y+$ wall treatment for fine meshes [60]. The heated simulations used thermophysical properties from the International Association for the Properties of Water and Steam (IAPWS-IF97), incorporated into the STAR-CCM+ software.

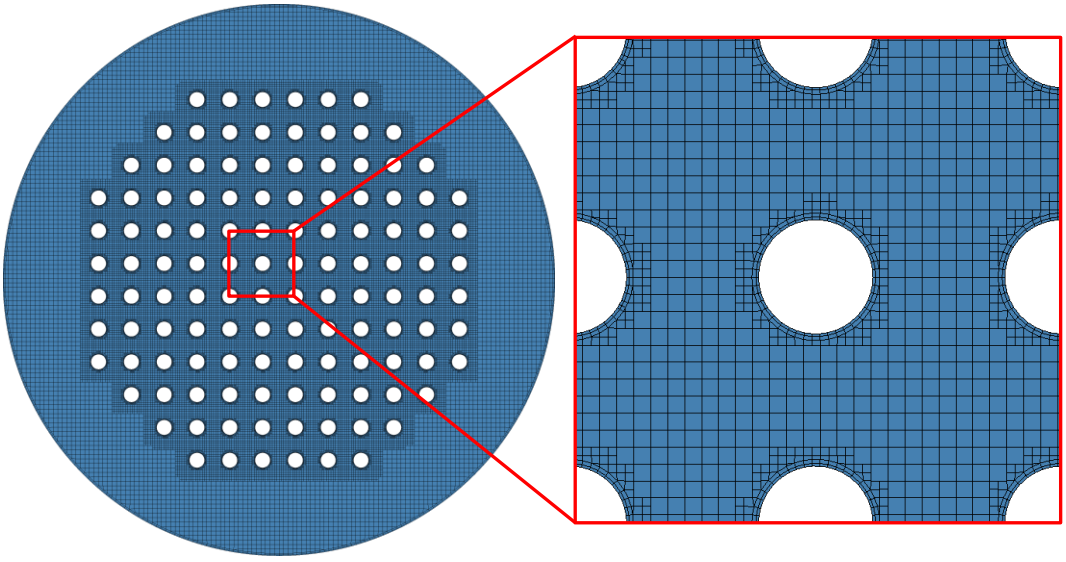

Figure 4-1: Example mesh with 4 mm base size at an *xy*-plane location inside the tube bank (left), with a detail view near a tube bank element (right)

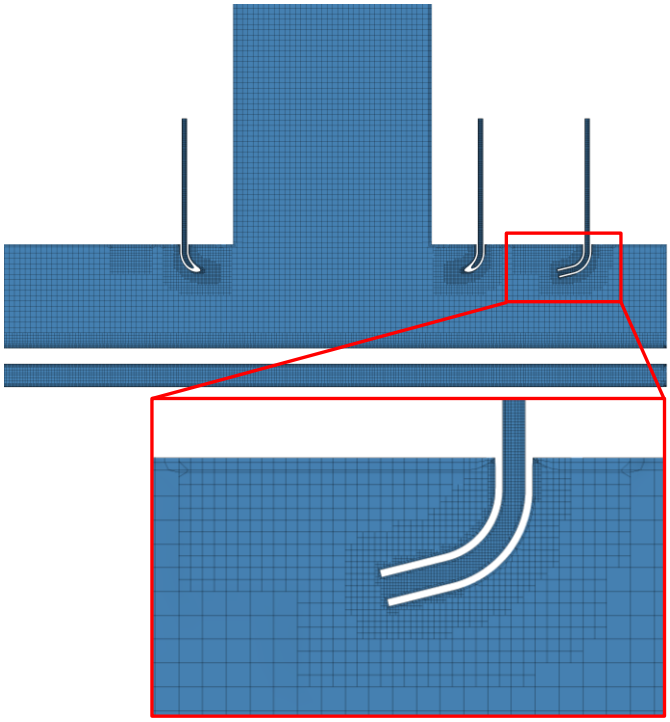

Figure 4-2: Example mesh with 4 mm base size at an *yz*-plane location intersecting three inlet jets above the tube bank (top), with a detail view near the exit of an inlet nozzle (bottom)

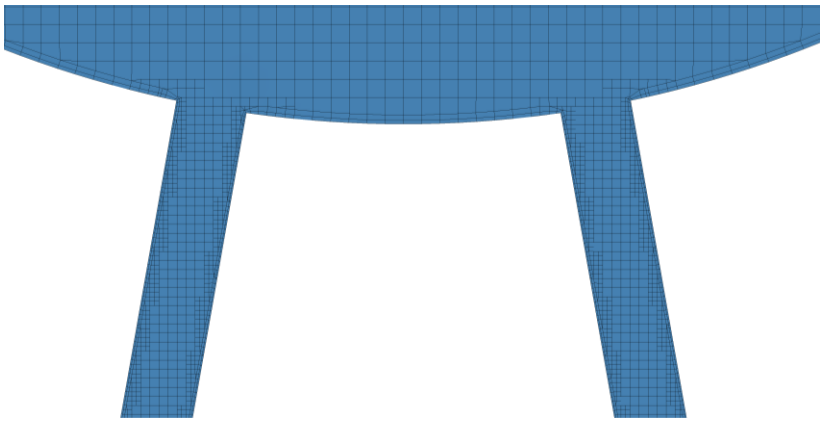

Figure 4-3: Example mesh with 4 mm base size at an *xy*-plane location intersecting the vessel outlets

4.1.2 Boundary Conditions

A summary of the various simulation cases that were run are shown in Table 4-1. For the heated cases, the total inlet flow rates and applied power corresponded to time-averaged measurements made in the corresponding experimental cases (i.e. – each simulated case corresponded directly to an existing experimental case). In addition, two isothermal cases were simulated at two inlet flow rates.

Table 4-1: Summary of the simulated power and flow rate combinations

Simulation ID	Flow [L/min]	Power [kW]	T_{in} [°C]	*Ar*
isoth30LPM-KEreal-4mm	24.0	0.00	25.0	0
isoth30LPM-KEreal-4mm	30.0	0.00	25.0	0
sim0908-KEreal-4mm	30.1	9.85	20.0	1.28×10^{-3}
sim0308-KEreal-4mm	30.0	19.93	22.4	3.05×10^{-3}
sim0831-KEreal-4mm	24.0	19.77	27.3	7.05×10^{-3}
sim0309-KEreal-4mm	30.0	39.80	34.3	8.96×10^{-3}
sim0922-KEreal-4mm	30.0	37.58	40.8	9.43×10^{-3}
sim1017-KEreal-4mm	15.1	9.35	19.8	1.02×10^{-2}
sim1018-KEreal-4mm	8.2	11.87	23.1	1.03×10^{-1}

Heat addition to the test section was modelled as a wall heat flux applied at the boundaries of the central 52 tube bank elements, with the outer 68 tube bank walls specified as adiabatic. No radial power variation was assumed within the heated region of the tube bank (i.e. – individual heated tube elements were assumed to be at the same power). The heat flux profile $q''(z)$ as shown in Equation 4.1 was applied to describe the local heat flux variation in the axial direction over the heated length of 0.5 m. This corresponded to a peak to average heat flux of 1.4 and a minimum to average heat flux of 0.4 as shown in Figure 4-4.

$$q''(z) = q''_{av} \times F(z)$$

$$q''(z) = q''_{av} \times (0.7785 + 0.6215 \times \cos(8.902z - 2.2255)) \qquad (4.1)$$

$$q''_{av} = \frac{q}{n\pi d_{tube} L_{heated}} = \frac{q}{52\pi(1.34\times10^{-2}\ \mathrm{m})(5.00\times10^{-1}\ \mathrm{m})} \qquad (4.2)$$

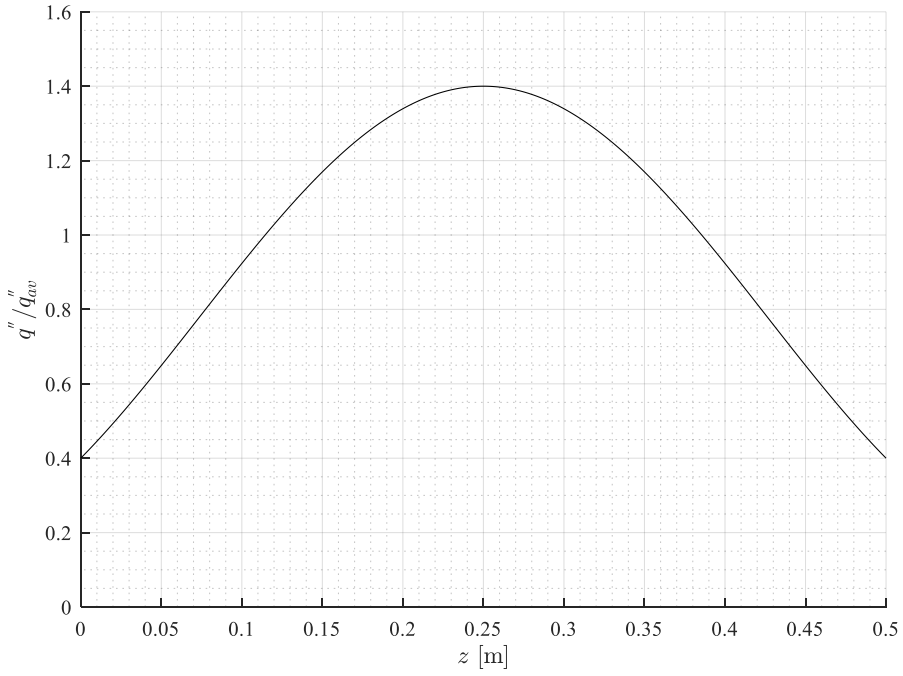

Figure 4-4: Axial heat flux profile applied to the heated tube bank elements

The inlet flow was split between the individual nozzles in a similar manner to the experiments, with two-thirds of the total flow divided across the 16 'booster' inlet nozzles and the remaining one-third divided across to the six 'booster-bypass' inlet nozzles. The flow was assumed to be split evenly across each nozzle type, with each 'booster-bypass' nozzle having $1/18^{th}$ of the total inlet flow and each 'booster' nozzle having $1/24^{th}$ of the total inlet flow. The inlet boundaries were defined as the top of each inlet nozzle; the flow through each nozzle and its geometry was simulated. Turbulence at the inlets was specified with an intensity of 1% and a length-scale of 4.0×10^{-4} m (corresponding to approximately 10% of the inlet inner diameter).

The above assumption involving equal flow rates within each group of nozzle types was akin to assuming even mass flow distribution along the inlet headers shown in Figure 3-12 on page 57. Concurrent to the performance of the numerical study, the flow distribution along the actual headers used in the experiment was extensively

studied by Hollingshead [61]. It was reported that the measured mass flow rate at the individual header ports $\dot{m}_i$ was within ± 2% of the average (i.e. – for a header with N ports and a total flow rate of $\dot{m}_T$, the mass flow at an individual port $\dot{m}_i$ was within 2% of $\dot{m}_T/N$).

Results from the experimental heat balance tests shown in Appendix E section E.1 suggested that heat losses from the test section to the surrounding room were small, typically less than 2%. As a result, heat losses from the outer vessel walls were not modelled.

4.1.3 Initial Conditions

Based upon preliminary simulation results from this study that were reported in [58], unsteady behaviour was expected and transient simulations were performed. The fluid was initially assumed to have zero velocity everywhere within the volume and a uniform temperature equal to the average of the inlet and outlet temperatures from the corresponding experimental case. Steady simulations were initially performed for 4000 – 8000 iterations to reach a 'pseudo-steady' state solution. These conditions from this steady-state solution were used as the initial conditions for the transient simulations. All transient simulations on the fine mesh were performed with a time-step size of 0.05 s, with twelve inner iterations per calculated time step and a total physical time of 250 s.

Simulations were performed in parallel across 48 CPU cores. In this configuration, each inner iteration took approximately 25.1 seconds of calculation time to perform, or approximately 1200 CPU-seconds per iteration. For calculations on 48 CPUs, this corresponded to a calculation run time of 28 to 56 hours to reach the pseudo-steady state solution and an additional 418 hours to complete the calculation of the 250 s transient. This resulted in a total calculation time of approximately 20 days per simulated case.

4.1.4 Captured Data

Due to file storage and file output overhead considerations, it was not practical to save the full solution record for each time step throughout the transient. Snapshots of the velocity and temperature data were taken at 15 *xy*, *xz*, and *yz* planes (45 planes total) and saved every 0.5 physical seconds (i.e. – once every tenth timestep for the fine mesh). Additionally, temperature data snapshots were taken along probe lines corresponding to the regions traversed by the 13 thermocouple probes in the experiment and saved for each time step (i.e. – every 0.05 s for the fine mesh). A summary of the sampled locations is provided in Table 4-2 and Table 4-3.

4.2 Model Sensitivity Studies

The sensitivity of the modelled solution to time-step size and mesh size were studied by examining the temperature distributions in the test section. In the following sections, time-averaged temperature profile data in the x-direction is presented as calculated by Equation 4.3. The standard deviation s_T over the time-average period was also calculated using Equation 4.4.

$$\bar{T}(x) = \frac{1}{N}\sum T(x, t_i) \tag{4.3}$$

$$s_T(x) = \sqrt{\frac{1}{N-1}\sum(\bar{T}(x) - T(x, t_i))^2} \tag{4.4}$$

Table 4-2: Locations of exported velocity and temperature planes

Plane ID (*yz*)	*x* [mm]	Plane ID (*xz*)	*y* [mm]	Plane ID (*xy*)	*z* [mm]
pyz_x0	-202.2	pxz_y0	-202.2	pxy_z0	473.0
pyz_x1	-174.3	pxz_y1	-174.3	pxy_z1	441.5
pyz_x2	-145.3	pxz_y2	-145.3	pxy_z2	410.0
pyz_x3	-116.2	pxz_y3	-116.2	pxy_z3	378.4
pyz_x4	-87.2	pxz_y4	-87.2	pxy_z4	346.9
pyz_x5	-58.1	pxz_y5	-58.1	pxy_z5	315.4
pyz_x6	-29.1	pxz_y6	-29.1	pxy_z6	283.9
pyz_x7	0.0	pxz_y7	0.0	pxy_z7	252.4
pyz_x8	29.1	pxz_y8	29.1	pxy_z8	220.8
pyz_x9	58.1	pxz_y9	58.1	pxy_z9	189.3
pyz_x10	87.2	pxz_y10	87.2	pxy_z10	157.8
pyz_x11	116.2	pxz_y11	116.2	pxy_z11	126.3
pyz_x12	145.3	pxz_y12	145.3	pxy_z12	94.8
pyz_x13	174.3	pxz_y13	174.3	pxy_z13	63.2
pyz_x14	202.2	pxz_y14	202.2	pxy_z14	31.7

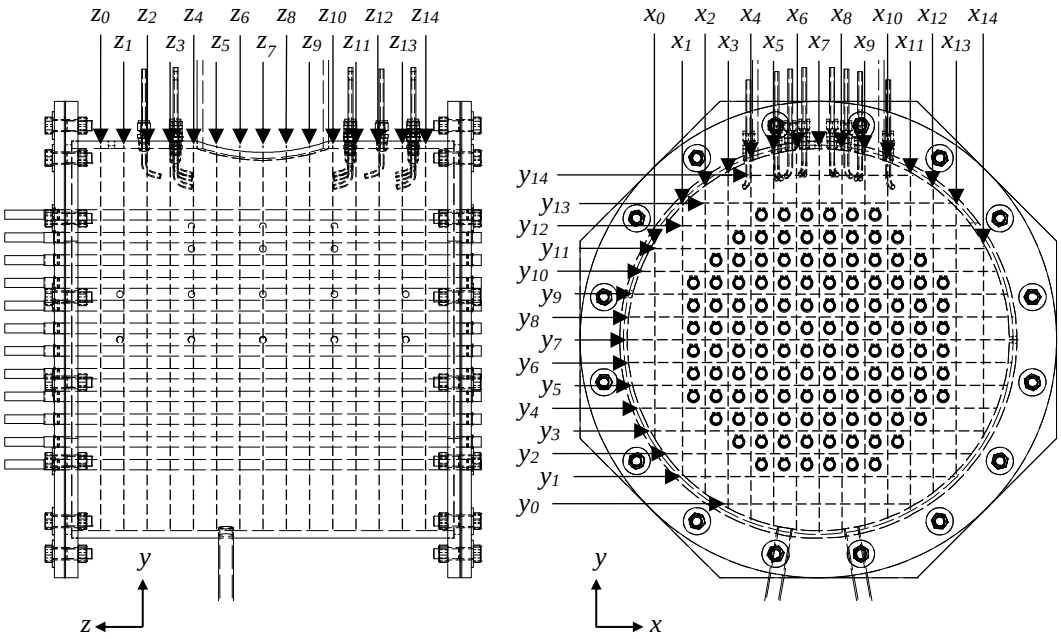

Figure 4-5: Locations of the *xy*, *xz*, and *yz* planes used for saved temperature and velocity snapshots during the transient simulation

Table 4-3: Coordinates for exported temperature probe lines for the transient simulations

Probe ID	*y* [mm]	*z* [mm]	Probe ID	*y* [mm]	*z* [mm]
TCM1-00	58.1	73.3	TCM1-07	116.2	347.6
TCM1-01	58.1	164.7	TCM1-08	0.0	73.3
TCM1-02	58.1	256.2	TCM1-09	0.0	164.7
TCM1-03	58.1	347.6	TCM1-10	0.0	256.2
TCM1-04	58.1	439.1	TCM1-11	0.0	347.6
TCM1-05	116.2	164.7	TCM1-12	0.0	439.1
TCM1-06	116.2	256.2			

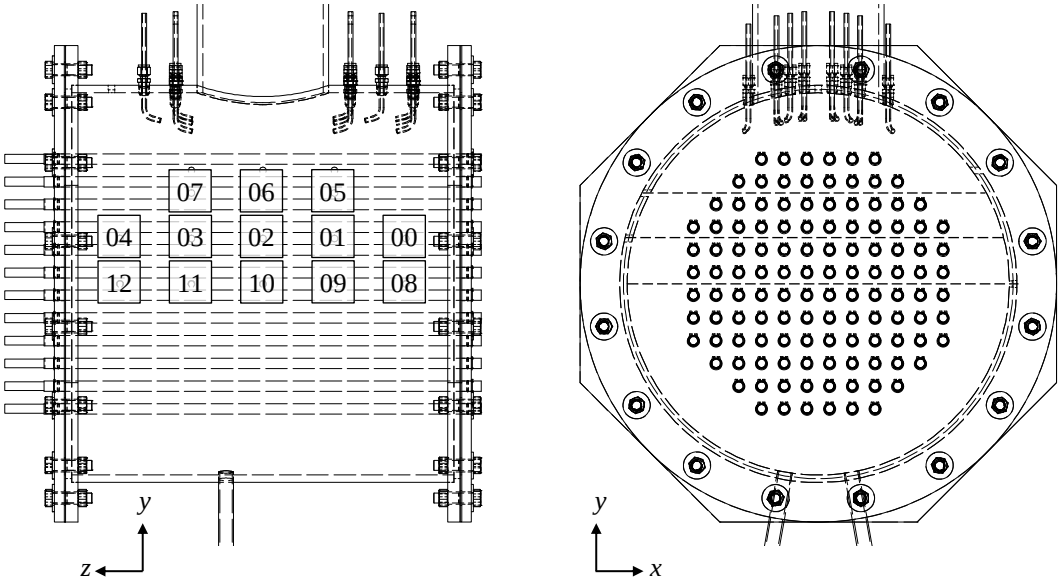

Figure 4-6: Relative *yz*-locations of temperature probe lines (left) and profile lines captured by the temperature probe lines (right) for the transient simulations

4.2.1 Time Step Size Study

A study of the time-step size was performed on the coarse mesh (8 mm base size) using test conditions corresponding to the 0309-00 test case (P_e = 39.80 kW, Q = 30.0 L/min, T_{inlet} = 34.3 ºC, ΔT = 18.8 ºC, Ar = 0.00896). Time step sizes of 0.5 s, 0.25 s, 0.1 s, and 0.05 s were considered with each time step consisting of 10 to 15 inner iterations. Temperature profile data along the lines traversed by the thermocouples in the experiments were saved for each time step for later averaging

and comparison to experimental data. Additionally, a steady simulation was performed using the same test conditions for a total of 15 000 iterations with 'snapshots' of the pseudo-steady state temperature data saved every tenth iteration.

A comparison of the time-averaged temperature result for each timestep size is included in Figure 4-8. The transient solutions were averaged over a period corresponding to 5 s < t < 120 s. It was found that the average temperature solution did not appear to be sensitive to time step size. Similar behaviour was noted for the standard deviation s_T as seen in Figure 4-9. It was also observed that the result obtained from averaging the snapshots of the pseudo-steady state solutions corresponded well to the time-averaged result from transient simulations. However, the standard deviation results obtained from the pseudo-steady state solution snapshots did differ from the transient simulations, especially in the regions outside of the tube bank and in upper regions of the tube bank closer to the inlet jets. Snapshots from the steady state simulations tended to describe larger fluctuations in these regions than observed in any of the transient experiments, suggesting that transient simulations would be necessary in order to examine any unsteady behaviour in these regions.

To further examine the effect of time-step size, temperature behaviour at individual locations within the test section were studied for the various time step sizes. One example is shown in Figure 4-7 for (x, y, z) = (12.2, 58.1, 91.4) mm; this location corresponded to the peak time-averaged temperature over the 120 s transient. To confirm the assertion that the time-step size had little impact on the prediction of the time-averaged behaviour, the grid convergence index (GCI) described by Roache [62] was calculated for the time-averaged temperature at this location:

$$GCI_{ij} = F_S \frac{|\epsilon_{ij}|}{(r_{ij})^p - 1} \tag{4.5}$$

$$\epsilon_{ij} = \frac{f_j - f_i}{f_i} \qquad r_{ij} \cong \left(\frac{N_i}{N_j}\right)^{1/N_d} \tag{4.6}$$

In this case, the factor of safety F_S corresponded to 1.25 as per [63]. The number of dimensions N_d corresponded to 1 (only the time-scale is refined) and the order of accuracy p corresponded to 1 since the implicit unsteady solver used in STAR-CCM+ was first-order accurate in time. The calculation results are shown in Table 4-5. The results suggested that the refining the timestep had little impact on the predicted average temperature result; the GCI estimated that the result changed by approximately 0.4% when refining the timestep from dt = 0.50 s to 0.25 s, with subsequent refinements having an order of magnitude smaller impact. These results corresponded with the above observations regarding Figure 4-8 and Figure 4-9.

Next, the time-dependent behaviour shown in Figure 4-7 was examined. The overall range of temperatures observed at this probe location appeared similar, regardless of timestep size. As expected, higher frequency fluctuating behaviour was visible at smaller time steps. It was also noted that the relatively large amplitude fluctuation at 80 s < t < 120 s was resolved differently as dt was decreased, with similar behaviour noted between dt = 0.1 s and 0.05 s. A timestep size of 0.1 s was ultimately selected for the coarse mesh as a compromise between economizing computational resources and resolving the transient behaviour shown in Figure 4-7. Based upon selecting a timestep size of 0.1 s for the coarse mesh, a timestep size of 0.05 s was selected for the fine mesh. This timestep size was selected to maintain a similar Courant number as for the coarse mesh case with dt = 0.1 s:

$$C = \frac{u\Delta t}{\Delta x} \tag{4.7}$$

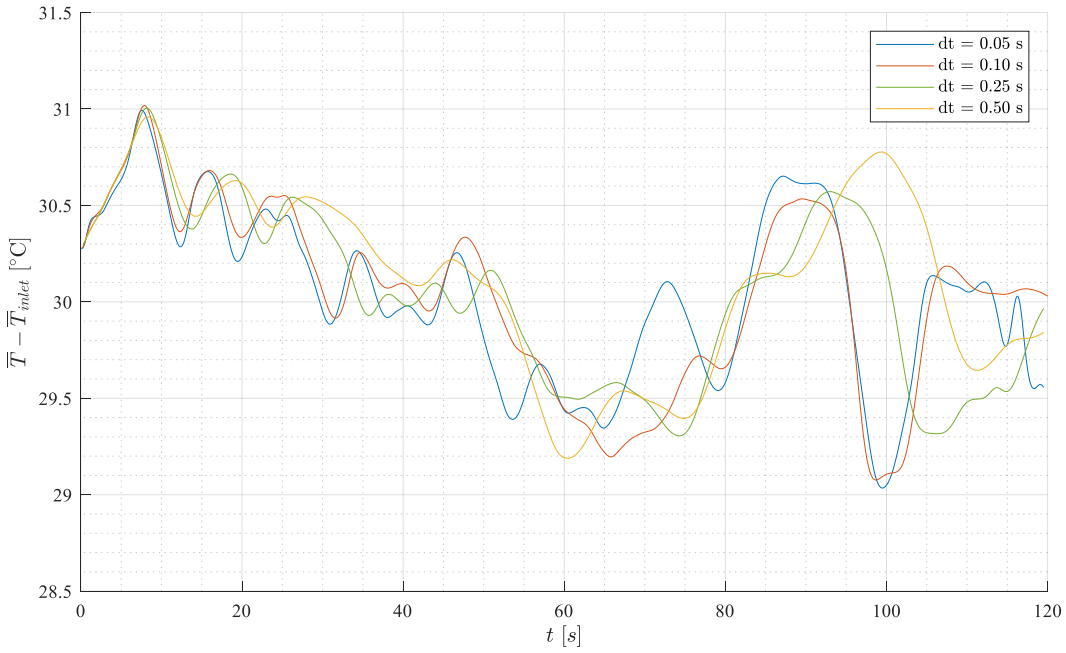

Figure 4-7: Time-dependent temperature behaviour on the coarse mesh at (*x*, *y*, *z*) = (12.2, 58.1, 164.7) mm for various time-step sizes. Simulated conditions correspond to test ID 0309-00

Table 4-4: Average temperature values for 0 < *t* < 120 s corresponding to the temperature probe data shown in Figure 4-7

	***dt* = 0.05 s**	***dt* = 0.10 s**	***dt* = 0.25 s**	***dt* = 0.50 s**
$\overline{T} - \overline{T}_{inlet}$ [°C]	30.0339	30.0319	30.0418	30.1408

Table 4-5: Relative errors and grid convergence indices corresponding to Table 4-4. The subscripts 1, 2, 3, and 4 correspond to dt = 0.05 s, 0.10 s, 0.25 s, and 0.50 s respectively

	ϵ_{12}	ϵ_{23}	ϵ_{34}	GCI_{12}	GCI_{23}	GCI_{34}
$\overline{T} - \overline{T}_{inlet}$	6.5×10^{-5}	3.3×10^{-4}	3.3×10^{-3}	0.008%	0.028%	0.412%

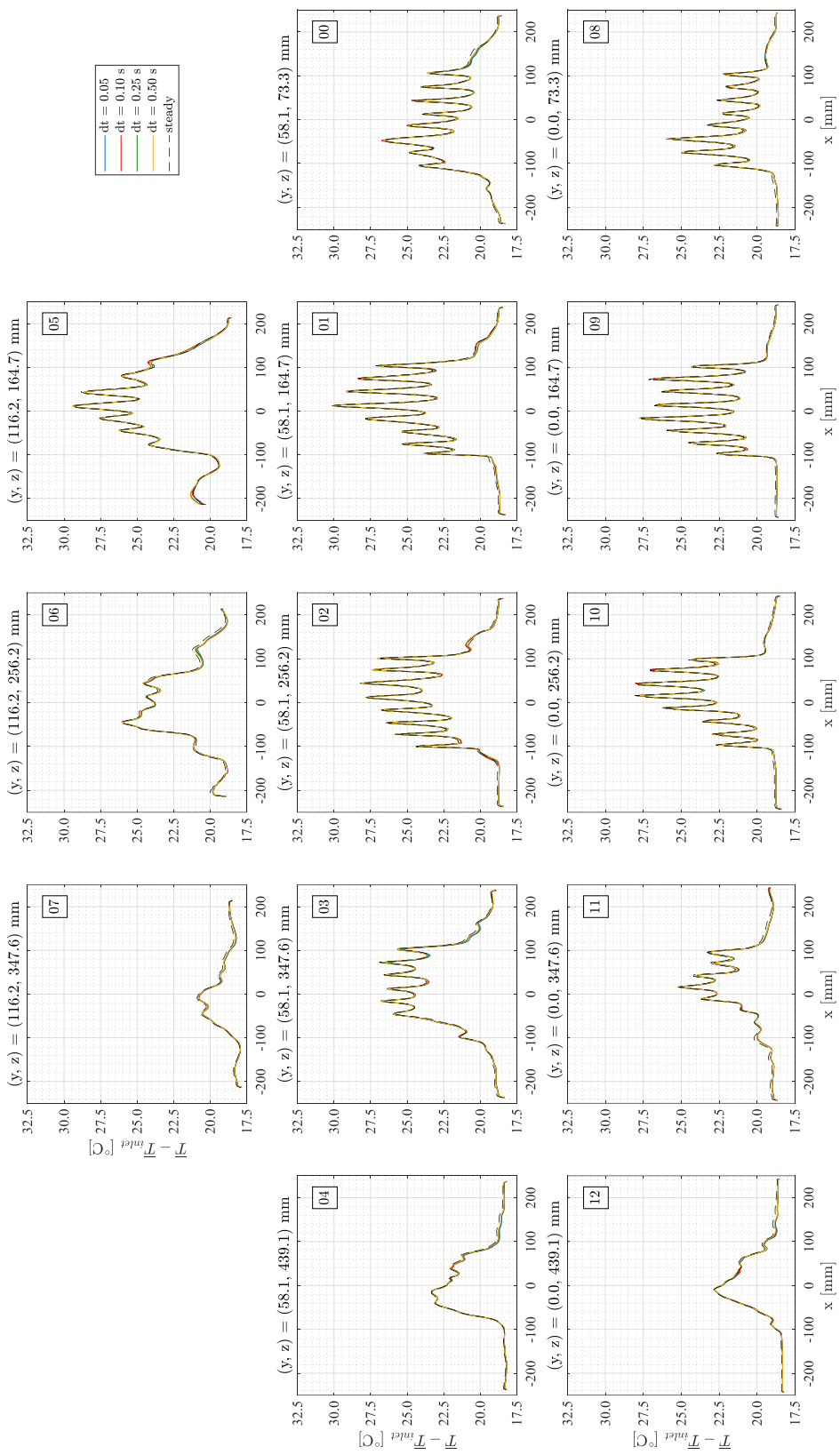

Figure 4-8: Comparison of average temperature profiles from coarse mesh simulations (8 mm base size) with varying timestep size *dt*. Test conditions correspond to test ID 0309-00 (P_e = 39.80 kW, Q = 30.0 L/min, Ar = 0.00896)

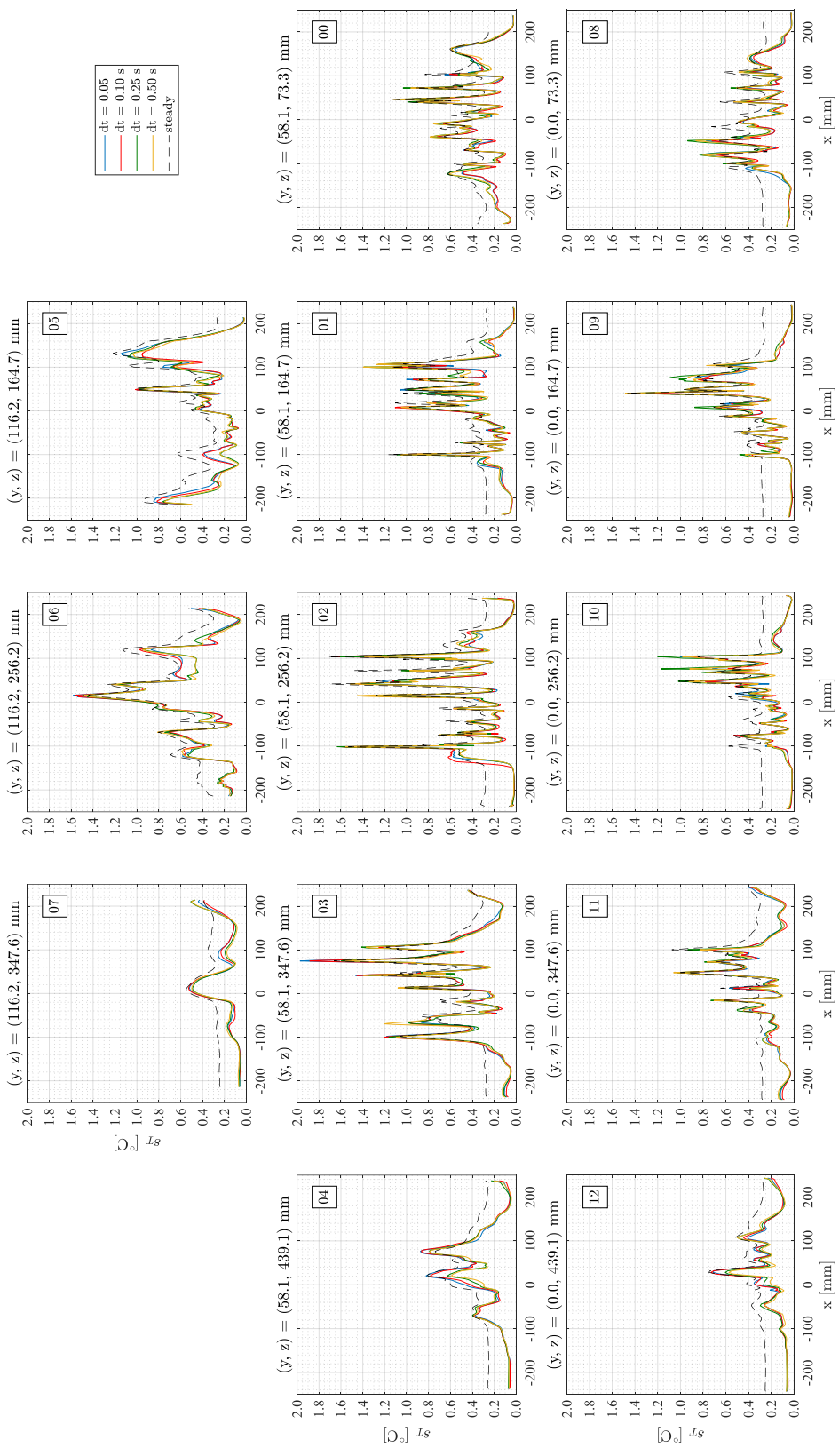

Figure 4-9: Comparison of standard deviation s_T from coarse mesh simulations (8 mm base size) with varying timestep size *dt*. Test conditions correspond to test ID 0309-00 (P_e = 39.80 kW, Q = 30.0 L/min, Ar = 0.00896)

4.2.2 Grid Size Study

A mesh size sensitivity study was performed on the fine, medium, and coarse mesh sizes using test conditions corresponding to the 0309-00 test case (P_e = 39.80 kW, Q = 30.0 L/min, T_{inlet} = 34.3 ºC, ΔT = 18.8 ºC, Ar = 0.00896). Temperature profile data along the lines traversed by the thermocouples in the experiments were saved for each time step for later averaging and comparison to experimental data. Transient simulations on the fine and medium mesh size used a timestep size of 0.05 s while simulations on the coarse mesh used a timestep size of 0.10 s.

A comparison of the time-averaged temperature results for each grid size is shown in Figure 4-10. Qualitatively, the average temperature distributions were similar across all three grid sizes with the predicted result not changing significantly with mesh refinement level, with a few exceptions. The simulated temperature profiles in the regions traversed by thermocouple probes TCM1-03 and TCM1-07 appeared sensitive to mesh size. Due to the arrangement of the inlet nozzles, these regions of the vessel were expected to have large temperature gradients as a result of the interaction between downward, cool flow from the booster-bypass inlets and warm buoyant flows from the heated tube bank elements.[11] The differences between the three grids at these locations were attributed to this high gradient region being resolved differently as the mesh was refined.

In order to quantify the level of grid convergence, the grid convergence index (GCI) described by Roache [62] was calculated for the coarse-medium and medium-fine grid refinements.

$$GCI_{ij}(x) = F_S \frac{|\epsilon_{ij}(x)|}{(r_{ij})^p - 1} \tag{4.8}$$

[11] A further investigation and discussion of the transient temperature behaviour in this region is covered in Chapter 5 section 5.2.1

$$\epsilon_{ij} = \frac{f_j - f_i}{f_i} \qquad r_{ij} \cong \left(\frac{N_i}{N_j}\right)^{1/3} \tag{4.9}$$

In this case, the GCI was calculated as a local parameter using Equation 4.8 at each sampled *x* location shown in Figure 4-10. A global averaged value was calculated for each temperature profile as well as overall using Equation 4.10.

$$\overline{GCI}_{ij} = \sqrt{\frac{1}{N}\sum\left(GCI_{ij}(x)\right)^2} \tag{4.10}$$

A factor of safety F_S of 1.25 was used as suggested for studies using three grid sizes [63]. The order of accuracy *p* was assumed to be 2 (since the spatial solver used in STAR-CCM+ was second-order accurate). For the fine-medium mesh comparison, the refinement level was estimated as $r_{12} \cong (20.0/8.70)^{1/3} = 1.32$. Similarly, for the medium-coarse mesh comparison, the refinement level was estimated as $r_{23} \cong (8.70/5.21\ )^{1/3} = 1.20$. The results of the calculations are shown in Table 4-6.

Table 4-6: Grid convergence indices for time-averaged temperature profile data shown in Figure 4-10

Location ID	$\overline{GCI}_{12}$ (fine-medium) [%]	$\overline{GCI}_{23}$(medium-coarse) [%]
TCM1-00	2.26	6.89
TCM1-01	3.01	8.72
TCM1-02	2.69	6.90
TCM1-03	8.80	18.84
TCM1-04	3.00	10.08
TCM1-05	3.03	17.46
TCM1-06	6.25	13.11
TCM1-07	2.35	14.21
TCM1-08	1.80	6.64
TCM1-09	3.32	7.38
TCM1-10	3.26	7.88
TCM1-11	2.91	6.75
TCM1-12	2.44	5.63
Overall	3.91	10.75

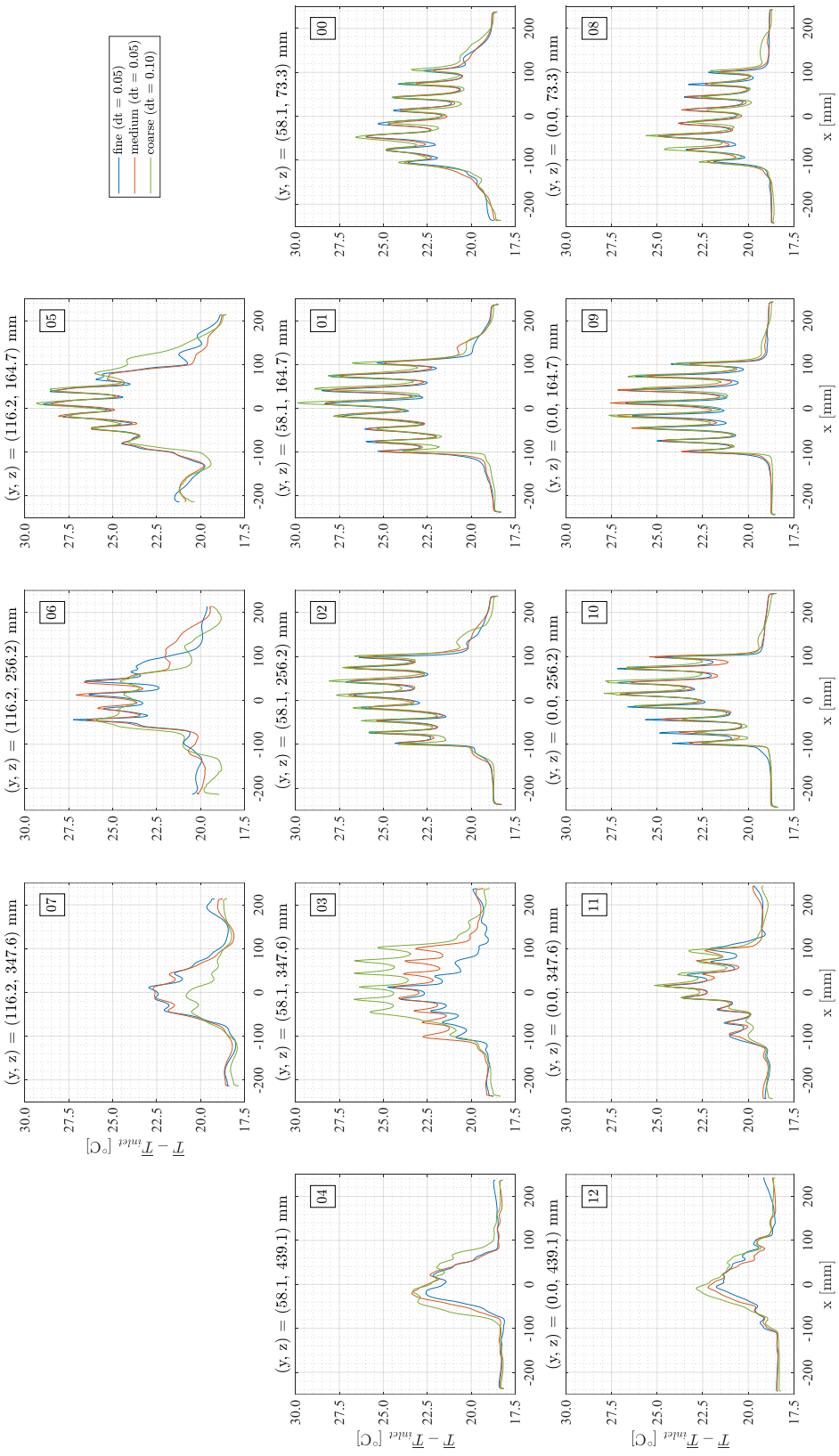

Figure 4-10: Comparison of average temperature profiles from transient simulations (0 s < t < 250 s) on various mesh sizes. Simulated conditions correspond to test ID 0309-00 (P_e = 39.80 kW, Q = 30.0 L/min, Ar = 0.00896)

The global averaged grid convergence indices were 10.75% and 3.91% for the coarse-medium and medium-fine refinements respectively. The smaller GCI values for the medium-fine refinement indicated that the solution was becoming less grid-dependent as the mesh was refined, as expected. Examining the average GCI values for each temperature profile in Table 4-6, for each location $\overline{GCI}_{12}$ was less than half of $\overline{GCI}_{23}$ in all cases, suggesting that the differences between the fine and medium meshes was notably smaller than between the medium and coarse meshes. $\overline{GCI}_{12}$ was notably larger for temperature probes TCM1-03 and TCM1-07 (in the high temperature gradient regions) compared to elsewhere in the domain, further suggesting that the predicted behaviour in this region was sensitive to the mesh size. Due to constraints on available computational resources, it was not feasible to refine the mesh further beyond the fine mesh case. As a result, the fine mesh was selected for the computational study.

One of the goals of the computational study was to evaluate the effectiveness of the model at predicting the peak instantaneous temperature within the vessel. The peak temperatures were expected to occur in the 'eastern' end of the vessel (i.e. – closer to z = 0, corresponding to temperature probes TCM-01, 02, and 05). The grid convergence index in these regions were low, suggesting that the prediction of the maximum temperatures in the vessel was less sensitive to the grid size.

4.2.3 Transient Length

In determining if a simulated transient length of 250 s was appropriate, the time-dependent temperature behaviour was examined at several locations, with examples shown in Figure 4-11. At each location, the instantaneous temperature was plotted, along with a running average $RA_T(t)$ calculated up to time t using Equation 4.11, and compared to the average value $\bar{T}$ obtained over 0 s < t < 250 s.

$$RA_T(t) = \frac{1}{N_t}\sum_0^t T(t) \tag{4.11}$$

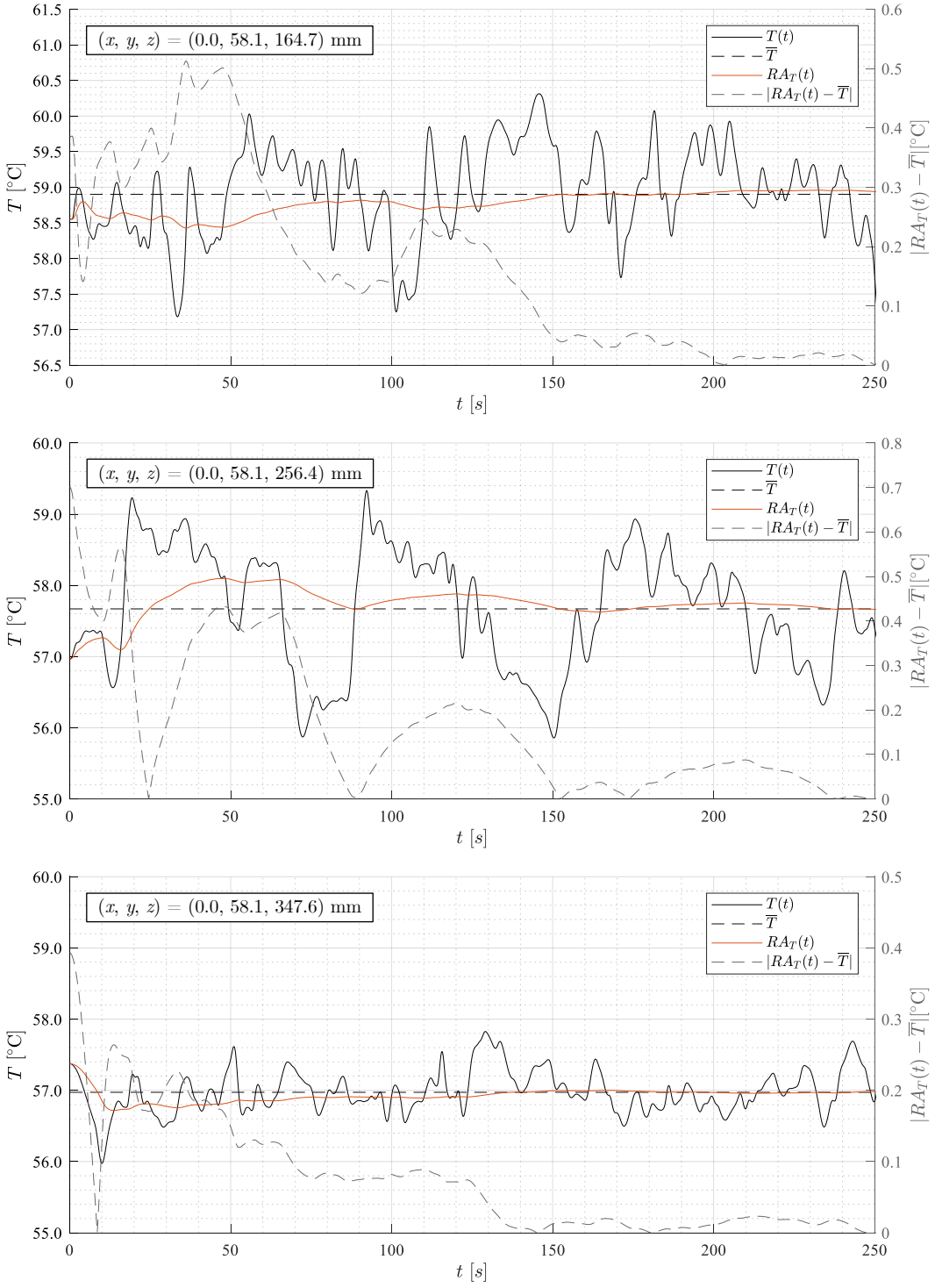

Figure 4-11: Time-dependent and running average temperature behaviour for test ID 0309-00 on the fine mesh at the indicated (*x*, *y*, *z*) locations

For the first and third selected locations, it appeared that the running average $RA_T(t)$ did not change significantly (within 0.05 ºC) for values of *t* longer than 150 s. At the second location, cyclical behaviour with a characteristic time scale of approximately 75 – 80 s was observed. It was desired to capture two to three cycles of this behaviour over the transient, suggesting that a run time of at least 160 to 240 seconds would sufficient. With this criterion, a transient time of 250 s was deemed appropriate.

4.3 Summary

This chapter presented a description of the computational model used to simulate the experimental conditions studied in the small-scale Bruce A test facility. Unsteady RANS simulations were performed using STAR-CCM+ version 11.02 on a computational mesh with 20 million cells and a timestep size of 0.05 s. Turbulence was modelled with the realizable *k*-ε model with the all $y+$ wall treatment.

Fluid properties for the heated cases were obtained using IAPWS-IF97. Heat addition to the test section was modelled as a wall heat flux applied at the boundaries of the central 52 tube bank elements with a coaxial heat flux profile matching the behaviour of the heaters used in the experiments. Two-thirds of the inlet flow was split evenly across the 16 'booster' inlet nozzles and the remaining one-third split evenly across the six 'booster-bypass' inlet nozzles.

A time-step size study was performed on the coarse mesh which resulted the selection of a 0.10 s timestep size, corresponding to a 0.05 s timestep size on the refined mesh. Additionally, the prediction of the time-averaged temperatures did not appear sensitive to timestep size.

A grid-size study examining the prediction of time-averaged temperatures was performed on fine, medium, and coarse grids containing 20 million cells, 8.7

million cells, and 5.2 million cells respectively. The time-averaged temperature solutions did not appear highly sensitive to grid size in regions where the peak temperatures were expected. The predicted temperature profile in a region toward the ‘western’ or rear end of the vessel did appear sensitive to mesh size; this behaviour was attributed to a high gradient region being resolved differently as the mesh was refined.

Transient simulations were performed for up to 250 s on the fine mesh for the range of applied power and inlet flow conditions tested in the experimental study. Results from the modelling studies and comparisons to the experimental results follow in Chapter 5.

Chapter 5

Results and Discussion

5.1 Time-Averaged Behaviour

5.1.1 Temperature Measurements

Temperature measurements were obtained under steady state conditions within the test section for a variety of power levels. Steady state conditions were defined as the measured heat balance being within ± 5% and that the measured inlet temperature had changed less than ± 0.2 ºC over a five-minute period. Temperature profiles within the tube bank were measured with an *x*-position spacing equal to 1/2 of the tube bank pitch (14.5 mm), such that measurement locations corresponded to locations centred directly above a tube bank element or centered within the subchannel between tube bank columns.

Time-averaged temperature measurements at a selection of range of power and flow rate conditions are provided in Figure 5-1 through Figure 5-5 and are presented in order of increasing *Ar*. The temperature measurements are plotted with predicted temperature profiles from the corresponding simulations. A complete set of time-averaged temperature measurements for all experimental conditions are included in Appendix E section E.2.

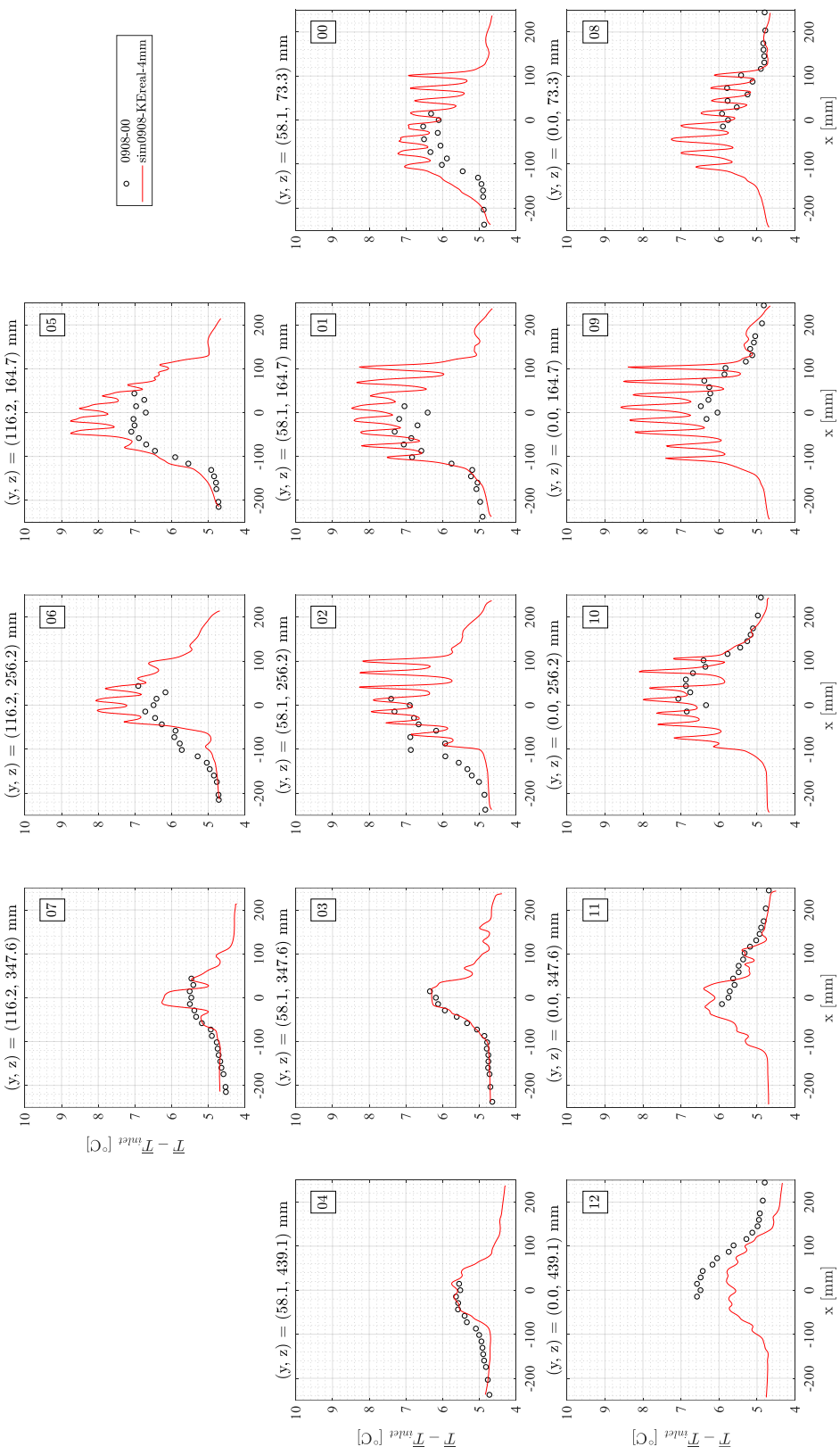

Figure 5-1: Time-averaged temperature measurements (circles) and simulation results (line) for test ID 0908-00 (P_e = 9.85 kW, Q = 30.1 L/min, T_{inlet} = 20.0 °C, ΔT = 4.8 °C, Ar = 0.0013)

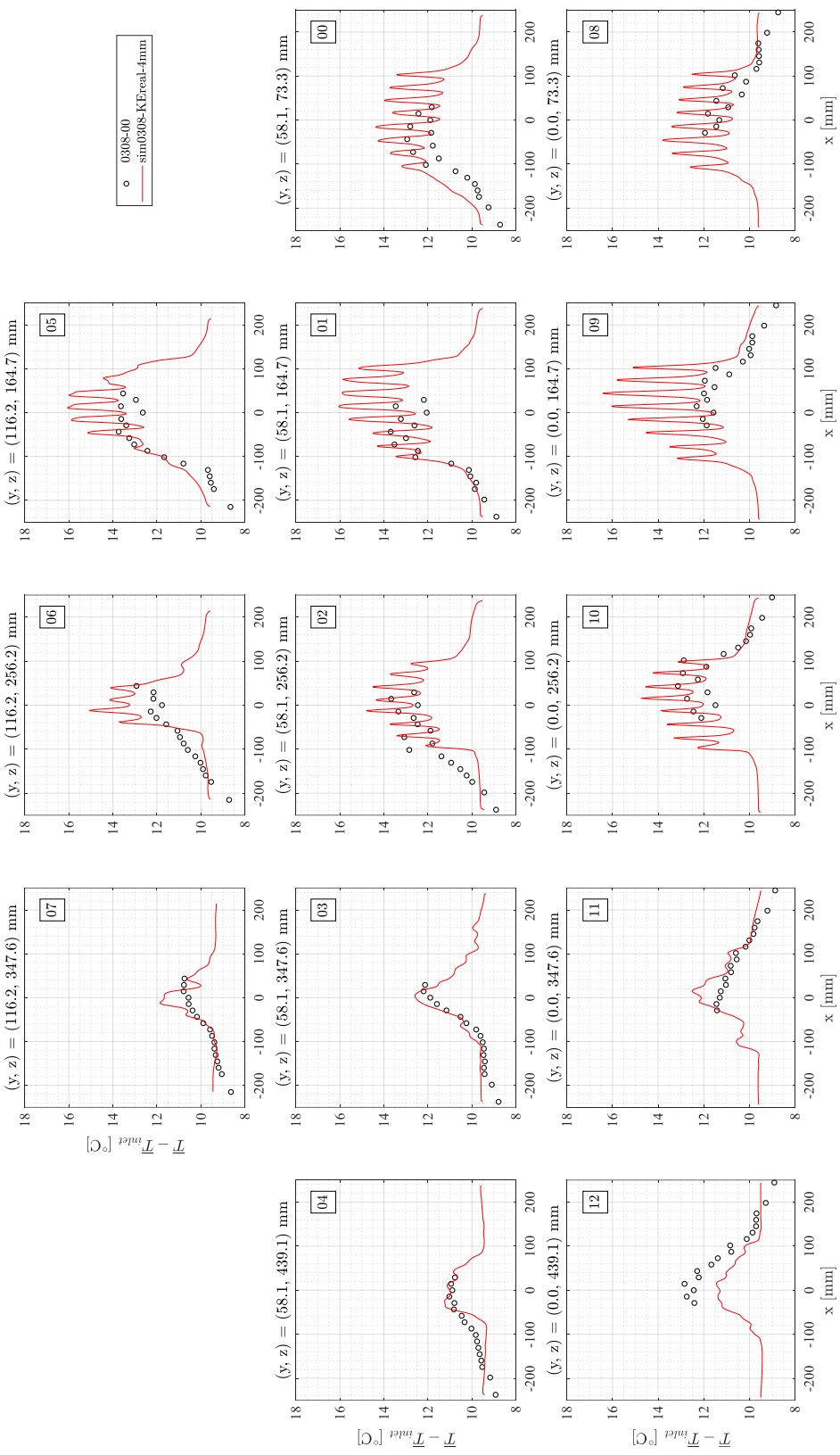

Figure 5-2: Time-averaged temperature measurements (circles) and simulation results (line) for test ID 0308-00 (P_e = 19.93 kW, Q = 30.0 L/min, T_{inlet} = 22.4 °C, ΔT = 9.5 °C, Ar = 0.0031)

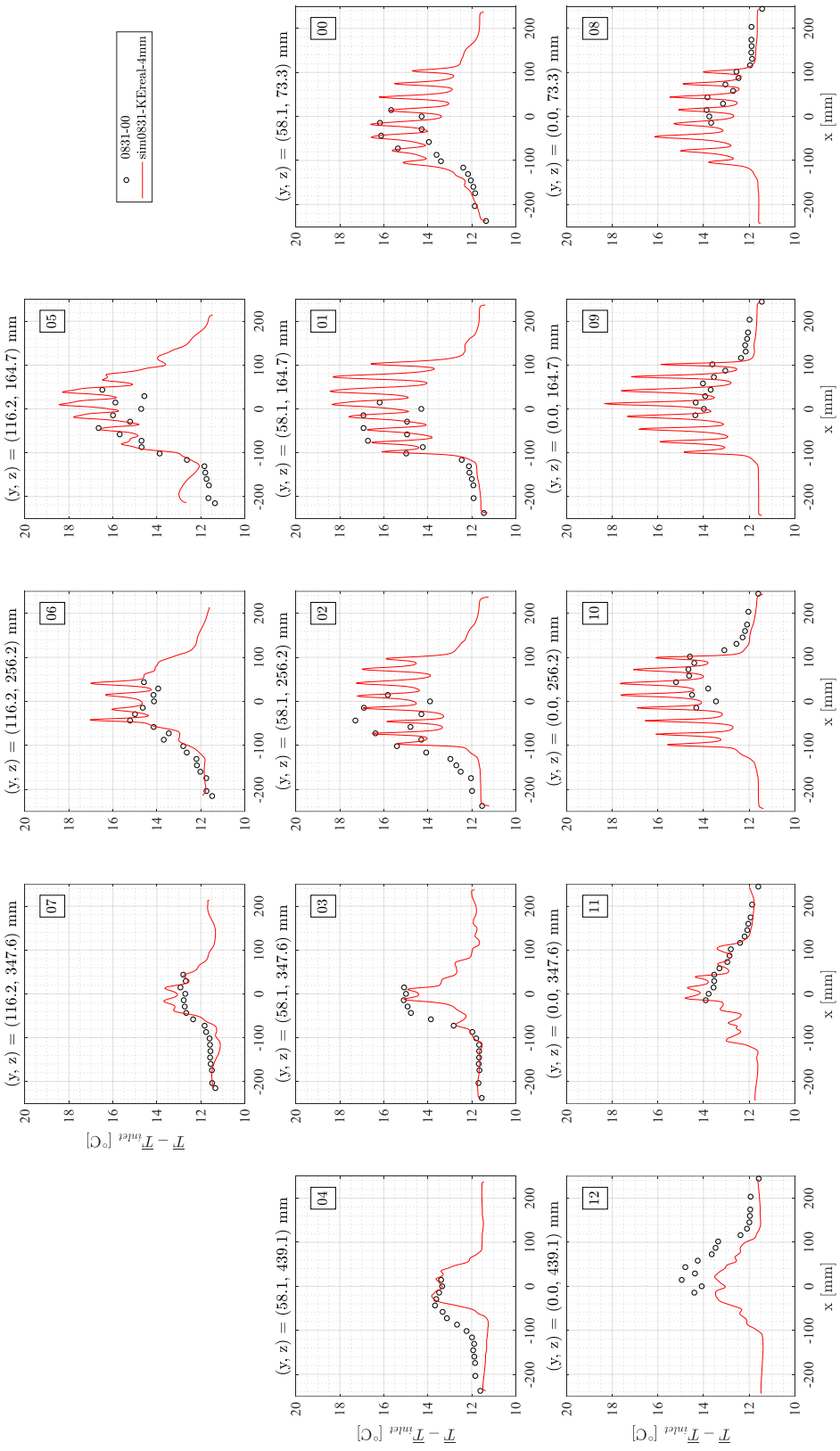

Figure 5-3: Time-averaged temperature measurements (circles) and simulation results (line) for test ID 0831-00 (P_e = 19.77 kW, Q = 24.0 L/min, T_{inlet} = 27.3 °C, ΔT = 11.8 °C, Ar = 0.0071)

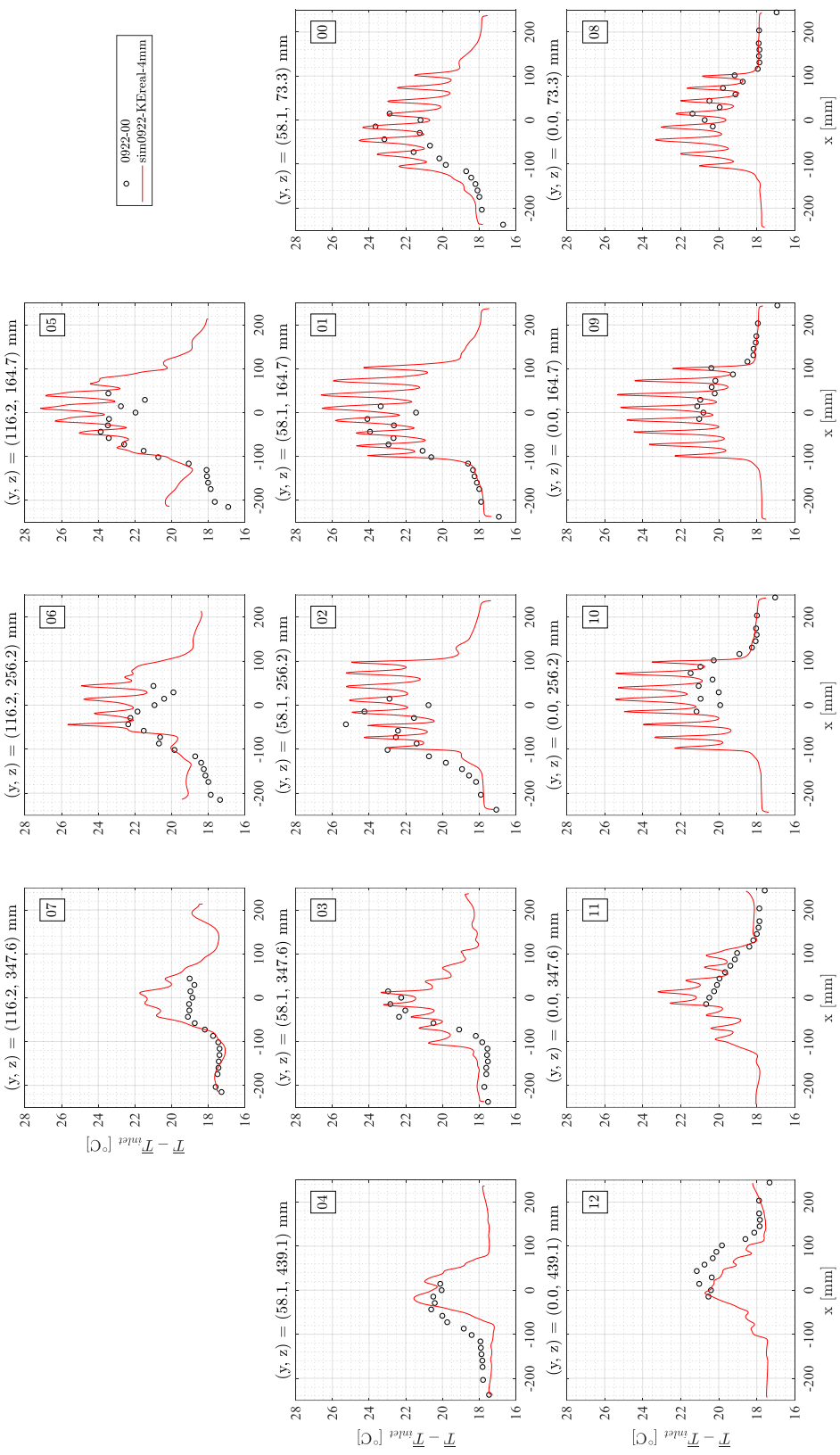

Figure 5-4: Time-averaged temperature measurements (circles) and simulation results (line) for test ID 0922-00 (P_e = 37.58 kW, Q = 30.0 L/min, T_{inlet} = 40.8 °C, ΔT = 17.9 °C, Ar = 0.0094)

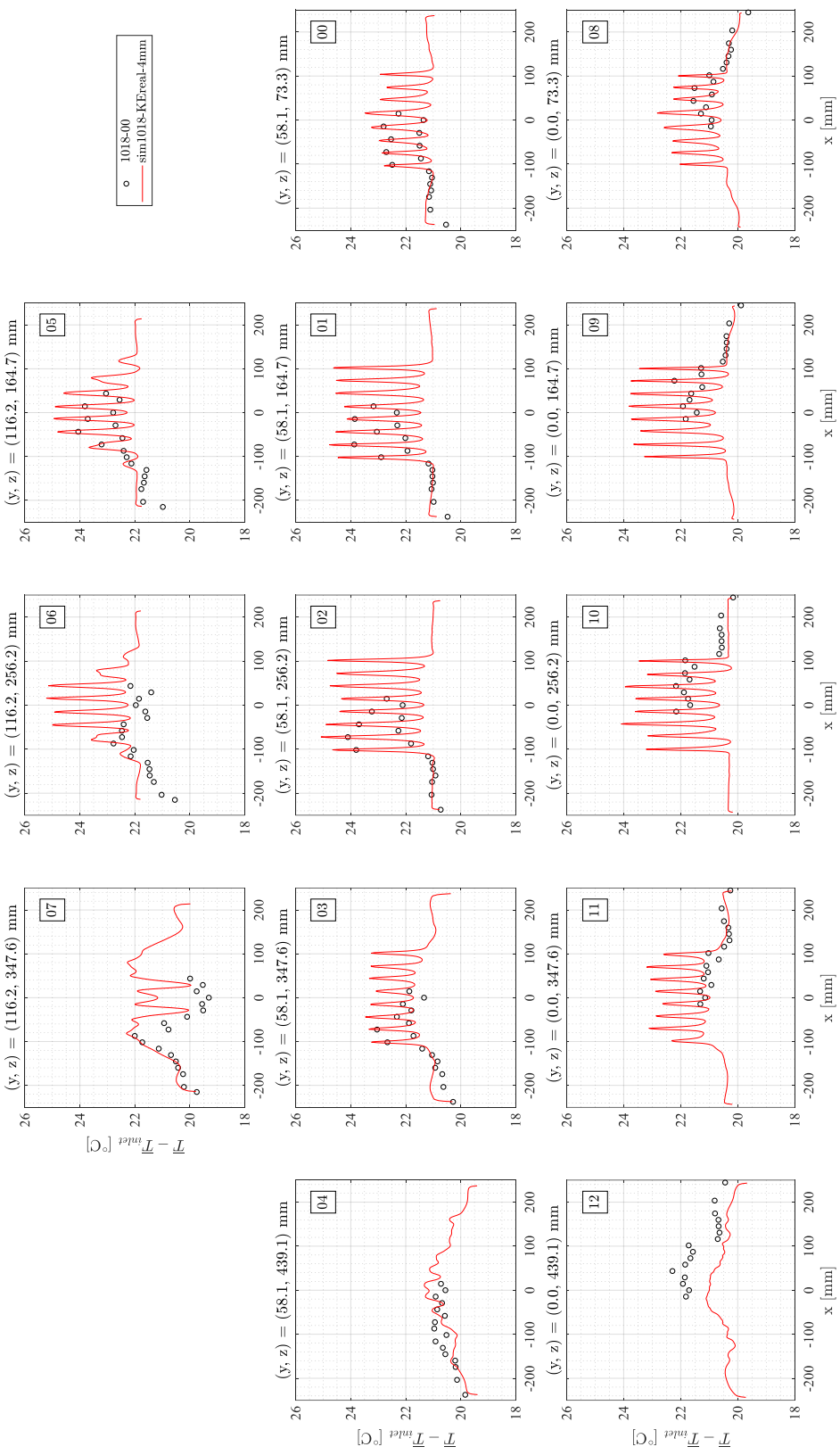

Figure 5-5: Time-averaged temperature measurements (circles) and simulation results (line) for test ID 1018-00 (P_e = 11.87 kW, Q = 8.2 L/min, T_{inlet} = 23.1 °C, ΔT = 20.2 °C, Ar = 0.10)

In general, it was observed that the temperature was higher towards the radial centre of the tube bank, with the local temperature approaching the outlet temperature at *x*-locations outside of the central heated region. Temperatures were also observed to be higher directly above a heated tube bank element compared to the adjacent open channel in between two tube bank elements. This was visible as alternating higher and lower temperatures between measurement points within the heated section of the tube bank. This is especially visible in the temperature maps at *x* locations near the centre of the vessel for the thermocouples nearest the eastern end of the vessel (e.g. – probe locations 00, 01, 05, 08, and 09). This behaviour was also predicted in the simulations, although the model tended to overpredict the temperatures above the heated tube bank elements.

Next, the modelled temperature results from the simulations were compared to the experimental measurements. For each temperature measurement location, the difference between the experiment and simulated result was calculated using Equations 5.1 and 5.2. Due to the experimental positional uncertainty, the measured value at a position *x* was compared to simulated values at location *x* ± 1 mm, with the minimum difference taken:

$$e_{\bar{T}}(x,y,z) = \min\left(e_{\bar{T}}(x_{-1},y,z), e_{\bar{T}}(x_0,y,z), e_{\bar{T}}(x_1,y,z)\right) \tag{5.1}$$

$$e_{\bar{T}}(x_i,y,z) = \left|\bar{T}_{exp}(x,y,z) - \bar{T}_{sim}(x+i,y,z)\right| \tag{5.2}$$

For each temperature probe line, the overall difference between the experimental data and simulation results was quantified by the maximum and RMS differences along the probe line using Equations 5.3 and 5.4. These quantities are summarized for the given experimental cases in Table 5-1 and show that on average, the simulations were able to predict temperatures within the test section within 0.5 – 4 ºC.

$$e_{T_{max}} = \max\left(e_{\bar{T}}(x)\right) \tag{5.3}$$

$$e_{T_{RMS}} = \sqrt{\frac{1}{N}\sum e_{\bar{T}}(x)^2} \tag{5.4}$$

Table 5-1: Maximum and RMS error between simulated and experimental average temperature data along the temperature probe lines for the cases presented in Figure 4-8 through Figure 5-5

Case / Probe Line	0908-00 ($Ar \approx 0.001$)		0308-00 ($Ar \approx 0.003$)		0831-00 ($Ar \approx 0.007$)		0922-00 ($Ar \approx 0.01$)		1018-00 ($Ar \approx 0.1$)	
	$e_{T_{RMS}}$ [ºC]	$e_{T_{max}}$ [ºC]	$e_{T_{RMS}}$ [ºC]	$e_{T_{max}}$ [ºC]	$e_{T_{RMS}}$ [ºC]	$e_{T_{max}}$ [ºC]	$e_{T_{RMS}}$ [ºC]	$e_{T_{max}}$ [ºC]	$e_{T_{RMS}}$ [ºC]	$e_{T_{max}}$ [ºC]
00	0.57	0.98	0.88	1.47	0.47	0.91	0.76	1.45	0.22	0.69
01	0.53	1.11	0.85	2.46	0.43	1.08	0.50	1.26	0.41	0.83
02	0.59	1.76	0.80	2.21	0.91	1.95	0.88	1.77	0.39	0.81
03	0.06	0.13	0.37	0.73	0.85	2.27	0.96	2.55	0.39	0.94
04	0.19	0.33	0.38	0.80	0.81	1.75	0.94	1.98	0.36	0.72
05	0.70	1.48	1.07	2.18	0.92	1.76	1.69	3.21	0.46	1.20
06	0.59	1.24	0.83	1.63	0.59	1.79	1.52	3.46	1.17	2.50
07	0.27	0.74	0.47	1.10	0.35	0.72	1.14	2.46	1.06	2.31
08	0.28	0.91	0.60	1.59	0.49	0.99	0.66	1.85	0.28	0.80
09	0.72	1.50	1.55	3.90	0.76	1.71	0.79	2.24	0.57	1.11
10	0.26	0.95	0.43	0.88	0.89	2.07	1.34	2.98	0.59	1.20
11	0.26	0.55	0.50	1.21	0.29	0.87	0.69	2.03	0.43	1.02
12	0.54	0.90	0.86	1.40	1.00	1.75	0.88	1.64	0.83	1.44
Overall	0.47	1.76	0.81	3.90	0.71	2.27	1.05	3.46	0.63	2.50

5.1.2 Velocity Measurements

This section examines and compares selected LDV measurements to time-averaged velocity data from the simulations; Additional velocity measurements are included in Appendix F. The results presented in section 5.1.1 demonstrated that the simulations tended to overpredict the average temperatures within the heated regions of the tube bank. It was speculated that this could have been caused by the model underpredicting velocities within the tube bank, causing an underprediction of local heat transfer rates with associated higher temperatures.

Time-averaged velocity magnitude contour plots at a range of test conditions are included in Figure 5-6 through Figure 5-10 for an *yz*-plane located at x = 0 mm,

corresponding to the centre of the test section. Unit length vectors are included to indicate flow direction and empty regions in the contour plots corresponded to areas where LDV measurements were not possible. Unsteady temperature gradients within the tube bank further limited the reach of the LDV measurements, with a greater impact seen at higher power levels; this issue is discussed in Appendix F section F.1. The contour plots for the measurements and the simulations are presented on the same colour-bar scale and have been cropped to show a comparable field of view.

Qualitatively, the simulated velocity magnitude contour plots agreed well with the measurements. Due to the arrangement of the inlet nozzles, a recirculation pattern was expected in the vessel which would result in upward flow in this region of the vessel. This behaviour was observed in both the measurements and simulations for the isothermal case, shown in Figure 5-6. For this case, the velocities within the tube bank appeared to be underpredicted in the simulation. For example, in central tube bank region (-116 mm < y < 116 mm) the experimental measurements showed speeds in the range of 0.03 – 0.05 m/s whereas the simulation predicted speeds in the range of 0.01 m/s – 0.03 m/s.

The impact of heat addition was also observed qualitatively in both the simulations and the experiments. For the heated cases, it was expected that buoyancy forces induced in the heated region of the tube bank (-116 mm < y < 116 mm) would accelerate the flow in the upward direction. This was visible in all heated cases where the velocity magnitude was seen to increase in the *y* direction throughout the heated region of the tube bank. The cosine heat flux profile caused this effect to be greater near the axial centre of the tube bank. Additionally, for tests at higher *Ar*, buoyancy effects were more pronounced and the qualitative agreement between the simulated and experimental velocity magnitude contours appeared to improve.

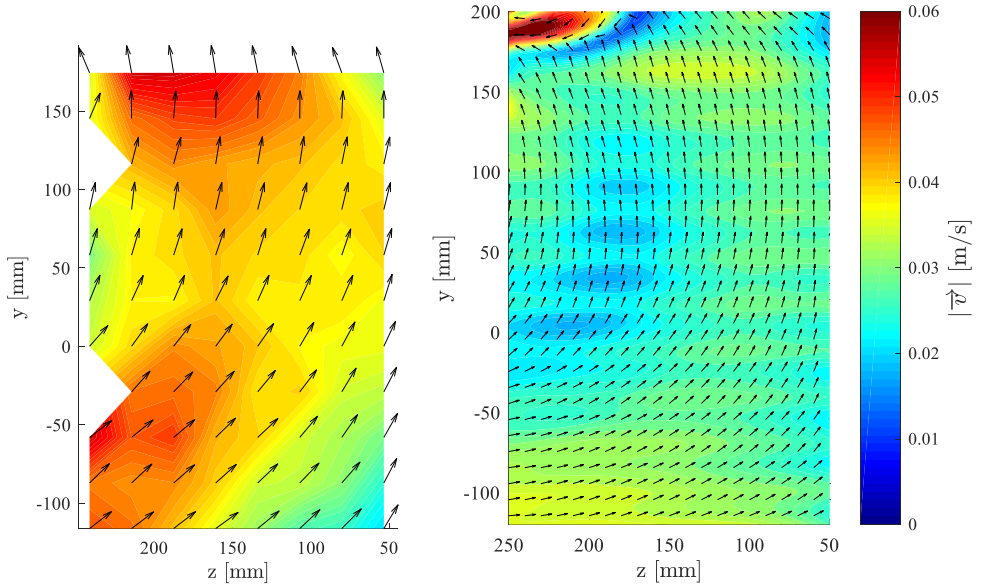

a) Measured (test ID 0717-00) b) Simulated (i30-KEreal-4mm)

Figure 5-6: Time-averaged velocity magnitude contour with unit vectors at the X0 measurement plane (Isothermal, 30 L/min)

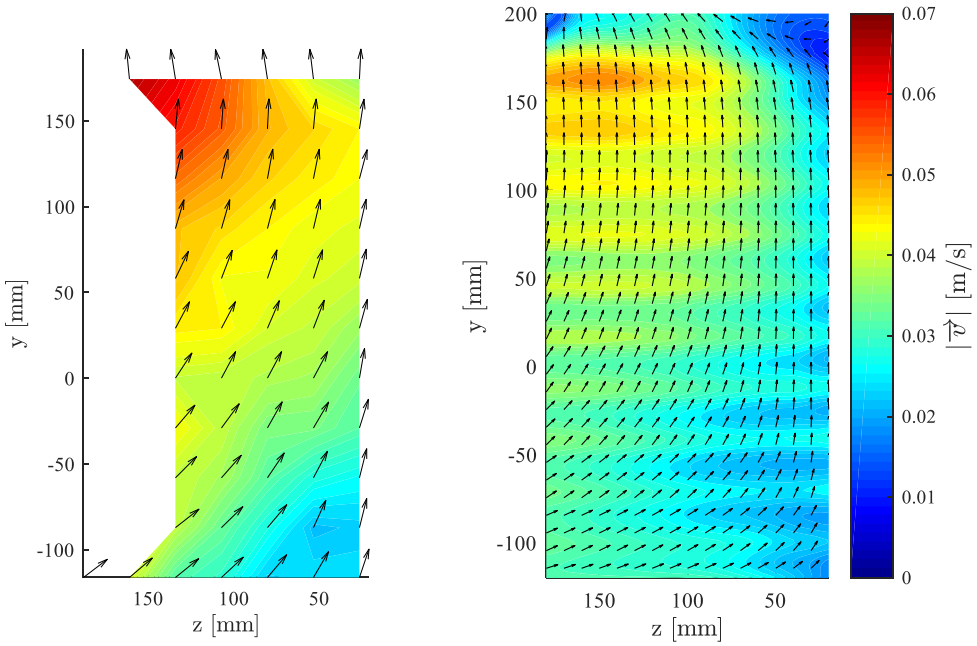

a) Measured (test ID 0901-01) b) Simulated (sim0908-KEreal-4mm)

Figure 5-7: Time-averaged velocity magnitude contour with unit vectors at the X0 measurement plane (10 kW, 30 L/min, Ar ~ 0.0013)

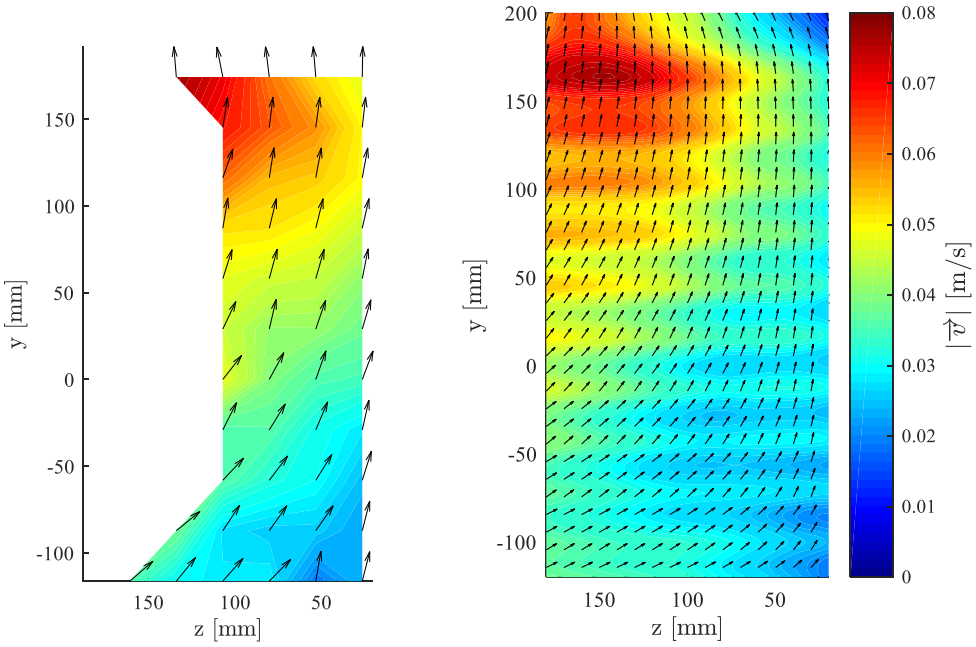

a) Measured (test ID 0823-02) b) Simulated (sim0308-KEreal-4mm)

Figure 5-8: Time-averaged velocity magnitude contour with unit vectors at the X0 measurement plane (20 kW, 30 L/min, Ar ~ 0.0035)

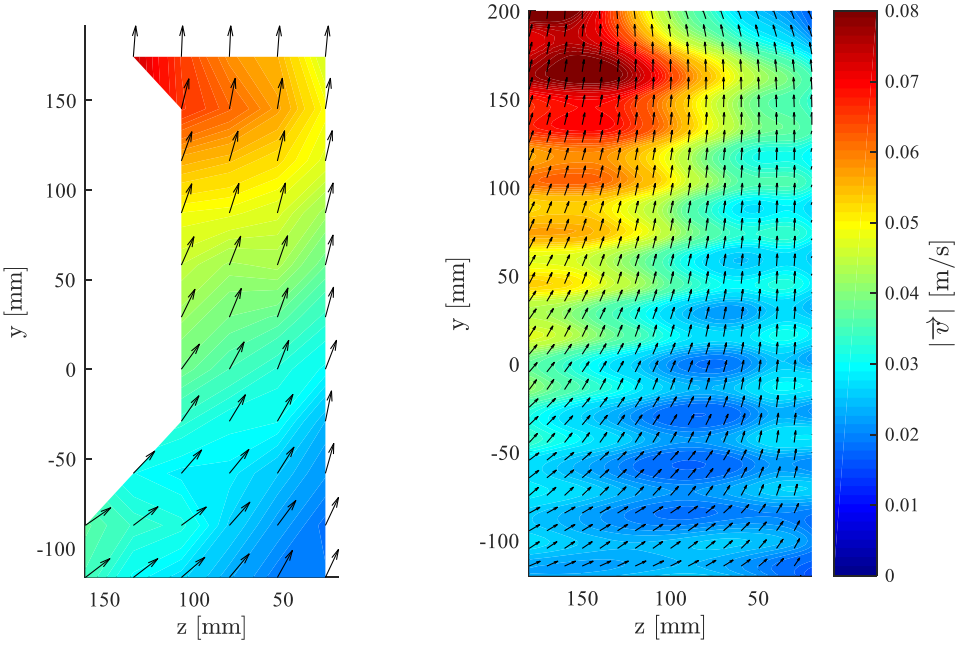

a) Measured (test ID 0830-01) b) Simulated (sim0831-KEreal-4mm)

Figure 5-9: Time-averaged velocity magnitude contour with unit vectors at the X0 measurement plane (20 kW, 24 L/min, Ar ~ 0.0072)

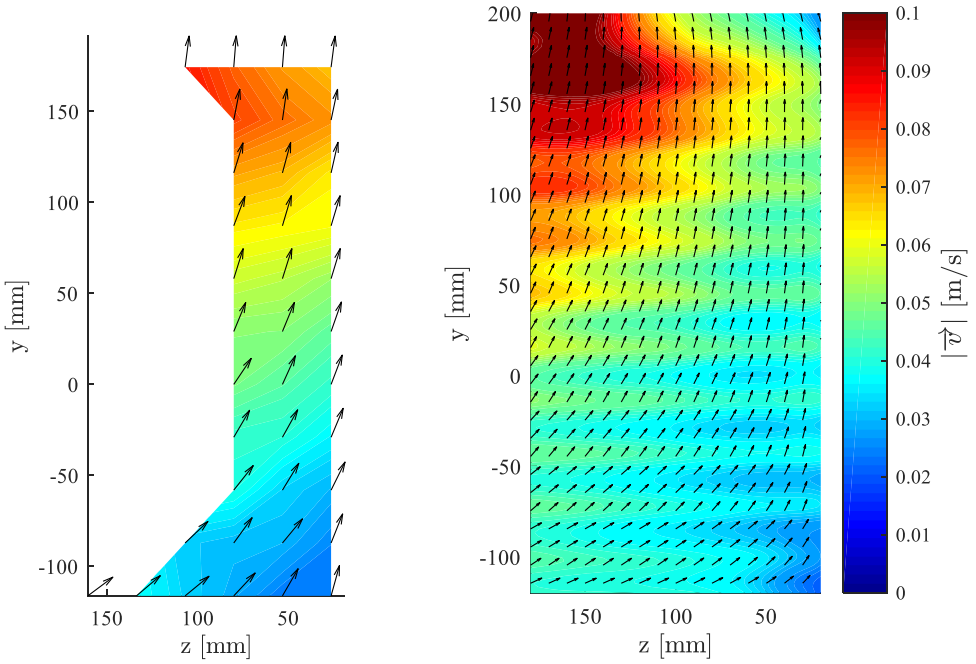

a) Measured (test ID 0920-00) b) Simulated (sim0922-KEreal-4mm)

Figure 5-10: Time-averaged velocity magnitude contour with unit vectors at the X0 measurement plane (38 kW, 30 L/min, Ar ~ 0.0092)

The measured and predicted velocity profiles in the *y*-direction were more closely examined at two locations within the X0 measurement plane across a range of test conditions. Figure 5-11 shows the *v*-velocity profile versus *y* position at $x = 0$ mm and $z = 107$ mm. This *z* position in the test section corresponded to the furthest depth within the test section where LDV data was obtainable in the X0 measurement plane at higher *Ar* conditions. Figure 5-12 shows the *v*-velocity profile versus *y* position at $x = 0$ mm and $z = 80$ mm; this *z* position in the test section was located close to the region crossed by the thermocouple probe lines TCM1-00 and TCM1-08. LDV measurements were not attainable in the regions traversed by other thermocouple probes.

At each measurement location, the relative difference between the simulated velocity and LDV measurement was calculated for the vertical velocity component *v* using Equation 5.5. The calculation results corresponding to the profiles shown

in Figure 5-11 and Figure 5-12 are summarized in Table 5-2 and Table 5-3 respectively.

$$\delta_{u_i} = 100\% \times \frac{u_{i_{sim}} - u_{i_{LDV}}}{u_{i_{LDV}}} \tag{5.5}$$

For the isothermal case, the *v*-velocity values were underpredicted by approximately 30% at all measured vertical positions. For the heated cases, agreement between the simulations and experiments improved at higher elevations, with the level of agreement improving with *Ar*. Referring to Figure 5-11 (x = 0 mm and z = 107 mm), it was observed that regardless of *Ar* the model underpredicted the *v*-velocity component at the base of the heated section of the tube bank (y = -116 mm) by about 30%. At positions above the heated section of the tube bank (y > 116 mm), the relative error was smaller – on the order of -20%, -10% and -5% for the cases at *Ar* = 0.001, 0.004, and 0.007 respectively. This suggested that while the simulations were underpredicting the upward velocities entering the base of the tube bank at this location, the induced velocities caused by buoyancy effects were more correctly predicted. As *Ar* was increased, buoyancy effects became a more significant contributor to the vertical velocities at the top of the tube bank and agreement between the simulations and experiments was improved. This behaviour was also observed in Figure 5-12 (x = 0 mm and z = 80 mm), but to a lesser degree due to lower heat fluxes in this region.

Since an underprediction of local velocity was expected to result in an overprediction of local temperature, these observations are consistent with the predicted temperature behaviour shown in section 5.1.1. Referring to Figure 5-2 through Figure 5-5, it was observed that the simulations tended to overpredict the average temperatures to a greater degree for probe lines 08, 09, and 10 (located at y = 0 mm) compared to probe lines 00, 01, and 02 (located at y = 58.1 mm), and that the agreement between predicted temperatures in the 00, 01, and 02 probe regions also tended to improve at *Ar* was increased.

The underprediction of the isothermal velocities in the tube bank could be related to issues with the modelling of the inlet jets. It has been established that *k*-*ε* turbulence models perform poorly in the modelling of round free jets without modifications; Launder and Spalding [64] noted that the coefficients of the standard *k*-*ε* turbulence model required modifications in order to predict the behaviour of axisymmetric jets and it has been reported by Pope [65] that the standard *k*-*ε* turbulence model overpredicts the spreading rate of a round jet by approximately 40%.

The realizable *k*-*ε* model defined by Shih *et al.* has been shown to yield better predictions of the spreading rate of a round jet compared to the standard model [59]. However, a validation study of RANS modelling of turbulent free jets performed by Ishay showed that the realizable *k*-*ε* model tended to overpredict the dispersion of round jets at a distance of 20 diameters from the nozzle exit ($z/d = 20$) and that the model tended to overpredict the decay of the centreline velocity [66]. Similar results were noted in a validation study performed by Pérez *et al.* at distance of $z/d = 32$ [67].

Under isothermal conditions, the recirculation pattern in the test vessel would be driven entirely by the round inlet jets. The jets were approximately 4 mm in diameter and were positioned such that flow would travel an axial distance of approximately 120 mm to 160 mm from the nozzle exit before entering the tube bank or interacting with an opposing jet (corresponding to $z/d = 30 – 40$). As discussed above, the realizable *k*-*ε* model could result in the overprediction of jet dispersion in this region, resulting in lower flow momentum entering the tube bank and underpredicted velocities within the tube bank. For heated cases, as *Ar* was increased and buoyancy effects become dominant, modelling errors of the inlet jets would become relatively less significant. In this case, the predicted velocities would more closely match the measurements; this is consistent with the behaviour shown in Figure 5-11 and Figure 5-12.

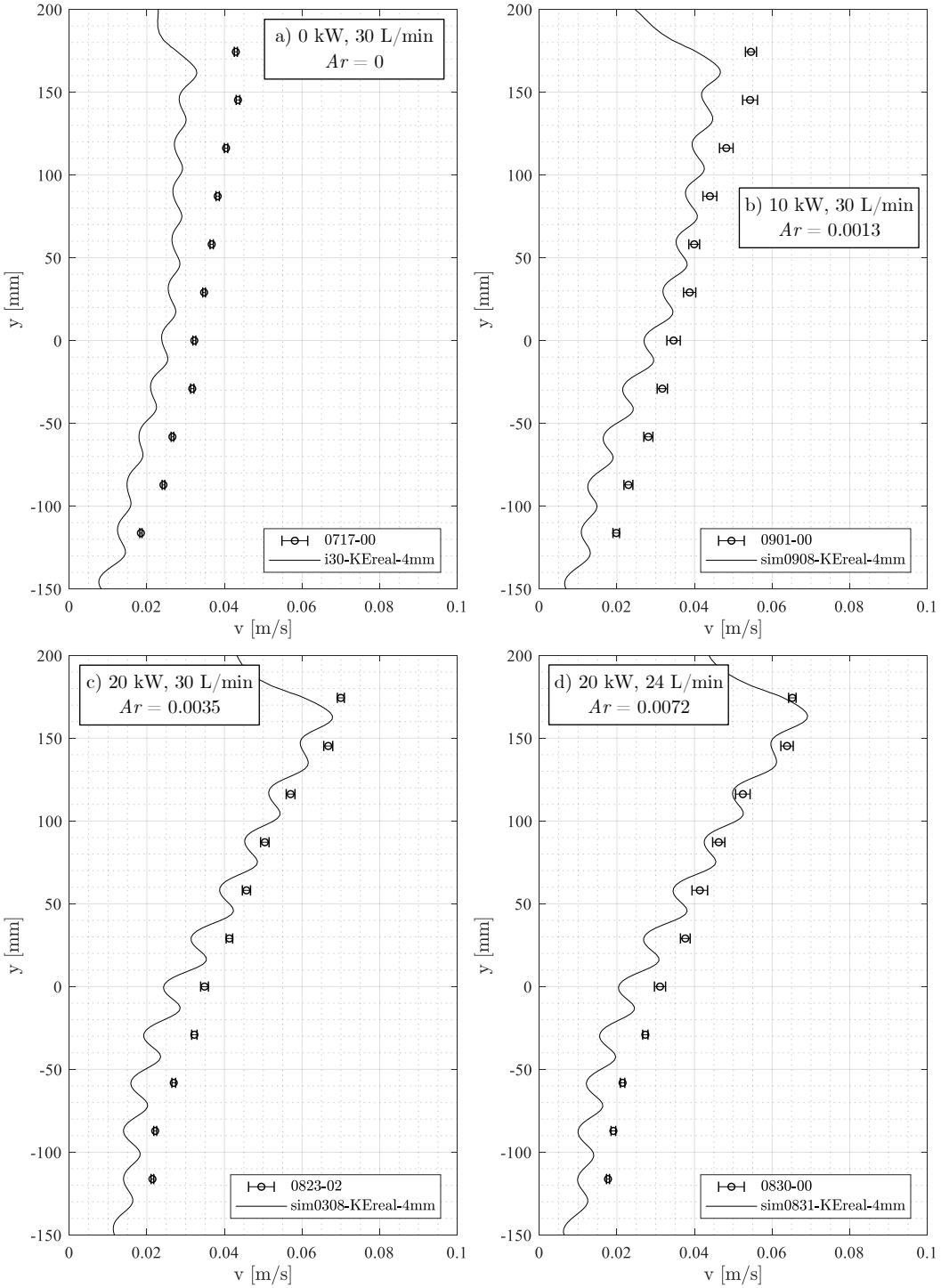

Figure 5-11: Measured and simulated vertical *v*-velocity profiles at *x* = 0 mm and *z* = 107 mm for various test conditions

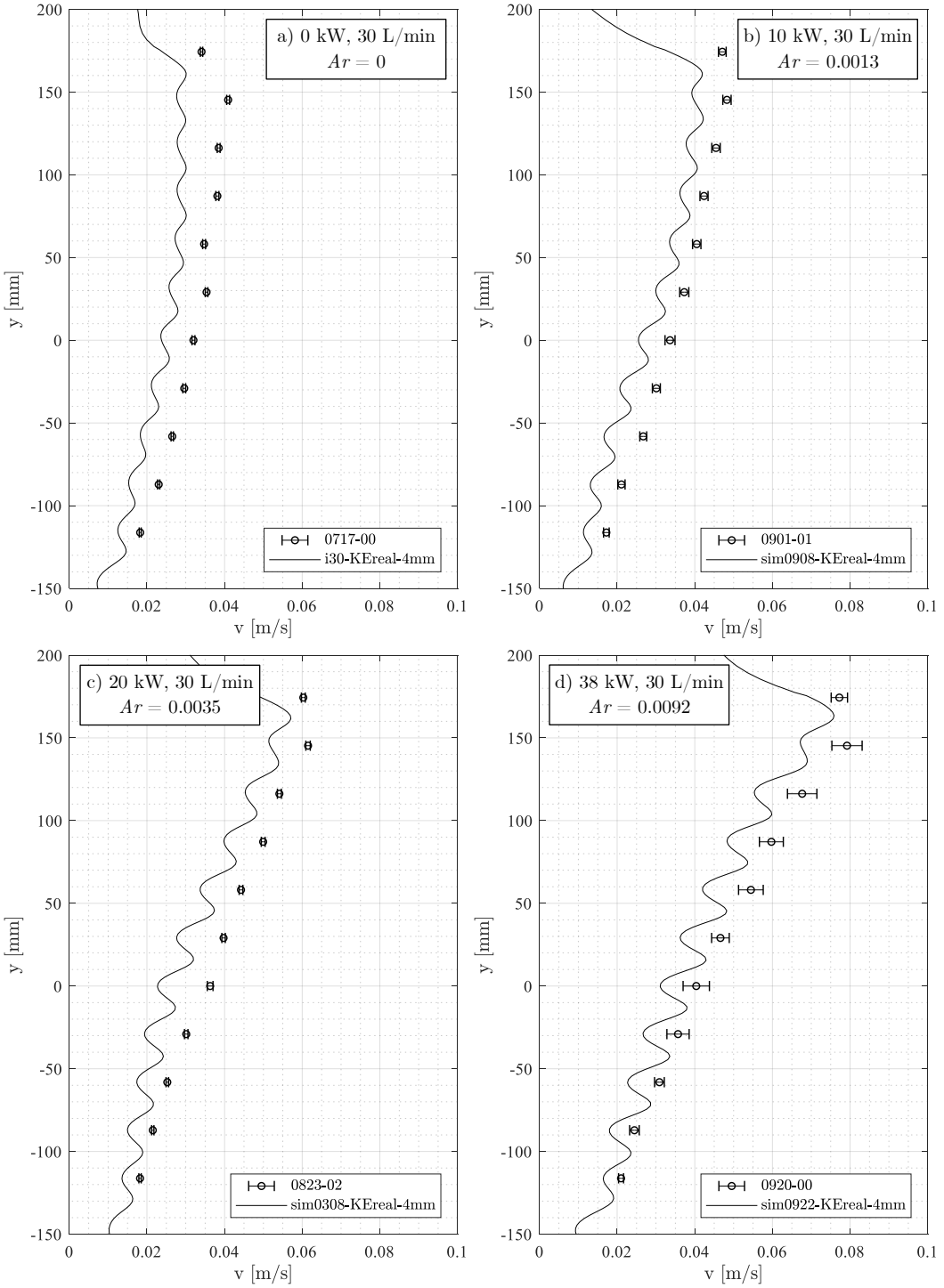

Figure 5-12: Measured and simulated vertical *v*-velocity profiles at *x* = 0 mm and *z* = 80 mm for various test conditions

Table 5-2: Relative *v*-velocity error δ_v between simulation and experiment at $x = 0$ mm and $z = 107$ mm for various test conditions

Case / y [mm]	0717-00 ($Ar = 0$) δ_v [%]	0901-00 ($Ar \approx 0.0013$) δ_v [%]	0823-02 ($Ar \approx 0.0035$) δ_v [%]	0830-00 ($Ar \approx 0.0072$) δ_v [%]
174.4	-35	-26	-14	-4
149.3	-35	-22	-11	-6
116.2	-33	-18	-10	-5
87.2	-30	-14	-10	-8
58.1	-28	-12	-15	-17
29.1	-26	-18	-24	-28
0.0	-26	-22	-30	-34
-29.1	-34	-32	-40	-43
-58.1	-32	-41	-41	-44
-87.2	-39	-45	-37	-48
-116.2	-32	-45	-35	-44
Overall (RMS)	32	29	27	31

Table 5-3: Relative *v*-velocity error δ_v between simulation and experiment at $x = 0$ mm and $z = 80$ mm for various test conditions

Case / y [mm]	0717-00 ($Ar = 0$) δ_v [%]	0901-00 ($Ar \approx 0.0013$) δ_v [%]	0823-02 ($Ar \approx 0.0035$) δ_v [%]	0830-00 ($Ar \approx 0.0072$) δ_v [%]	0920-00 ($Ar \approx 0.0092$) δ_v [%]
174.4	-30	-29	-18	-16	-10
149.3	-32	-18	-16	-21	-15
116.2	-27	-17	-16	-25	-18
87.2	-27	-15	-20	-28	-19
58.1	-21	-17	-24	-31	-23
29.1	-27	-20	-30	-39	-22
0.0	-26	-24	-37	-43	-23
-29.1	-28	-31	-36	-43	-25
-58.1	-31	-38	-31	-41	-27
-87.2	-33	-38	-30	-43	-26
-116.2	-31	-34	-26	-37	-22
Overall (RMS)	29	27	27	35	21

5.2 Time-Dependent Behaviour

For steady-state conditions, unsteady behaviour was observed in the temperature measurements. The fluctuating temperature behaviour was observed to have different characteristic behaviour in different regions of the test section depending

on the nature of the local flow conditions. Factors such as the asymmetric arrangement of inlet nozzles in the east-west direction, inlet nozzle rotation, and the concentration of the heat source to the center of the tube bank contributed to the three-dimensional nature of the flow in the test section. Inertial flows from the inlets were expected to oppose buoyancy induced flows in certain regions while assist in others.

In order to further explore the nature of the temperature fluctuations that were observed within the test section, the relationship between local velocity and temperature fluctuations was examined at several points of interest. Due to the point-wise and non-simultaneous nature of the measurements, it was not possible to directly link fluctuations in a particular temperature measurement to velocity measurements using strictly experimental data. Additionally, velocity measurements were limited in many regions of the test section. Instead, simulation data were examined to gain insight into the relationship between local temperature and velocity fluctuations. At each location, comparisons between the simulation data and the experimental temperature measurements were also made. This was done to demonstrate that the transient behaviour observed in the simulation data was comparable to observations made in the experiments.

As introduced in Table 3-13, the thermocouples in the experiment had a response time described by a time constant τ. To account for this behaviour in the simulated results, the time-dependent temperature data from the transient simulations (with a timestep *dt*) were filtered with an exponential smoothing function:

$$T(x,y,z,t) = \alpha T(x,y,z,t) + (1-\alpha)T(x,y,z,t-dt) \tag{5.6}$$

$$\alpha = 1 - \left(e^{\frac{-dt}{\tau}}\right) \tag{5.7}$$

Three-dimensional velocity data are reported as a velocity magnitude with two angular directions. These values are calculated from the cartesian vector

components *u*, *v*, and *w* as shown in Equation 5.8 through Equation 5.10. The angle ϕ represents the angle between the velocity vector projected onto the *xy* plane and the *x* axis. An angle ϕ = 0º corresponds to flow in the positive *x* direction while ϕ = 90º corresponds to flow in the positive *y* direction. The angle θ represents the angle between the velocity vector and the *xy* plane. Angles 0º < θ < 90º correspond to flow in the positive *z* direction (toward the western end of the test section) while angles -90º < θ < 0º correspond to flow toward the eastern end of the test section.

$$|\vec{v}| = \sqrt{u^2 + v^2 + w^2} \tag{5.8}$$

$$\phi = \arctan\left(\frac{v}{u}\right) \tag{5.9}$$

$$\theta = \arctan\left(\frac{w}{\sqrt{u^2+v^2}}\right) \tag{5.10}$$

The temperature results are reported as a normalized excess temperature (i.e. – the difference between the local temperature measurement and the inlet temperature, normalized to the inlet/outlet temperature rise) as calculated by Equation 5.11.

$$T_{excess} = 100\% \times \frac{T-\bar{T}_{inlet}}{\bar{T}_{outlet}-\bar{T}_{inlet}} \tag{5.11}$$

In addition to the results presented in this section, selected time-dependent temperature records from each experimental case are included in Appendix E section E.4.

5.2.1 Interaction Between Inlet Jets and Buoyant Flows

A contour plot of the time-averaged excess temperature on the *yz*-plane for *x* = -29.1 mm is shown in Figure 5-13 corresponding to the highest buoyancy case where *Ar* = 1.03 × 10^{-1} (sim1018-KEreal-4mm). This location corresponds to a mid-plane between two tube columns, one tube pitch to the south of the centre of the tube bank. Temperature and velocity values were logged at the indicated

locations, corresponding to thermocouple locations in the experiments. Time-average and standard deviation values for excess temperature and velocity at the indicated locations are recorded in Table 5-4.

Cooler temperatures from the inlet jets are visible at the top of Figure 5-13. Due to the greater number of inlets located toward the eastern (z = 0 mm) end of the vessel, a cooler spot is formed toward the upper-western end of the vessel. Higher temperatures are visible toward the z-axis center of the vessel in the region above the heated rods (y = 116.2 mm). A high temperature gradient region is seen between these hot and cold zones. As noted in Table 5-4, the temperature fluctuations were larger in this gradient region in the western end of the vessel (locations EF04 and EF07) as compared to the eastern end of the vessel (locations EF00 and EF05). These larger temperature fluctuations were also accompanied by larger fluctuations in flow speed and direction.

Snapshots of the excess temperature field for this plane from 80 s < t < 120 s are shown in Figure 5-14. The location of the interface between the hot and cold region was not steady with time. Probe locations EF04 and EF07 were located in regions that saw either cooler downward flow from the inlet jets or warmer upward flow from the tube bank at different points throughout the transient. In contrast, probe locations EF00 and EF05 are both located in regions where flow was upward throughout the transient and smaller temperature fluctuations were recorded.

Plots of the simulated excess temperature, flow speed, and flow direction components throughout the 250 s transient at location EF04 are shown in Figure 5-15. The instances corresponding to higher recorded temperatures typically coincided with lower flow speeds. On average, the flow direction at this location was observed to be downward (ϕ = 266º) and toward the western end of the vessel (θ = 34º), temperature spikes were noted at instances where ϕ < 180º (upward flow) and θ < 0º (toward the east). This corresponds to a shift from relatively higher speed downward and westerly flow from the inlet jets to slower, upward, and warmer

flow from the tube bank. Likewise, temperature drops were observed when flow direction was near the time averaged value and flow speed was higher. Similar behaviour was also observed at location EF07 as shown in Figure 5-17.

In comparison, plots of the temperature and flow velocity components for location EF00 are shown in Figure 5-16. In this case, ϕ angle direction fluctuations are negligible and flow is predominantly directed upward (ϕ = 91°). Temperature fluctuations are smaller in magnitude and lower frequency. It was also noted that the recorded temperature followed the flow speed closely; as flow speed increased, the recorded temperature increased and vice versa. Similar behaviour was also observed at location EF05 as shown in Figure 5-18.

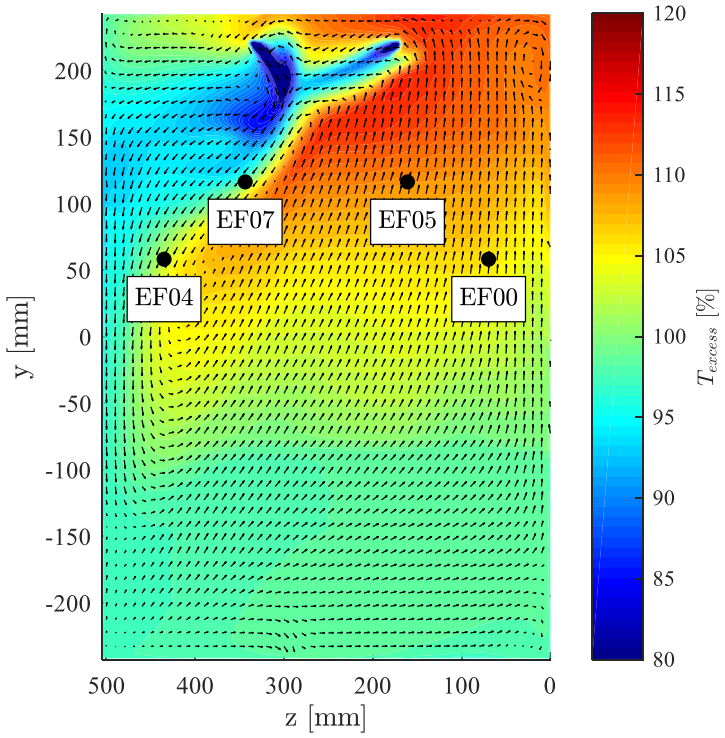

Figure 5-13: Simulated time-averaged excess temperature contour for *yz*-plane located at *x* = -29.1 mm from sim1018-KEreal-4mm (Ar = 1.03 × 10^{-1}). The arrows represent unit vectors indicating flow direction.

Table 5-4: Time average and standard deviation simulation values for excess temperature and velocity observed at the indicated locations in Figure 5-13

Location ID	*x* [mm]	*y* [mm]	*z* [mm]	$\overline{T}_{excess}$ [%]	$\overline{\lvert\vec{v}\rvert}$ [×10^{-2} m/s]	$\bar{\phi}$ [°]	$\bar{\theta}$ [°]
EF00	-29.1	58.1	73.3	105.7 ± 1.7	1.91 ± 0.63	91.4 ± 2.9	-9.9 ± 10.1
EF04	-29.1	58.1	439.1	102.6 ± 4.6	3.10 ± 1.55	265.7 ± 30.4	34.3 ± 15.3
EF05	-29.1	116.2	164.7	109.0 ± 1.6	2.09 ± 0.47	90.0 ± 1.5	-23.2 ± 5.8
EF07	-29.1	116.2	347.6	99.5 ± 4.9	4.99 ± 1.58	259.9 ± 24.8	50.4 ± 7.6

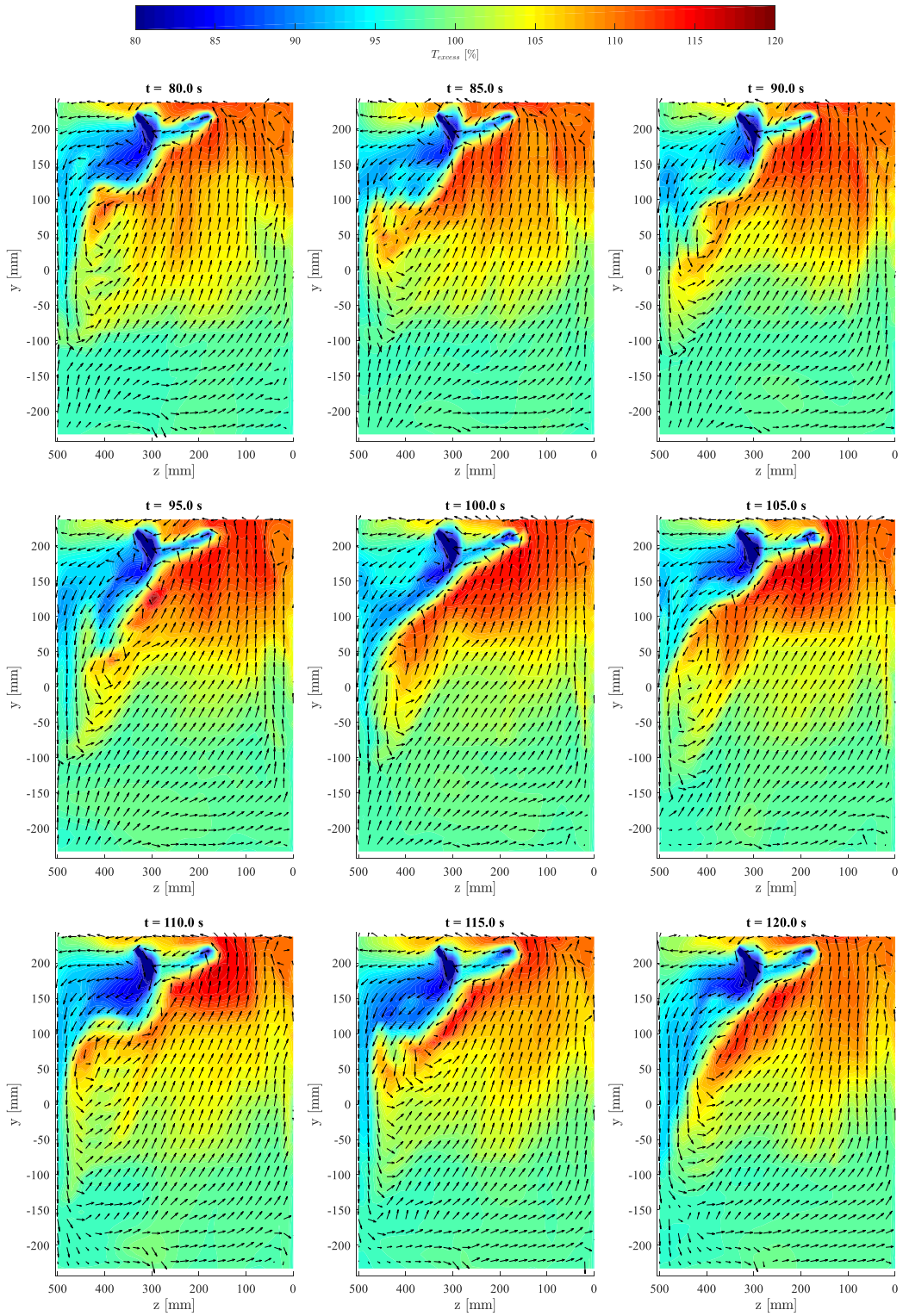

Figure 5-14: Simulated excess temperature contour snapshots for *yz*-plane located at *x* = -29.1 mm from sim1018-KEreal-4mm ($Ar = 1.03 \times 10^{-1}$)

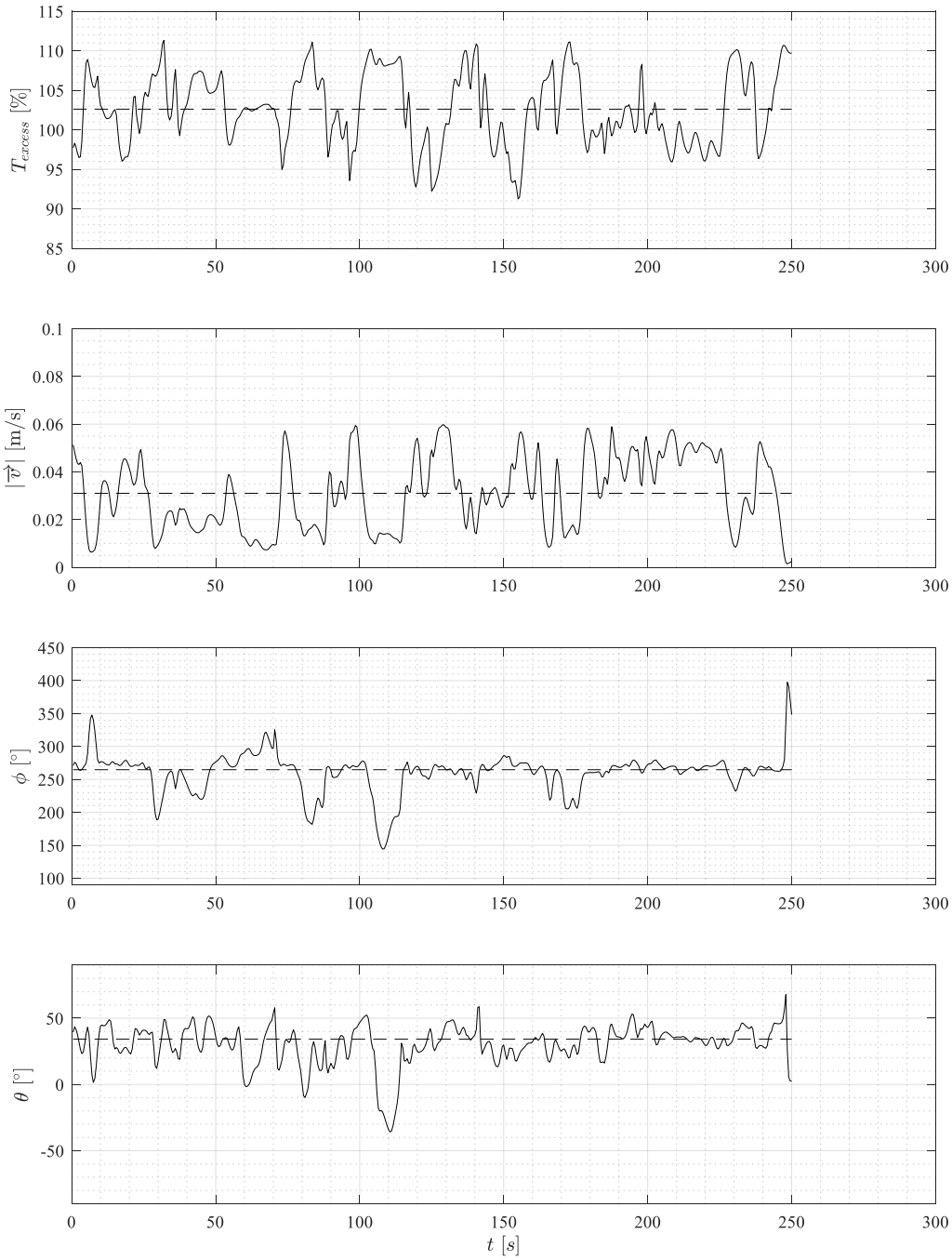

Figure 5-15: Simulated instantaneous excess temperature, speed and direction components for sim1018-KEreal-4mm (Ar = 1.03 × 10^{-1}) located at EF04 (-29.1, 58.1, 439.1) mm

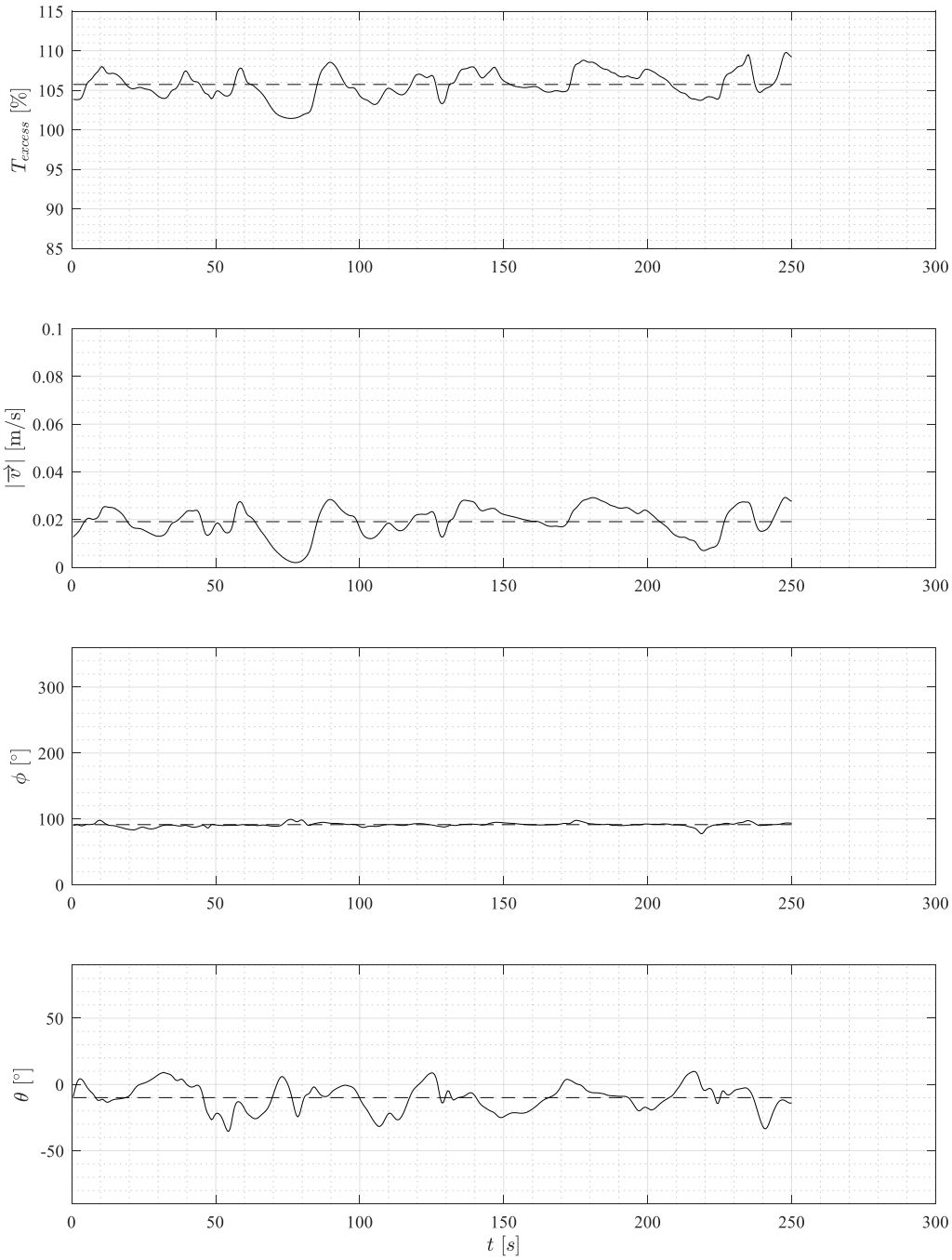

Figure 5-16: Simulated instantaneous excess temperature, speed and direction components for sim1018-KEreal-4mm (Ar = 1.03 × 10^{-1}) located at EF00 (-29.1, 58.1, 73.3) mm

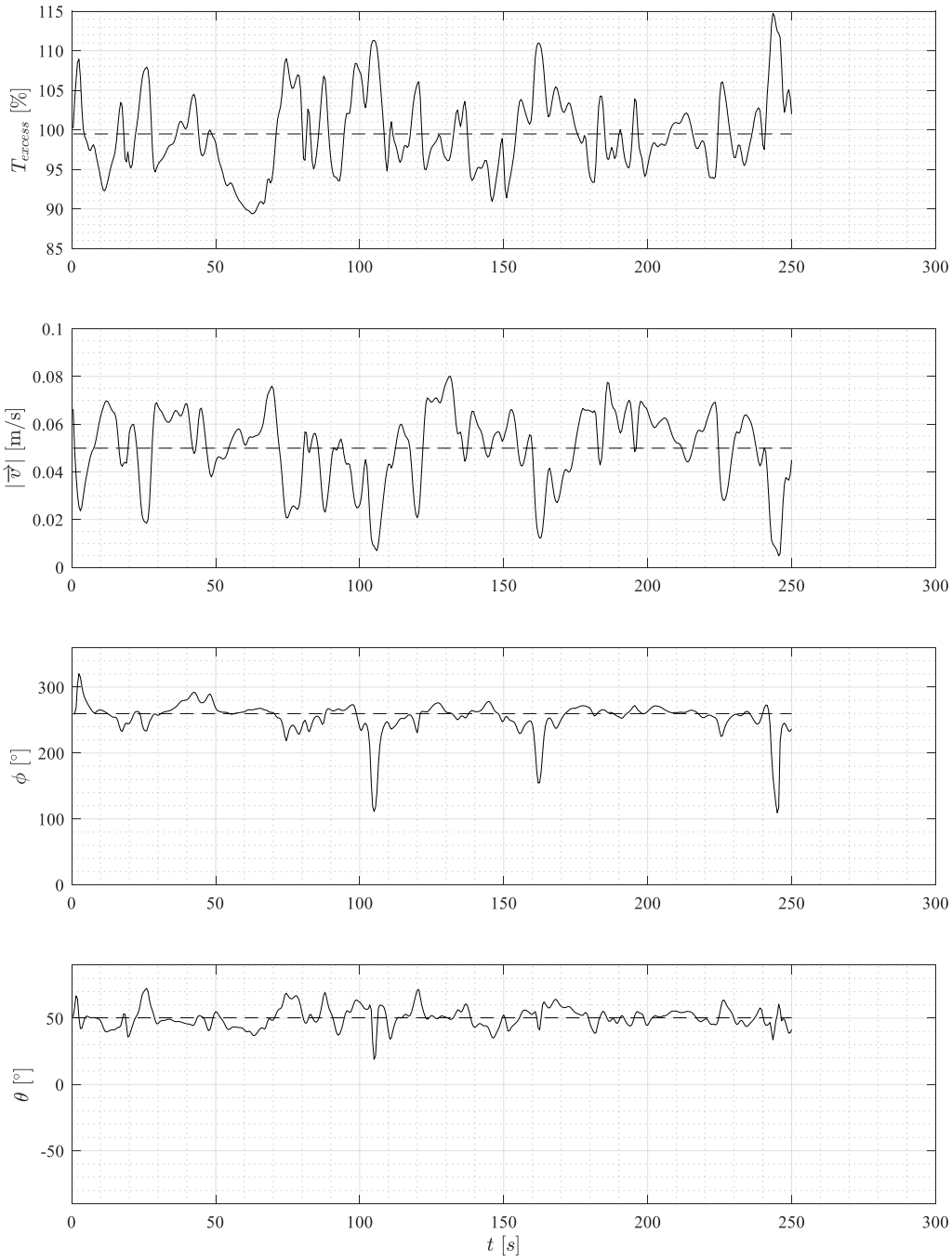

Figure 5-17: Simulated instantaneous excess temperature, speed and direction components for sim1018-KEreal-4mm (Ar = 1.03 × 10^{-1}) located at EF07 (-29.1, 116.2, 347.6) mm

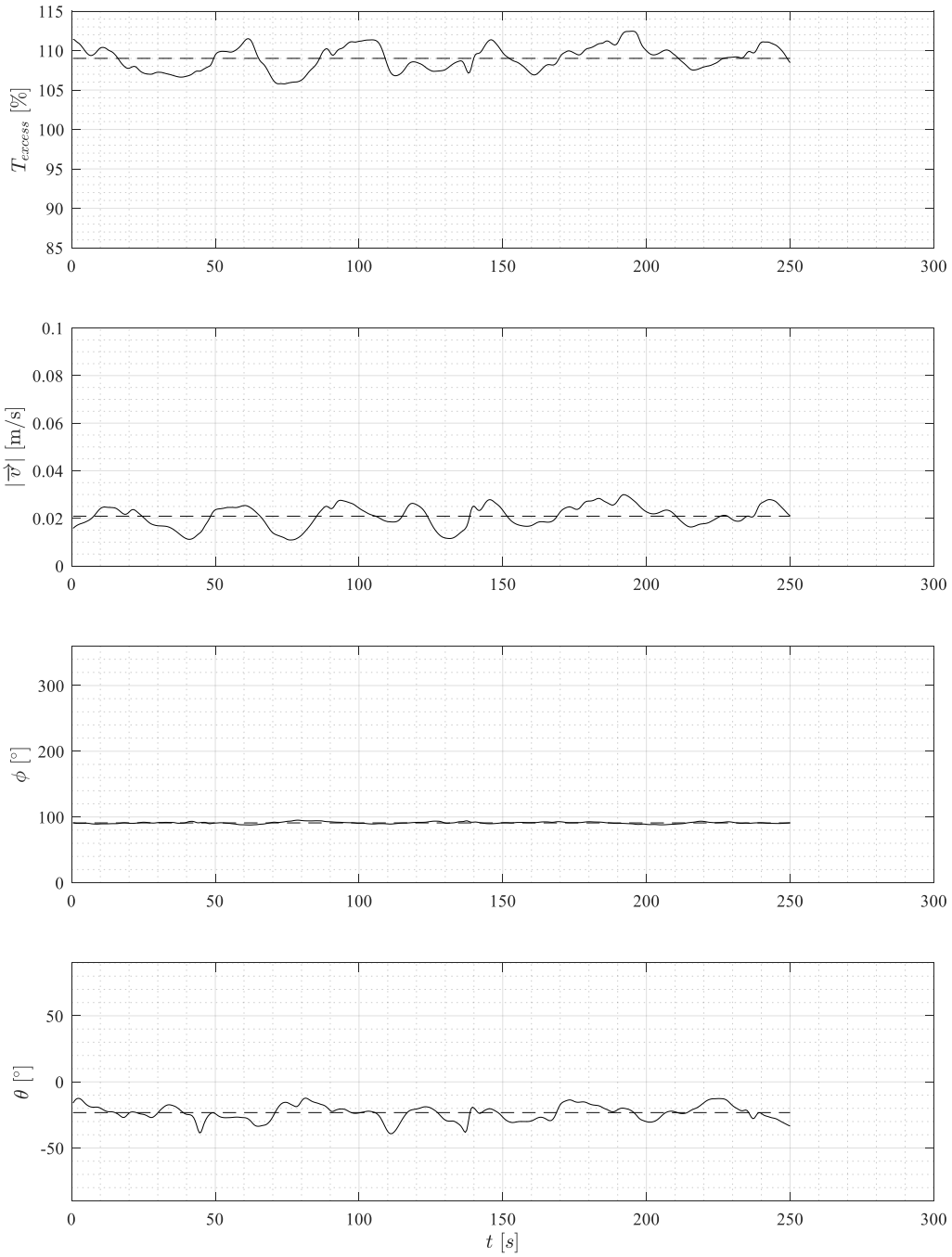

Figure 5-18: Simulated instantaneous excess temperature, speed and direction components for sim1018-KEreal-4mm (Ar = 1.03 × 10^{-1}) located at EF05 (-29.1, 116.2, 164.7) mm

5.2.1.1 Comparison to Experimental Transient Behaviour

Average and standard deviation values for the temperature observed at probe locations EF00, EF04, EF05, EF06, and EF07 from experiment test ID 1018-00 are shown in Table 5-5 alongside the corresponding simulation results. Plots comparing the temperature transient behaviour between the experiment and simulation for locations EF00 and EF04 are shown in Figure 5-19 and Figure 5-20 while plots for locations EF05, EF06, and EF07 are shown in Figure 5-21 and Figure 5-22. Velocity measurements were not available at these locations for this experimental test.

Table 5-5: Comparison of measured and simulated average temperatures observed at selected probe locations for test ID 1018-00 ($Ar = 1.03 \times 10^{-1}$)

Location ID	x [mm]	y [mm]	z [mm]	Measured		Simulated	
				$\overline{T}_x$ [ºC]	$\overline{T}_{excess}$[%]	$\overline{T}_x$ [ºC]	$\overline{T}_{excess}$[%]
EF00	-29.1	58.1	73.3	44.5 ± 0.3	106.1 ± 1.3	44.4 ± 0.3	105.7 ± 1.7
EF04	-29.1	58.1	439.1	43.7 ± 0.8	102.0 ± 4.1	43.8 ± 0.9	102.6 ± 4.6
EF05	-29.1	116.2	164.7	45.8 ± 0.4	112.5 ± 1.9	45.1 ± 0.3	109.0 ± 1.6
EF06	-29.1	116.2	256.2	44.7 ± 0.9	106.7 ± 4.7	45.3 ± 0.2	109.7 ± 1.2
EF07	-29.1	116.2	347.6	42.6 ± 1.0	96.7 ± 4.8	43.2 ± 1.0	99.5 ± 4.9

Table 5-6: Comparison of measured and simulated minimum and maximum temperatures at selected probe locations for test ID 1018-00 ($Ar = 1.03 \times 10^{-1}$)

Location ID	x [mm]	y [mm]	z [mm]	Measured		Simulated	
				T_{min} [ºC]	T_{max} [ºC]	T_{min} [ºC]	T_{max} [ºC]
EF00	-29.1	58.1	73.3	44.0	45.7	43.6	45.2
EF04	-29.1	58.1	439.1	42.2	45.6	41.5	45.6
EF05	-29.1	116.2	164.7	44.9	46.7	44.5	45.8
EF06	-29.1	116.2	256.2	42.1	46.3	44.7	45.9
EF07	-29.1	116.2	347.6	41.5	45.9	41.1	46.3

The transient temperature behaviour at locations EF00 and EF04 predicted by the simulation corresponded well to the experiment, with the range of observed temperatures being comparable and fluctuations appearing with a similar dominant frequency. As shown in Table 5-6, the simulated maximum and minimum temperatures at locations EF00 and EF04 agreed within 0.7 ºC which was

comparable to the measurement uncertainty of 0.5 ºC. Referring to Figure 5-19, the experimental measurements appeared to show a low amplitude, high frequency component to the fluctuations not captured by the transient simulation. Based on the overall similarities between the measurements and simulations, the discussion in 5.2.1 linking temperature fluctuations to velocity fluctuations in the simulations appears applicable to the experiment at these locations.

Referring to Figure 5-21 and Figure 5-22, some differences between the transient behaviour for the simulations and experiments was observed at locations EF05, EF06, and EF07. The simulated behaviour at both locations EF05 and EF06 appeared similar to the measured behaviour at EF05, with similar average temperatures and lower range of fluctuations. The characteristics of the temperature measurements at location EF07 differed from the simulated behaviour. In both cases, large swings between lower temperatures associated with downward flow from the inlets and higher temperatures associated with upward heated flow from the tube bank were observed. However, the experiment showed longer periods of time at lower temperatures. Furthermore, the experimental temperature fluctuations at EF06 appeared qualitatively closer to the simulated fluctuations at EF07.

The aforementioned differences in transient behaviour suggest that the location of the high gradient region identified in Figure 5-13 could differ between the simulation and experiment. A possible source of this difference could arise from uncertainties in the inlet nozzle bend angle and rotation angle. As designed, the test section contained symmetrically opposing ‘booster’ inlet nozzles. However, the uncertainty in the inlet bend and rotation angle was 5º and this misalignment could cause the interactions between these opposing nozzles to differ in the experiment.

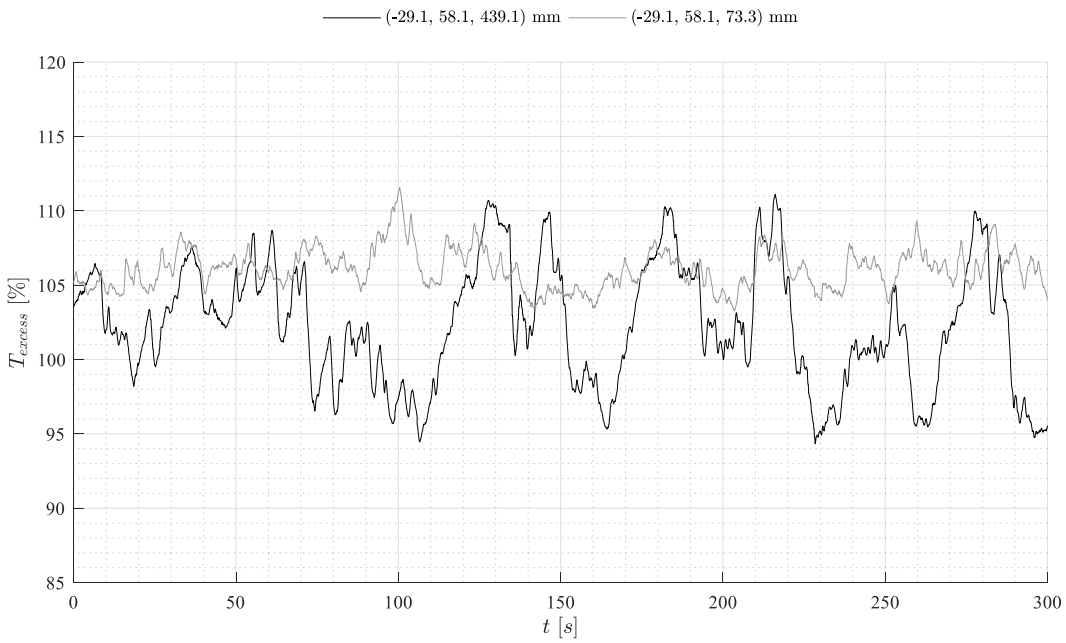

Figure 5-19: Experimental excess temperature versus time for test ID 1018-00 (Ar = 1.03 × 10^{-1}) at locations EF04 and EF00

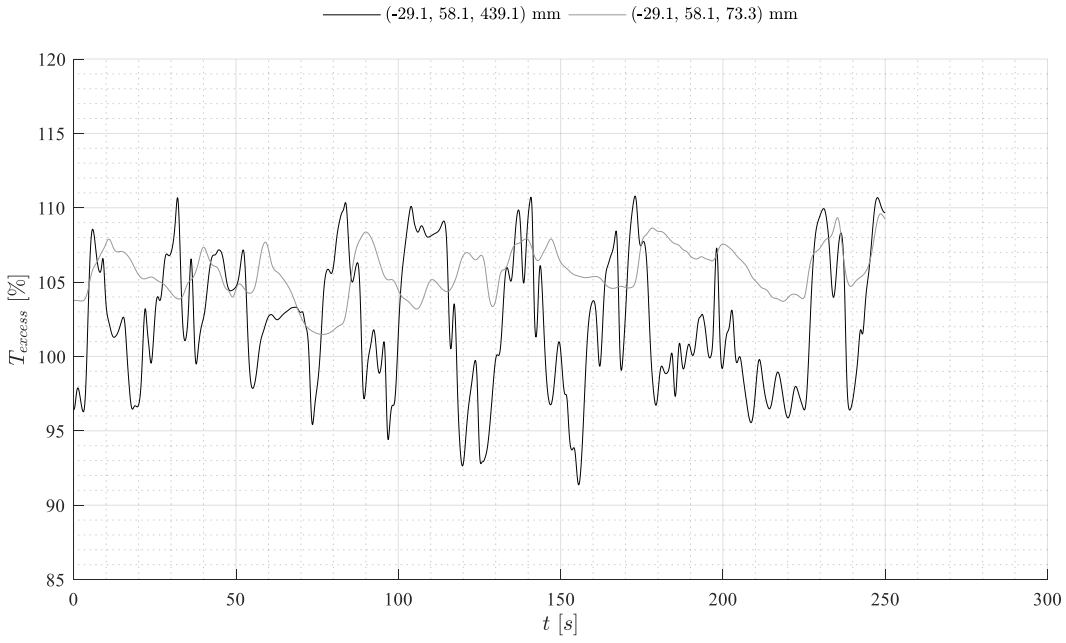

Figure 5-20: Simulated excess temperature versus time for sim1018-KEreal-4mm (Ar = 1.03 × 10^{-1}) at locations EF04 and EF00

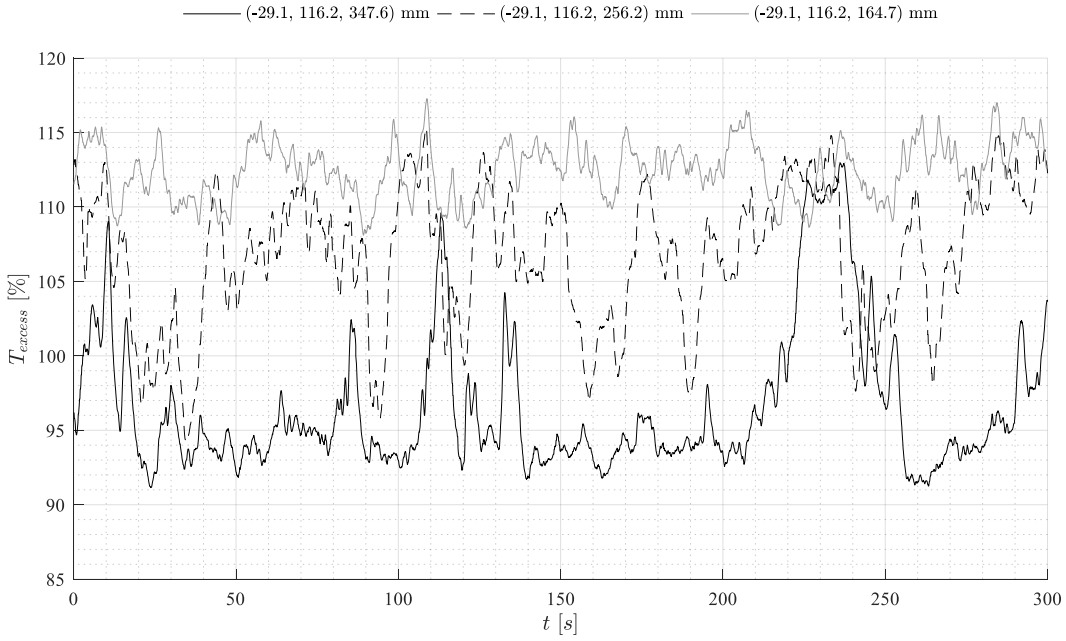

Figure 5-21: Experimental excess temperature vs time for test ID 1018-00 (Ar = 1.03 × 10^{-1}) at locations EF07, EF06, and EF05

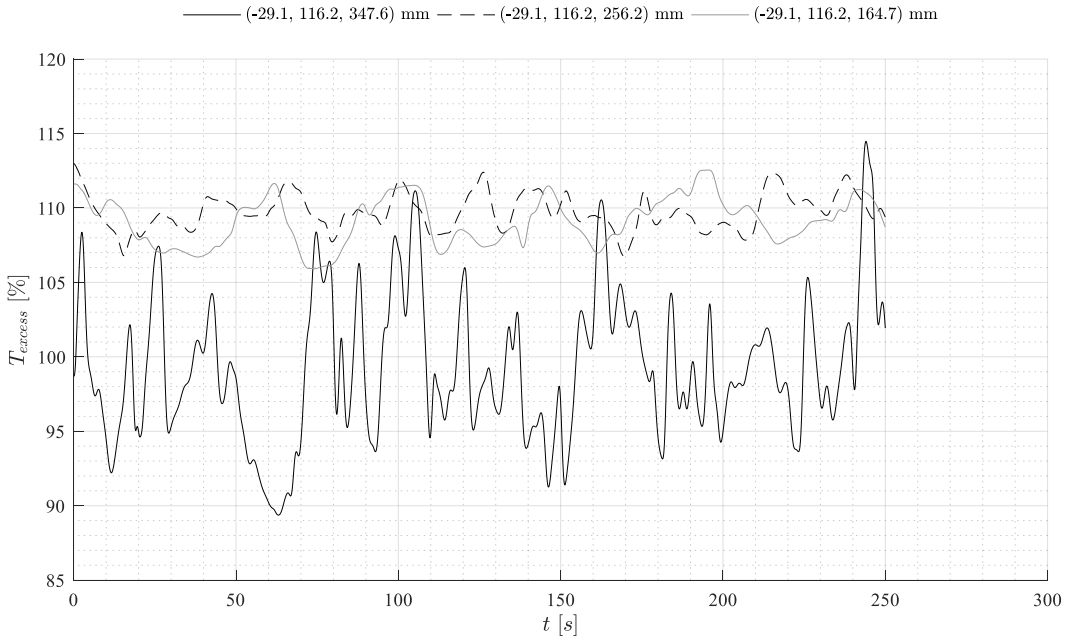

Figure 5-22: Simulated excess temperature vs time sim1018-KEreal-4mm (Ar = 1.03 × 10^{-1}) at locations EF07, EF06, and EF05

5.2.2 Edge of Heated Region

Due to the three-dimensional nature of the flow, temperature fluctuations were also observed within the vessel arising from side-to-side changes in flow direction in some locations. A contour plot of the time-averaged excess temperature on an *xy*-plane for z = 158.4 mm is shown in Figure 5-23 corresponding to a 20 kW, 30 L/min case ($Ar = 3.05 \times 10^{-3}$). This *xy*-plane is located near a thermocouple insertion location (z = 164.7 mm) and corresponds to the region where inertial flow through the tube bank is typically upward and assisting buoyant flow. The marked location C01 corresponds to a measurement point directly above the outward most heated tube element in the tube bank. Time-average and standard deviation values for excess temperature and velocity at the indicated location is recorded in Table 5-7.

At location C01, large temperature fluctuations were observed that were caused by north/south and east/west fluctuations rather than upward/downward fluctuations. This can be seen in Figure 5-24 which presents snapshots of the excess temperature field centered at C01 for 128.5 s < t < 140.0 s. The flow direction was initially upward, causing the temperature observed at C01 to peak due to warm, buoyant flow rising from the heater element. As the flow direction changed to be upward and inward toward the centre of the tube bank, cooler fluid from outside the heated region of the tube bank caused low temperatures to be observed.

The above observations can be further assessed using Figure 5-25 which presents plots of the simulated excess temperature, flow speed, and flow direction components throughout the 250 s transient at location C01. The peak temperatures typically corresponded to instances when the flow is directed nearly upward ($\phi \approx 90^o$). Conversely, minimum temperatures typically corresponded to instances when flow is directed upward and inward toward the centre of the tube bank ($0^o < \phi < 90^o$). The directional angle θ was also observed to have momentary spikes from $\theta \approx -50^o$ to $\theta \approx 50^o$ coinciding with instances where $0^o < \phi < 90^o$. These occurrences also coincided with minimum temperatures; this flow direction

corresponds to flow from outside the tube bank near the east end of the vessel where the bulk fluid temperature is low. Instances where $\theta > 90^{o}$ were associated with temperatures lower than the peak but above the minimum values. This corresponds to flow directed upward and outwards toward the vessel wall. With this flow direction, C01 is downstream from rising flow within the heated region of the tube bank. Temperatures in this region are higher than outside the tube bank but cooler than the plume rising directly from the heater.

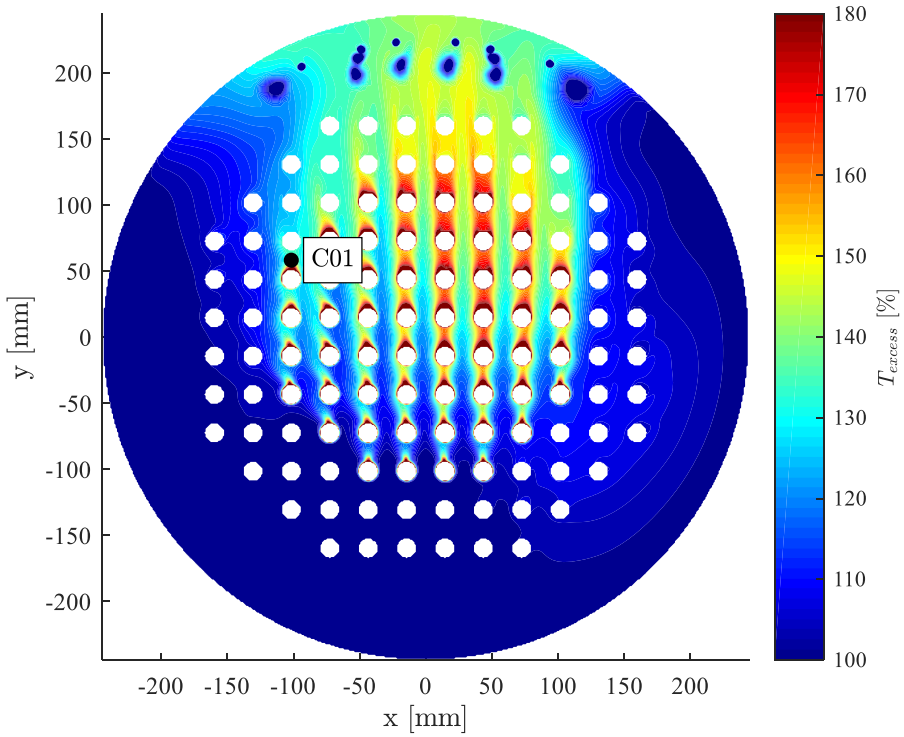

Figure 5-23: Simulated time-averaged excess temperature contour for *xy*-plane located at *z* = 158.4 mm from sim0308-KEreal-4mm ($Ar = 3.05 \times 10^{-3}$)

Table 5-7: Time average and standard deviation simulation values for excess temperature and velocity observed at the indicated locations in Figure 5-23

Location ID	*x* [mm]	*y* [mm]	*z* [mm]	$\overline{T}_{excess}$ [%]	$\overline{\lvert\vec{v}\rvert}$ [$\times 10^{-2}$ m/s]	$\bar{\phi}$ [º]	$\bar{\theta}$ [º]
C01	-101.7	58.1	158.4	140.5 ± 15.0	1.45 ± 0.66	113.3 ± 31.2	-46.3 ± 23.2

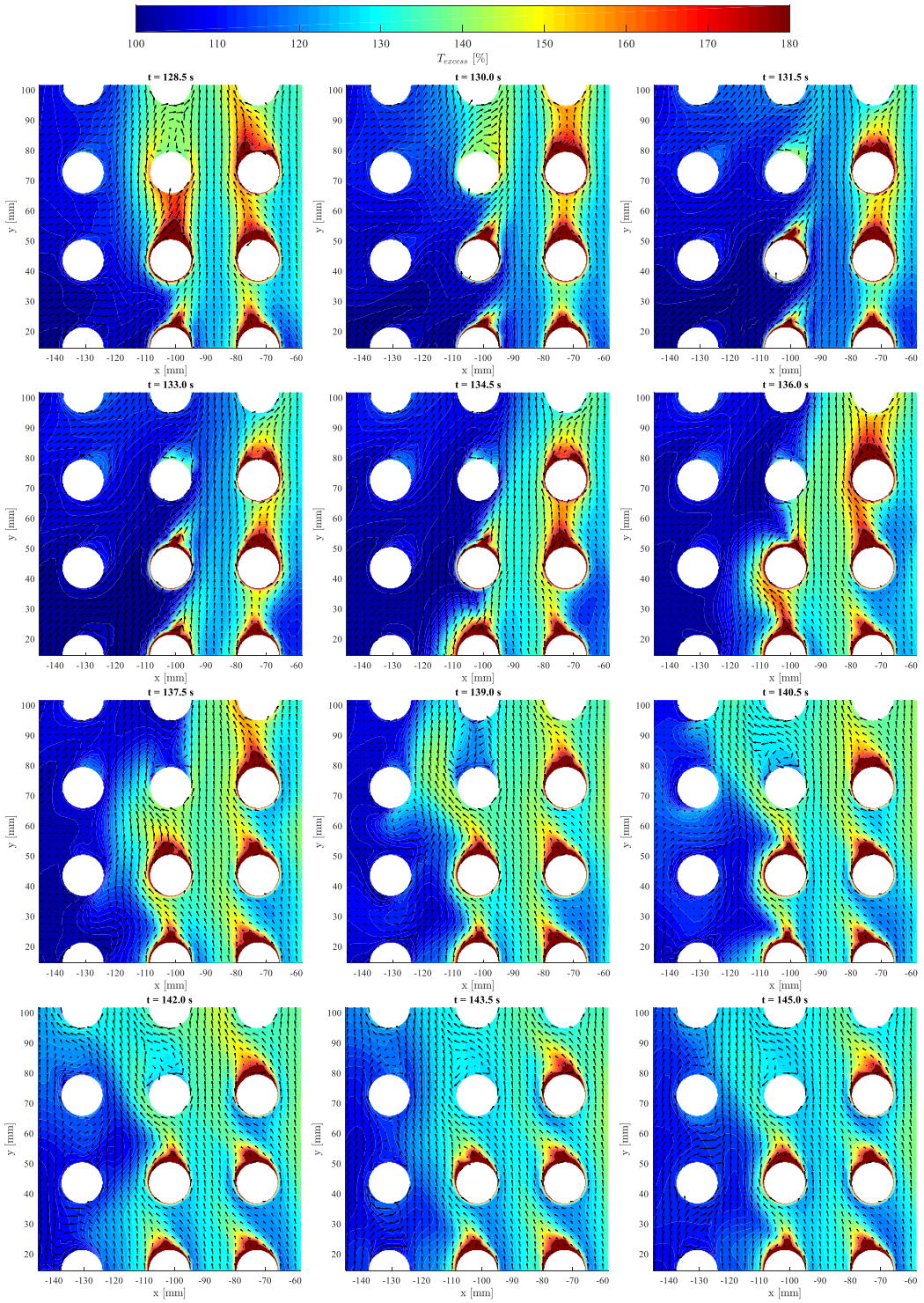

Figure 5-24: Simulated excess temperature contour snapshots for *xy*-plane located at *z* = 158.4 mm from sim0308-KEreal-4mm ($Ar = 3.05 \times 10^{-3}$), detail view for point C01

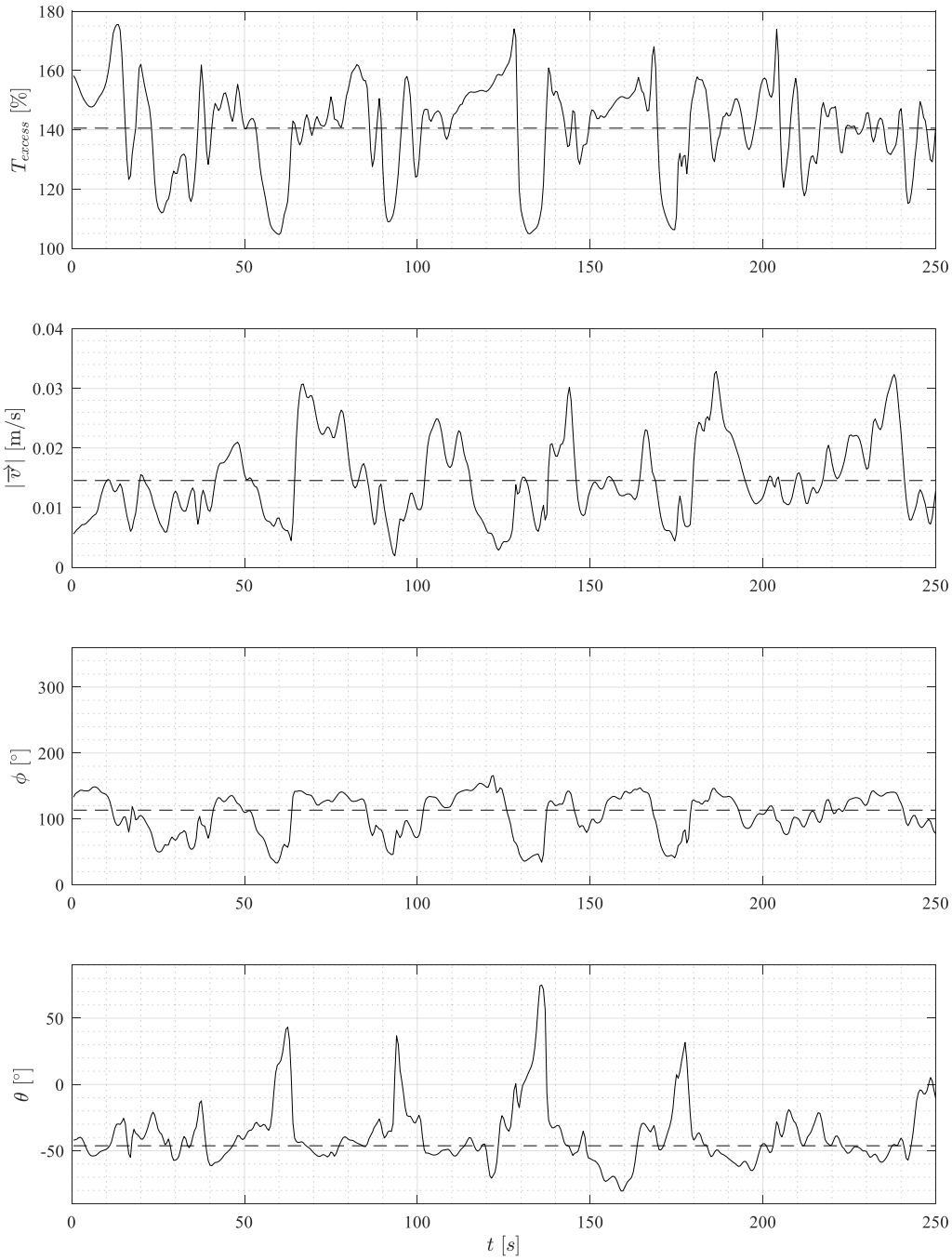

Figure 5-25: Simulated instantaneous excess temperature, speed and direction components for sim0308-KEreal-4mm (Ar = 3.05 × 10^{-3}) located at C01 (-102.0, 58.1, 158.4) mm

5.2.2.1 Comparison to Experiments

Average and standard deviation values for the temperature observed at probe location C01 from experiment test ID 0308-00 are shown in Table 5-8 alongside the corresponding simulation results. Plots comparing the temperature transient behaviour between the experiment and simulation for location C01 are shown in Figure 5-26 and Figure 5-27. Velocity measurements were not available at these locations for this experimental test.

Table 5-8: Comparison of measured and simulated average temperatures observed at selected probe locations for test ID 0308-00 ($Ar = 3.05 \times 10^{-3}$)

Location ID	x [mm]	y [mm]	z [mm]	Measured $\overline{T}_x$ [ºC]	Measured $\overline{T}_{excess}$[%]	Simulated $\overline{T}_x$ [ºC]	Simulated $\overline{T}_{excess}$[%]
C01	-101.7	58.1	158.4	34.9 ± 1.0	132.4 ± 10	35.7 ± 1.4	140.5 ± 15.0

Table 5-9: Comparison of measured and simulated minimum and maximum temperatures at selected probe locations for test ID 0308-00 ($Ar = 3.05 \times 10^{-3}$)

Location ID	x [mm]	y [mm]	z [mm]	Measured T_{min} [ºC]	Measured T_{max} [ºC]	Simulated T_{min} [ºC]	Simulated T_{max} [ºC]
C01	-101.7	58.1	158.4	32.7	38.3	32.4	39.6

The transient temperature behaviour at C01 predicted by the simulation qualitatively appeared to correspond to the experiment. Similar to case discussed in section 5.2.1.1, the fluctuations appear with a similar dominant frequency. Consistent with the behaviour described in section 5.1 for simulations at lower *Ar* numbers, the simulation over-predicted the peak temperature.

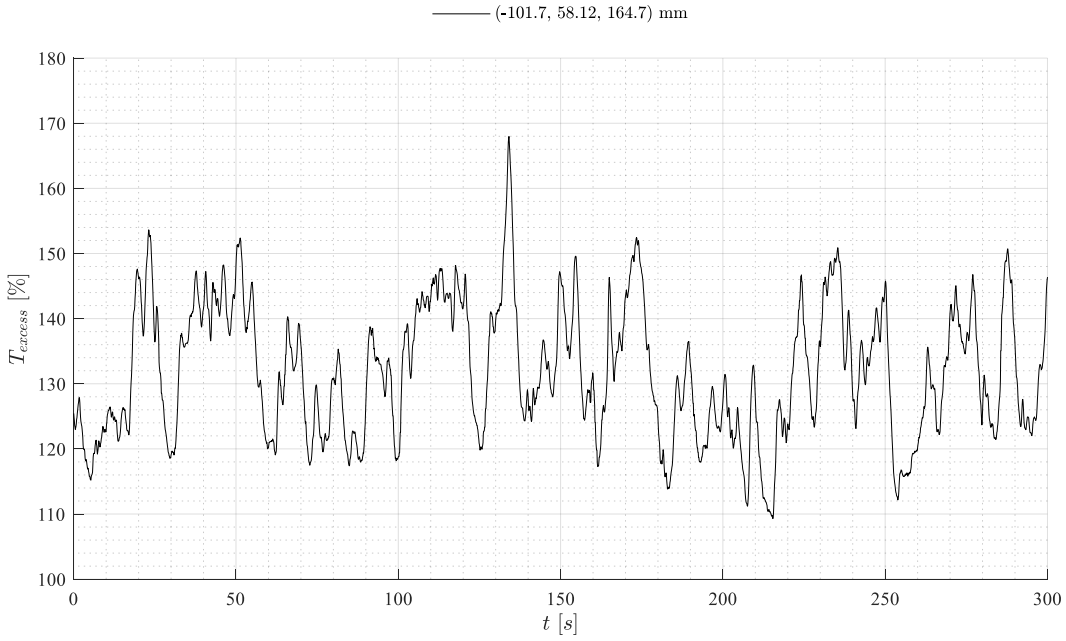

Figure 5-26: Experimental excess temperature versus time for test ID 0308-00 (Ar = 3.05 × 10^{-3}) at location C01

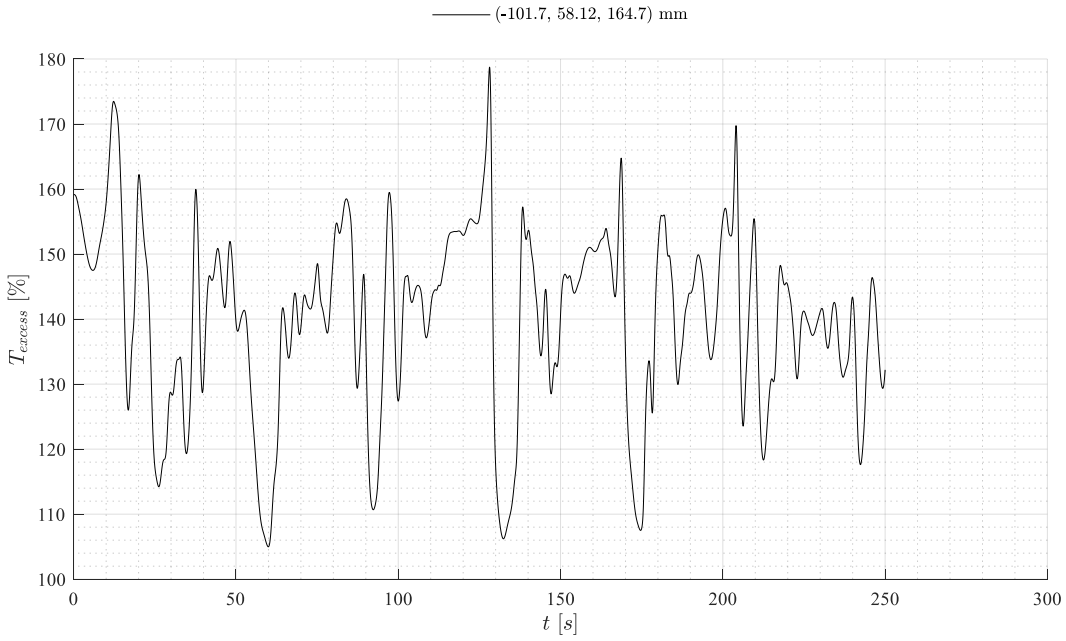

Figure 5-27: Simulated excess temperature versus time for sim0308-KEreal-4mm (Ar = 3.05 × 10^{-3}) at location C01

5.3 Prediction of Maximum Instantaneous Temperature

5.3.1 Comparisons Within Thermocouple Regions

As noted in section 1.1, the maximum instantaneous temperature within the moderator volume (and thus, the minimum available subcooling) is an important safety consideration. In order to further explore the effectiveness of the computer model used in this study, the maximum temperatures recorded during each experimental test were compared to the maximum temperatures recorded in each corresponding transient simulation run.

For each transient simulation case, temperature profile snapshot data were recorded for each timestep (i.e. – each 0.05 s) along horizonal lines in the *x* dimension corresponding to the 13 thermocouple positions in the experiments. The maximum recorded temperature, excess temperature, and corresponding location within the fluid volume along were noted for each case and are summarized in Table 5-10. The inlet flow rate and heater power conditions for each simulation directly correspond to the measured conditions from an actual experimental test (i.e. – sim0908-KEreal-4mm corresponds to test ID 0908-00). Additional repeat experiments were performed for certain power and flow combinations; these results were also compared to simulation data. A mapping of corresponding simulation and experimental cases are summarized in Table 5-11.

For each experimental case listed, the maximum temperature was predicted using the corresponding maximum excess temperatures listed in Table 5-10 using Equation 5.12 with the results summarized in Table 5-12. The peak excess temperature, rather than the peak absolute temperature, was used in order to account for day-to-day variations in inlet temperature conditions between repeated temperature measurement cases.

$$T_{peak,predicted} = T_{excess_{sim}} \times (T_{out} - T_{in})_{exp} + T_{in_{exp}} \qquad (5.12)$$

Table 5-10: Maximum instantaneous temperature, excess temperature, and corresponding locations for each transient simulation case observed along thermocouple positions in the test section

Simulation ID	*Ar*	T_{in} [°C]	T_{out} [°C]	T_{peak} [°C]	*x* [mm]	*y* [mm]	*z* [mm]
sim0908-KEreal-4mm	1.28×10^{-3}	20.0	24.8	31.9 (248%)	70.9	58.1	256.2
sim0308-KEreal-4mm	3.05×10^{-3}	22.4	31.9	42.1 (207%)	47.7	0.0	164.7
sim0831-KEreal-4mm	7.05×10^{-3}	27.3	39.1	48.3 (178%)	40.3	58.1	164.7
sim0309-KEreal-4mm	8.96×10^{-3}	34.3	53.1	65.2 (164%)	73.4	58.1	164.7
sim0922-KEreal-4mm	9.43×10^{-3}	40.8	58.7	70.1 (164%)	47.7	116.2	164.7
sim1017-KEreal-4mm	1.02×10^{-2}	19.8	28.7	37.1 (194%)	102.7	58.1	256.2
sim1018-KEreal-4mm	1.03×10^{-1}	23.1	43.3	50.4 (135%)	41.6	116.2	256.2

Table 5-11: Corresponding simulation cases for each set of experimental data

Test ID	Flow [L/min]	Power [kW]	T_{in} [°C]	T_{out} [°C]	Corresponding Simulation ID
0308-00	30.0 ± 0.2	19.93 ± 0.08	22.4 ± 0.5	31.9 ± 0.5	sim0308-KEreal-4mm
0309-00	30.0 ± 0.2	39.80 ± 0.20	34.3 ± 0.5	53.1 ± 0.5	sim0309-KEreal-4mm
0823-00	29.8 ± 0.2	19.77 ± 0.08	26.8 ± 0.5	36.3 ± 0.5	sim0308-KEreal-4mm
0831-00	24.0 ± 0.1	19.77 ± 0.08	27.3 ± 0.5	39.1 ± 0.5	sim0831-KEreal-4mm
0908-00	30.1 ± 0.2	9.85 ± 0.04	20.0 ± 0.5	24.8 ± 0.5	sim0908-KEreal-4mm
0915-01	30.1 ± 0.2	19.76 ± 0.08	28.6 ± 0.5	38.1 ± 0.5	sim0308-KEreal-4mm
0922-00	30.0 ± 0.2	37.58 ± 0.20	40.8 ± 0.5	58.7 ± 0.5	sim0922-KEreal-4mm
1011-00	30.0 ± 0.2	19.81 ± 0.08	26.2 ± 0.5	35.7 ± 0.5	sim0308-KEreal-4mm
1011-01	29.9 ± 0.2	19.79 ± 0.08	26.1 ± 0.5	35.6 ± 0.5	sim0308-KEreal-4mm
1011-02	29.9 ± 0.2	19.78 ± 0.08	26.2 ± 0.5	35.7 ± 0.5	sim0308-KEreal-4mm
1017-01	15.1 ± 0.1	9.35 ± 0.04	19.8 ± 0.5	28.7 ± 0.5	sim1017-KEreal-4mm
1018-00	8.2 ± 0.1	11.87 ± 0.05	23.1 ± 0.5	43.3 ± 0.5	sim1018-KEreal-4mm

Table 5-12: Comparison of maximum observed temperatures between corresponding simulation and experiment cases.

Test ID	*Ar*	Measured[12]				Predicted			
		T_{peak} [°C]	*x* [mm]	*y* [mm]	*z* [mm]	T_{peak} [°C]	*x* [mm]	*y* [mm]	*z* [mm]
0908-00	1.28×10^{-3}	28.9	-72.6	58.1	256.2	31.9 (+3.0)	70.9	58.1	256.2
0308-00	3.05×10^{-3}	38.3	-101.7	58.1	164.7	42.1 (+3.8)	47.7	0.0	164.7
1011-00	3.43×10^{-3}	43.0	14.5	58.1	256.2	45.9 (+2.8)	47.7	0.0	164.7
1011-01	3.44×10^{-3}	42.4	14.5	58.1	256.2	45.8 (+3.4)	47.7	0.0	164.7
1011-02	3.45×10^{-3}	42.2	14.5	58.1	256.2	45.9 (+3.6)	47.7	0.0	164.7
0823-00	3.53×10^{-3}	43.4	-101.7	58.1	164.7	46.5 (+3.0)	47.7	0.0	164.7
0915-01	3.63×10^{-3}	44.4	-14.5	58.1	256.2	48.3 (+3.8)	47.7	0.0	164.7
0831-00	7.05×10^{-3}	46.4	-43.6	58.1	256.2	48.3 (+1.9)	40.3	58.1	164.7
0309-00	8.96×10^{-3}	63.1	-43.6	58.1	256.2	65.2 (+2.1)	73.4	58.1	164.7
0922-00	9.43×10^{-3}	67.9	-43.6	58.1	256.2	70.1 (+2.3)	47.7	116.2	164.7
1017-01	1.02×10^{-2}	35.2	-101.7	58.1	256.2	37.0 (+1.8)	102.7	58.1	256.2
1018-00	1.03×10^{-1}	49.9	-72.6	58.1	256.2	50.4 (+0.5)	41.6	116.2	256.2

The results in Table 5-12 show that in all cases the simulation over-predicted the maximum temperature within the test section. Figure 5-28 shows that a downward trend was typically observed with increasing *Ar* (i.e. – the peak temperature was over-predicted to a smaller degree for higher *Ar*). For the repeated experiment cases for 30 L/min flow and 20 kW power (*Ar* ~ 0.003), the simulations overpredicted the peak temperature by approximately 3 – 4 ºC, while simulation cases at *Ar* ~0.01 overpredicted the peak temperature by approximately 2 ºC. The case at *Ar* ~0.1, closest to the conditions in the full-scale reactor, overpredicted the peak

[12] Uncertainty for all temperature measurements is ± 0.5ºC

temperature by approximately 0.5 ºC which is comparable to the measurement uncertainty of the experimental data.

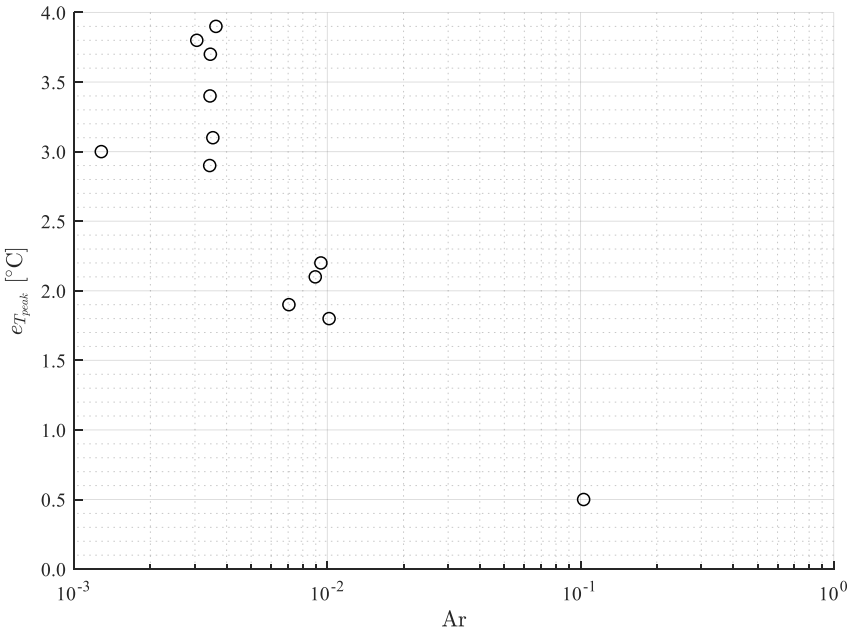

Figure 5-28: Error in predicted peak instantaneous temperature versus Archimedes number

The larger error at lower *Ar* is consistent with observations made in section 5.1.2; there it was shown that the simulations tended to underpredict the local velocities at lower *Ar*, with agreement improving with increased *Ar*. This behaviour was attributed to issues with the modelling of the inlet jets (i.e. – the realizable *k-ε* model would generally overpredict the inlet jet dispersion in the region above the tube bank, resulting in lower flow inertia entering the tube bank).

As shown in Table 5-12, the peak instantaneous temperatures consistently occurred near the axial center of the heated region of the tube bank, shifted toward the eastern end of the vessel. In these regions, inertial flows were upward and assisted by buoyancy induced flows. While velocity measurements were not attainable at these locations, the velocity characteristics were expected to be similar to the region shown in Figure 5-11. As *Ar* was increased and local buoyancy effects became more significant in determining the local velocity, the modelling errors of the inlet

jet behaviour would become relatively less significant. As the prediction of the local velocity improved, an improvement of the peak instantaneous would be expected. This is consistent with the behaviour shown in Figure 5-11 where the predicted velocities above the heated region of the tube bank (y = 116.2 mm) were seen to improve with increasing Ar.

It was also noted that the locations of the peak temperatures did not directly correspond between the experiments and the simulations. The thermocouple positions were relatively coarsely spaced in the z dimension. As a result, there was a possibility that higher temperatures were occurring in the experiments outside of the regions accessible by the thermocouples. If the temperature distributions in simulations differed from the experiments due to modelling uncertainties, there would then exist the possibility that higher temperatures could be recorded in the simulation data if these areas were shifted into the thermocouple regions. However, simulation data using a finer sampling of the fluid domain in the z dimension were examined and found that peak temperatures within the thermocouple regions were reasonable at predicting the peak within the entire vessel (within 1.5 ºC). Further discussion of this point is present in section 5.3.2.

It was also noted that the locations of the peak temperatures for the repeated 20 kW, 30 L/min experiments (test IDs 0308-00, 0823-00, 0915-00, 1011-00, 1011-01, and 1011-02) did not correspond directly day-to-day. This result was not considered unusual allowing for repeatability and measurement uncertainty factors. As discussed in section E.3, repeated temperature measurements day-to-day were expected to be within 0.7 ºC. Additionally, for mixed convection flows the location of the peak temperature may be unsteady and therefore its location will be a transient. Aside from the single locations identified for each experiment in Table 5-12, there could exist several other measurement locations where the peak instantaneous temperature would fall within this close range.

For example, a fixed location of (-14.5, 58.1, 256.2) mm was considered for all 20 kW, 30 L/min cases; this corresponds to the overall peak temperature location for the 0915-00 case. The maximum instantaneous temperatures at this location are summarized in Table 5-13. After correcting for differences in the inlet temperature, the peak temperatures at this location corresponded across experiments over a range of 1.1ºC; aside from a single outlier case of test ID 1011-00, the observed temperatures agreed within the measurement uncertainty.

Table 5-13: Maximum instantaneous temperature T_x recorded at (-14.5, 58.1, 256.2) mm for 20 kW, 30 L/min

Test ID	Flow [L/min]	Power [kW]	T_{in} [ºC]	T_{out} [ºC]	T_x [ºC]	$T_x - T_{in}$ [ºC]
0308-00	30.0 ± 0.2	19.93 ± 0.08	22.4 ± 0.5	31.9 ± 0.5	37.0 ± 0.5	14.6 ± 0.7
0823-00	29.8 ± 0.2	19.77 ± 0.08	26.8 ± 0.5	36.3 ± 0.5	41.7 ± 0.5	14.9 ± 0.7
0915-01	30.1 ± 0.2	19.76 ± 0.08	28.6 ± 0.5	38.1 ± 0.5	43.1 ± 0.5	14.5 ± 0.7
1011-00	30.0 ± 0.2	19.81 ± 0.08	26.2 ± 0.5	35.7 ± 0.5	41.5 ± 0.5	15.3 ± 0.7
1011-01	29.9 ± 0.2	19.79 ± 0.08	26.1 ± 0.5	35.6 ± 0.5	40.3 ± 0.5	14.2 ± 0.7
1011-02	29.9 ± 0.2	19.78 ± 0.08	26.2 ± 0.5	35.7 ± 0.5	40.6 ± 0.5	14.4 ± 0.7

5.3.2 Comparison of Thermocouple Regions to Entire Fluid Volume

The 13 thermocouple probes in the experiment were limited to five fixed *y*-locations (vertical) and five fixed *z*-locations (front-to-back) within the test section. In addition to data from the thermocouple regions, snapshots of the simulation temperature data were exported every tenth timestep (i.e. – each 0.5 s) along 15 *xz* planes as described in section 4.1.4. These *xz* planes, corresponding to the horizontal midplanes between each row of tube elements, provided a finer sampling of locations in the *z* dimension, with *dz* ranging from 2 mm to 4 mm depending on local mesh refinement. Temperature data within these exported planes was examined to evaluate the effectiveness of the selected thermocouple installation locations at capturing the peak instantaneous temperature within the test section.

The maximum instantaneous temperatures from within the exported *xz* planes are summarized in Table 5-14 and compared to the maximum simulated temperatures

within the thermocouple regions. For all simulation cases, marginally higher peak temperatures were recorded outside of the thermocouple regions with a typical difference of about 1 – 1.5 ºC. These results suggest that the selected thermocouple locations provided reasonable coverage of the peak temperature within the test section, but also that peak temperatures within the experimental test section could be approximately 1 – 2 ºC higher than measured by the thermocouples.

Table 5-14: Comparison of maximum instantaneous temperature for each simulated case within thermocouple regions and *xz* planes

Sim ID	*Ar*	Within Thermocouple Regions				Within *xz* Planes			
		T_{peak} [ºC]	*x* [mm]	*y* [mm]	*z* [mm]	T_{peak} [ºC]	*x* [mm]	*y* [mm]	*z* [mm]
sim0908-KEreal-4mm	1.28×10^{-3}	31.9	70.9	58.1	256.2	33.0 (+1.1)	44.0	-29.1	210.4
sim0308-KEreal-4mm	3.05×10^{-3}	42.1	47.7	0.0	164.7	43.0 (+0.9)	72.0	58.1	230.4
sim0831-KEreal-4mm	7.05×10^{-3}	48.3	40.3	58.1	164.7	49.2 (+0.9)	42.0	58.1	156.4
sim0309-KEreal-4mm	8.96×10^{-3}	65.2	73.4	58.1	164.7	66.5 (+1.3)	72.0	58.1	196.4
sim0922-KEreal-4mm	9.43×10^{-3}	70.1	47.7	116.2	164.7	71.6 (+1.5)	72.0	58.1	184.4
sim1017-KEreal-4mm	1.02×10^{-2}	37.1	102.7	58.1	256.2	37.9 (+0.8)	42.0	58.1	208.4
sim1018-KEreal-4mm	1.03×10^{-1}	50.4	41.6	116.2	256.2	50.9 (+0.5)	-16.0	116.2	258.4

When examining the temperature data across all *xz* planes it was noted that the peak temperatures occurred within or directly above the heated region of the tube bank. Of all cases, the 12 kW, 8 L/min case ($Ar \sim 0.1$) had the peak temperature occur at the highest *y* location ($y = 116.2$ mm), which corresponds to the plane directly above the highest row of heated elements. This result suggests that additional

thermocouples located at higher elevations would not be necessary for capturing the peak temperature within the test section.

5.4 Impact of Archimedes Number on Temperature Distributions

5.4.1 Impact of Increasing Ar

In order to examine the impact of Archimedes number on the temperature distributions, time-average excess temperature contour plots from various simulation conditions were compared. Figure 5-29 through Figure 5-33 present the simulated excess temperature contour for the *yz*-plane located at x = -29.1 mm, coinciding with the plane examined in section 5.2.1. The plots are presented in order of increasing *Ar*, starting with the 10 kW, 30 L/min case (least buoyancy significance) up to the 12 kW, 8 L/min case (most buoyancy significance).

Referring to Figure 5-29 (low buoyancy condition), a clockwise recirculation pattern corresponding to the flow pattern caused by the asymmetric east/west arrangement of the inlet nozzles is visible at the centre of the plot. As flow from the inlet jets enters the top of the tube bank (y = 167 mm), the average flow direction remains constant until reaching $y \approx$ -116 mm where the flow direction changes to horizontal, corresponding to the bottom heated row in the tube bank.

As *Ar* is increased through the range of $0.003 < Ar < 0.01$ (Figure 5-30 through Figure 5-32), only slight changes in the distribution were noted. The shape of this recirculation region is 'pushed' upwards and towards the western end of the vessel. For the higher buoyancy cases, the average flow path of the inlet jet is deflected increasingly upward as flow enters the heated region of the tube bank (at y = 116 mm), becoming directed horizontally toward the rear of the vessel. The high-temperature region at the upper eastern end of the vessel was also observed to grow with increasing *Ar* number. In the highest buoyancy case shown in Figure 5-33, this leads to the development of a small recirculation zone near the top of the plane near z = 0.

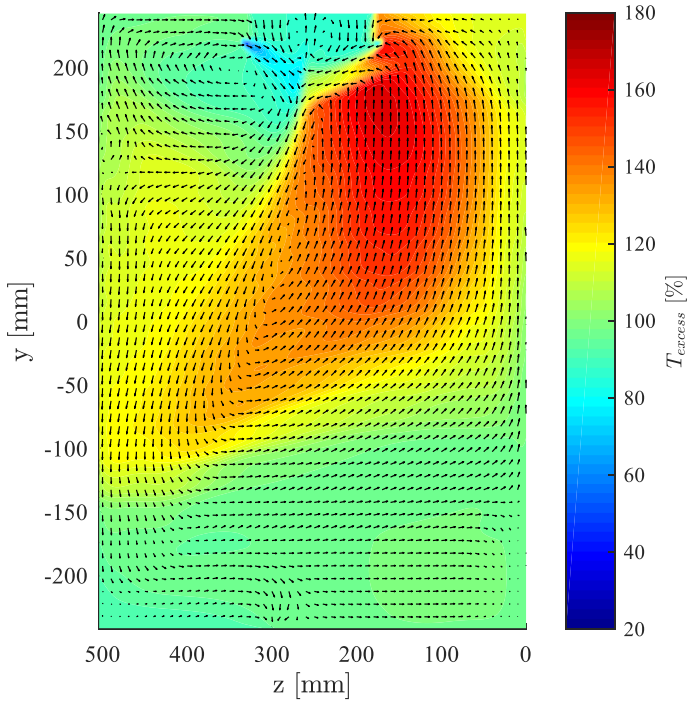

Figure 5-29: Simulated time-averaged excess temperature contour for *yz*-plane located at *x* = -29.1 mm from sim0908-KEreal-4mm ($Ar = 1.28 \times 10^{-3}$)

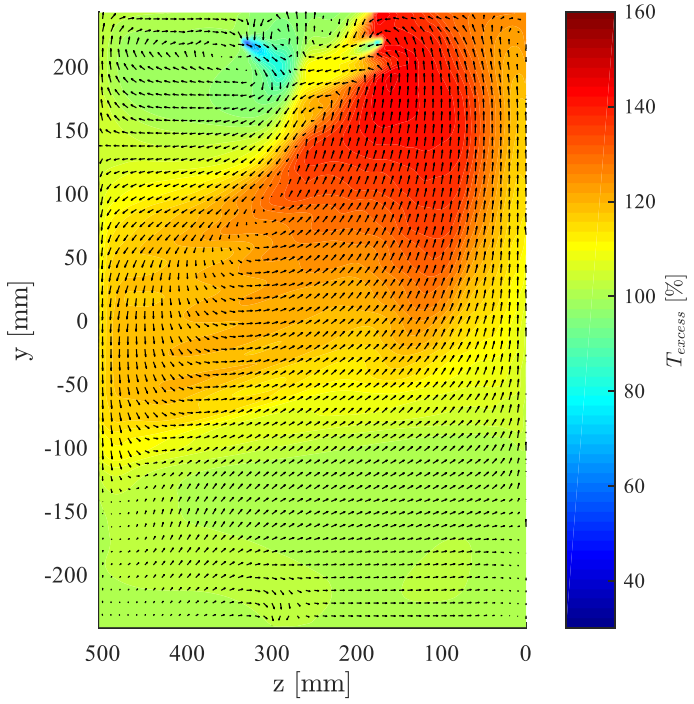

Figure 5-30: Simulated time-averaged excess temperature contour for *yz*-plane located at *x* = -29.1 mm from sim0308-KEreal-4mm ($Ar = 3.05 \times 10^{-3}$)

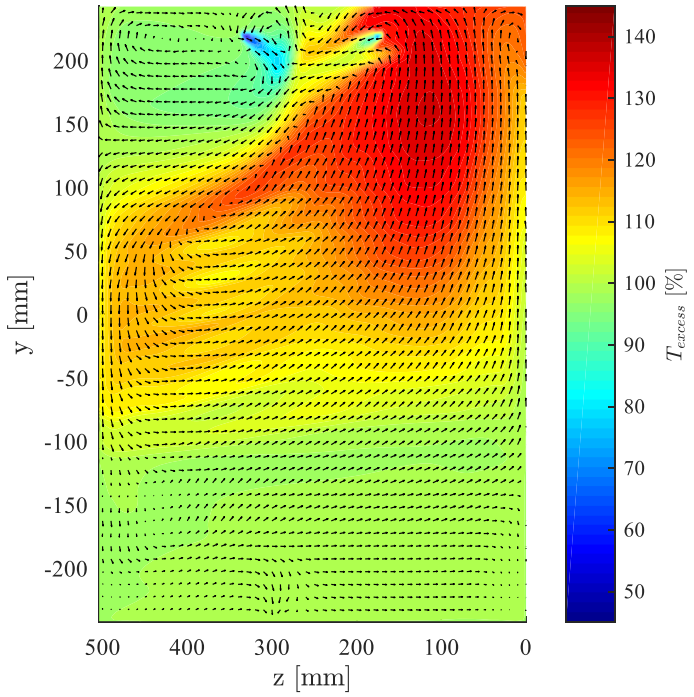

Figure 5-31: Simulated time-averaged excess temperature contour for *yz*-plane located at *x* = -29.1 mm from sim0831-KEreal-4mm (*Ar* = 7.05 × 10^{-3})

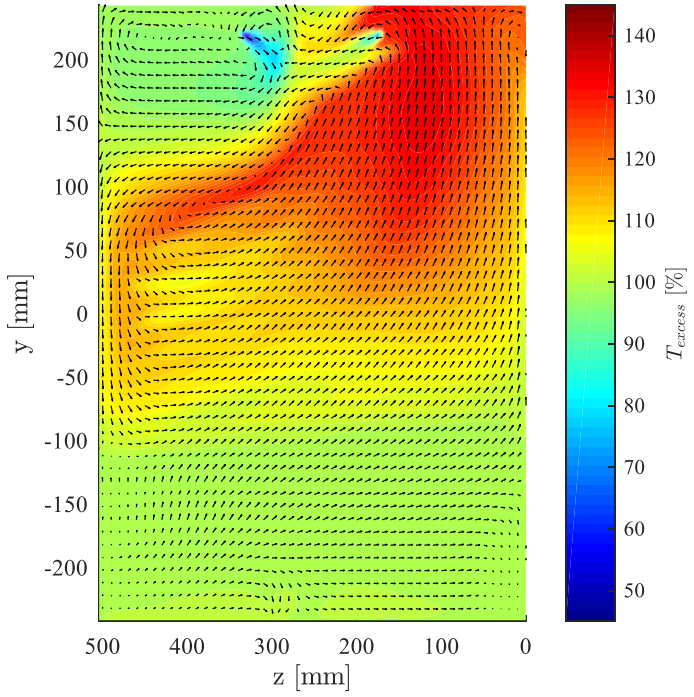

Figure 5-32: Simulated time-averaged excess temperature contour for *yz*-plane located at *x* = -29.1 mm from sim0922-KEreal-4mm (Ar = 9.43 × 10^{-3})

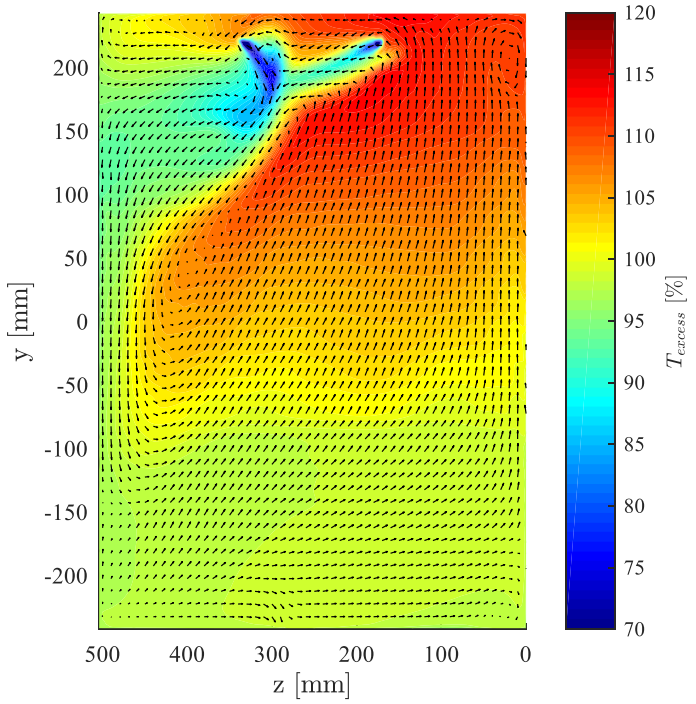

Figure 5-33: Simulated time-averaged excess temperature contour for *yz*-plane located at *x* = -29.1 mm from sim1018-KEreal-4mm ($Ar = 1.03 \times 10^{-1}$)

5.4.2 Changing Test Conditions While Maintaining Ar

For a targeted *Ar* number, there existed multiple possible combinations of heater power and flow rate. Using test ID 0922-00 as a baseline (P_e = 37.58 kW, Q = 30.0 L/min, $Ar = 9.43 \times 10^{-3}$), test ID 1017-01 was conducted at lower power and flow rate to achieve a comparable *Ar* number (P_e = 9.35 kW, Q = 15.1 L/min, $Ar = 1.02 \times 10^{-2}$). These tests were performed to investigate how well *Ar* could be used to predict behaviour within the test section across different sets of test conditions. For the following discussion, case 0922-00 is referred to as the 'high flow' condition while case 1017-01 is referred to as the 'low flow' case.

The time-average experimental excess temperature measurements for test IDs 0922-00 and 1017-01 are presented and compared in Figure 5-34. The error bars for each data point represent the standard deviation of the measurements over the 300 s period of measurement at the corresponding location. For both experimental

cases, the absolute measurement accuracy of the temperature measurements was 0.5 ºC. For test ID 0922-00 (ΔT = 17.9 ºC), the measurement uncertainty corresponded to an excess temperature value of 2.8%; for test ID 1017-01 (ΔT = 8.9 ºC), this corresponded to an excess temperature value of 5.6%.

As shown in Figure 5-34, the excess temperature measurements corresponded closely (i.e. – within measurement uncertainty) in most locations within the vessel. agreement within the buoyancy dominated regions of the vessel was good. These areas are of interest since they correspond to regions where the maximum temperatures within the fluid volume are expected.

While the general temperature distribution was qualitatively similar, agreement between the two sets of measurements was poorer towards the upper western end of the vessel (i.e. – locations where $y > 0$ mm and $z > 256.2$ mm). These regions were previously identified as areas where inertial flow from the inlet jets was downward and opposing upward, buoyant flow from the heated tube bank elements. Noteworthy differences were present for profiles 03, 04, and 07 at x locations between -29.1 mm and -116.2 mm. Lower average excess temperatures were recorded at these locations for the high flow case, suggesting that the inlet jets were penetrating further into the tube bank region as compared to the low flow case.

A possible cause of these differences could arise from differences in the inlet jet momentum between the high and low flow cases, which would lead to different degrees of jet penetration into the tank, or from the lower Reynolds number which can impact jet dissipation. The Reynolds number at the exit of the inlet nozzle is given by Equation 5.13, for a given volumetric flow rate Q_{inlet}, kinematic viscosity v, and inlet diameter D_{inlet}. The Reynolds numbers for each type of inlet nozzle for the two tests are shown in Table 5-15.

$$Re = \frac{4Q_{inlet}}{\pi v D_{inlet}} \tag{5.13}$$

Table 5-15: Reynolds number at the exit of inlet nozzles for cases 0922-00 and 1017-01

Test ID	T_{inlet} [°C]	$Q_{inlet,\ total}$ [L/min]	ν [m^2/s]	Booster		Booster-bypass	
				Q_{inlet} [m^3/s]	*Re*	Q_{inlet} [m^3/s]	*Re*
0922-00	40.8	30.0	6.49×10^{-7}	2.08×10^{-5}	11 000	2.78×10^{-5}	14 000
1017-01	19.8	15.1	1.01×10^{-6}	1.05×10^{-5}	3500	1.40×10^{-5}	4700

A previous study by Abdel-Rahmen *et al.* using circular jets in the range of $1400 < Re < 19400$ found that for lower Re, the centreline velocity decayed faster and the potential core was shorter [46]. Comparing the high and low flow cases in Table 5-15, this suggests that the in the distance between the inlets and the tube bank, the jet centreline velocity for the low flow case would have decayed more relative to the high flow case, resulting in lower velocities entering the tube bank and relatively lower inertia. This effect is not captured by the Archimedes number since its inertial term depends on the exit velocity at the inlet rather than the velocity entering the tube bank.

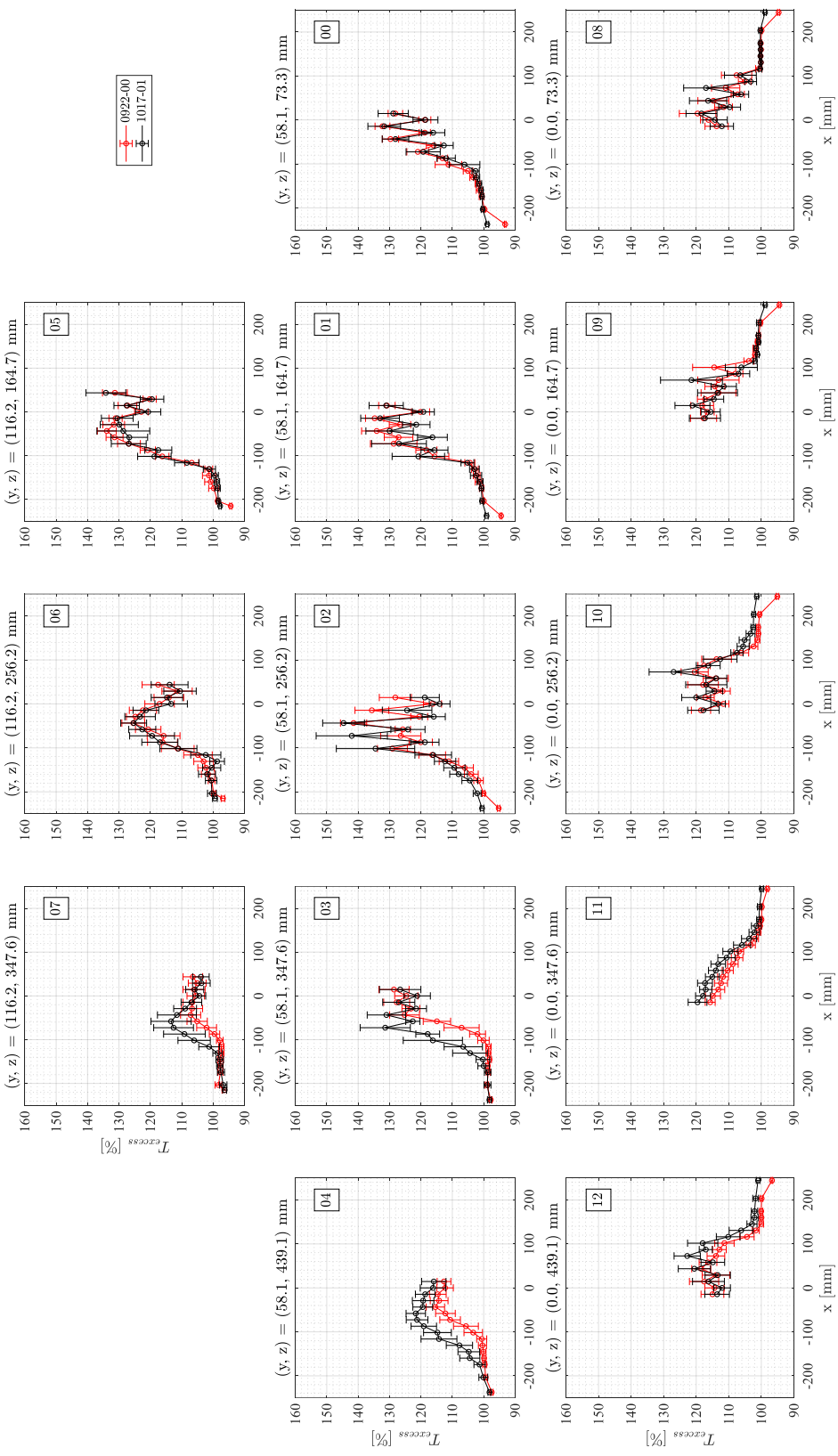

Figure 5-34: Comparison of the time-averaged excess temperature maps for test IDs 0922-00 (P_e = 37.58 kW, Q = 30.0 L/min, Ar = 9.43 × 10^{-3}) and 1017-01 (P_e = 9.35 kW, Q = 15.1 L/min, Ar = 1.02 × 10^{-2}). The error bars correspond to s_T.

5.5 Comparisons to Full-Scale Bruce A Moderator

Unsteady RANS simulations of the full-scale Bruce A moderator under 88% full-power conditions using STAR-CCM+ were reported by Ashgriz and Behzad [44]. Where possible, qualitative comparisons were made between temperature fields predicted by Ashgriz and Behzad for the full-scale facility and those predicted for the test facility used for this study.

Figure 5-35 depicts the locations of the planes used by Ashgriz and Behzad to report simulation results from the Bruce A full-scale facility. Comparable planes from the simulation results of the small-scale Bruce A test section are shown in Figure 5-36. Note that the locations between the two facilities do not correspond directly but were selected to be as comparable as possible:

- Plane X_0 from the full-scale facility was located at the x center for the calandria and located between tube columns. This corresponded closely with the x_7 plane for the small-scale facility.
- Planes X_1 and X_2 from the full-scale facility were yz-planes located between tube columns and relative to the locations of inlets. Plane X_1 intersected two 'booster' inlets while plane X_2 was located at the mid point between two 'booster' inlets. Due to the fewer number of tube columns in the small-scale facility, the booster inlets did not line up with a gap between tube columns. Planes x_8 and x_9 in the small-scale facility were selected as the closest available yz-planes located near the corresponding 'booster' inlets.

While the small-scale facility replicated key features of the full-scale facility, several differences existed:

- The length-to-diameter (L/d) ratio of the full-scale facility was 0.75 while it was 1.0 for the small-scale facility. The presented *yz* plane data from the small-scale facility have been displayed with a 0.75 aspect ratio.
- The small-scale facility features a relatively larger gap between the tube bank and the vessel walls compared to the full-scale facility.
- The aiming of the 'booster-bypass' nozzles was modified in the small-scale facility. In the full-scale facility, the central four bypass nozzles are aimed 30º off-centre towards the outer vessel walls while these nozzles are aimed directly towards the western end of the vessel as shown in Figure 5-36. Early tests indicated a large portion of flow bypassing the heated region of the tube bank as a result of the above differences. The nozzle aiming in the small-scale facility was modified to counteract this effect.
- The outer two rows of the tube column in the small-scale facility were not heated and inertial flow effects would be relatively higher in these regions. Comparisons to the full-scale facility were not made in these regions.
- The heating method of the full-scale facility was a volumetric heat source while surface heating was used in the small-scale facility. This would result in relatively higher temperatures to be seen near the heater walls in the small-scale case.

Temperature contour data from the full-scale Bruce A facility simulations were reported in the range of either 33 ºC to 83 ºC or 45 ºC to 83 ºC coinciding with a facility inlet temperature of 33 ºC, outlet temperature of 66.8 ºC and reference inlet velocity of 2.5 m/s [44]. These conditions corresponded to $Ar \approx 0.2$ and an inlet Re of 754 000. The temperature range of 33 ºC to 83 ºC corresponded to an excess temperature range of 0% to 148% whereas the range of 45 ºC to 83 ºC corresponded to a range of 36% to 145%.

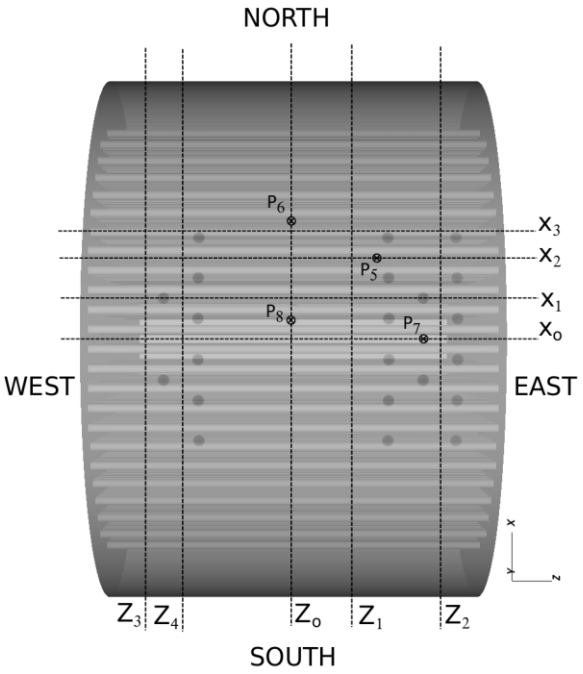

Figure 5-35: Locations of planes used by Ashgriz and Behzad for the presentation of Bruce A full-scale facility simulation results. Reproduced from [44]

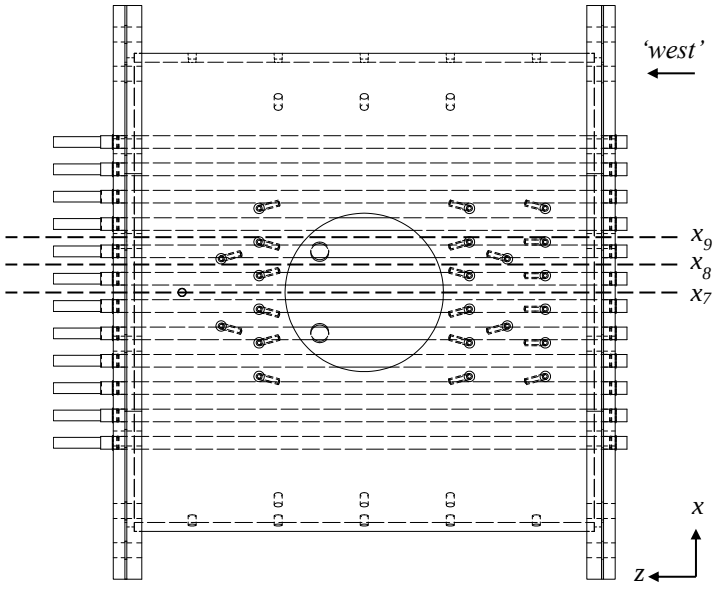

Figure 5-36: Locations of planes in the small-scale facility selected for comparison to the Bruce A full-scale facility simulation results

5.5.1 Time Averaged Behaviour

Average temperature contour plots comparing the full-scale facility simulations to the small-scale facility simulations are shown in Figure 5-37 through Figure 5-39. Unit vectors are provided to show the flow direction within the plane. Overall, the observed temperature distributions were qualitatively similar between both facilities despite the differences in scale and other simplifications made for the small-scale model. Both facilities showed the expected circulation pattern caused by the inlet asymmetry in the east-west direction, with flow largely directed downward at the western end of the tube bank and upward in the eastern end. This arrangement led to cooler temperatures in the upper-west end of the vessel for both cases.

Unlike the full-scale facility, only the central tube elements in the tube bank were heated in the small-scale facility, with the heated region corresponding to -116 mm < y < 116 mm. This was seen to impact the temperature distribution resulting in lower temperatures at the bottom of the tube bank relative to the full-scale facility.

A notable difference was the range of temperatures experienced for each facility. For the small-scale facility, the excess temperatures observed in the selected planes was approximately 45 – 145% for the $Ar \approx 0.1$ case and 70 – 120% for the $Ar \approx 0.01$ case. Conversely, the comparable range for the full-scale facility corresponded to an excess temperature 36 – 148%, closer to the range observed for the $Ar \approx 0.01$ in the small-scale facility.

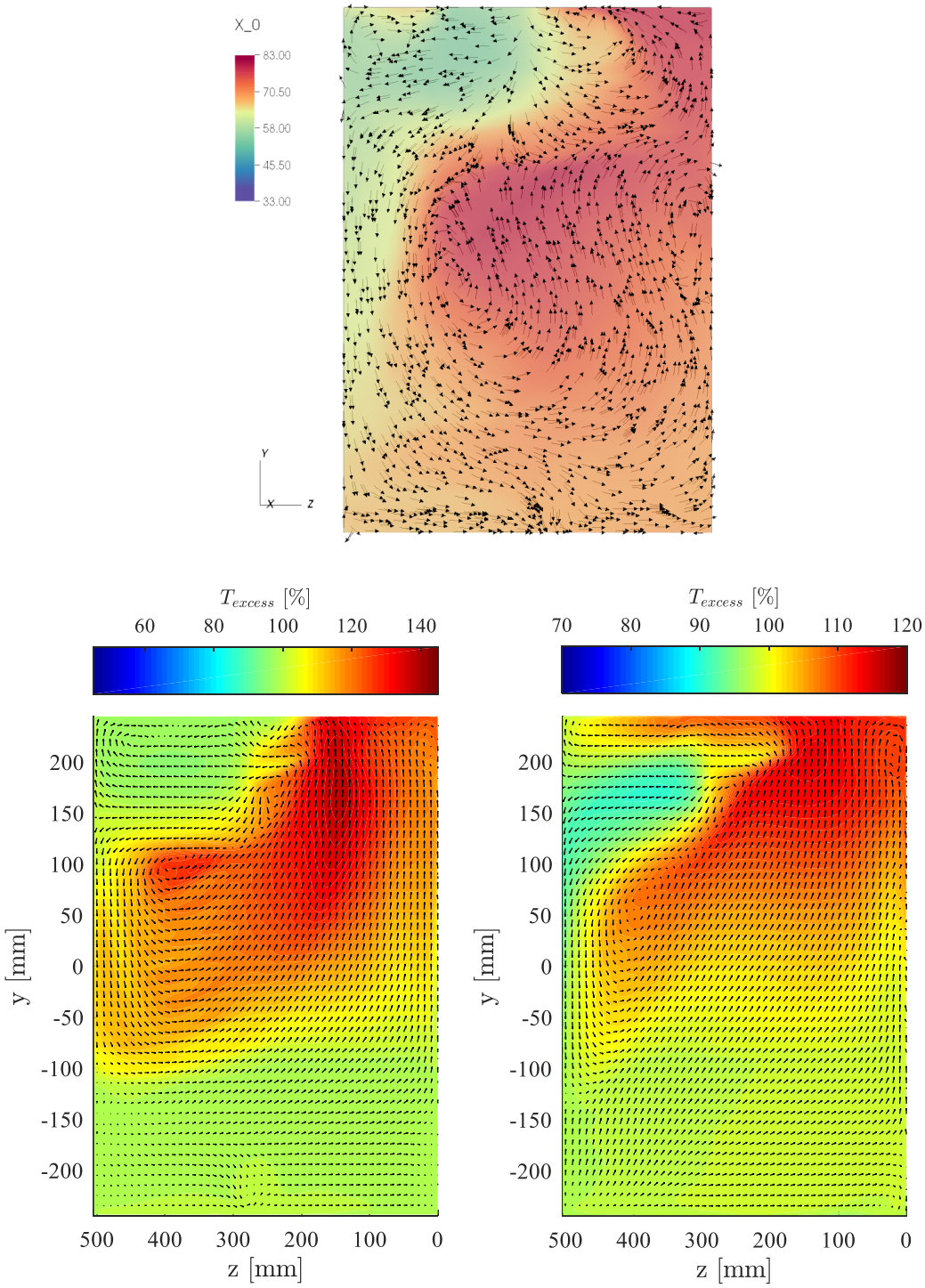

Figure 5-37: Simulated time average temperature contour. Plane X_0 from the full-scale facility ($Ar \approx 0.2$), reproduced from [44] (top). Plane x_7 from the small-scale facility for sim0922-KEreal-4mm ($Ar \approx 0.01$) (bottom left) and sim1018-KEreal-4mm ($Ar \approx 0.1$) (bottom right)

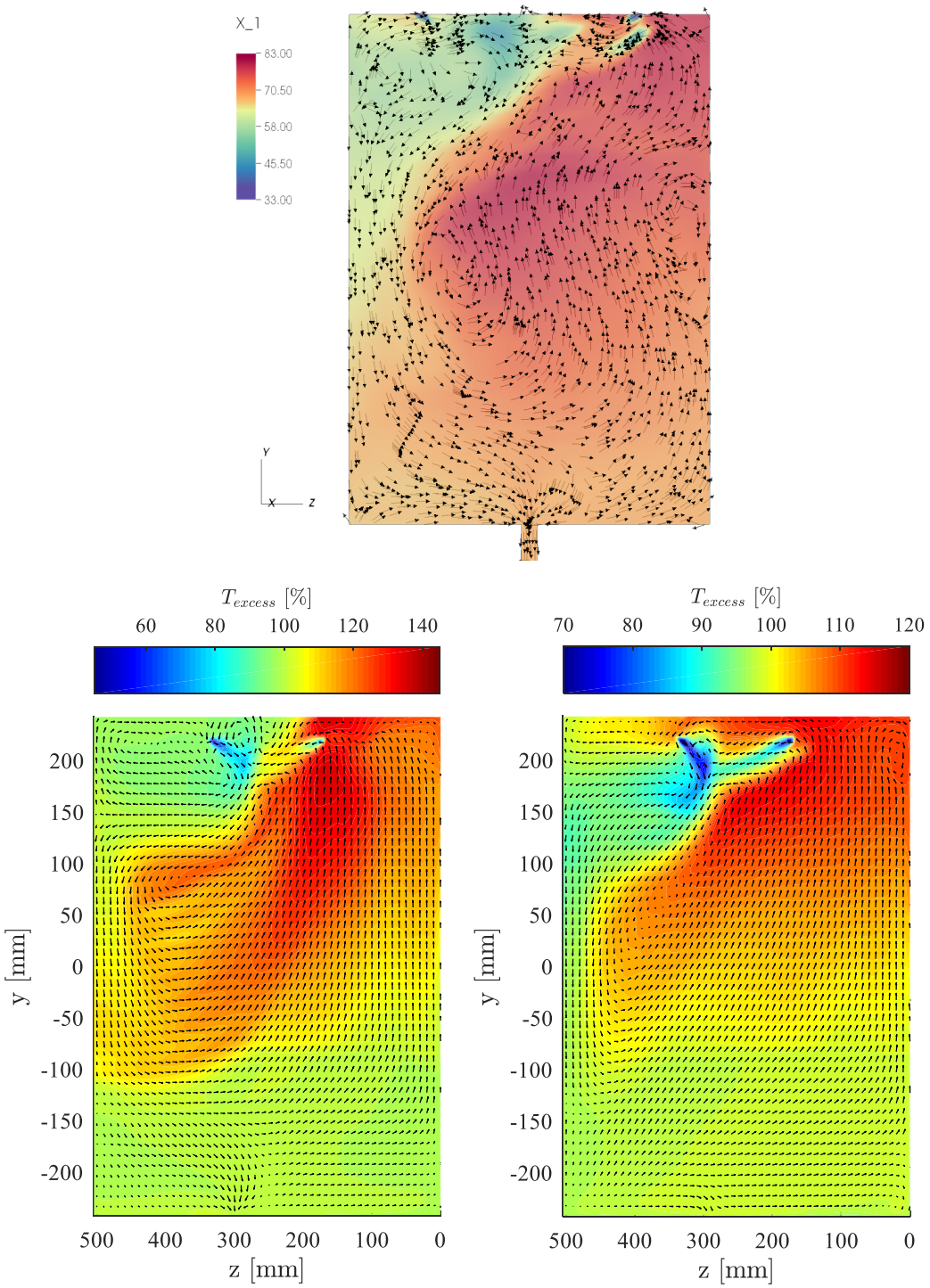

Figure 5-38: Simulated time average temperature contour. Plane X_1 from the full-scale facility ($Ar \approx 0.2$), reproduced from [44] (top). Plane x_8 from the small-scale facility for sim0922-KEreal-4mm ($Ar \approx 0.01$) (bottom left) and sim1018-KEreal-4mm ($Ar \approx 0.1$) (bottom right)

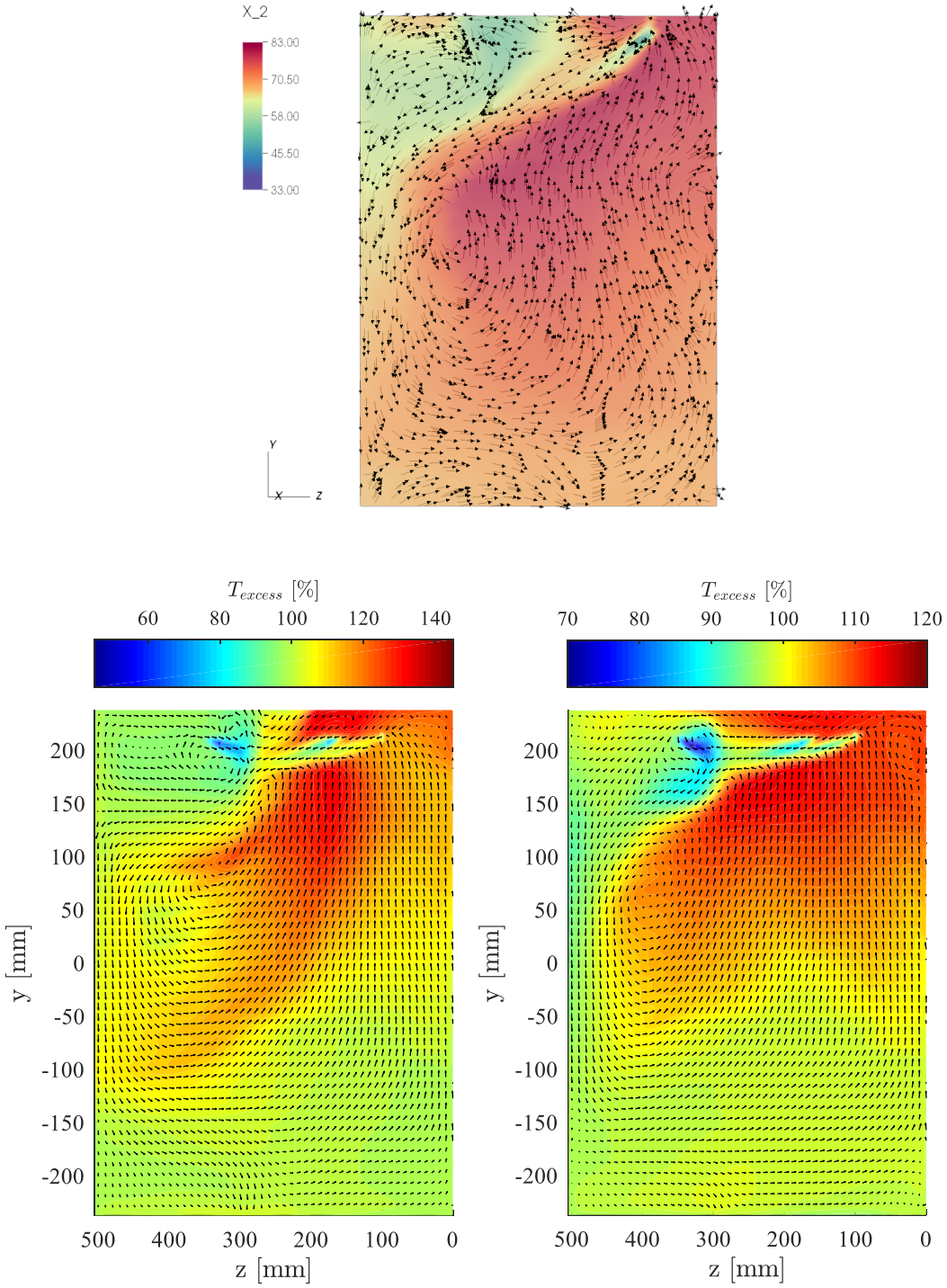

Figure 5-39: Simulated time average temperature contour. Plane X_2 from the full-scale facility ($Ar \approx 0.2$), reproduced from [44] (top). Plane x_9 from the small-scale facility for sim0922-KEreal-4mm ($Ar \approx 0.01$) (bottom left) and sim1018-KEreal-4mm ($Ar \approx 0.1$) (bottom right)

Figure 5-37 shows a comparison between plane X_0 in the full-scale facility and plane x_7 in the small-scale facility. The flow pattern in the full-scale facility shows flow toward the eastern end of the vessel in this plane near the upper-east portion of the tube bank. For the small-scale facility, flow is upward in this region for both *Ar* cases. This difference likely arose from the differences in the 'booster-bypass' nozzle aiming as discussed in section 5.5.

For both *Ar* conditions in the small-scale facility, a 'hot-zone' developed above the inlet nozzles, appearing larger for the higher *Ar* case and shifting towards the western end of the vessel. The movement of this zone as *Ar* increased appeared to impact the recirculation zone around the nozzles located at the upper-west end of the vessel. This effect is visible for all three selected planes. Considering these recirculation zones, the small-scale facility at $Ar \approx 0.01$ (as opposed to $Ar \approx 0.1$) more closely resembled the full-scale facility ($Ar \approx 0.2$).

Considering all three planes in the full-scale facility a flow pattern was observed consisting of downward from the top of the tube bank at the western end of the vessel, then horizontally in the eastern direction along the base of the tube bank before being directed upward near the east/west centre of the vessel. For the small-scale facility similar behaviour was observed for $Ar \approx 0.01$. For the $Ar \approx 0.1$ case at the western end of the vessel, flow was observed to turn around more sharply and become upward over a shorter distance upon reaching the base of the tube bank.

These observations suggest that for comparable *Ar* between the small-scale and full-scale facilities, the small-scale facility showed a larger 'hot-spot' located in the upper-eastern end of the vessel and increased upward flow at the base of the tube bank in the western end of the vessel. Based on the earlier examination of the impacts of increasing *Ar* in section 5.4.1, this could suggest that for similar *Ar* numbers, buoyancy effects were more significant in the small-scale facility compared to the full-scale facility in the selected planes.

This increased buoyancy significance could have resulted from both the use of surface heating in the small-scale facility. The buoyancy term in *Ar* is determined from the temperature rise between the vessel inlets and outlets which depends only on the total amount of applied heat in the vessel. As discussed in section 2.2.3, the impact of using surface heating versus volumetric heating have previously been investigated by Sarchami *et al.* and was shown to cause increased buoyancy effects caused by higher temperature gradients from higher tube wall temperatures [39].

Changes in the tube bank design for the small-scale facility would have had an additional impact on local buoyancy forces. For practical reasons, the total number of elements in the tube bank was changed from 480 for the full-scale case to 120 in the small-scale case, with the central 52 elements being heated. This caused a reduction in total tube bank surface area which would result in higher local surface heat fluxes, exacerbating the issue discussed by Sarchami. This led to higher surface temperatures within the heated region of the tube bank, resulting in greater buoyancy effects. Nevertheless, the temperature fields showed remarkably similar patterns in the small-scale and full-scale results, albeit at different values of *Ar*.

5.6 Summary

Time-averaged temperature measurements were presented for a range of inlet flow and power conditions and compared to predicted values from the simulations. Higher temperatures were observed in the eastern regions of the tube bank (toward $z = 0$ mm, where inertial flows were upward) compared to the western regions of the tube bank (toward $z = 500$ mm, where inertial flows were downward). This behaviour was predicted qualitatively correct in the simulations, although the model tended to overpredict the temperatures by up to 4 ºC, especially in the eastern regions of the test section.

Time-averaged velocity measurements were compared to predicted velocities from the simulations within the eastern tube bank region at $x = 0$ mm. Inertial flows in

this region were upward and assisted by buoyancy induced flows. The vertical velocity components entering the heated region of the tube bank were shown to be underpredicted by about 30%, regardless of *Ar*. This underprediction of velocities was linked to the overprediction of temperatures in the heated region of the tube bank, since the underpredicted velocities would result in an underprediction of the convective heat transfer from the heaters. As buoyancy effects became more significant in determining the local velocities (i.e. – for conditions at higher *Ar* and at higher elevations in the heated region of the tube bank), the agreement between the measured and predicted velocities improved.

Large temperature fluctuations that were observed within the vessel were investigated in several locations and resulted from the unsteady, three-dimensional flow in the test section. Fluctuations observed near the upper western end of the vessel were found to be related to the unstable interaction between cool downward flow from the inlet jets and upward buoyant flow from the heaters, with cooler temperatures associated with faster, downward flow and warmer temperatures associated with slower, upward flow. Fluctuations near the edge of the heated regions of the tube bank were associated with side-to-side flow direction fluctuations. In the buoyancy dominated regions of the vessel, flow direction was relatively consistent in the upward direction. Temperature fluctuations were smaller in magnitude and depended more on flow speed changes rather than directional changes.

The simulated maximum instantaneous temperatures within the test section were compared to the experimental measurements across all tested conditions. The simulations were found to overpredict the maximum instantaneous temperatures under all conditions by approximately 0.5 – 3.8 ºC. The degree of overprediction was found to decrease with *Ar*; for cases where buoyancy was more significant, the predicted maximum temperature was closer to the experimental result. This improvement in peak temperature prediction with *Ar* was attributed to the increased

relative importance of buoyancy, which was previously shown to improve the model's prediction of local velocities in a similar region of the tube bank. In the context of nuclear safety analysis, this over-prediction of the peak temperature would result in a conservative estimate of the available subcooling in the moderator.

Using simulation data, the maximum instantaneous temperatures for each case within regions accessible by the thermocouples were compared to the entire fluid volume in order to evaluate the effectiveness of the selected locations at capturing the peak temperature within the test section. Peak temperatures in the thermocouple regions was found to correspond to the peak temperatures elsewhere in the vessel within 1.5 ºC.

The impact of increasing *Ar* on the temperature distribution within the vessel was investigated. A large east-west recirculation pattern resulting from the asymmetric arrangement of the inlets was identified. This recirculation pattern was observed to be shifted upward and toward the western end of the vessel as *Ar* was increased. The flow patterns within the moderator did not appear highly sensitive to small changes in *Ar* (over a range of $0.003 < Ar < 0.01$).

Two test cases performed at comparable *Ar* numbers of 0.01 but with different heater powers and flow rates were compared. The time-averaged excess temperature measurements agreed within measurement uncertainty at most locations within the vessel. Differences were noted in the upper western region of the vessel where downward inlet flows opposed rising buoyant flows. Measured temperatures in these regions were higher for the low flow rate case, suggesting that the inlet jets were not penetrating as far into the tube bank. This difference was attributed to differences in the Reynolds number at the exit of the inlets for the two cases, with the centerline velocity for inlet jets in the lower flow decaying over a shorter distance resulting in lower flow inertia entering the tube bank.

Simulated average temperature contours and flow fields within the heated region of the small-scale facility at $Ar \approx 0.01$ and 0.1 were compared to simulations of the full-scale Bruce A facility at $Ar \approx 0.2$. Despite differences in scale, the temperature distributions and flow patterns appeared qualitatively similar between the small and large-scale facilities. The small-scale facility behaviour at $Ar \approx 0.01$ appeared to more closely match the full-scale facility, suggesting that buoyancy effects were more significant in the small-scale facility. This difference in behaviour was attributed to the use of surface heating (as opposed to volumetric heating) and higher surface heat fluxes caused by the reduced number of tube elements and heating only the central tubes.

Chapter 6

Concluding Remarks

6.1 Summary

An important safety feature of a CANDU PHWR reactor is the ability of the moderator to act as an emergency heat sink following postulated loss of coolant accidents, provided that the moderator is sufficiently subcooled. Safety analyses to determine the local available subcooling in the moderator typically rely on computational tools which require benchmarking against experimental data to ensure that the key physical phenomena are adequately reproduced. Small-scale experimental facilities designed to match the Archimedes number (Ar) – representing the ratio of buoyancy forces to inertial forces – and the dimensionless heat source (q^*) to the full-size reactor are typically deployed for this purpose.

The Bruce A CANDU units utilize a moderator inlet and outlet configuration which differs from the typical CANDU designs. As a result, a new small-scale experimental facility was designed and constructed in order to obtain experimental temperature and velocity data representative of the Bruce A moderator under normal operating conditions. Goals of the study included the assessment of the unique moderator inlet configuration in Bruce A on the flow patterns inside the calandria vessel and how well existing CFD modelling approaches can replicate these features. In addition, this study aimed to analyze this data further to assess the

importance of scaling between this facility and the full-scale reactors. This included examination of issues arising from geometric simplifications as well as issues that arose from a large difference in scale between the model and the facility.

A new test facility with features representative of the Bruce A calandria vessel was designed and constructed for this work. The facility was approximately 1/16 scale and featured 120 horizonal tubes arranged in the same pitch-to-diameter ratio as the full-scale calandria vessel. The central 52 tubes were heated and featured a representative cosine axial power profile while the remaining tubes were unheated. Flow entered the top of the vessel from 22 inlet nozzles of similar geometry and positioning to the full-scale calandria vessel. Tests were performed over a range of $0 < Ar < 0.1$, with inlet flow rates ranging from 8 – 30 L/min and electrical power ranging from 0 – 38 kW. Temperatures within the tube bank were mapped using thermocouples and velocities were measured using a 3D LDV measurement probe.

Unsteady RANS simulations of the small-scale facility were performed in STAR-CCM+ using the realizable k-ε model with all y+ wall treatment for conditions corresponding to the experimental cases. Averaged and time-dependent measurements from the experiments were compared to the numerical results in order to assess the selected modelling approach. The ability of the numerical model to predict the maximum temperature in the facility was assessed. Unsteady temperature behaviour observed in the experiments was further explored by studying the time-dependent temperature and velocity fields from the simulations. Predicted flow fields and temperatures from simulations of the small-scale facility were also compared to existing simulations of the full-scale Bruce A calandria vessel.

Time-averaged temperature and velocity measurements, and time-dependent temperature measurements were generated for a wide range of test conditions as part of this study. While the specific geometry in the small-scale model differs from a typical CANDU calandria vessel, it replicated several phenomena common to

both, including three-dimensional flow through a tube bank, interaction of inlet jets with a tube bank at a variety of angles, and the interaction of cool inlet jets with buoyant flows in the tube bank leading to unsteady features. Therefore, the experimental measurements included in this thesis provide valuable benchmark data which can be used in future numerical studies of CANDU moderator flows.

6.2 Conclusions

- The Archimedes number – which is calculated using global parameters such as the vessel diameter, inlet velocity, and thermal power – is a useful parameter in describing the relative importance of inlet inertia and buoyancy effects in a calandria-like vessel at a fixed geometric scale, with some limitations.
    - Within the small-scale facility, normalized excess temperature measurements corresponded well at most locations in the vessel across experiments performed at different power and flow conditions yielding $Ar = 0.01$.
    - For the low flow case, temperatures were higher in regions where inlet jet penetration into the tube bank was an important factor in determining local temperatures. This difference was attributed to inlet jet dissipation over a shorter distance due to the lower inlet jet *Re* – an effect not captured by *Ar*.
- Large differences in scale between full-size CANDU calandria vessels and small-scale test facilities can lead to scaling issues not captured by the current strategy of maintaining *Ar* and q^*_{av}.
    - The use of surface-heating in small-scale experiments distorts the local heat distribution in the vessel. Further geometric simplifications – such as reducing the number of heated tube elements – can impact the local importance of buoyancy effects due

to higher local heat fluxes at the same power levels. This effect is not captured by q^*_{av}.

- The prescribed scaling procedure results in reduced inlet *Re* at smaller scales. Depending on the power level, maintaining *Ar* at 1/16 scale can result in low inlet *Re* (*Re* < 10 000) which impacts the dissipation of the inlet jets in the region above the tube bank. This can impact the relative importance of inlet jet inertia within the tube bank, an effect not captured by *Ar*.

- Despite a large difference in scale and geometric simplifications, the observed behaviours in the small-scale facility appeared qualitatively similar to the full-size Bruce A reactor, albeit at lower *Ar* conditions.
  - Simulated flow fields and temperature results from the small-scale facility at a range of conditions (*Ar* ≈ 0.003, 0.007, 0.01, and 0.1) were compared to simulations of the full-scale Bruce A calandria (*Ar* ≈ 0.2).
  - The small-scale facility behaviour within the heated region of the tube bank at *Ar* ≈ 0.01 appeared to most closely match the full-scale facility, suggesting that buoyancy effects were more significant in the small-scale facility. This behaviour was attributed to the use of surface heating (as opposed to volumetric heating) and higher surface heat fluxes caused by the reduced number of tube elements and heating only the central tubes.
- For the Bruce A inlet arrangement, the observed flow patterns and temperature distributions did not appear highly sensitive to changes in *Ar*.
  - For all tested conditions (0.001 < *Ar* < 0.1), a large east-west recirculation pattern resulted from the asymmetric inlet arrangement. This recirculation pattern was observed to be shifted upward and toward the rear of the vessel as *Ar* was increased. The

flow patterns within the moderator did not appear highly sensitive to small changes in Ar (over a range of $0.003 < Ar < 0.01$).

- Under steady-state conditions, flows within the small-scale facility are unsteady and three-dimensional.
    - Fluctuations observed near the upper western end of the vessel were found to be related to the unstable interaction between cool downward flow from the inlet jets and upward buoyant flow from the heaters.
    - Fluctuations near the edge of the heated regions of the tube bank were associated with side-to-side flow direction changes.
    - In the eastern regions of the vessel, flow direction was relatively consistent in the upward direction. Temperature fluctuations were smaller in magnitude and depended more on flow speed changes rather than directional changes.
- Peak temperatures consistently occurred in the eastern regions of the vessel within or directly above the heated regions, where inertial flows are assisted by buoyancy induced flows.
- The selected modelling approach using the realizable k-ε turbulence model tended to overpredict the maximum temperatures within the tube bank region. Agreement between the predicted and measured maximum temperatures improved with increasing Ar.
    - For all tested conditions ($0.001 < Ar < 0.1$), the simulations were found to overpredict the maximum instantaneous temperatures by approximately 0.5 – 3.8 ºC.
    - Comparisons of the measured and simulated velocities in similar tube bank regions showed that the model consistently underpredicted the velocities entering the heated region of the tube bank by approximately 30%. This underprediction of velocities was attributed to issues with the selected turbulence model tending to

overpredict the dispersion of the inlet jets in the region above the tube bank. An underprediction of local velocities in the heated tube bank region was linked to the overprediction of local temperatures.

- As *Ar* increased and buoyancy effects became more significant in determining the local velocities, the predicted and measured velocities agreed more closely.
- In the context of nuclear safety analysis, this over-prediction of the peak temperature would result in a conservative estimate of the available subcooling in the moderator.

6.3 Future Work

6.3.1 Future Modelling Work

- Improve the specified inlet boundary conditions to more closely match experimental conditions.
  - Currently, the inlet mass flow is assumed to be split evenly within each group of inlet nozzles. An experimental investigation of the flow split along the inlet headers used for the facility has since been reported by Hollingshead [61], which showed variations along the header length (± 2%). The actual flow split from each header could be used to improve the fidelity of the numerical model.
- Perform simulations with all tube elements heated and compare to the current simulation results.
  - Heating all tube bank elements may improve the similarity between the small-scale facility and the Bruce A reactor at the same *Ar*. For a given power level, heating all 120 tube bank elements as opposed to the central 52 heaters would result in lower local heat fluxes. It is expected that this would reduce the local relative importance of buoyancy effects without changing *Ar*. Additionally, due to the outer tube bank elements being unheated, it is expected that flow

from the outermost inlet nozzles in the *x*-direction penetrated the tube bank further in the small-scale facility compared to the Bruce A calandria.

- Investigate the sensitivity of velocities in the tube bank to the selected turbulence model.
    - The existing simulations tended to underpredict the velocities in the recirculation pattern entering the eastern regions of the tube bank, which caused the overprediction of temperatures in this region. It was thought that this was due in part to the realizable k-ε model overpredicting the dispersion of the inlet jets in the region above the tube bank, leading to reduced inertial flow velocities in the tube bank. Such observations are consistent with literature. Isothermal simulations could be performed with different turbulence models and compared to the isothermal LDV results to study if these predictions can be improved.
- Refine the mesh in the western regions of the vessel where large temperature gradients were observed.
    - In the grid-size sensitivity study presented in section 4.2.2, it appeared that the results in these regions were most sensitive to grid size. These regions also corresponded to large temperature and velocity fluctuations; if these fluctuations are to be investigated further it important to ensure mesh independence in this region.
- Investigate the impact of outlet position on the three-dimensional flow field within the calandria.
    - The outlets in the small-scale model were offset from the centre toward the western end of the vessel, as shown Figure 3-5, configured similarly to the full-scale Bruce A calandria vessel. The impacts of this outlet position (compared to a central location, or an eastern end offset location) were not included in this study.

6.3.2 Future Experimental Work

- Perform additional experiments at a wider range of power and flow conditions corresponding to a fixed *Ar*.
    - Two experimental cases were performed for *Ar* = 0.01 at high and low flow rate conditions. Differences between these two cases were observed that were attributed to lower inlet jet penetration into the tube bank at low flow rates. This behaviour could be studied over a wider range of flow conditions to confirm this hypothesis.
- Provide additional thermocouple measurement positions within the test section.
    - The simulations of the small-scale facility indicated high temperature gradients in the western regions of the test section associated with large temperature fluctuations in time. Additional thermocouple positions at a finer *z* spacing and at additional elevations (e.g. – above position TCM1-04) would allow more detailed study of this region.
    - No temperature measurements were possible in the regions above the tube bank. Temperature measurements in this region could provide further insight into the interaction of warm buoyant flows from the tube bank and cool downward flows from the inlet jets, and how the inlet jets dissipate in this region where velocity measurements were not possible.
- Investigate methods to improve the fidelity and depth of the velocity measurements.
    - Velocity measurements in the western regions of the vessel would provide additional insight into the unsteady interactions observed in these regions in the simulations. Measurements were only made in the eastern regions of the vessel due to visual obstructions caused by the electrical connections to the heaters. Measurements in the

western regions would be possible provided that the heaters were installed in the opposite orientation.

  - Methods such as particle image velocimetry (PIV) allow for the collection of instantaneous 2D velocity fields. This method also provides additional challenges such as requiring optical access in additional planes and difficulties in obtaining measurements in shadow regions. A novel method for internally generating the PIV light sheet in a tube bank element was employed in the KAERI MCT [28] [29]; the feasibility of a using a similar method in the current small-scale facility could be investigated.

- Collect temperature measurements for longer durations at select locations within the test section.
  - Temperature measurements in the small-scale facility were collected over a 5-minute period. For CANDU-6 geometries, Mehdi Zadeh *et al*. [36] noted unsteady temperature behaviour occurring over time scales on the order of hours. While it was not feasible to perform measurements at each selected location in the tube bank for this length of time, longer duration temperature measurements could be performed at a selected few locations where interesting temperature fluctuations were observed.

References

[1] G. Bereznai, "Reactor and Moderator," in *Nuclear Power Plant Systems and Operation: Reference Text*, Hamilton, McMaster University, 2005.

[2] J. T. Rogers, "CANDU Moderator Provides Ultimate Heat Sink in LOCA," *Nuclear Engineering International*, vol. 24, no. 208, pp. 38-41, 1979.

[3] G. E. Gillespie, "An Experimental Investigation of Heat Transfer From a Reactor Fuel Channel to Surrounding Water," in *Proceedings of the 2nd Annual Conference of the Canadian Nuclear Society*, Ottawa, 1981.

[4] G. E. Gillespie, R. G. Moyer and P. D. Thompson, "Moderator Boiling on the External Surface of a Calandria Tube in a CANDU Reactor During a Loss-of-Coolant Accident," in *Proceedings of the International Meeting on Thermal Nuclear Reactor Safety*, Chicago, 1982.

[5] G. E. Gillespie, R. G. Moyer and G. I. Hadaller, "An Experimental Investigation of the Creep Sag of Pressure Tubes Under LOCA Conditions," in *Proceedings of the 5th Annual Conference of the Canadian Nuclear Society*, Saskatoon, 1984.

[6] G. E. Gillespie, R. G. Moyer, G. I. Hadaller and J. G. Hildebrandt, "An Experimental Investigation into the Development of Pressure Tube/Calandria Tube Contact and Associated Heat Transfer Under LOCA Conditions," in *Proceedings of the 6th Annual Conference of the Canadian Nuclear Society*, Ottawa, 1985.

[7] H. Z. Fan, R. Aboud, P. Neal and T. Nitheanandan, "Enhancement of the Moderator Subcooling Margin Using Glass-Peened Calandria Tubes in

CANDU Reactors," in *Proceedings of the 30th Annual Conference of the Canadian Nuclear Society*, Calgary, 2009.

[8] T. K. De, W. M. Collins and R. W. Holmes, "Prediction of CANDU-6 Moderator System Response Following a Large Break LOCA Using a 3D Model," in *Proceedings of the 16th Annual Conference of the Canadian Nuclear Society*, Saskatoon, 1995.

[9] G. Austman, J. Szymanski, M. Garceau and W. I. Midvidy, "Measuring Moderator Temperatures in a CANDU Reactor," in *Proceedings of the 6th Annual Conference of the Canadian Nuclear Society*, Ottawa, 1985.

[10] N. Sion, "In-Core Moderator Temperature Measurement Within CANDU Reactors," *Nuclear Instruments and Methods*, vol. 206, pp. 527-536, 1983.

[11] H. F. Khartabil, W. W. R. Inch, J. Szymanski, D. R. Novog, V. Tavasoli and J. Mackinnon, "Three-Dimensional Moderator Circulation Experimental Program for Validation of CFD Code MODTURC_CLAS," in *Proceedings of the 21st CNS Nuclear Simulation Symposium*, Ottawa, 2000.

[12] Canadian Nuclear Safety Commission, "4.4.5: Computer Codes," 2014. [Online]. Available: http://nuclearsafety.gc.ca/eng/acts-and-regulations/regulatory-documents/published/html/regdoc2-4-1/.

[13] L. N. Carlucci, V. Agranat, G. M. Waddington, H. F. Khartabil and J. Zhang, "Validation of the MODTURC_CLAS Moderator Circulation Code for CANDU 9 Steady-State and Transient Conditions," in *Proceedings of the 21st CNS Nuclear Simulation Symposium*, Ottawa, 2000.

[14] M. Vuong, J. Szymanski and B. Bowman, "GAI 95G05 - Moderator Temperature Predictions: Validation Exercise for MODTURC_CLAS V2.9-IST Using Data from In-Reactor Moderator Temperature Measurments in Bruce Unit 3," NSS Limited, Toronto, 2003.

[15] D. Koroyannakis, R. D. Hepworth and G. Hendrie, "An Experimental Study of Combined Natural and Forced Convection Flow in a Cylindrical Tank," AECL, 1983.

[16] C. Yoon, B. W. Rhee and B. J. Min, "Validation of a CFD Analysis Model for Predicting CANDU-6 Moderator Temperature Against SPEL Experiments," in *Proceedings of the 10th International Conference on Nuclear Engineering*, Arlington, 2002.

[17] M. S. Quraishi, "Experimental verification of 2DMOTH computer code temperature predictions," AECL, 1985.

[18] W. M. Collins, "Simulation of the SPEL Small Scale Moderator Experiments Using the General Purpose Fluid-Flow, Heat Transfer Code PHOENIX," AECL, 1988.

[19] M. Kim, S. O. Yu and H. J. Kim, "Analyses on Fluid Flow and Heat Transfer Inside Calandria Vessel of CANDU-6 Using CFD," *Nuclear Engineering and Design,* vol. 236, pp. 1155-1164, 2006.

[20] A. K. Kansal, J. B. Joshi, N. K. Maheshwari and P. K. Vijayan, "CFD Analysis of Moderator Flow and Temperature Fields Inside a Vertical Calandria Vessel of Nuclear Reactor," *Nuclear Engineering and Design,* vol. 287, pp. 95-107, 2015.

[21] R. G. Huget, J. K. Szymanski and W. I. Midvidy, "Status of Physical and Numerical Modelling of CANDU Moderator Circulation," in *Proceedings of the 10th Annual Conference of the Canadian Nuclear Society*, Ottawa, 1989.

[22] R. G. Huget, J. K. Szymanski, P. F. Galpin and W. I. Midvidy, "MODTURC-CLAS: An Efficient Code for Analyses of Moderator Circulation in CANDU Reactors," in *Proceedings of the Third International Conference on Simulation Methods in Nuclear Engineering*, Montreal, 1990.

[23] H. T. Kim and B. W. Rhee, "Scaled-Down Moderator Circulation Test Facility at Korea Atomic Energy Research Institute," *Science and Technology of Nuclear Installations,* vol. 2016, 2016.

[24] B. W. Rhee, H. T. Kim, S. K. Park, J. E. Cha and H. L. Choi, "A Scaling Analysis of a CANDU-6 Moderator Tank Scaled-Down Test Facility," in *Proceedings of the 2013 21st International Conference on Nuclear Engineering*, Chengdu, 2013.

[25] H. T. Kim, S. H. Im, H. J. Sung, H. Seo and I. C. Bang, "Preliminary Test Results and CFD Analysis for Moderator Circulation Test at Korea," in *Proceedings of the 19th Pacific Basin Nuclear Conference*, Vancouver, 2014.

[26] H. T. Kim, J. E. Cha, H. Seo and I. C. Bang, "Measurement of Velocity and Temperature Profiles in the 1/40 Scaled-Down CANDU-6 Moderator Tank,"

Science and Technology of Nuclear Installations, vol. 2015, p. 439863, 2015.

[27] S. Im, H. T. Kim, B. W. Rhee and H. J. Sung, "PIV Measurements of the Flow Patterns in a CANDU-6 Model," *Annals of Nuclear Energy,* vol. 98, pp. 1-11, 2016.

[28] B. W. Rhee, H. T. Kim, M. D. Atkins and T. Kim, "Validation Test Plan of a CANDU-6 Moderator Tank Scanled-Down Test Facility," in *Proeedings of NURETH-16,* Chicago, 2015.

[29] M. D. Atkins and T. Kim, "Isotropic-Planar Illumination for PIV Experiments," *Experiments in Fluids,* vol. 56, no. 3, p. 63, 2015.

[30] M. D. Atkins, D. J. Rossouw, M. Boer, T. Kim, B. W. Rhee and H. T. Kim, "Mixed Convection Around Calandria Tubes in a 1/4 Scale CANDU-6 Moderator Circulation Tank," *Nuclear Engineering and Design,* vol. 316, pp. 151-162, 2017.

[31] H. T. Kim, B. W. Rhee, S. Im, H. J. Sung, M. D. Atkins, D. J. Rossouw and T. Kim, "The Isothermal-Fluidic Field of a Secondary Moderator Jet in a 1/4 Scale CANDU-6 Model," *Nuclear Engineering and Design,* vol. 323, pp. 394-406, 2017.

[32] G. I. Hadaller, R. A. Fortman, J. Szymanski, W. I. Midvidy and D. J. Train, "Frictional Pressure Drop in Aligned and Staggered Tube Banks with Large Pitch to Diameter Ratio," in *Proceedings of the 17th Annual Nuclear Simulation Symposium*, Kingston, 1992.

[33] G. Austman, J. Szymanski and W. I. Midvidy, "MODCIR: A Three-Dimensional Transient Code Used In Thermal-Hydrauic Analyses of CANDU Power Reactors," *Mathematics and Computers in Simulation,* vol. XXV, pp. 493-496, 1983.

[34] Robin Williams Davies & Irwin Inc., "A Review of Computer Codes MODTURC_CLAS and PHOENICS," Atomic Energy Control Board, Ottawa, 1996.

[35] L. N. Carlucci and I. Cheung, "The Effects of Symmetric/Asymmetic Boundary Conditions on the Flow of an Internally Heated Fluid," *Numerical Methods for Partial Differential Equations,* vol. 2, pp. 47-61, 1986.

[36] F. Mehdi Zadeh, S. Étienne and A. Teyssedou, "2-D CFD Time-Dependent Thermal-Hydraulic Simulations of CANDU-6 Moderator Flows," *Nuclear Engineering and Design,* vol. 309, pp. 122-135, 2016.

[37] A. Sarchami, N. Ashgriz and M. Kwee, "Three Dimensional Numerical Simulation of a Full Scale CANDU Reactor Moderator to Study Temperature Fluctuations," *Nuclear Engineering and Design,* vol. 266, pp. 148-154, 2014.

[38] A. Sarchami, N. Ashgriz and M. Kwee, "Temperature Fluctuations Inside the CANDU Reactor Moderator Test Facility," *Annals of Nuclear Engineering,* vol. 60, pp. 157-162, 2013.

[39] A. Sarchami, N. Ashgriz and M. Kwee, "Comparison Between Surface Heating and Volumetric Heating Methods inside CANDU Reactor Moderator Test Facility (MTF) Using 3D Numerical Simulation," *International Journal of Nuclear Energy Science and Engineering,* vol. 3, no. 2, pp. 15-21, 2013.

[40] A. Sarchami, "Investigation of Thermal Hydraulics of a Nuclear Reactor Moderator," PhD Thesis, University of Toronto, 2011.

[41] H. Seo, H. T. Kim, J. E. Cha and I. C. Bang, "Measurements and Visualization of Velocity Profiles in a Scaled CANDU6 Moderator Tank Using Particle Image Velocimetry," *Annals of Nuclear Energy,* vol. 73, pp. 361-372, 2014.

[42] A. Teyssedou, R. Necciari, M. Reggio, F. Mehdi Zadeh and S. Étienne, "Moderator Flow Simulation Around Calandria Tubes of CANDU-6 Nuclear Reactors," *Engineering Applications of Computational Fluid Mechanics,* vol. 8, no. 1, pp. 178-192, 2014.

[43] H. T. Kim, S. M. Chang, J. H. Shin and Y. G. Kim, "The Feasibility of Multidimensional CFD Applied to the Calandria System in the Moderator of CANDU-6 PHWR Using Commercial and Open-Source Codes," *Science and Technology of Nuclear Engineering,* vol. 2016, p. 3194839, 2016.

[44] N. Ashgriz and M. Behzad, "Numerical Simulations of Bruce A and Pickering A Moderator Flows," CANDU Owners Group, June 2016.

[45] B. W. Rhee and H. T. Kim, "A Review of the Scaling Study of the CANDU-6 Moderator Circulation Test Facility," *Journal of Power and Energy Engineering,* vol. 2014, no. 2, pp. 64-73, 2014.

[46] A. A. Abdel-Rahman, S. F. Al-Fahed and W. Chakroun, "The Near-Field Characteristics of Circular Jets at Low Reynolds Numbers," *Mechanics Research Communications,* vol. 23, no. 3, pp. 313-324, 1996.

[47] F. Mehdi Zadeh, S. Étienne, R. Chambon, G. Marleau and A. Teyssedou, "Effect of 3-D Moderator Flow Configurations on the Reactivity of CANDU Nuclear Reactors," *Annals of Nuclear Energy,* vol. 99, pp. 136-150, 2017.

[48] Stern Laboratories Inc., *Technical Specification SLTS-88,* Hamilton, 2015.

[49] Alicat Scientific, "Alicat Liquid Flow Controller Specifications," [Online]. Available: http://www.alicat.com/documents/specifications/Alicat_Liquid_Controller_Specs.pdf. [Accessed 26 May 2015].

[50] Omega Engineering, "Wire Color Codes and Limits of Error," [Online]. Available: https://www.omega.ca/techref/colorcodes.html. [Accessed 12 February 2018].

[51] Omega Engineering, "Thermocouple Response Time," [Online]. Available: https://www.omega.com/techref/ThermocoupleResponseTime.html. [Accessed 12 February 2018].

[52] Omega Engineering, "Precision RTD Thermometer," [Online]. Available: http://www.omega.com/Temperature/pdf/DP250.pdf. [Accessed 8 January 2013].

[53] Regatron AG, "TC.P.32.100.480.S datasheet," [Online]. Available: https://www.regatron.com/en/products-topcon/topcon-quadro-tc-p/technical-datasheets. [Accessed 11 February 2018].

[54] Watanabe Electric Industry Co., Ltd., "WAP-DS/DZ specifications," [Online]. Available: https://www.watanabe-electric.co.jp/product/document/documentCode/28893/. [Accessed 11 February 2018].

[55] National Instruments, "Analog Input Modules," [Online]. Available: http://sine.ni.com/nips/cds/view/p/lang/en/nid/208784. [Accessed 26 May 2015].

[56] TSI Inc., *Model TR360 5-Beam Fiberoptic Probe,* Revision B ed., 2010.

[57] P. R. Bevington and D. K. Robinson, Data Reduction and Error Analysis, 3rd edition ed., New York: McGraw-Hill, 2003.

[58] J. Strack, A. Rashkovan and D. Novog, "Test Facility for the Measurement and Modelling of CANDU Reactor Moderator Flow and Temperature Distributions," in *Proceedings of NURETH-17,* Xi'an, 2017.

[59] T. Shih, W. W. Liou, A. Shabbir, Z. Yang and J. Zhu, "A New k-ε Eddy Viscosity Model for High Reynolds Number Turbulent Flows," *Computers & Fluids,* vol. 24, no. 3, pp. 227-238, 1995.

[60] CD-adapco, "Using Wall Treatment Models," in *STAR-CCM+ User Guide,* 2017.

[61] C. W. Hollingshead, "Characterization of the Inlet Flow Conditions for the Moderator Test Facility," MASc Thesis, McMaster University, 2017.

[62] P. J. Roache, "Perspective: A Method for Uniform Reporting of Grid Refinement Studies," *Journal of Fluids Engineering,* vol. 116, pp. 405-413, 1994.

[63] J. W. Slater, "Estimating Spatial (Grid) Convergence," 17 July 2008. [Online]. Available: https://www.grc.nasa.gov/www/wind/valid/tutorial/spatconv.html.

[64] B. E. Launder and D. B. Spalding, "The Numerical Computation of Turbulent Flows," *Computer Methods in Applied Mechanics and Engineering,* vol. 3, pp. 269-289, 1974.

[65] S. B. Pope, "An Explanation of the Turbulent Round-Jet/Plane-Jet Anomaly," *AIAA Journal,* vol. 16, no. 3, pp. 279-281, 1978.

[66] L. Ishay, "Mixing Effects in Fluid Flows with Buoyancy and Stratification," PhD Thesis, Ben-Gurion University, 2017.

[67] C. C. Pérez, C. V. Barreto, G. Lopes, J. N. E. Carneiro, J. K. Abrantes, J. M. Barros and A. O. Nieckele, "Evaluation of Different Turbulence Models to

Predict a Turbulent Free Jet," in *Proceedings of the 18th International Congress of Mechanical Engineering*, Ouro Preto, 2005.

[68] M. Holmgren, "X Steam, Thermodynamic properties of water and steam," 1 August 2007. [Online]. Available: https://www.mathworks.com/matlabcentral/fileexchange/9817-x-steam--thermodynamic-properties-of-water-and-steam. [Accessed 1 February 2018].

[69] IAPWS, "Revised Release on the IAPWS Industrial Formulation 1997 for the Thermodynamic Properties of Water and Steam," August 2007. [Online]. Available: http://www.iapws.org/relguide/IF97-Rev.pdf. [Accessed 28 February 2018].

[70] A. H. Harvey, J. S. Gallagher and J. M. H. Levelt Sengers, "Revised Formulation for the Refractive Index of Water and Steam as a Function of Wavelength, Temperature and Density," *Journal of Physical and Chemical Reference Data,* vol. 27, no. 4, 1998.

[71] S. Kang, B. Patil and R. P. Roy, "Effects of coincidence window and measuring volume size on laser Doppler velocimetry measurement of turbulence," *Experiments in Fluids,* vol. 30, no. 4, pp. 365-370, 2001.

[72] A. Sarchami, N. Ashgriz and M. Kwee, "Effect of Scaling on the Thermalhydraulics of the Moderator of a CANDU Reactor," in *Proceedings of the International Conference on Mathematics and Computational Methods Applied to Nuclear Science and Engineering*, Rio de Janeiro, 2011.

[73] B. W. Rhee, H. T. Kim and Y. M. Song, "Reconsideration of a Scaling Study of CANDU-6 Moderator Tank Scaled-Down Test Facility," in *Proceedings of the 2014 22nd International Conference on Nuclear Engineering*, Prague, 2014.

[74] C. Yoon, B. W. Rhee and B. J. Min, "3-D CFD Analysis of the CANDU-6 Moderator Circulation Under Normal Operating Conditions," *Journal of the Korean Nuclear Society,* vol. 36, no. 6, pp. 559-570, 2004.

[75] L. N. Carlucci, "Numerical Simulation of Moderator Flow and Temperature Distributions in a CANDU Reactor Vessel," in *Proceedings of the International Symposium on Refined Modelling of Flows*, Paris, 1982.

Appendix A

Standard Operating Procedures

This procedure describes the process for collecting velocity and temperature measurements with the 'Bruce A' test vessel. This procedure consists of several sub-steps to be completed in the listed order in this appendix.

A.1 Safety Considerations

A.1.1 Flow Loop Safety Considerations

- Hearing protection is recommended while pumps are operating.
- The flow loop is constructed of PVC pipe rated for a maximum temperature of 60ºC. Do not allow the temperature to exceed 60ºC at the inlet or outlet of the test section.
- Do not allow foreign objects to be placed near the drains of the holding tank. Damage to the pumps may occur.

A.1.2 Laser Safety Considerations

- Laser safety googles are recommended for any operations where the total laser optical power exceeds 100 mW. Goggles are mandatory for operations where total laser optical power exceeds 150 mW. Required: Optical Density (OD) 5 or better at 476.5 – 514.5 nm.

- Never look directly into the laser beam. Only view the laser beam from an angle and in the direction that the beam is travelling.
- All windows in the room must be blacked out.
- Use the laser in a closed room and only with people who have been instructed in laser safety.

A.1.3 Power Supply Safety Considerations

- A high voltage and high current DC power supply is used in this experiment. Electrical connections must be inspected daily to ensure that all terminals are properly insulated to prevent accidental human contact and electrical shorting between heaters.
- The power supply is equipped with an emergency shutdown system which can be actuated by one of three actions. Any one switch will prevent the power supply from operating (i.e. – all three must be in a 'safe' state for the experiment to be performed). The three switches are:
    - Emergency stop button on power supply front panel
    - Emergency stop button located near the laser head
    - Emergency stop relay operated through LabVIEW (in 'shutdown' state before the LabVIEW panel is started)

A.2 Responsibilities

For all tests, the operator is responsible for ensuring that:

- Hearing protection is available for each person in the room while the process pumps are operating.
- For tests involving velocity measurements, the operator is responsible for ensuring that:
    - One pair of laser safety goggles is available for each person in the room.

  - Each person in the room has been instructed in laser safety.
  - Adequate signage is placed at the entryway of the room to indicate that the laser is in use.
- For tests involving electrical heating of the test section, the operator is responsible for ensuring that:
  - All occupants of the room are aware of the emergency power supply shutdown procedures.
  - All electrical terminals and connections are securely fastened.
  - All electrical wiring and terminals are enclosed to prevent accidental human contact.

A.3 Procedure

A.3.1 Primary Flow Loop Startup Procedure

1. Power up the instrumentation and measurement systems:
   a. Magnetic flow meters
   b. Data acquisition hardware
   c. 24 V loop power supply (flow controllers and current loop transmitters)
2. Load the LabVIEW interface for the primary flow loop ('TSAR_BruceA_Loop_v9.vi'). In the 'Settings' tab, ensure that the data acquisition channels and serial port set to the corresponding hardware locations and begin logging data to a temporary file.
3. Ensure that all six (6) Alicat flow controllers are powered on and each have a flow rate setting of 0.000 LPM (litres per minute).
4. Ensure that holding tank is at least 75% full. This water level is marked in red on the outside of the tank.
5. Locate the two (2) test section isolation valves and set them to the 'OPEN' position:
   a. Valve located at the discharge of the primary pump.

   b. Valve located behind the test vessel on the flow return line.
6. Ensure that each of the six (6) valves downstream of the flow controllers is 'CLOSED'.
7. Engage the power supply to the pump drive by unlocking and turning the safety switch to the 'ON' position.
8. Turn the primary flow pump on by turning the switch for 'PUMP B' to 'ON' using the remote-control panel. Adjust the drive frequency such that the pressure reading on the flow controllers is 100 kPa.
   a. All six flow controllers should read approximately the same pressure. The pressure readings can be monitored in the LabVIEW interface under the 'Settings' tab.
9. Set all six (6) flow controllers to 5.000 LPM using the LabVIEW interface.
10. Open the valves downstream of each flow controller, one at a time. Allow the flow rate for the flow controller to stabilize and reach the set-point before opening the valve downstream of the next flow controller.
11. Perform the Flow Controller Bleed Procedure as outlined below.

A.3.2 Flow Controller Bleed Procedure

1. Ensure that the primary flow loop is operating, and all flow controllers have a setpoint of 5.000 LPM.
2. Ensure each flow controller has the 'AUTO TARE' function enabled. This option is accessible through the menu on the panel of the flow controller.
3. Block the flow downstream of flow controller 'A' by closing the downstream value. Leave the flow from the other five flow controllers undisturbed.

4. Using a hex key, loosen the bleed screw on flow controller ‘A’ located closest to the supply side by one full turn (flow direction marked on controller). Allow water to flow out for at least 60 seconds.
    a. Tap the body of the flow controller with a screwdriver to promote the release trapped air bubbles.
    b. Use a bucket to catch the dripping water.
5. Tighten the supply side bleed screw.
6. Repeat steps 4 and 5 for the bleed screw on flow controller ‘A’ located closest to the discharge side.
7. Change the setpoint on flow controller ‘A’ to 0.000 LPM. This will tare the flow measurement.
8. Change the setpoint on flow controller ‘A’ to 5.000 LPM.
9. Open the valve downstream of flow controller ‘A’ and wait for the flow rate reported by the controller to reach its set point.
10. Repeat steps 3 through 9 for all remaining flow controllers.

A.3.3 Laser Startup and Traverse Homing Procedure

This step is only necessary when performing velocity measurements and must be performed each time the traverse is power cycled. Skip this section if only performing temperature measurements.

This section assumes that the LDV system has been set up and aligned with a TSI TR360 5-beam measurement probe.

1. Connect the remote-control panel to the 3-axis traverse motor controller and turn both ON.
2. Ensure that the space surrounding the 3-axis traverse is free of obstructions and all limit switches are present and operational.
3. Set the control mode of the traverse to ‘FAST’.

4. Find the 'absolute reference' location using the 'REF' buttons on the control panel in the following order (directions are referenced to the front of the test vessel):
    a. Press the 'Z-REF' button. The traverse will move to the lowest Z (up/down) limit switch and stop.
    b. Press the 'Y-REF' button. The traverse will move to the furthest Y (in/out) limit switch and stop.
    c. Press the 'X-REF' button. The traverse will move to the furthest right X limit switch and stop.
5. Set the control mode of the traverse to 'SLOW'.
6. Move the traverse a minimum of +5.00 mm in each of the X, Y, and Z directions.
7. Repeat step 4 with the traverse mode set to 'SLOW'.
8. Adjust the X and Z position of the traverse such that the measurement probe is roughly centred on the front face of the test vessel
9. Adjust the Y position of the traverse such that the front surface of the measurement probe is located approximately 25 – 30 cm from the front of the test vessel endplate.

Steps 10 through 28 are to be performed without laser safety goggles. Dim the room lights if necessary to aid visibility of the low power laser beams.

10. Set the Fiberlight optical density filter dial to the 'CLOSED' position.
11. Set the optical coupler shutters on the 'shifted 488 nm' and 'unshifted 488 nm' beams to the 'OPEN' position.
12. Set all other four (4) optical coupler shutters to the 'CLOSED' position

13. Turn the laser system on with a beam supply current of 13.5 A and laser aperture setting of 10. The optical output power reading on the control panel should read approximately 180 ± 10 mW.
    a. If the optical power is below this value, it may be necessary to iteratively adjust both laser cavity alignment knobs to maximize the laser output power.
14. Remove the yellow lens cap from the LDV measurement probe.
15. Set the Fiberlight optical density filter dial to the 'OD1' position. A pair of angled dim blue beams should be visible.
16. Adjust the Y-position of the traverse to position the beam crossing at the inside surface of the vessel front end-plate as shown in the centre of Figure A-1 (i.e. – the beams should cross at the interface between the front endplate and the fluid volume inside the vessel). Record this Y-position (Y_0).
    a. Fine-tuning of position (± 0.0125 mm) is possible with the traverse in the 'SLOW' and 'STEP' modes.
17. Set the optical coupler shutters on the 'shifted 488 nm' and 'unshifted 488 nm' beams to the 'CLOSED' position.
18. Set the Fiberlight optical density filter dial to the 'OD2' position.
19. Set the optical coupler shutters on the 'shifted 514.5 nm' beam to the 'OPEN' position. A dim green beam should be visible, emitted from the centre of the measurement probe.
20. Adjust the X and Z-positions of the traverse to position the green beam at position X_1 as indicated in Figure A-2. Record this X-position (X_1).
    a. Fine-tuning of position (± 0.0125 mm) is possible with the traverse in the 'SLOW' and 'STEP' modes.
21. Leaving the Z-position of the traverse fixed, adjust the X-position of the traverse to position the green beam at position X_2 as indicated in Figure A-2. Record this X-position (X_2).

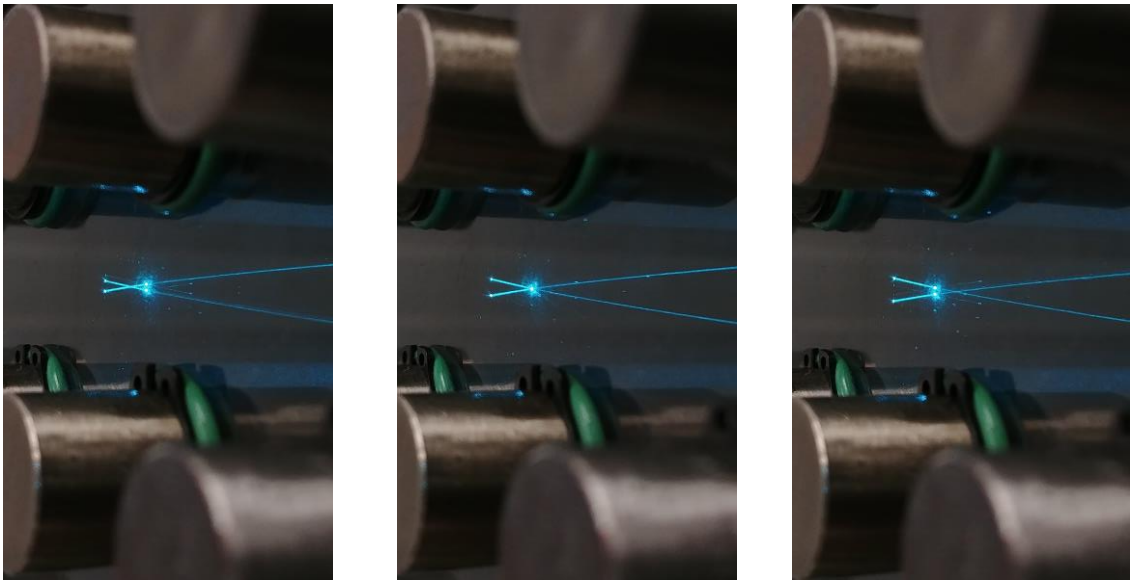

Figure A-1: Positioning of beam crossing to locate position Y_0 (centre image). The centre image shows the correct positioning at the inside interface between the end plate and the fluid volume. The left and right images illustrate incorrect positioning of the beam crossing, with the beam crossing occurring inside the end plate (left) or inside the fluid volume (right)

22. Adjust the X and Z-positions of the traverse to position the green beam at position Z_1 as indicated in Figure A-2. Record this Z-position (Z_1).
    a. Fine-tuning of position (± 0.0125 mm) is possible with the traverse in the 'SLOW' and 'STEP' modes.
23. Leaving the X-position of the traverse fixed, adjust the Z-position of the traverse to position the green beam at position Z_2 as indicated in Figure A-2. Record this Z-position (Z_2).
24. Move the traverse to the position X_0, Y_0, Z_0:
    a. $X_0 = (X_1 + X_2) / 2$
    b. Y_0 as found in step 16
    c. $Z_0 = (Z_1 + Z_2) / 2$

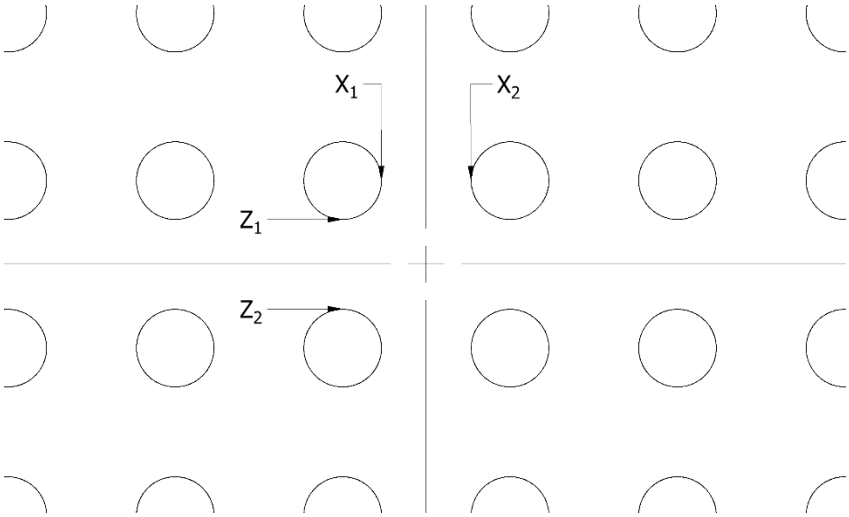

Figure A-2: Locations of X and Z reference points as viewed from the front of the test vessel, with the cross indicating the centre of the vessel end plate

25. Observe and verify the position of the green beam. It should be located at the centre of the tube bank. If not, repeat steps 20 through 24.
26. Set the Fiberlight optical density filter dial to the 'OD1' position.
27. Set the shutters on all six (6) optical coupler assemblies to the 'OPEN' position. Five intersecting beams should be visible. The intersection should be located at the inside centre of the front end-plate.
    a. The shifted green (514.5 nm) and unshifted violet (476.5 nm) beams are emitted colinearly from the center of the measurement probe. The six beams emitted from the Fiberlight will be visible as five beams emitted from the measurement probe.
    b. The violet (476.5 nm) beams may be too dim to be visible at this power level. If this is the case, close the four (4) shutters for the 514.5 nm and 488.0 nm beams and set the Fiberlight optical density filter dial to the 'OPEN' position to confirm the positioning of the violet beams.
28. Turn the shutter knob on the top of the laser to the 'CLOSED' position.

29. Disconnect the remote-control panel from the traverse motor controller by pressing the 'ON/OFF' button on the remote.
    a. Do **NOT** turn the power for the traverse motor controller off as this will cause the reference location to be lost.
30. Load FlowSizer (LDV measurement software) on the PC connected to the FSA 3500 signal processor. Start the traverse manager by selecting "Traverse" and "Start Traverse" in the top menu bar.
31. The current position of the traverse should be displayed in the traverse manager window. Press the 'Set Rel Home' button in the traverse manager. This will cause the displayed position to read (0.00, 0.00, 0.00).

A.3.4 Cooling Flow Loop Startup Procedure

This step is only necessary when preparing to perform heated tests. Skip this section if performing isothermal tests.

1. Set the chilled water supply valve to the 'OPEN' position and note the temperature of the chilled water using the temperature gauge located immediately downstream of the valve.
    a. Allow the chilled water to flow for at least 10 minutes before recording the temperature.
    b. Chilled water temperatures vary based on other cooling loads in the building and seasonal conditions. The expected range is 4.5 – 7.5 ºC. Test section powers may be limited at the higher range of chilled water temperatures due to reduced cooling capacity.
2. Slowly set the chilled water supply valve to the 'CLOSED' position.
3. Connect the inlet of the cooling loop to a fresh tap water supply (i.e. – faucet).
4. Connect the outlet of the cooling loop to a drain.

5. With the cooling pump OFF, flush the heat exchanger with warm water for at least 15 minutes.
    a. Typical flow rates from the faucet are expected to be approximately 8 – 9 GPM (verify using flow meter installed in cooling loop).
    b. The cooling loop is equipped with a shell and tube heat exchanger. The tube manifold is constructed of cast iron which may cause rust build up between experiments. If an interval of one week or longer has elapsed between experiments, flush for an additional 15 – 30 minutes.
6. Close the valves located at the inlet and outlet of the cooling loop and disconnect the supply line from the faucet. Close the outlet valve first to ensure that the cooling loop remains filled.
7. Connect the ½" drain of the primary loop holding tank to the inlet of the cooling loop.
8. Connect the outlet of the cooling loop to the inlet of the water filter on the primary cooling loop holding tank.
9. Open three (3) valves in the following order:
    a. Valve located at the ½" drain of the holding tank
    b. Cooling loop inlet valve
    c. Cooling loop outlet valve
10. Turn the cooling loop pump on by turning the switch for 'PUMP A' to 'ON' using the remote-control panel. Adjust the drive frequency to maintain a flow rate of 10.0 GPM.

A.3.5 Power Supply Startup Procedure

This step is only necessary when preparing to perform heated tests. Skip this section if performing isothermal tests.

1. Ensure that the AC power source to power supply cabinet #2 is disengaged with the safety switch locked in the 'OFF' position.

2. Examine the power supply leads at the rear of the test section to ensure that the insulating boots are properly covering all terminals.[13]
3. Examine the test section power distribution busses to verify the following:
    a. Branch terminals are securely fastened to the bus bars
    b. Supply lines from the DC power supply are securely fastened to the bus bars
4. Using a multimeter, verify electrical isolation between:
    a. Heater sheath and terminals
    b. Heater sheath and test vessel
    c. Heater terminals and test vessel
    d. Heater terminals and vessel support structure
    e. Heater terminals and loop support structure
    f. Distribution busses and bus bar support structure
5. Press the 'Emergency Stop" button on the front panel of the power (shutdown state).
6. Unlock and engage connect the power source to power supply cabinet #2 by turning the safety switch to the 'ON' position.
7. Turn the power switch on the power supply cabinet to the 'ON' position.
8. Navigate to the 'Limit settings' section of front panel menu on the power supply. Verify that the safety limits on maximum voltage and current limits are set to:
    a. Voltage: 100 V
    b. Current: 700 A
9. Exit the menu on the front panel of the power supply.

[13] The heaters are wired together in a 4 x 13 configuration (i.e. – 4 heaters in series per string, 13 strings in parallel). This results in an expected resistance of 120 - 150 mΩ between the positive and negative bus bars. This resistance is too small to be directly measured with a typical handheld multimeter. Detection of continuity using a handheld multimeter between the positive and negative bus bars therefore does not indicate an electrical short within the test section wiring.

A.3.6 Primary Flow Loop Set Point Procedure

1. Ensure that the primary flow loop, instrumentation, and data acquisition systems are have been running for at least one hour. This ensures that the instrumentation is sufficiently warmed up.
2. Create a subdirectory for the current experimental run. Using the LabVIEW interface for the primary flow loop, create a new measurement log file to keep track of process variables while steady state is reached.
    a. The file should typically be named 'Startup.csv' or similar.
3. Set the flow controller setpoints to reach the desired inlet flow rate. For standard operating conditions, set each flow controller to the same set point.
    a. For example, to achieve 30 LPM total inlet flow, set each flow controller to 5.000 LPM.
4. Verify that each flow controller has been properly tared by manually closing the valve downstream of each flow controller, one at a time.
    a. Do not adjust the set points for the flow controllers at this step.
    b. When the flow is flow is blocked downstream of the flow controller, it should read 0.000 ± 0.050 LPM. If this is not the case, perform the Flow Controller Bleed Procedure before continuing to the next step.
5. Verify the balance between the measured inlet flow rate by subtracting the measured inlet flow rate (magnetic flow meter) from the sum of the flow rates from each flow controller.
    a. This balance is calculated automatically in the LabVIEW interface and is displayed as the 'Alicat Balance'.
    b. The inlet magnetic flow meter is displayed as the 'Inlet [LPM]' indicator in LabVIEW.
    c. Allow the flow measurements to settle for two minutes before observing the flow balance.

6. Adjust the setpoints of the flow controllers evenly in increments no finer than 0.050 LPM until the magnetic flow meter inlet flow measurement matches the desired set point.
    a. For example, if the flow balance observed at step 5 is +0.6 LPM, increase the set point of each flow controller by 0.100 LPM.
    b. Allow the flow measurements to settle for two minutes before observing the flow balance.
7. Repeat step 6 until the inlet magnetic flow meter measurement is with ± 0.1 LPM of the desired setting.

Steps 8 through 18 are only performed for heated tests and can only be completed following the Power Supply Startup Procedure and Cooling Flow Loop Startup Procedure. **Under no circumstances should power be applied to the heaters while water is not flowing through the test vessel.** Skip these steps if performing isothermal tests.

8. Load and run the LabVIEW interface for the power supply ('PS_DLL_PH_Control.vi').
9. Ensure that the appropriate serial port is selected in the LabVIEW power supply interface and click 'CONNECT'.
    a. Review the status messages to ensure that the connection was successful
    b. Upon successful connection, the status indicators should match the values shown on the physical front panel of the power supply.
10. Change the 'Set Point Source' in the dropdown menu from 'HMI' to 'RS232'.
11. Enter the following setting values for voltage, current, and power:
    a. Voltage [V]: 5
    b. Current [A]: 50
    c. Power [kW]: 0

12. Reset the emergency stop button on the physical front panel of the power supply: twist, release and the switch will pop out.
13. Press the "RUN/SET" button in the power supply LabVIEW interface.
    a. The power supply will adjust voltage and current until the limits set in step 11 are reached (i.e. – voltage and current should remain at zero due to the power set point of 0 kW)
    b. The power supply will shut down and sound an alarm if any one of the three emergency-stop switches have been activated. If this occurs, reset the power supply using the rotary switch on the front panel and restart the LabVIEW power supply interface. Verify the state of the three emergency-stop switches:
        i. Red shutdown switch on front panel
        ii. Red shutdown switch near laser head
        iii. Relay in data acquisition system (controlled via primary flow loop LabVIEW interface)
14. Keeping the power set point at 0 kW, change the power supply set points to the following values in the LabVIEW interface. The measured electrical power in the primary flow loop LabVIEW interface should remain at 0 kW.
    a. Voltage [V]: 80
    b. Current [A]: 700
    c. Power [kW]: 0
15. From this step onwards, the power supply output will immediately change following a new entry in the 'Power' setpoint field. In the power supply LabVIEW window, change the power setting to 0.512 kW and press 'ENTER'.
    a. The reported voltage, current, and power values in the power supply LabVIEW window should be non-zero and match the values displayed on the power supply front panel.

b. The measured voltage, current, and power values in the primary flow loop LabVIEW are measured independently of the power supply and may differ by about 2%. Power values below 1 kW are reported as 0 kW.

16. Verify that the cooling loop flow rate is 10.0 GPM and set the chilled water supply valve to the 'OPEN' position.
    a. Pause for 10 minutes to verify that chilled water temperatures are in the expected range observed during the Cooling Flow Loop Startup Procedure.
17. Increase the power set point to the desired operating condition for the test, in steps of no larger than 5.0 kW at a time. **Pause for two minutes** between power level step changes.
    a. For example: to reach a power level of 20 kW, first increase the power setting to 5.0 kW and wait for 120 seconds. Increase to 10.0 kW and wait for 120 seconds, and so on.
    b. Pay close attention to the reported outlet temperature measurements. **Do not allow the outlet temperatures to exceed 60ºC at any time.** Internal test section temperatures may be allowed to exceed 60ºC.
18. Once the desired power level has been reached, wait until steady state has been reached.
    a. Conditions are considered steady state when both conditions are satisfied:
        i. The heat balance is within ± 5%, and
        ii. The inlet temperature has changed less than 0.2 ºC over a period of five minutes.
    b. The primary flow loop LabVIEW interface calculates and displays the live heat balance as: $\frac{(P_{electric}-P_{thermal})}{P_{electric}}$. The thermal power is calculated as $P_{thermal} = \dot{m}C_p(T_{outlet} - T_{inlet})$. Water fluid properties are evaluated at the measured inlet temperature.

A.3.7 Velocity Measurement Procedure

This procedure assumes that the operator is trained to use the LDV system, associated measurement settings and is familiar with the FlowSizer measurement software. Please refer to the TSI FlowSizer software manual and TR360 measurement probe manual for additional details. This procedure can only be performed following completion of the Laser Startup and Traverse Homing Procedure.

1. Identify a XZ or YZ measurement plane to be measured within the test section.
    a. Due to the laser probe configuration, XY and YZ planes that enter the tube bank are limited to the mid planes between rows and columns of tube elements
    b. The TR360 LDV measurement probe has a focal distance of 250 mm (in air). Considering the thickness of the end shield and clearance between the probe and tube elements, the maximum depth traverse coordinate is approximately 220 mm. Other factors such as light absorption and distortions caused by temperature gradients may also limit the achievable measurement depth.
2. Using a spreadsheet, outline desired the X, Y, and Z traverse coordinates for the selected measurement plane. Enter the X, Y, and Z coordinates in the first three columns with no header row. Save the file as a comma separated values (CSV) file.
    a. Facing the test section from the front face:
        i. Traverse X = 0 is referenced to the centre of the tube bank, with the positive X direction to the left.
        ii. Traverse Y = 0 is referenced to the interface between the fluid volume and the front endplate, with the positive Y direction into the fluid volume.

iii. Traverse Z = 0 is referenced to the centre of the tube bank, with the positive Z direction upwards.

3. Load FlowSizer and ensure that the software has successfully connected to the FSA 3500 signal processor.
4. Create a new Experiment Folder for the measurement plane and create a new Run file.
    a. Name this run file 'PlaneID_Settings', where 'PlaneID' is replaced with a meaningful name identifying the measurement plane.
5. Start the traverse manager and move the traverse to a measurement point contained in the measurement plane.

Laser safety goggles are required for steps 6 through 25.

6. Set the shutters on all six optical couplers to the 'CLOSED' position.
7. Rotate the optical density filter knob on the Fiberlight to the 'OPEN' position
8. Turn the shutter knob on the top of the laser to the 'OPEN' position.
9. Using the laser control console, increase the supply current to 29.5 A. The optical output power reading on the control panel should read approximately 1.90 ± 0.10 W.
    a. If the optical power is below this value, it may be necessary to iteratively adjust both laser cavity alignment knobs to maximize the laser output power.
10. The optical coupler focus may shift slightly between alignment power and measurement power. Verify focus of the measurement probe fibers and couplers, one beam at a time:
    a. Set the coupler shutter to the 'OPEN' position
    b. Verify that a beam is visible. Iteratively and slowly adjust the **coarse** X, Y, and Z adjustment knobs to maximize beam intensity.

i. Turn the coarse adjustment knobs no more than 1/8 turn. At measurement power it is possible to damage the optical fiber if the beam is grossly misaligned.
ii. If no beam is visible, close the shutter on the coupler. Reduce the laser supply current to 13.5 A and repeat the Probe Coupler Focussing Procedure as described in the LDV system installation manual.

c. Set the coupler shutter to the 'CLOSED' position and repeat for the other five beams.

11. Set the shutters on all six optical couplers to the 'OPEN' position.
12. Verify all beams are visible and that the 'shifted' and 'unshifted beam' pairs for each wavelength are balanced in intensity.
13. Add seed particles (10 μm hollow glass spheres) to the primary loop holding tank and allow five minutes for dispersal in the test section.
14. Verify the LDV settings on all three channels in FlowSizer (PMT Voltage, Burst Threshold, Band Pass Filter, SNR, and Downmix Frequency) such that the:
    a. Channels are not saturated
    b. Data rate and burst efficiency are maximized
    c. Measurement velocity range covers the expected velocities in the measurement plane.
15. Select 'Run Setup" in FlowSizer and verify settings for the following tabs:
    a. Run Settings
        i. Maximum Particle Measurement Attempts: 200000
        ii. Screen Update Interval: 0
        iii. Time Out: 120 seconds
    b. Optics: refer to TR360 probe manual for the correct parameters
    c. Processor/Matrix: refer to Figure A-3. Further details regarding the 3D transformation matrix are provided in Appendix C.

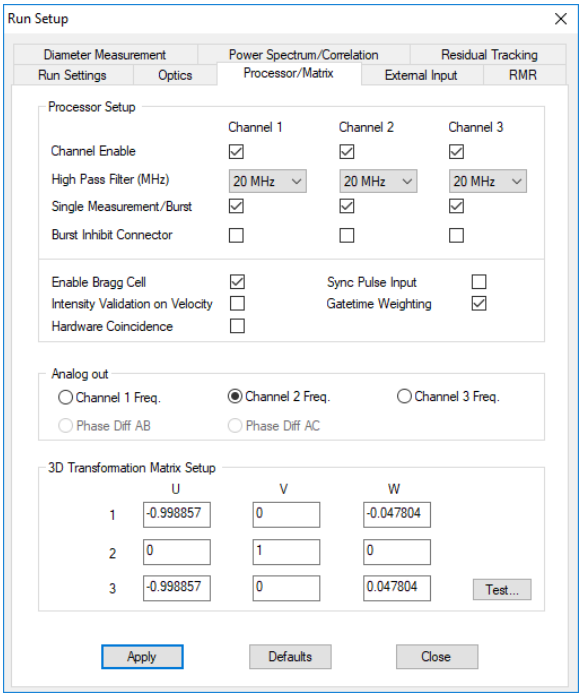

Figure A-3: Processor/Matrix settings in FlowSizer

16. Ensure that software coincidence mode is switched off during data collection.
17. Select ‘Begin Capture’ and collect data for about 30 seconds to verify all settings.
18. Stop the capture and save the run file.
19. In the traverse manager, select the ‘Scan Matrix’ tab. Open the CSV file created in step 2. The X_AXIS, Y_AXIS, and Z_AXIS columns should populate with values from the CSV file.
20. In row 1, enter the name of the run file created in step 4.a in the ‘Run Setup’ cell.
21. In the ‘Save As Name’ field below the table, enter ‘PlaneID_’, where ‘PlaneID’ is replaced with a meaningful name identifying the measurement plane.
22. Click ‘Apply’. The ‘Run Setup’ and ‘Save As’ cells for the remaining rows will populate automatically.

23. Set the ‘Start Position’ to 1 and the ‘Stop Position’ to the index of the last row in the scan matrix.
24. Click ‘Save As’ to save the current measurement place coordinate settings.
    a. This file is necessary to later link up each measurement point with the traverse coordinates.
    b. This traverse setup file can also be used to re-run measurements in the same plane.
25. In FlowSizer, select ‘Traverse’ and then ‘Scan Capture’ to begin the automated data collection routine.
    a. The traverse will automatically advance through the provided coordinates and collect data for 120 seconds.
    b. Run files will be automatically saved with the name entered in step 21 followed by a number (e.g. – ‘PlaneID_00001’, ‘PlaneID_00002, etc.).
    c. Additional seed particles may be added every 30 – 45 minutes to help maintain acceptable data rates.
    d. It is necessary to monitor the data collection process throughout the scan capture. It may be necessary to stop the data acquisition to adjust the LDV settings in different regions of the vessel:
        i. Note the current position / scan matrix row number in the traverse manager
        ii. Press the ‘Stop Capture’ button in FlowSizer
        iii. Create a new run file with a meaningful name, such as ‘PlaneID_modifiedSetup’ where ‘PlaneID’ is replaced with a descriptive name of the measurement plane.
        iv. Adjust LDV settings as required and ‘Save’ the run file
        v. Modify the ‘Scan Matrix’ to use the new run file, starting at the row for the current traverse position.

vi. Set the 'Start Position' to the row for the current traverse position. 'Save' the traverse settings file.
vii. Select Traverse, and then Scan Capture to resume data acquisition.

A.3.8 Temperature Measurement Procedure

1. Create a new temporary log output file in the LabVIEW interface to allow monitoring of process variables when moving the thermocouples.
2. Locate the sixteen (16) thermocouple feedthrough fittings located on both sides of the test section, eight per side.
3. Loosen the knurled nut on the fitting for thermocouple TCM1-00 ¼" turn to allow the thermocouple to be repositioned.
    a. Do not fully loosen or remove the knurled nut from the fitting.
4. Grasping the thermocouple sheath near the fitting, slide the thermocouple to reposition the tip to the desired location.
    a. The thermocouple sheath is marked every ½ tube pitch (14.5 mm). These markings should be lined up with the outside surface of the knurled nut on the thermocouple fitting. The red marking corresponds to the fully inserted position and should be used as the starting point.
    b. Avoid grasping the thermocouple sheath greater than 20 – 40 mm away from the fitting to avoid bending the thermocouple assembly.
5. Visually confirm the location of the thermocouple tip.
    a. When moving a half-pitch at a time, the tip should be located directly above a tube element, or directly in between two tube columns.
6. Tighten the knurled nut on the thermocouple fitting to be finger tight.
7. Repeat steps 3 through 6 for the remaining fifteen (15) thermocouples (TCM1-01 through TCM-15).

8. Create a new measurement log file using the primary flow loop LabVIEW interface
    a. Note the positions of each thermocouple and record them in the 'Additional Notes' field in the 'Settings' tab before re-running the LabVIEW interface
9. Collect data for at least five minutes.
10. Stop execution of the LabVIEW interface after the five minutes have elapsed and before moving the thermocouple assemblies
11. Repeat steps 2 through 10, withdrawing the thermocouple assemblies by ½ tube pitch until all desired measurement locations have been observed.

A.3.9 Laser Shutdown Procedure

1. Turn the shutter knob on top of the laser to the 'CLOSED' position.
2. Reduce the supply current on the laser control console to 13.5 A.
3. Turn the laser off by pressing the 'ON/OFF' button on the laser control console. A relay in the power supply unit should trigger and the 'LASER EMISSION' indicator on the laser control console should turn off.
4. Turn the laser power supply off by turning the key on the power supply unit counter-clockwise.
    a. Maintain cooling water supply to the laser for at least **five minutes** following laser power supply shutdown.
5. Disengage the power source to the laser by turning and locking the safety switch to the 'OFF' position.
6. Place the yellow lens cap on the LDV measurement probe.

A.3.10 Power Supply and Cooling Loop Shutdown Procedure

1. Using the LabVIEW interface for the primary flow loop, create a new measurement log file to keep track of process variables while the power supply is shut down.

   a. The file should typically be named ‘Cooldown.csv’ or similar.
2. Reduce the power supply set point in steps of 5.0 kW at a time. **Pause for two minutes** between power level step changes.
   a. For example: from a power level of 20 kW, first decrease the power setting to 15.0 kW and wait for 120 seconds. Decrease to 10.0 kW and wait for 120 seconds, and so on.
3. Upon reaching 0 kW, disengage the ‘ON/SET’ button in the power supply LabVIEW interface.
4. Change the ‘Set Point Source’ in the dropdown menu from ‘RS232’ to ‘HMI’.
5. Click ‘DISCONNECT’ in the power supply LabVIEW interface.
6. Turn the rotary switch on the front panel of the power supply to the ‘OFF’ position.
7. Wait until the display on the front panel turns off and then disengage the power source to the power supply by turning and locking the safety switch to the ‘OFF’ position.
8. Maintain operation of the cooling loop until both of the following conditions are met:
   a. Test section outlet temperature readings are below 35ºC
   b. Difference between inlet and outlet readings is less than 5ºC
9. Slowly turn the chilled water supply valve to the ‘CLOSED’ position.
10. Turn the cooling loop pump off by setting the switch for ‘PUMP A’ on the remote-control panel to ‘OFF’.
11. Close these three (3) valves:
    a. Valve located at the ½” drain of the holding tank
    b. Cooling loop inlet valve
    c. Cooling loop outlet valve

A.3.11 Primary Flow Loop Shutdown Procedure

1. Using the primary flow loop LabVIEW interface, create a new temporary log file.
2. Turn the valves downstream of each flow controller to the 'CLOSED' position, one at a time (six valves total).
3. Change the setpoints of all flow controllers to zero using the primary flow loop LabVIEW interface. A shortcut button labelled 'ZERO ALL' is provided for this purpose.
    a. Leaving the flow controllers with a non-zero setpoint and no water flow for an extended period can cause overheating and damage to the electronic valve.
4. Turn the primary flow loop pump off. by setting the switch for 'PUMP B' on the remote-control panel to 'OFF'.
5. Disengage the power supply from the pump drive circuit by turning and locking the safety switch to the 'OFF' position.
6. Set the two test section isolation valves to the 'CLOSED' position:
    a. Valve located at the discharge of the primary pump.
    b. Valve located behind the test vessel on the flow return line.
7. Stop the LabVIEW interface for the primary loop.
8. Power down the instrumentation measurement systems:
    a. Magnetic flow meters
    b. Data acquisition hardware
    c. 24 V loop power supply (flow controllers and current loop transmitters)

A.3.12 Velocity Export Procedure

This procedure is performed to export the time-averaged velocities collected during the Velocity Measurement Procedure to a single comma separated values (CSV) file for plotting in an external software package.

1. Open FlowSizer and select the desired experiment folder.
2. Select and open the run file corresponding to the first measurement point.
3. Verify that the 3D transformation matrix is correctly set under 'Run Setup' in the 'Processor/Matrix' tab and select 'Apply'. The correct values are provided in Figure A-3.
4. Enable 'Software Coincidence' mode under the 'Run' menu.
5. Under 'LDV Controls', change the software 'Coincidence Int.' to 500 µs and select 'Apply.
6. Under the 'Run' menu, select 'Export Data Sets to CSV file'
7. Ensure that the following properties are included in the 'Exported Data Sets':
    a. Sequence Number
    b. Valid Vel. Count Ch. 1
    c. Trans. Vel. Mean Ch. 1 (U)
    d. Trans. Vel. Mean Ch. 2 (V)
    e. Trans. Vel. Mean Ch. 3 (W)
    f. Trans. Vel. RMS Ch. 1 (U)
    g. Trans. Vel. RMS Ch. 1 (V)
    h. Trans. Vel. RMS Ch. 1 (W)
    i. Reynolds Stress U′V′
    j. Reynolds Stress U′W′
    k. Reynolds Stress V′W′
8. Set the '# Decimal Places' to 10
9. Set the 'Export Format' to 'Comma Separated Values (CSV)'
10. Deselect 'Export Headings' and select both 'Export to 1 file' and 'Apply current settings to all runs'
11. In the 'Runs to Export', select all numbered run files (e.g. – 'PlaneID_00001', 'PlaneID_00002', etc.)
12. Choose an 'Export File' name and select 'Export.

The next steps involve linking the traverse coordinates for each location with the exported velocity data. **The directions of X, Y, and Z for the traverse differ from the coordinate system defined for the exported velocity U, V, and W directions.** The coordinate system selected for the exported velocities is shown in Figure A-4. It is therefore required to modify the traverse coordinates.

13. Open the traverse settings CSV file that was saved in step 24 of the Velocity Measurement Procedure for the selected measurement plane in a spreadsheet software package.
14. Modify the coordinates as follows:
    a. Multiply all X values by -1
    b. Swap Y and Z values
15. Open the CSV file containing the velocity data that exported in step 12 in a spreadsheet software package. Verify that the number of rows corresponds to the number of rows in the traverse settings CSV file.
16. Add three columns to the velocity data file and label the corresponding header cells:
    c. X [mm]
    d. Y [mm]
    e. Z [mm]

Copy the modified coordinates from step 14 and paste into the new columns for X, Y, and Z in the velocity measurement file.

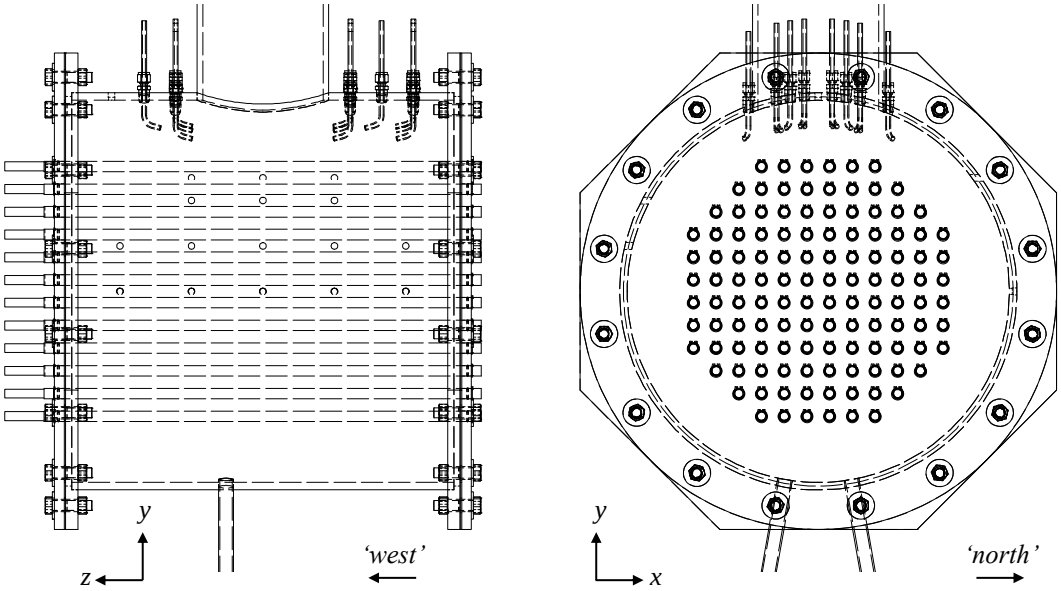

Figure A-4: Coordinate directions for exported velocities

Appendix B

Calibration Data

B.1 Thermocouple Calibration Data

The thermocouples used in the experiment were calibrated in-house against a high-precision resistive temperature detector (RTD) probe (Omega DP251 precision RTD thermometer with PRP-3 probe). This system is specified to have 0.025ºC accuracy over a range of -50ºC to 250ºC [52]. The sheathed thermocouple probes were placed in an insulated and heated oil bath with the temperature monitored by the RTD. The heater power was adjusted and the RTD and thermocouple temperature readings were allowed to stabilize. The oil bath was assumed to be at a uniform temperature. To reduce systematic errors, the thermocouple hookup wire and data acquisition device channels used during calibration were identical to those used during the experiment.

A least-squares fit to a straight line was performed for each data set (thermocouple reading versus RTD reading). The resulting relationship in the form $y = ax + b$ was used to relate uncalibrated thermocouple measurements (x) to calibrated temperatures (y). To provide an estimate of the uncertainty in the calibrated temperature σ_T, the sample variance is used [57]:

$$\sigma_T^2 \cong s^2 = \frac{1}{N-m}\sum(y_i - \bar{y}_i)^2 \tag{B.1}$$

Here, *N* is the number of data points for the calibration curve, *m* is the number of fit parameters, y_i are the reference RTD measurements and $\bar{y}_i$ are the results from the best fit equation:

$$\sigma_T \cong s = \sqrt{\frac{1}{N-2}\sum\left(y_{ref} - ax_i - b\right)^2} \tag{B.2}$$

Finally, it was assumed that the resulting calibrated measurements would have an uncertainty of at least one order of magnitude worse than the reference instrument. Therefore, the calibrated temperature uncertainty was taken to be the larger of 0.25°C and the result from Equation B.2.

B.1.1 Vessel Temperature Probe Calibration Data

All temperature probes were of Omega TMTSS-125G type (T-type 0.125 in diameter stainless steel T304 sheathed with grounded tip). Due to space limitations in the calibration apparatus, four probes were calibrated per run.

Table B-1: Vessel internal temperature probe calibration data (group 1)

RTD [°C]	TCT-00 [°C]	TCT-01 [°C]	TCT-02 [°C]	TCT-03 [°C]
25.09	25.1274	25.1189	25.1361	25.1236
30.57	30.6147	30.6195	30.6350	30.6284
35.18	35.2844	35.2911	35.3101	35.2940
40.62	40.7492	40.7662	40.7870	40.7694
45.43	45.5823	45.6178	45.6307	45.6172
50.40	50.5510	50.5897	50.6111	50.5814
55.38	55.5546	55.6015	55.6229	55.6039
60.13	60.3539	60.4127	60.4261	60.4098
65.30	65.5479	65.6146	65.6293	65.6124
70.23	70.5050	70.5964	70.5974	70.5925
75.38	75.6269	75.7145	75.7346	75.7139
80.21	80.5278	80.6555	80.6358	80.6466
85.33	85.6207	85.7326	85.7470	85.7310
90.37	90.6820	90.8116	90.8177	90.8071
95.20	95.5028	95.6330	95.6564	95.6374
100.47	100.8236	100.9716	100.9796	100.9663

RTD [°C]	TCT-00 [°C]	TCT-01 [°C]	TCT-02 [°C]	TCT-03 [°C]
105.36	105.7047	105.8613	105.8783	105.8601
110.40	110.7912	110.9554	110.9648	110.9572

Table B-2: Vessel internal temperature probe calibration data (group 2)

RTD [°C]	TCT-04 [°C]	TCT-05 [°C]	TCT-06 [°C]	TCT-07 [°C]
24.89	24.9320	24.9377	24.9488	24.9464
30.14	30.1874	30.1985	30.1792	30.1987
35.30	35.3796	35.4009	35.3493	35.3827
40.13	40.2602	40.2831	40.1966	40.2635
45.15	45.3021	45.3271	45.2100	45.2861
50.19	50.3944	50.4122	50.2690	50.3626
55.23	55.4331	55.4536	55.2867	55.3902
60.26	60.5379	60.5711	60.3580	60.4903
65.06	65.3175	65.3456	65.1235	65.2596
70.46	70.7784	70.8061	70.5413	70.6992
75.57	75.8839	75.9098	75.6310	75.7987
80.30	80.6376	80.6580	80.3553	80.5389
85.23	85.6350	85.6721	85.3160	85.5212
90.34	90.7739	90.8048	90.4219	90.6443
95.47	95.9283	95.9515	95.5520	95.7857
100.27	100.7835	100.8191	100.3743	100.6279
105.15	105.7019	105.7311	105.2658	105.5311
110.35	110.9120	110.9417	110.4469	110.7303

Table B-3: Vessel internal temperature probe calibration data (group 3)

RTD [°C]	TCT-08 [°C]	TCT-09 [°C]	TCT-10 [°C]	TCT-11 [°C]
24.68	24.7304	24.7080	24.8511	24.8267
30.27	30.3578	30.3562	30.4682	30.4330
35.35	35.4609	35.4767	35.5844	35.5237
40.20	40.3693	40.3611	40.5092	40.4007
45.04	45.1842	45.2011	45.3246	45.2118
50.05	50.2161	50.2546	50.3732	50.2271
55.47	55.6485	55.7090	55.8164	55.6407
60.18	60.4018	60.4629	60.5918	60.3787
65.26	65.4796	65.5674	65.6690	65.4393
70.51	70.7522	70.8533	70.9582	70.6958
75.19	75.4619	75.5454	75.6819	75.3886
80.20	80.4788	80.5982	80.7014	80.3913

RTD [°C]	TCT-08 [°C]	TCT-09 [°C]	TCT-10 [°C]	TCT-11 [°C]
85.40	85.7023	85.8318	85.9437	85.5961
90.14	90.4402	90.5837	90.6875	90.3156
95.31	95.6199	95.7996	95.8806	95.4802
100.43	100.7294	100.9187	101.0090	100.5728
105.64	105.9299	106.1456	106.2142	105.7596
110.43	110.7492	110.9596	111.0520	110.5659

Table B-4: Vessel internal temperature probe calibration data (group 4)

RTD [°C]	TCT-12 [°C]	TCT-13 [°C]	TCT-14 [°C]	TCT-15 [°C]
24.32	24.4328	24.4593	24.4323	24.4465
30.09	30.2460	30.2681	30.2566	30.2567
35.40	35.5716	35.5901	35.5819	35.5708
40.16	40.3668	40.3989	40.3870	40.3779
45.28	45.5115	45.5439	45.5267	45.5102
50.07	50.3687	50.3961	50.3941	50.3589
55.43	55.7141	55.7468	55.7342	55.7247
60.42	60.7339	60.7645	60.7494	60.7384
65.30	65.6574	65.6900	65.6803	65.6568
70.49	70.8474	70.8868	70.8725	70.8626
75.17	75.5631	75.5980	75.5868	75.5696
80.34	80.7608	80.7959	80.7824	80.7705
85.30	85.7529	85.7889	85.7774	85.7581
90.27	90.7475	90.7808	90.7785	90.7456
95.21	95.6982	95.7259	95.7254	95.7020
100.40	100.9386	100.9692	100.9728	100.9291
105.50	106.0624	106.0901	106.0838	106.0592
110.36	110.9165	110.9442	110.9426	110.9165

Table B-5: Vessel internal temperature probe calibration data (group 5)[14]

RTD [°C]	TCT-16 [°C]	TCT-17 [°C]	TCT-18 [°C]	TCT-19 [°C]
24.35		24.3854	24.4106	24.3845
30.24		30.2939	30.3243	30.3098
35.50		35.5794	35.6116	35.6089
40.15		40.2767	40.3167	40.3150
44.87		45.0353	45.0827	45.0661
50.05		50.2211	50.2708	50.2643

[14] Thermocouple junction TCT-16 was defective and failed during calibration

RTD [°C]	TCT-16 [°C]	TCT-17 [°C]	TCT-18 [°C]	TCT-19 [°C]
55.16		55.3435	55.4015	55.3973
60.34		60.5618	60.6295	60.6160
65.32		65.5221	65.5960	65.6016
70.22		70.4615	70.5523	70.5325
75.18		75.4363	75.5236	75.5131
80.15		80.4258	80.5229	80.5197
85.23		85.5123	85.6185	85.6110
90.48		90.8129	90.9297	90.9213
95.48		95.7890	95.9091	95.9060
100.12		100.4810	100.6120	100.5941
105.35		105.6980	105.8349	105.8325
110.45		110.8041	110.9545	110.9512

Table B-6: Linear best-fit coefficients for vessel temperature probes

Probe ID	*a*	*b*	*s*
TCT-00	9.96117×10^{-1}	3.65409×10^{-2}	2.374×10^{-2}
TCT-01	9.94038×10^{-1}	9.99238×10^{-2}	2.739×10^{-2}
TCT-02	9.94147×10^{-1}	7.94668×10^{-2}	2.017×10^{-2}
TCT-03	9.94106×10^{-1}	9.59293×10^{-2}	2.466×10^{-2}
TCT-04	9.93777×10^{-1}	1.29637×10^{-2}	1.849×10^{-2}
TCT-05	9.93566×10^{-1}	1.19367×10^{-1}	2.065×10^{-2}
TCT-06	9.99419×10^{-1}	-3.48196×10^{-2}	1.421×10^{-2}
TCT-07	9.96168×10^{-1}	4.00305×10^{-2}	1.764×10^{-2}
TCT-08	9.97003×10^{-1}	-1.63859×10^{-2}	2.445×10^{-2}
TCT-09	9.94214×10^{-1}	8.36879×10^{-2}	1.715×10^{-2}
TCT-10	9.94764×10^{-1}	-6.33169×10^{-2}	2.379×10^{-2}
TCT-11	1.00027×10^{0}	-1.90142×10^{-2}	2.270×10^{-2}
TCT-12	9.94746×10^{-1}	3.37082×10^{-2}	1.377×10^{-2}
TCT-13	9.94682×10^{-1}	-2.25246×10^{-2}	1.500×10^{-2}
TCT-14	9.94507×10^{-1}	-1.05967×10^{-2}	1.708×10^{-2}
TCT-15	9.94852×10^{-1}	-7.34915×10^{-3}	1.103×10^{-2}
TCT-16	N/A	N/A	N/A
TCT-17	9.96239×10^{-1}	3.32405×10^{-2}	1.990×10^{-2}
TCT-18	9.94778×10^{-1}	5.17401×10^{-2}	1.876×10^{-2}
TCT-19	9.94693×10^{-1}	6.61579×10^{-2}	1.748×10^{-2}

B.1.2 Process Temperature Probe Calibration Data

All temperature probes were of Omega TMTSS-062U-6 type (T-type 0.0625 in diameter stainless steel T304 sheathed with ungrounded tip).

Table B-7: Process temperature probe calibration data

RTD [°C]	TCT-23 [°C]	TCT-24 [°C]	TCT-25 [°C]	TCT-26 [°C]	TCT-27 [°C]
24.86	24.8576	24.8688	24.8863	24.8913	24.8776
29.83	29.8319	29.8471	29.8571	29.8697	29.8558
35.28	35.3415	35.3474	35.3644	35.3726	35.3547
40.16	40.2580	40.2592	40.2728	40.2934	40.2765
44.97	45.0849	45.0893	45.1021	45.1195	45.1049
49.96	50.1265	50.1313	50.1302	50.1698	50.1535
55.13	55.2857	55.2994	55.3060	55.3197	55.3017
60.14	60.3257	60.3439	60.3424	60.3593	60.3583
65.26	65.4518	65.4654	65.4719	65.4851	65.4845
70.09	70.3475	70.3645	70.3595	70.3851	70.3951
75.51	75.7612	75.7875	75.7817	75.7996	75.8066
80.24	80.5181	80.5401	80.5400	80.5674	80.5697
85.04	85.3220	85.3530	85.3449	85.3580	85.3790
90.11	90.4090	90.4376	90.4350	90.4523	90.4683
95.29	95.6463	95.6636	95.6509	95.6943	95.7070
100.48	100.8333	100.8604	100.8574	100.8761	100.8978
105.29	105.6612	105.6857	105.6822	105.6955	105.7220
110.40	110.7721	110.7931	110.7809	110.8110	110.8361
115.38	115.8178	115.8376	115.8301	115.8731	115.8911
120.55	120.9475	120.9891	120.9808	120.9971	121.0286

Table B-8: Linear best-fit coefficients for process temperature probes

Probe ID	*a*	*b*	*s*
TCT-23	9.95637×10^{-1}	8.66956×10^{-2}	2.239×10^{-2}
TCT-24	9.95378×10^{-1}	8.74703×10^{-2}	1.959×10^{-2}
TCT-25	9.95651×10^{-1}	6.69067×10^{-2}	1.763×10^{-2}
TCT-26	9.95495×10^{-1}	5.77463×10^{-2}	2.409×10^{-2}
TCT-27	9.94958×10^{-1}	9.29853×10^{-2}	2.202×10^{-2}

B.2 Voltage Transmitter Calibration Data

The voltage transmitters used in the experiments were calibrated using an Agilent (Keysight) 34401A 6.5-digit digital multimeter which had been calibrated by Keysight against traceable standards. Relevant uncertainty data from the calibration certificate is presented in Table B-9.

Table B-9: DC voltage measurement uncertainties for the Agilent 34401A digital multimeter used for calibration

Range	Typical uncertainty	Maximum uncertainty
100 mV	1.1 µV	3.5 µV
1 V	1.2 µV	7 µV
10 V	6.6 µV	0.05 mV
100 V	0.17 mV	0.6 mV

The voltage transmitters were calibrated by applying a DC voltage to their input terminals from an adjustable bench top power supply. The input voltage was additionally monitored by the reference multimeter (Agilent 34401A). The output current (4 – 20 mA range) was measured by a National Instruments data acquisition system using a NI 9203 current module. To reduce systematic errors, the data acquisition device channel and current loop wiring used during calibration were identical to those used during the experiment.

A least-square fit to a straight line was performed for the data set (measured current output versus input voltage reading). The resulting relationship in the form $y = ax + b$ was used to relate uncalibrated current loop measurements (x) to calibrated voltages (y). The fitted coefficients are shown in Table B-10.

To provide an estimate of the uncertainty in the calibrated voltage σ_V, the sample variance is used [57]:

$$\sigma_V^2 \cong s^2 = \frac{1}{N-m}\sum(y_i - \bar{y}_i)^2 \tag{B.3}$$

Here, *N* is the number of data points for the calibration curve, *m* is the number of fit parameters, y_i are the reference voltage measurements and $\bar{y}_i$ are the results from the best fit equation:

$$\sigma_V \cong s = \sqrt{\frac{1}{N-2}\sum(y_i - ax_i - b)^2} \tag{B.4}$$

Finally, it was assumed that the resulting calibrated measurements would have an uncertainty of at least one order of magnitude worse than the reference instrument. Therefore, the calibrated temperature uncertainty was taken to be the larger of 10 times the corresponding value in Table B-9 and the result from Equation B.4.

Table B-10: Linear best fit coefficients for the voltage transmitters

Instrument	*a*	*b*	*s*
WAP-DS-99A-3	6.25440×10^{3}	-2.50124×10^{1}	3.241×10^{-2}
WAP-DS-16A-3	3.12323×10^{0}	-1.24749×10^{-2}	1.483×10^{-5}

Table B-11: Calibration data for the Watanabe WAP-DS-99A-3 voltage transmitter (0 – 100 V input range)

Reference voltage [V]	Measured current [A]
0.0085	4.01×10^{-3}
3.013	4.48×10^{-3}
5.999	4.96×10^{-3}
9.002	5.44×10^{-3}
12.051	5.92×10^{-3}
15.004	6.40×10^{-3}
18.011	6.88×10^{-3}
21.010	7.37×10^{-3}
24.038	7.84×10^{-3}
27.001	8.32×10^{-3}
30.010	8.76×10^{-3}
32.683	9.22×10^{-3}
32.697	9.23×10^{-3}

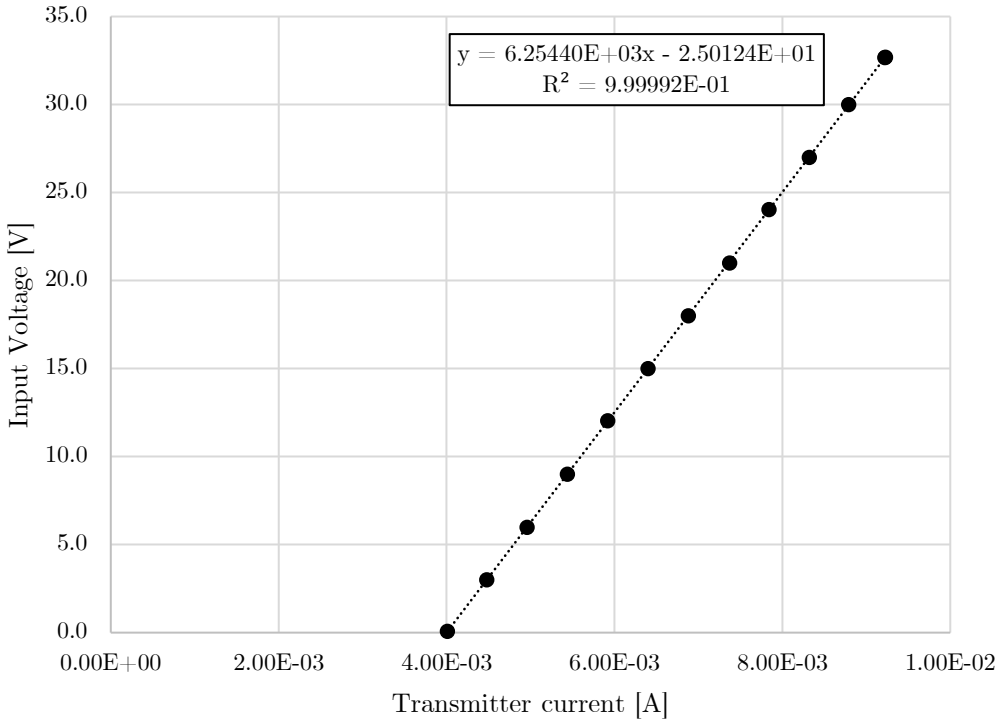

Figure B-1: Calibration data for the Watanabe WAP-DS-99A-3 voltage transmitter (0 – 100 V input range)

Table B-12: Calibration data for the Watanabe WAP-DS-16A-3 voltage transmitter (0 – 50 mV input range)

Reference voltage [V]	Measured current [A]
0.04085×10^{-3}	4.13×10^{-3}
5.018×10^{-3}	5.60×10^{-3}
10.006×10^{-3}	7.20×10^{-3}
15.033×10^{-3}	8.81×10^{-3}
20.016×10^{-3}	10.40×10^{-3}
25.027×10^{-3}	12.00×10^{-3}
30.015×10^{-3}	13.60×10^{-3}
35.060×10^{-3}	15.22×10^{-3}
40.020×10^{-3}	16.80×10^{-3}
45.012×10^{-3}	18.41×10^{-3}
49.932×10^{-3}	19.99×10^{-3}
49.983×10^{-3}	20.00×10^{-3}

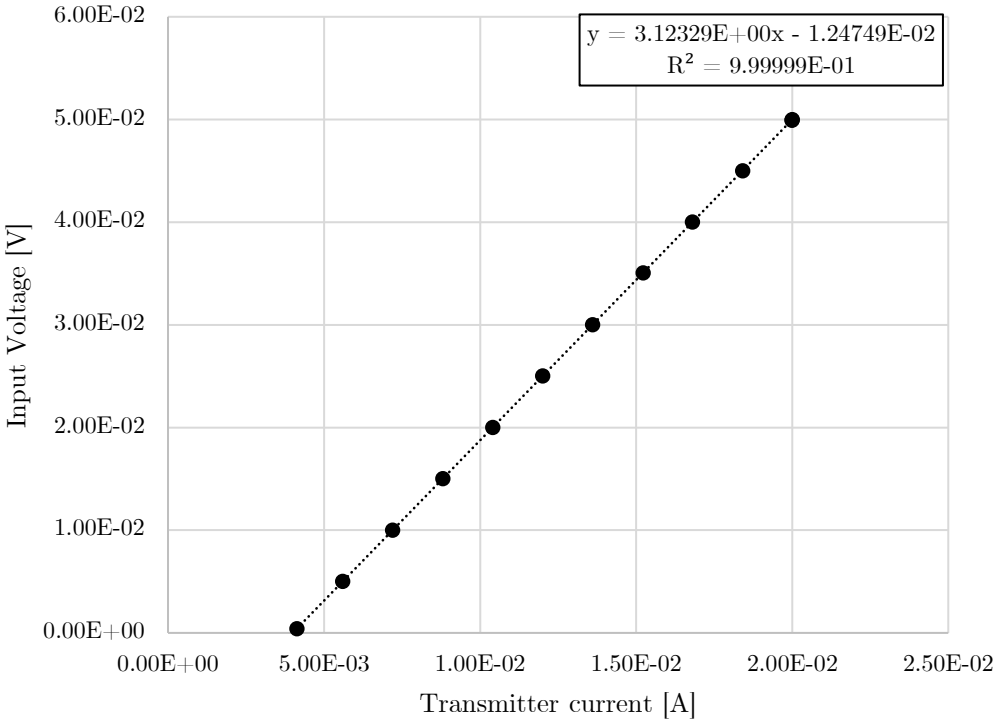

Figure B-2: Calibration data for the Watanabe WAP-DS-16A-3 voltage transmitter (0 – 50 mV input range)

Appendix C

LDV System Overview

Laser Doppler velocimetry (LDV) is a non-invasive optical measurement technique used to measure the velocity at a single point in a flowing liquid or gas. Provided that optical access is available to the region of interest, the measurement equipment can be placed outside of the fluid flow, preventing disruption of the measured flow field which may be caused by other measurement techniques. Measurements obtained using LDV provide the instantaneous flow velocity within the measurement volume. Average flow velocity and turbulence statistics can be measured by gathering repeated measurements at a single point over time.

C.1 Operating Principles

An LDV system consists of four major components: a laser which provides monochromatic, collimated, and coherent light source; transmitting optics; receiving optics; and a signal processing system. A diagram illustrating a simple one-dimensional LDV system is shown in Figure C-1. In this system, a single beam from a laser first passes through a beam splitter. The two exiting beams are coherent and are focussed on a point by the transmitting optics. The measurement volume consists of the region where the beams intersect, the size of which is a function of the beam width and angle of crossing. Within the measurement volume, the crossing beams interfere and a series of fringes are observed.

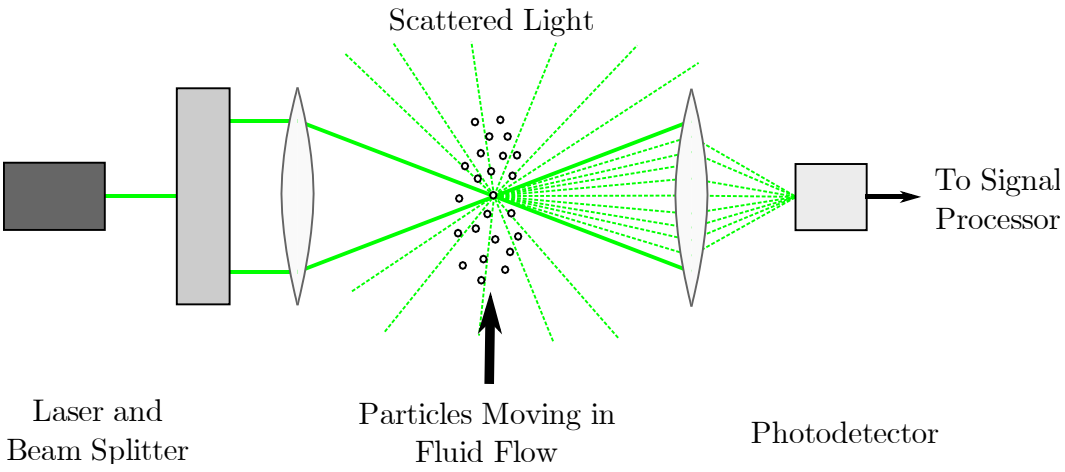

Figure C-1: Laser Doppler velocimetry overview in one-dimension

The spacing of the interference fringes d_f is a function of the beam crossing half angle κ and the wavelength of light λ:

$$d_f = \frac{\lambda}{2 \sin \kappa} \tag{C.1}$$

As particles within the flow pass through the fringes in the measurement volume, light is deflected and focussed by the receiving optics onto a photodetector. The intensity of the deflected light will vary as a function of time as it passes through the light and dark fringes. Since the spacing of the interference fringes is fixed by the laser light wavelength and the beam crossing angle, the velocity of the particle u_x is proportional to the frequency of the signal detected at the receiver f_d:

$$u_x = f_d d_f \tag{C.2}$$

A limitation of this arrangement is that the direction of the particle motion is ambiguous; the observed signal would be the same for a particle travelling upwards through the measurement volume and for a particle travelling downwards through the measurement volume. To overcome this, one of the beams is first fed through a Bragg cell. The Bragg cell oscillates at a fixed frequency (f_{Bragg}) which causes the beam to be frequency shifted by f_{Bragg} ('shifted' beam). When the shifted and

unshifted beams interfere within the measurement volume, the generated fringe pattern will appear to be moving with a frequency of f_{Bragg} (unlike the case of stationary fringes for the interference of two coherent unshifted beams). In this case, the signal received by the photodetector will be Doppler shifted by the motion of the particle. For a motionless particle within the measurement volume, the detected signal would be at f_{Bragg}. For particles moving against the direction of fringe motion, the detected signal frequency will be higher than f_{Bragg}; for particles in the direction of fringe motion, the detected signal will be lower than f_{Bragg}.

The configuration shown in Figure C-1 depicts an arrangement for measuring velocities in one-dimension (i.e. – the measured velocity will be in the direction perpendicular to the direction of the interference fringes). Measurements in multiple directions can be performed with the use of multiple pairs of beams at different wavelengths arranged in different orientations.

C.2 Implementation

A three channel LDV system supplied by TSI Inc. consisting of an Innova 70C laser, Fiberlight beam splitter, PDM1000 photodetector module, and FSA 3500 signal processor was used with a TR360-250 5-beam measurement transceiver. The TR360 transceiver contains both transmitting and receiving optics and allows for the collection velocity measurements with a single probe. Specifications for the TR360-250 probe are provided in Table C-1.

Table C-1: LDV measurement probe specifications [56]

Parameter	514.5 nm	488 nm	476.5 nm
Probe beam diameter [mm][15]	1.8	1.8	1.8
Probe beam spacing [mm]	25.0	50.0	25.0
Lens focal distance [mm]	250.0	250.0	250.0
Beam crossing half angle κ [º]	2.74	5.49	2.74
Measurement volume diameter [μm]	104	99	97

[15] The edge of the beam is the region where beam intensity is $1/e^2$ of the maximum

Parameter	514.5 nm	488 nm	476.5 nm
Measurement volume length [μm]	2.1	1.0	2.0
Fringe spacing [μm]	5.38	2.55	4.98
Number of fringes	20	39	20

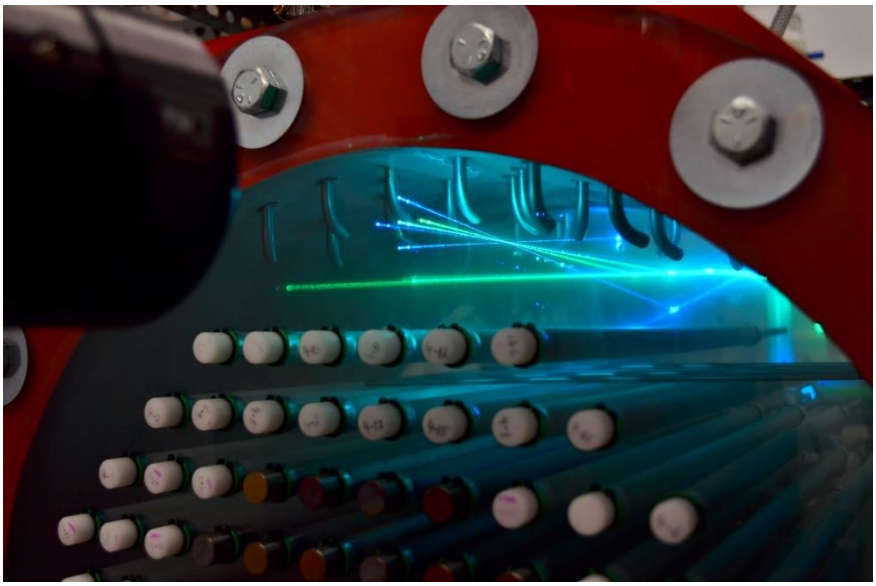

Figure C-2: Arrangement of LDV measurement probe for velocity measurements within the test section

This system produces laser light at three visible light wavelength peaks – 514.5 nm ('green'), 488 nm ('blue'), and 476.5 nm ('violet') – allowing for the simultaneous measurement of three velocity components.[16] In the 5-beam measurement arrangement, the measured velocity components are not orthogonal and do not correspond to the 'real-world' *x*, *y*, and *z* directions. The measurement directions for each channel with respect to *x*, *y*, and *z* directions are shown in Figure C-3 through Figure C-5. Note that the V_2 component corresponds to the *v* velocity component while the V_1 and V_3 components both depend on the *u* and *w* velocity components.

[16] There are six component beams (unshifted and shifted beams for each of 514.5 nm, 488 nm, 476.5 nm). In the 5-beam arrangement, the shifted green and unshifted violet beams are coincident.

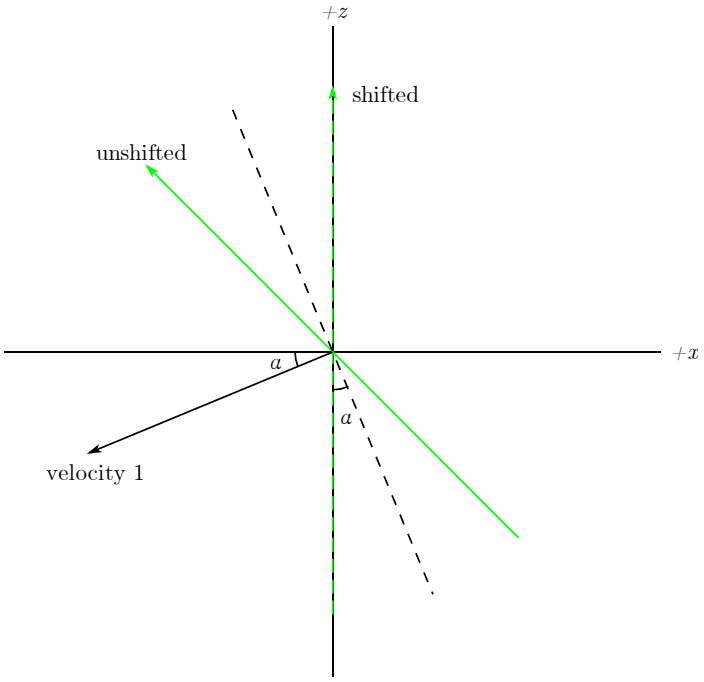

Figure C-3: Measurement direction for velocity component V_1 (514.5 nm). The half angle α corresponds to the beam half angle κ provided in Table C-1

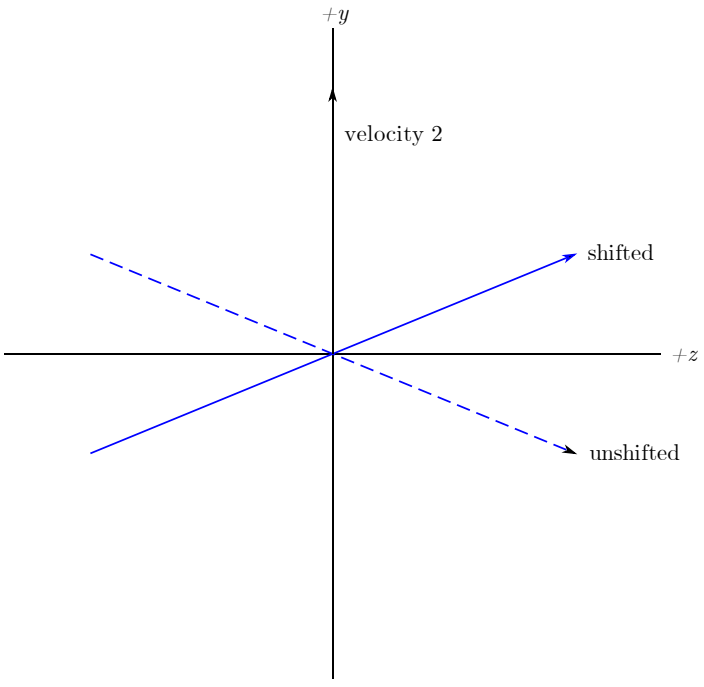

Figure C-4: Measurement direction for velocity component V_2 (488 nm)

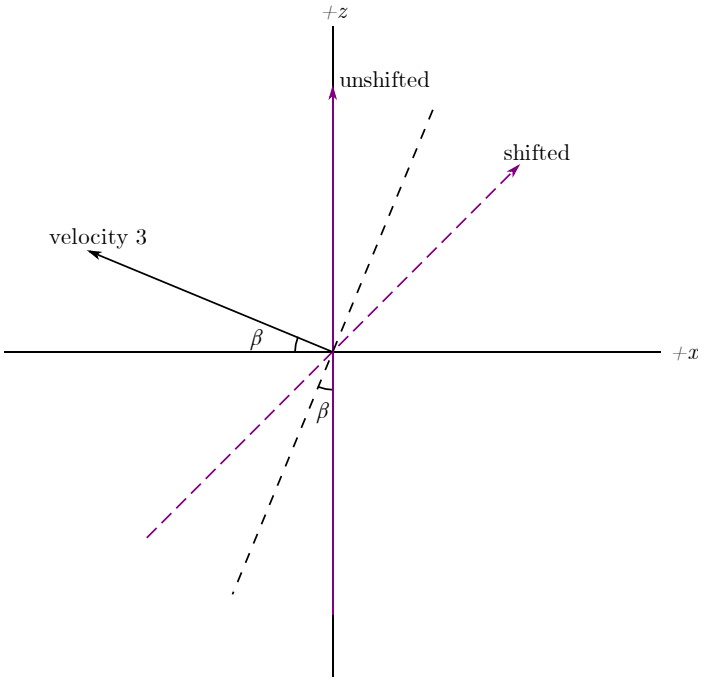

Figure C-5: Measurement direction for velocity component V_3 (478.5 nm). The half angle β corresponds to the beam half angle κ provided in Table C-1

C.2.1 Transformation Matrix

The projection of the orthogonal velocity components (u, v, w) onto the measurement directions can be represented by a transformation matrix E:

$$\begin{bmatrix} V_1 \\ V_2 \\ V_3 \end{bmatrix} = E \cdot \begin{bmatrix} u \\ v \\ w \end{bmatrix} \tag{C.3}$$

The inverse of the transformation matrix E^{-1} can be used to transform the measured velocity components V1, V2, V3 into orthogonal velocity components u, v, w:

$$\begin{bmatrix} u \\ v \\ w \end{bmatrix} = E^{-1} \cdot \begin{bmatrix} V_1 \\ V_2 \\ V_3 \end{bmatrix} \tag{C.4}$$

Referring to Figure C-6, the projection of the velocity components *u* and *w* onto the V_1 direction can be found from:

$$u_{V_1} = -u\cos\alpha \tag{C.5}$$

$$w_{V_1} = -w\sin\alpha \tag{C.6}$$

Therefore, the measured velocity component V_1 can be related to the *u* and *w* velocity components by:

$$V_1 = u_{V_1} + w_{V_1}$$

$$V_1 = -u\cos\alpha - w\sin\alpha \tag{C.7}$$

Referring to Figure C-7, the projection of the velocity components *u* and *w* onto the V_3 direction can be found from:

$$u_{V_3} = -u\cos\beta \tag{C.8}$$

$$w_{V_3} = w\sin\beta \tag{C.9}$$

Therefore, the measured velocity component V_3 can be related to the *u* and *w* velocity components:

$$V_3 = u_{V_3} + w_{V_3}$$

$$V_3 = -u\cos\beta + w\sin\beta \tag{C.10}$$

As noted above, the measured velocity component V_2 corresponds to the velocity component *v*.

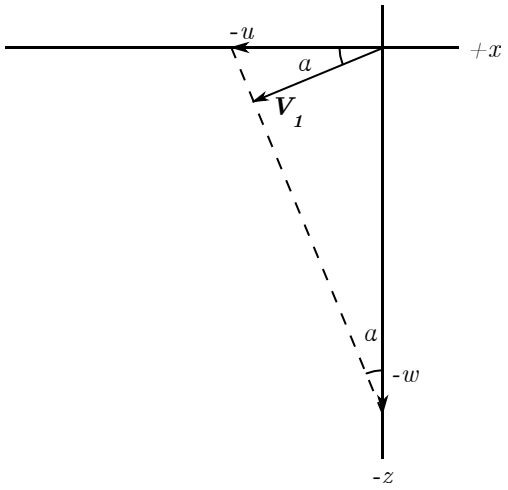

Figure C-6: Projection of *u* and *w* velocity components onto the V_1 direction

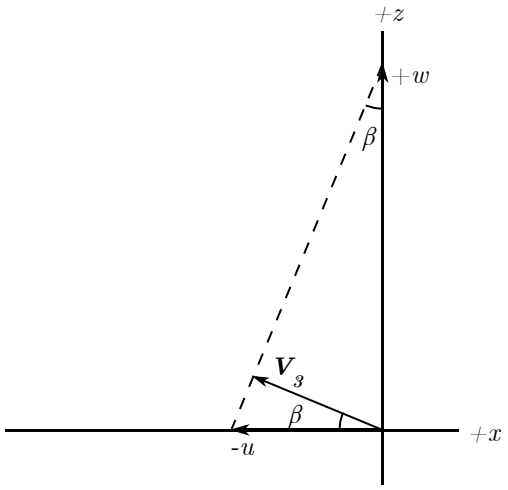

Figure C-7: Projection of *u* and *w* velocity components onto the V_3 direction

Equation C.3 can be rewritten as:

$$\begin{bmatrix} V_1 \\ V_2 \\ V_3 \end{bmatrix} = E \cdot \begin{bmatrix} u \\ v \\ w \end{bmatrix}$$

$$\begin{bmatrix} V_1 \\ V_2 \\ V_3 \end{bmatrix} = \begin{bmatrix} -\cos\alpha & 0 & -\sin\alpha \\ 0 & 1 & 0 \\ -\cos\beta & 0 & \sin\beta \end{bmatrix} \cdot \begin{bmatrix} u \\ v \\ w \end{bmatrix} \qquad \text{(C.11)}$$

For all experiments presented in this text, the probe arrangement used beam half angles $\alpha = \beta = 2.74^{o}$. The transformation matrix E and the inverse transformation matrix can be computed as:

$$E = \begin{bmatrix} -\cos 2.74° & 0 & -\sin 2.74° \\ 0 & 1 & 0 \\ -\cos 2.74° & 0 & \sin 2.74° \end{bmatrix} = \begin{bmatrix} -0.9988567 & 0 & -0.0478038 \\ 0 & 1 & 0 \\ -0.9988567 & 0 & 0.0478038 \end{bmatrix}$$

$$E^{-1} = \begin{bmatrix} -0.5005723 & 0 & -0.5005723 \\ 0 & 1 & 0 \\ -10.4594204 & 0 & 10.4594204 \end{bmatrix}$$

C.3 Measurement Position Correction

The measurement volume of the LDV measurement probe is formed at the location of the beam crossing, determined by the focal length of the transmitting optics. Given the beam separation at the lens face Δy and the half angle κ, the focal length can be calculated from:

$$F = \frac{\Delta y/2}{\tan \kappa_{air}} \tag{C.12}$$

The half angle κ listed in Table C-1 is referenced to air. In these experiments, the beam passes through multiple materials: air, polycarbonate (end plate), and water (fluid volume), with the centerline of the beam crossing normal to the end plate. This is illustrated in Figure C-8.

Given the index of refraction n in a material, the beam angle with respect to the centerline will change at each material interface according to Snell's law:

$$\frac{\sin \kappa_2}{\sin \kappa_1} = \frac{n_1}{n_2} \tag{C.13}$$

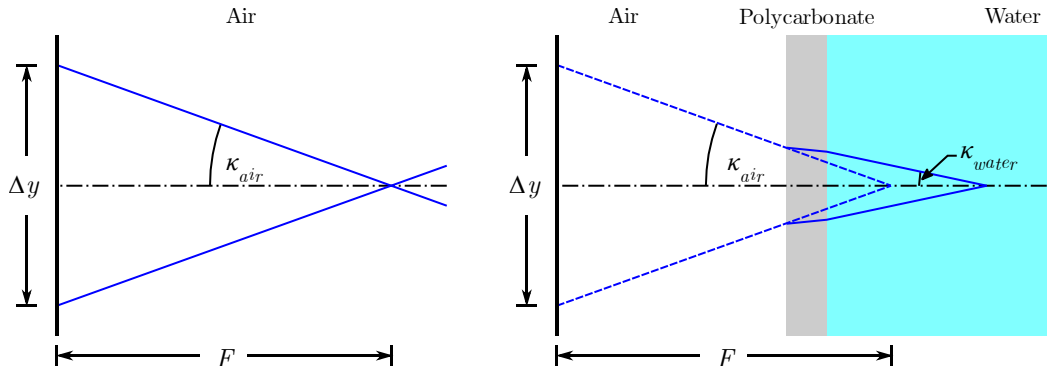

Figure C-8: Illustration of LDV probe beam crossing in air (left) and inside test section (right).

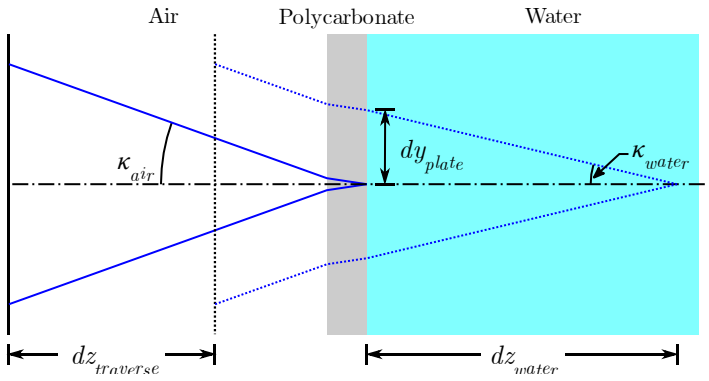

Figure C-9: Illustration of LDV probe beam crossing at traverse home (y = 0) and beam crossing at a location inside the test vessel

Therefore, the beam angles in the two materials can be calculated from:

$$\kappa_{PC} = \sin^{-1}\left(\frac{n_{air}}{n_{PC}}\,(\sin\kappa_{air})\right) \tag{C.14}$$

$$\kappa_{water} = \sin^{-1}\left(\frac{n_{PC}}{n_{water}}\,(\sin\kappa_{PC})\right)$$

$$\kappa_{water} = \sin^{-1}\left(\frac{n_{PC}}{n_{water}}\left(\sin\left(\sin^{-1}\left(\frac{n_{air}}{n_{PC}}\,(\sin\kappa_{air})\right)\right)\right)\right)$$

$$\kappa_{water} = \sin^{-1}\left(\frac{n_{air}}{n_{water}}\,(\sin\kappa_{air})\right) \tag{C.15}$$

Since $n_{water} > n_{air,}$ the half angle κ_{water} will be smaller than κ_{air}. This results in the measurement volume occurring deeper within the volume of water compared to in air. Referring to Figure C-9, for a traverse movement $dz_{traverse}$, the beams will cross the air-polycarbonate interface at a higher vertical distance above the centerline dy_{plate}:

$$dy_{plate} = dz_{traverse} \tan \kappa_{air} \tag{C.16}$$

The thickness of the polycarbonate plate is fixed. The vertical distance travelled dy_{PC} is constant. Thus, the vertical height change for the beam crossing will be the same at the front and the rear interface of the plate. For a vertical height change of the crossing at the plate dy_{plate}, the corresponding depth change of the crossing inside the fluid volume dz_{water} can be calculated from:

$$dz_{water} = \frac{dy_{plate}}{\tan \kappa_{water}}$$

$$dz_{water} = dz_{air} \frac{\tan \kappa_{air}}{\tan \kappa_{water}}$$

The coordinate system for the traversing mechanism in the test section axial direction is as the depth z = 0 corresponding to the interface between the polycarbonate end plate and the internal fluid volume. Therefore, the recorded traverse z-coordinates can be corrected to reflect the beam crossing depth within the vessel as:

$$z_{water} = z_{traverse} \frac{\tan \kappa_{air}}{\tan \kappa_{water}} \tag{C.17}$$

Appendix D

Experimental Uncertainties

This section discusses the individual sources of error that were considered for the experimental measurements. In order to estimate the uncertainties in the measured experimental data, the error propagation equation shown in Equation D.2 was used to propagate the individual sources of error for each measurement component [57].

$$y = f(x_0, x_1, x_2, \ldots, x_n) \tag{D.1}$$

$$\sigma_y^2 \cong \sum \sigma_i^2 \left(\frac{\partial y}{\partial x_i}\right)^2 \tag{D.2}$$

Note that Equation D.2 assumed that co-variance terms were insignificant by assuming that variables were un-correlated. A summary of the measurement uncertainties is shown in Table D-1.

Table D-1: Typical measurement uncertainties for a 95% confidence interval

Measurement	Uncertainty sources	Uncertainty value
Thermocouple temperature measurements	- RTD calibration - Standard deviation in measured data for averaged measurements	Larger of: σ_T = ± 0.50 ºC or $\sigma_T = \frac{1}{N-1}\sqrt{(\bar{T} - T_i)^2}$
Inlet flow rate measurement	- Flow meter system accuracy - Data acquisition gain and offset error	$\frac{\sigma_Q}{Q}$ = ± 0.6%
Heat load	- Measured temperature rise from inlet to outlet - Inlet flow rate uncertainty	$\sigma_{\dot{q}}$ = ± 1400 W

Measurement	Uncertainty sources	Uncertainty value
Electrical power	- Heater and shunt voltage transmitter calibration - Shunt resistance uncertainty	$\frac{\sigma_{P_e}}{P_e}$ = ± 0.4%
Thermocouple tip position	- Probe tip diameter - Probe straightness	σ_{x_i} = ± 3 mm
Velocity measurement position	- Manual location of beam crossing at z = 0 - Local variation of water refractive index	σ_x = ± 0.1 mm σ_y = ± 0.1 mm σ_z = ± 0.1 mm + 0.3%
Average velocity	- Statistical uncertainty from sample count n over measurement period	$\frac{\sigma_{u_i}}{u_i} = \frac{1}{\sqrt{n}}$

D.1 Thermocouple Measurements

The thermocouple and data acquisition instrument uncertainties were introduced in Table 3-13 and Table 3-16. All thermocouples were T-type conforming to special limits of error, with a quoted accuracy of ± 0.5 ºC. The overall typical accuracy of the data acquisition system operating in high speed mode was quoted as ± 0.88 ºC, with the cold-junction compensation uncertainty being the dominant source of error. Applying the error propagation equation, the uncertainty in the uncalibrated thermocouple measurements σ_T was estimated to be:

$$\sigma_T \cong \sqrt{(0.5\ ℃)^2 + (0.88\ ℃)^2} = 1.0\ ℃$$

As described in section B.1, each thermocouple probe was calibrated against a precision RTD thermometer in order to reduce this uncertainty. The uncertainty in the reference temperature readout was stated to be ± 0.025 ºC which was deemed insignificant with respect to the uncertainty in the uncalibrated temperatures. A linear least-squares fit to a straight line in the form $T_{cal} = aT + b$ was performed. The uncertainty in the calibrated temperatures was taken to be the largest of the data acquisition system resolution (± 0.1 ºC) or the uncertainty from the calibration fit parameters (± 0.027 ºC). It was also assumed that the resulting accuracy would be at least one order of magnitude lower than the reference thermometer instrumentation, noted above as ± 0.025 ºC. Therefore, the quoted accuracy of the

calibrated temperature measurements was ± 0.25 ºC for a 68% confidence interval, or ± 0.5 ºC for a 95% confidence interval.

For temperature measurements that were averaged over a period of time, the standard deviation was also calculated using Equation D.3 [57]:

$$\sigma_T \cong s_T = \frac{1}{N-1}\sum(\bar{T} - T_i) \tag{D.3}$$

For averaged temperature measurements, the reported uncertainty is the larger value of 0.5ºC (instrument uncertainty) or the value from Equation D.3.

D.2 Flow Rate Measurement

The magnetic flow meter and data acquisition system accuracies were introduced in Table 3-11 and Table 3-16. In order to estimate the accuracy of the flow rate measurement, the accuracy of the flow meter (overall system accuracy) as well as the data acquisition system (maximum gain and offset errors) were considered. The absolute uncertainties for each component are considered below for a typical inlet flow rate of 30 L/min.

Flow meter system uncertainty:

$$\sigma_{meter} = 30\ \text{L/min} \times 0.005 = 0.15\ \text{L/min}$$

Data acquisition gain error:

$$I_{output} = \frac{30\ \text{L/min}}{36\ \text{L/min}} \times 16\ \text{mA} + 4\ \text{mA} = 17.3\ \text{mA}$$

$$\sigma_{gain} = 36\ \text{L/min} \times \frac{\left(0.0018 \times I_{output}\right)}{20\ \text{mA} - 4\ \text{mA}} = 0.07\ \text{L/min}$$

Data acquisition offset error:

$$\sigma_{offset} = 36\ \text{L/min} \times \frac{(0.0006 \times 21.5\ \text{mA})}{20\ \text{mA} - 4\ \text{mA}} = 0.03\ \text{L/min}$$

Inlet flow rate measurement uncertainty:

$$\sigma_{inlet} = \sqrt{(\sigma_{meter})^2 + \left(\sigma_{gain}\right)^2 + \left(\sigma_{offset}\right)^2}$$

$$\sigma_{inlet} = \sqrt{(0.15\ \text{L/min})^2 + (0.07\ \text{L/min})^2 + (0.03\ \text{L/min})^2} = 0.17\ \text{L/min}$$

D.3 Heat Load Measurements

The steady state heat load of the test section was calculated from the inlet flow rate Q and temperature rise between the inlet and outlets:

$$\dot{q}_{TS} = Q_{inlet}\rho_{inlet}c_{P_{inlet}}(T_{outlet} - T_{inlet}) \tag{D.4}$$

The fluid properties ρ and c_P were evaluated at 1 atm and the measured inlet temperature using XSteam, an implementation of IAPWS-IF97 [68]. Applying Equation D.2, the uncertainty in the heat load $\sigma_{\dot{q}}$ can be estimated from:

$$\sigma_{\dot{q}}^2 \cong \sigma_Q^2\left(\frac{\partial \dot{q}}{\partial Q}\right)^2 + \sigma_\rho^2\left(\frac{\partial \dot{q}}{\partial \rho}\right)^2 + \sigma_{c_P}^2\left(\frac{\partial \dot{q}}{\partial c_P}\right)^2 + \sigma_{\Delta T}^2\left(\frac{\partial \dot{q}}{\partial \Delta T}\right)^2 \tag{D.5}$$

$$\sigma_{\dot{q}}^2 \cong \sigma_Q^2\left(\rho_{inlet}c_{P_{inlet}}\Delta T\right)^2 + \sigma_\rho^2\left(Q_{inlet}c_{P_{inlet}}\Delta T\right)^2 +$$

$$\sigma_{c_P}^2(Q_{inlet}\rho_{inlet}\Delta T)^2 + \sigma_{\Delta T}^2\left(Q_{inlet}\rho_{inlet}c_{P_{inlet}}\right)^2 \tag{D.6}$$

Uncertainties in the fluid properties resulting from uncertainties in IAPWS and from uncertainties in the inlet fluid temperature were determined to be insignificant and disregarded; further discussion is provided in section D.3.1. Therefore, the estimated uncertainty in the heat load is determined from:

$$\sigma_{\dot{q}} \cong \sqrt{\sigma_Q^2\left(\rho_{inlet}c_{P_{inlet}}\Delta T\right)^2 + \sigma_{\Delta T}^2\left(Q_{inlet}\rho_{inlet}c_{P_{inlet}}\right)^2} \qquad \text{(D.7)}$$

For the reference case for 30 L/min and 20 kW shown in Table D-2:

$$\sigma_{\dot{q}} \cong \dot{q}\sqrt{\left(\frac{\sigma_Q}{Q_{inlet}}\right)^2 + \left(\frac{\sigma_{\Delta T}}{\Delta T}\right)^2} = 19.77\text{ kW} \times \sqrt{(0.0057)^2 + (0.074)^2} = 1.5\text{ kW}$$

D.3.1 Impact of Fluid Property Uncertainties

In this section, the relative magnitudes of the uncertainties in Equation D.5 are examined in order to estimate their relative importance in determining the uncertainty in the measured heat load.

The estimated uncertainty in the heat load is shown in Equation D.5. Written in terms of relative uncertainties:

$$\frac{\sigma_{\dot{q}}}{\dot{q}} \cong \sqrt{\left(\frac{\sigma_Q}{Q_{inlet}}\right)^2 + \left(\frac{\sigma_\rho}{\rho_{inlet}}\right)^2 + \left(\frac{\sigma_{c_P}}{c_{P_{inlet}}}\right)^2 + \left(\frac{\sigma_{\Delta T}}{\Delta T}\right)^2} \qquad \text{(D.8)}$$

Note that the relative uncertainty in the heat load can be determined by adding the relative uncertainties of the parameters in quadrature. For the reference flow rate (30 L/min) and power level (20 kW), example steady-state experimental conditions are shown in Table D-2.

Table D-2: Example steady state conditions for the reference test case (20 kW, 30 L/min).

Parameter	Value	Absolute Uncertainty	Relative Uncertainty
T_{inlet} [ºC]	26.10	0.5	1.9%
T_{outlet} [ºC]	35.62	0.5	1.4%
ΔT [ºC]	9.52	0.71	7.4%
Q_{inlet} [L/min]	29.89	0.17	0.57%

Table D-3: Sensitivity of density and isobaric heat capacity for the reference test case (20 kW, 30 L/min) at P = 1 atm

Parameter	T_{inlet}	$T_{inlet} - \sigma_T$	$T_{inlet} + \sigma_T$
ρ (T) [kg/m^3]	996.76	996.89 (+0.014%)	996.63 (-0.013%)
C_P (T) [kJ/kg·K]	4.1814	4.1816 (+0.005%)	4.1812 (-0.005%)

The sensitivity of the fluid properties to temperature was examined and is shown in Table D-3. For the reference test case and the inlet temperature varying by two standard deviations from the mean, ρ varied by about 0.014% and C_P varied by about 0.0005%. These relative uncertainty values are 2 – 3 orders of magnitude smaller than the relative uncertainty in the measured ΔT, suggesting that these factors can be disregarded in determining the overall uncertainty in the heat load.

Additionally, the IAWPS provides uncertainty estimates for the IAWPS-IF97 formulation. For the conditions shown in Table D-2, $\sigma_\rho \approx 0.2\%$ and $\sigma_{C_P} \approx 0.001\%$ [69]. As with the above discussion, these values are small with respect to the uncertainty in ΔT. Applying Equation D.8 further illustrates this point:

$$\frac{\sigma_{\dot{q}}}{\dot{q}} \cong \sqrt{(0.0057)^2 + (0.002)^2 + (0.00001)^2 + (0.074)^2} = 7.42\%$$

This result demonstrates that the dominant factor in the heat load uncertainty is the uncertainty in the measured temperature (7.4%) and that disregarding the uncertainty in the fluid properties does not significantly impact the estimate of the heat load uncertainty.

D.4 Electrical Power Measurements

Example data for the reference test case at P_e = 20 kW is shown as an average over a five-minute period in Table D-4 and is used in the following sample calculations. Details for how the instrument uncertainty was estimated follow in section D.4.1 through section D.4.3.

Table D-4: Example five-minute averaged power measurement data for the reference test case at P_e = 20 kW

Parameter	Average Value	Standard Deviation	Instrument Uncertainty
V_{TS} [V]	48.452	0.003	0.060
V_{shunt} [mV]	10.211	0.004	0.035
P_e [kW]	19.790	0.008	0.077

D.4.1 Voltage Measurement Uncertainty

As discussed in section B.2, the test section voltage transmitter and data acquisition system channel used to measure the test section voltage was calibrated against a reference multimeter. A linear least-squares fit to a straight line in the form of $V_{TS} = aI_{transmitter} + b$ was performed. The uncertainty in the voltage measurement was taken to be the larger value of the uncertainty from the calibration fit parameters (± 32 mV), or one order of magnitude worse than the quoted accuracy of the reference instrument (± 6 mV). Therefore, the uncertainty in the voltage measurements was estimated to be:

$$\sigma_V \cong 60\ mV$$

D.4.2 Current Measurement Uncertainty

As discussed in section B.2, the voltage transmitter and data acquisition system channel used to measure the shunt resistor was calibrated against a reference multimeter. A linear least-squares fit to a straight line in the form of $V_{shunt} = aI_{transmitter} + b$ was performed. The uncertainty in the voltage measurement was taken to be the larger value of the uncertainty from the calibration fit parameters (± 0.015 mV), or one order of magnitude worse than the quoted accuracy of the reference instrument (± 0.0035 mV). Therefore, the uncertainty in the shunt voltage measurements was estimated to be:

$$\sigma_{V_{shunt}} \cong 0.035\ mV$$

The shunt was quoted as having a resistance $R_{shunt} = 25.000 \pm 0.025\ \mu\Omega$. The current through the shunt can be calculated using Ohm's law:

$$I = \frac{V_{shunt}}{R_{shunt}}$$

Applying Equation D.2 to estimate the uncertainty in the current measurement:

$$\sigma_I^2 \cong \left(\frac{\sigma_{V_{shunt}}}{R_{shunt}}\right)^2 + \left(\frac{\sigma_{R_{shunt}} V_{shunt}}{R_{shunt}^2}\right)^2$$

$$\sigma_I^2 \cong \left(\frac{3.5\times10^{-5}\text{V}}{2.5\times10^{-5}\Omega}\right)^2 + \left(\frac{(2.5\times10^{-8}\Omega)(V_{shunt})}{(2.5\times10^{-5}\Omega)^2}\right)^2 \quad \text{(D.9)}$$

Applying reference data shown in Table D-4:

$$I = \frac{10.211\times10^{-3}\ \text{V}}{2.5\times10^{-5}\Omega} = 408.4\ \text{A}$$

$$\sigma_I \cong \sqrt{\left(\frac{3.5\times10^{-5}\text{V}}{2.5\times10^{-5}\Omega}\right)^2 + \left(\frac{(2.5\times10^{-8}\Omega)(10.211\times10^{-3}\text{V})}{(2.5\times10^{-5}\Omega)^2}\right)^2} = 1.5\ \text{A}$$

D.4.3 Power Measurement Uncertainty

The electrical power delivered to the test section heaters was calculated from the product of the measured heater voltage drop and current. Applying Equation D.2:

$$P = VI$$

$$\sigma_P^2 \cong (\sigma_V I)^2 + (\sigma_I V)^2 \quad \text{(D.10)}$$

Applying reference data shown in Table D-4:

$$P = (48.45\ \text{V})(408.4\ \text{A}) = 1.979\times10^4\ \text{W}$$

$$\sigma_P \cong \sqrt{\left((0.060\ \text{V})(408.4\ \text{A})\right)^2 + \left((1.5\ \text{A})(48.45\ \text{V})\right)^2} = 77\ \text{W}$$

D.5 Positional Uncertainties

D.5.1 Location of Movable Thermocouples

As described in section 3.2.3, the internal test section temperature probes were repositionable. Thermocouple depths were pre-marked on the thermocouple sheaths at an interval of ½ tube bank pitch (14.5 mm) with a reference marking corresponding to the vessel center as located with the LDV laser. Positional uncertainty in the location of the probe tip resulted from the overall bulk of the probe tip diameter (3.2 mm), straightness of the probe assemblies, and play within the feedthrough fitting. The overall estimated positional uncertainty of the thermocouple was ± 3 mm.

D.5.2 Location of LDV Measurement Volume

The LDV measurement probe was mounted to a programmable 3-axis traverse mechanism. The traverse mechanism was controlled by stepper motors capable of moving the measurement probe in increments of 0.0125 mm in the horizonal directions (*x* and *z*) and 0.00625 mm increments in the vertical direction (*y*). In practice, the actual positional uncertainty is higher due to the manual process of referencing the location of the beam crossing to the internal *xy*-center of the test section front plate (described in section A.3.3). The uncertainty in the *x* and *y* coordinates is estimated to be ± 0.1 mm.

As described in section C.3, a position correction function was applied to the traverse depth coordinate to account for the change in refractive index between air and water:

$$z_{water} = z_{traverse} \frac{\tan \kappa_{air}}{\tan \kappa_{water}} \tag{D.11}$$

$$\kappa_{water} = \sin^{-1}\left(\frac{n_{air}}{n_{water}} \left(\sin \kappa_{air} \right) \right) \tag{D.12}$$

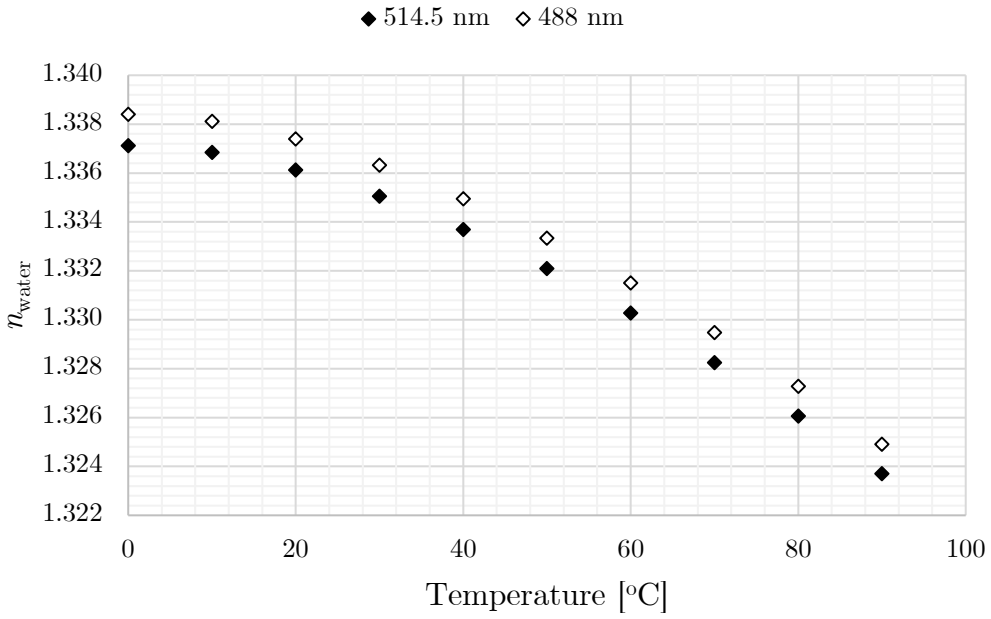

Figure D-1: Variation of the index of refraction of water n_{water} with temperature at p = 100 kPa [70]

As shown in Figure D-1, the refractive index of water (n_{water}) varies with temperature. When evaluating Equations D.11 and D.12, n_{air} and n_{water} were assumed to be uniform, with n_{water} evaluated at the measured outlet temperature. In practice, significant local temperature variations existed within the test section. This temperature variation resulted in an uncertainty in the refractive index when applying the position correction equation. The positional uncertainty associated with this variation would depend on the depth of the beam crossing within the tank (higher uncertainty at higher measurement depth). Applying the small-angle approximation ($\sin\theta \approx \theta$ and $\tan\theta \approx \theta$) to Equations D.11 and D.12 shows that the relationship between the water refractive index and the corrected beam crossing depth can be approximated as linear for small angles:

$$\kappa_{water} = \sin^{-1}\left(\frac{n_{air}}{n_{water}}\,(\sin\kappa_{air})\right) \approx \frac{n_{air}}{n_{water}}\,\kappa_{air}$$

$$z_{water} = z_{traverse}\frac{\tan\kappa_{air}}{\tan\kappa_{water}} \approx z_{traverse}\frac{\kappa_{air}}{\kappa_{water}}$$

$$z_{water} \approx z_{traverse} \frac{n_{air}}{n_{water}}$$

Table D-5: Water refractive indices (λ = 488 nm) evaluated at 100 kPa for typical inlet, outlet, and maximum observed internal temperatures for reference flow rate tests (30 L/min)

P_e [kW]	T_{in} [°C]	T_{out} [°C]	T_{max} [°C]	$n(T_{in})$	$n(T_{out})$	$n(T_{max})$
10	20.0	24.8	27.5	1.33739	1.33688	1.33659
20	26.1	35.6	40.0	1.33674	1.33555	1.33495
38	40.8	58.7	65.8	1.33482	1.33175	1.33033

In order to consider the maximum change in position caused by these variations in refractive index, the 38 kW case shown in Table D-5 was considered. The practical limit on the traverse movement in the *z*-coordinate direction was 220 mm. Evaluating Equations D.11 and D.12 for this temperature range:

At inlet temperature:

$$\kappa_{water} = \sin^{-1}\left(\frac{1.00003}{1.33482}\,(\sin 5.49°)\right) = 4.110°$$

$$z_{water} = 220\text{ mm} \times \frac{\tan 5.49°}{\tan 4.11°} = 294.25\text{ mm}$$

At maximum temperature:

$$\kappa_{water} = \sin^{-1}\left(\frac{1.00003}{1.33033}\,(\sin 5.49°)\right) = 4.124°$$

$$z_{water} = 220\text{ mm} \times \frac{\tan 5.49°}{\tan 4.11°} = 293.25\text{ mm}$$

This yields a variation in predicted depth of up to 1 mm (about 0.3%). Therefore, the estimated positional uncertainty in the measurement volume location resulting from temperature variations in the traverse *z*-coordinate is estimated to be 0.3%.

D.6 Velocity Measurement Uncertainty

At each measurement location, LDV measurements were collected for a period of 120 seconds. In this time period, a total of *n* samples were collected at random time intervals, depending on when particles within the flow passed through the measurement volume and were observed by the detector. The observed values are expected to have an associated statistical uncertainty:

$$\frac{\sigma_{u_i}}{u_i} = \frac{1}{\sqrt{n}} \tag{D.13}$$

Since data was collected for fixed 120 second intervals, the measured velocities were better determined in regions of the vessel where higher LDV data rates were observed. As the measurement depth within the tank was increased, data rates were observed to decrease as a result of increased light absorption.

Appendix E

Temperature Measurement Data

The test section conditions for all temperature measurement tests are summarized in Table E-1. The presented quantities represent time-averaged values over the duration of each entire test.

Table E-1: List of test conditions and measured heat load for the temperature measurement tests

Test ID	Flow [L/min]	Power [kW]	Heat Load [kW]	Inlet T [°C]	Outlet T [°C]	Room T [°C]
0308-00	30.0 ± 0.2	19.93 ± 0.08	19.8 ± 1.5	22.4 ± 0.5	31.9 ± 0.5	22.4 ± 0.5
0309-00	30.0 ± 0.2	39.80 ± 0.20	39.1 ± 1.5	34.3 ± 0.5	53.1 ± 0.5	24.2 ± 0.4
0823-00	29.8 ± 0.2	19.77 ± 0.08	19.8 ± 1.5	26.8 ± 0.5	36.3 ± 0.5	26.8 ± 0.6
0831-00	24.0 ± 0.1	19.77 ± 0.08	19.7 ± 1.2	27.3 ± 0.5	39.1 ± 0.5	25.2 ± 0.5
0908-00	30.1 ± 0.2	9.85 ± 0.04	10.0 ± 1.5	20.0 ± 0.5	24.8 ± 0.5	25.4 ± 0.5
0915-01	30.1 ± 0.2	19.76 ± 0.08	19.7 ± 1.5	28.6 ± 0.5	38.1 ± 0.5	26.6 ± 0.5
0922-00	30.0 ± 0.2	37.58 ± 0.20	36.7 ± 1.5	40.8 ± 0.5	58.7 ± 0.5	28.6 ± 1.2
1011-00	30.0 ± 0.2	19.81 ± 0.08	19.8 ± 1.5	26.2 ± 0.5	35.7 ± 0.5	24.0 ± 0.5
1011-01	29.9 ± 0.2	19.79 ± 0.08	19.8 ± 1.5	26.1 ± 0.5	35.6 ± 0.5	25.5 ± 0.6
1011-02	29.9 ± 0.2	19.78 ± 0.08	19.7 ± 1.5	26.2 ± 0.5	35.7 ± 0.5	26.2 ± 0.5
1017-01	15.1 ± 0.1	9.35 ± 0.04	9.4 ± 0.7	19.8 ± 0.5	28.7 ± 0.5	24.2 ± 0.5
1018-00	8.2 ± 0.1	11.87 ± 0.05	11.6 ± 0.4	23.1 ± 0.5	43.3 ± 0.5	23.8 ± 0.5

E.1 Test Section Heat Balance

The steady state heat load of the test section was calculated from the inlet flow rate Q and temperature rise between the inlet and outlets:

$$\dot{q}_{TS} = Q_{inlet}\rho_{inlet}c_{P\,inlet}(T_{outlet} - T_{inlet}) \quad \text{(E.1)}$$

The heat balance to the test section was calculated as the percentage difference between the measured electrical input power and the measured heat load:

$$\Delta P_e = \frac{P_e - \dot{q}_{TS}}{P_e} \quad \text{(E.2)}$$

The heat balance error was calculated for each test listed in Table E-1 and the results are summarized in Table E-2. In all cases, the heat balance error was less than 3% which was regarded as excellent considering that the exterior walls of the test section were not insulated. The calculated heat balance was also less than the estimated uncertainty in the measured heat load in all cases.

The dominant source of uncertainty in the calculated heat load and resulting heat balance is the uncertainty in the measured inlet and outlet temperatures. For individual temperature measurements with an uncertainty of 0.5ºC, the corresponding uncertainty in the temperature difference is 0.7ºC. This uncertainty was applied for all measurement cases. This resulted in larger relative uncertainties for experiments where the inlet to outlet temperature rise was lower (e.g. – for experiments conducted at 30 L/min, the heat load uncertainty increased as power level is decreased due to a smaller test section ΔT).

In two cases (test IDs 0908-00 and 1017-01), a small negative heat balance was recorded as a result of the calculated heat load being larger than the applied electrical power. It was additionally noted that the inlet temperatures in these two cases was below the room temperature, suggesting that a small heat gain from the surroundings was possible. However, in both cases, the small negative values were attributed to the relatively high uncertainty of the heat load measurements at low power levels – as the magnitude of the negative heat balance was approximately an order of magnitude smaller than the measurement uncertainty.

Table E-2: Heat balance and scaling parameter *Ar* for all tested temperature measurement cases

Test ID	Flow [L/min]	Power [kW]	Heat Load [kW]	Heat Balance [%]	*Ar*
0308-00	30.0 ± 0.2	19.93 ± 0.08	19.8 ± 1.5	0.9 ± 7.5	3.05×10^{-3}
0309-00	30.0 ± 0.2	39.80 ± 0.20	39.1 ± 1.5	1.9 ± 3.8	8.96×10^{-3}
0823-00	29.8 ± 0.2	19.77 ± 0.08	19.8 ± 1.5	0.1 ± 7.4	3.53×10^{-3}
0831-00	24.0 ± 0.1	19.77 ± 0.08	19.7 ± 1.2	0.4 ± 6.0	7.05×10^{-3}
0908-00	30.1 ± 0.2	9.85 ± 0.04	10.0 ± 1.5	-1.8 ± 15.0	1.28×10^{-3}
0915-01	30.1 ± 0.2	19.76 ± 0.08	19.7 ± 1.5	0.4 ± 7.5	3.63×10^{-3}
0922-00	30.0 ± 0.2	37.58 ± 0.20	36.7 ± 1.5	1.6 ± 4.0	9.43×10^{-3}
1011-00	30.0 ± 0.2	19.81 ± 0.08	19.8 ± 1.5	0.3 ± 7.5	3.43×10^{-3}
1011-01	29.9 ± 0.2	19.79 ± 0.08	19.8 ± 1.5	0.2 ± 7.5	3.44×10^{-3}
1011-02	29.9 ± 0.2	19.78 ± 0.08	19.7 ± 1.5	0.2 ± 7.5	3.45×10^{-3}
1017-01	15.1 ± 0.1	9.35 ± 0.04	9.4 ± 0.7	-0.3 ± 7.9	1.02×10^{-2}
1018-00	8.2 ± 0.1	11.87 ± 0.05	11.6 ± 0.4	2.4 ± 3.6	1.03×10^{-1}

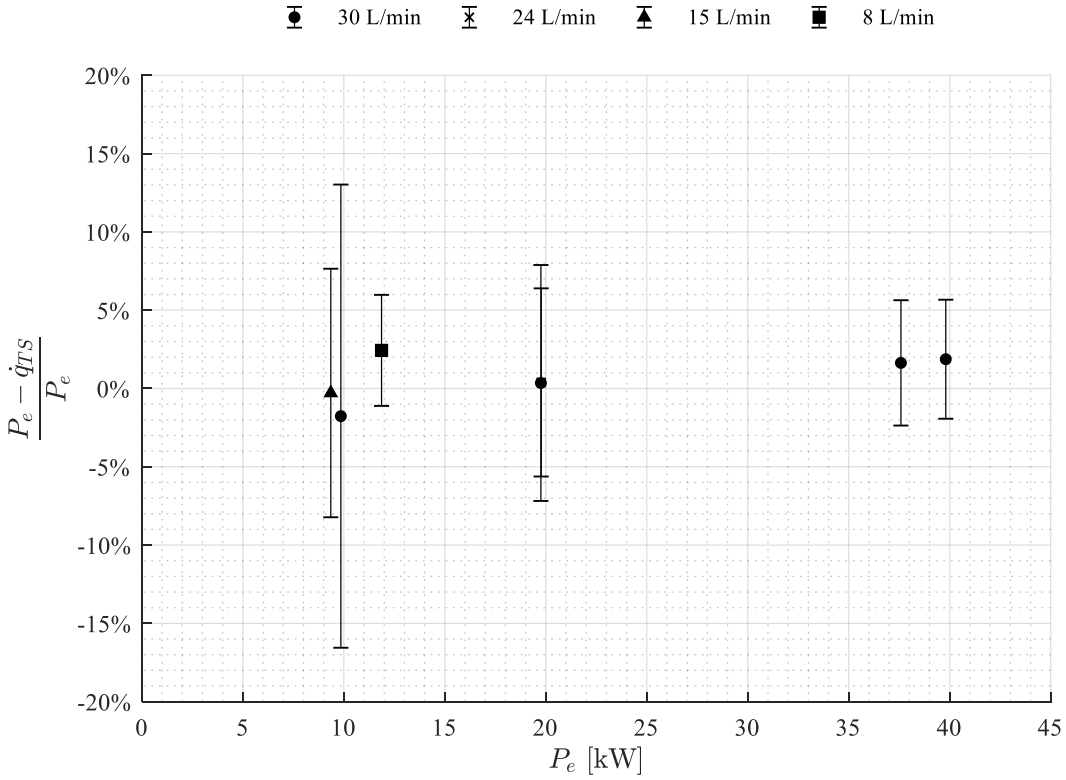

Figure E-1: Typical heat balance versus test section power. The reported uncertainty in the calculated heat balance was determined using the relative uncertainty in the measured test section heat load

E.2 Time-Averaged Temperature Data

This section presents the average and standard deviation temperature measurements from each experimental run:

$$\bar{T}(x) = \frac{1}{N}\sum T(x, t_i) \tag{E.3}$$

$$s_T = \sqrt{\frac{1}{N-1}\sum(\bar{T}(x) - T(x, t_i))^2} \tag{E.4}$$

The temperature measurement at each (*x*, *y*, *z*) coordinate represents an average of measurements collected at a sampling rate of 10 Hz over a period of 300 seconds.

Table E-3: Thermocouple feedthrough locations (*y* and *z* coordinates)

ID	*y* [mm]	*z* [mm]	ID	*y* [mm]	*z* [mm]
TCM1-00	58.1	73.3	TCM1-07	116.2	347.8
TCM1-01	58.1	164.7	TCM1-08	0.0	73.3
TCM1-02	58.1	256.2	TCM1-09	0.0	164.7
TCM1-03	58.1	347.6	TCM1-10	0.0	256.2
TCM1-04	58.1	439.1	TCM1-11	0.0	347.6
TCM1-05	116.2	164.7	TCM1-12	0.0	439.1
TCM1-06	116.2	256.2			

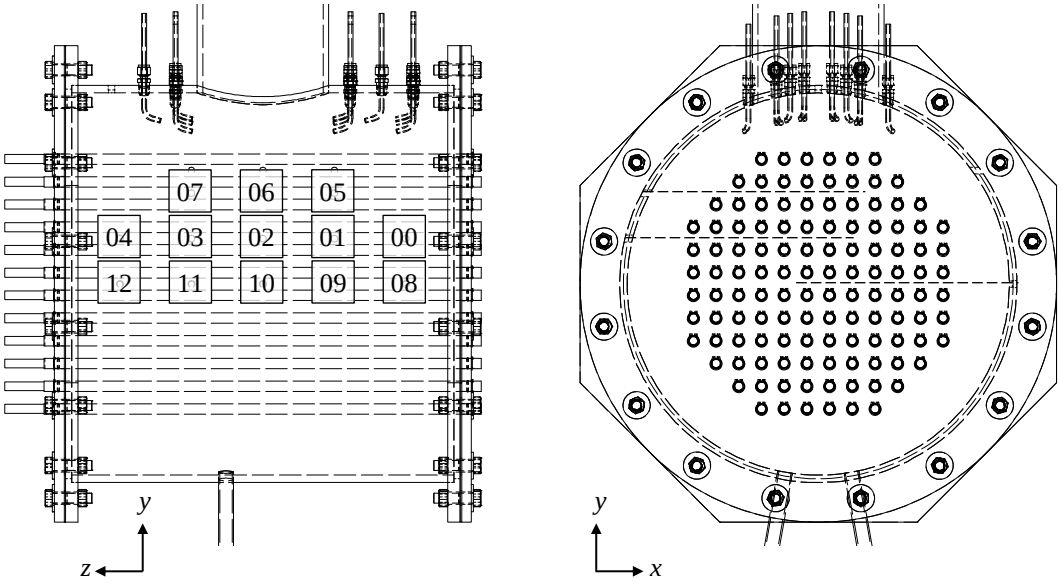

Figure E-2: Location of thermocouple feedthrough fittings (left) and lines traversed by thermocouples (right)

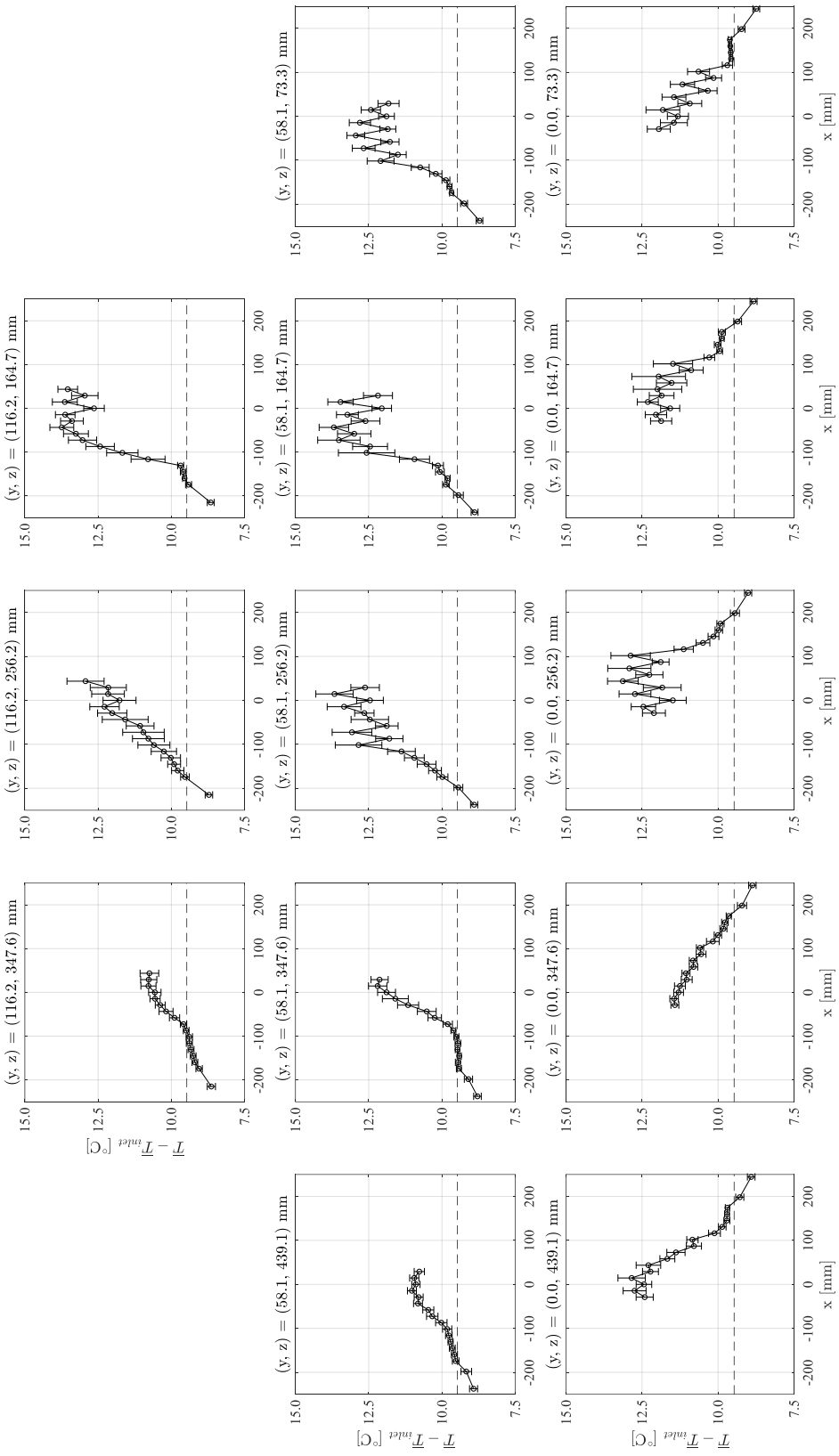

Figure E-3: Time-averaged temperature measurement map for test ID 0308-00 (P_e = 19.93 kW, Q = 30.0 L/min, T_{inlet} = 22.4 °C, ΔT = 9.5 °C, Ar = 0.00305). The dashed line corresponds to outlet conditions and error bars correspond to s_T

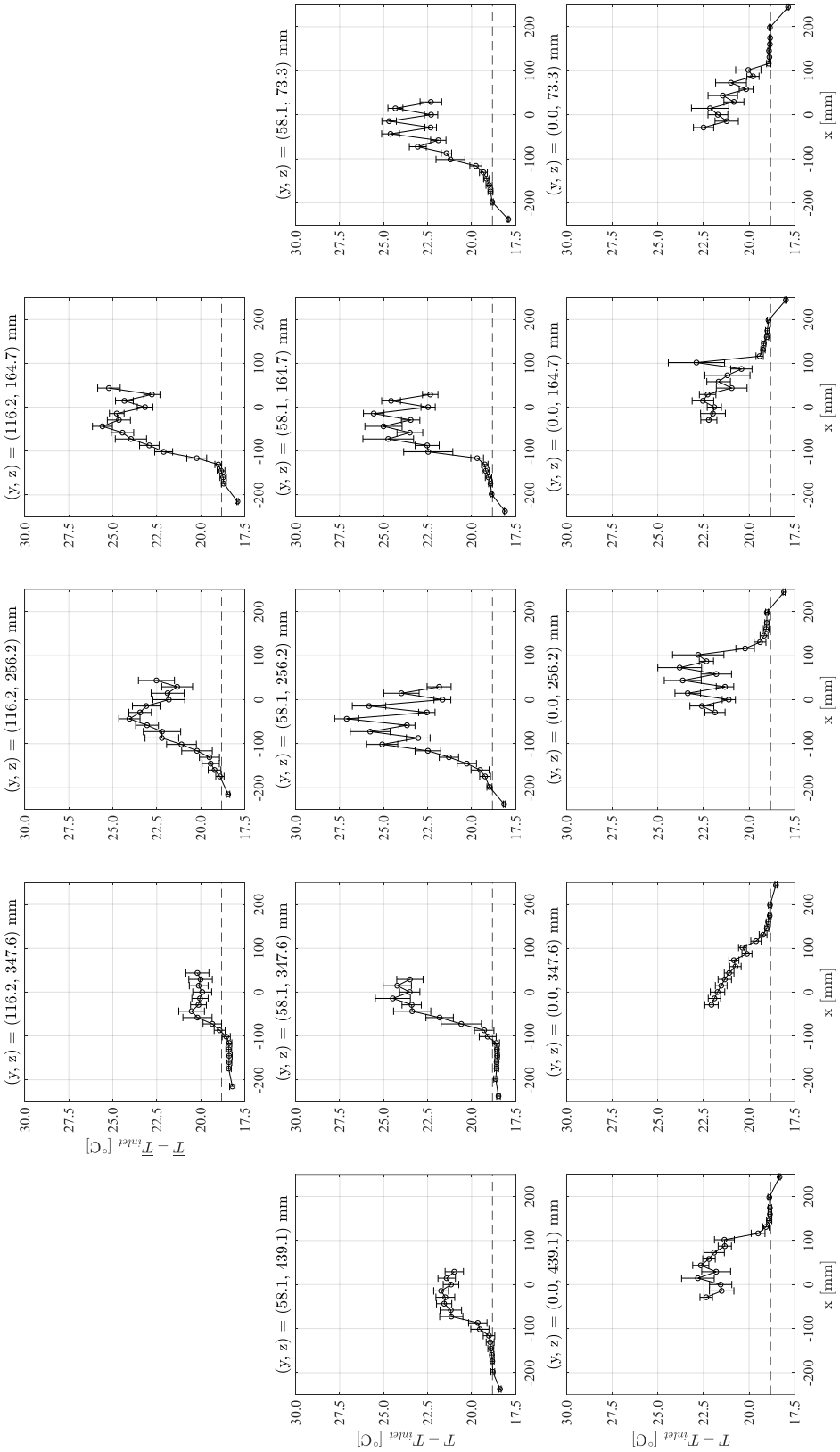

Figure E-4: Time-averaged temperature measurement map for test ID 0309-00 (P_e = 39.80 kW, Q = 30.0 L/min, T_{inlet} = 34.3 °C, ΔT = 18.8 °C, Ar = 0.00896). The dashed line corresponds to outlet conditions and error bars correspond to s_T

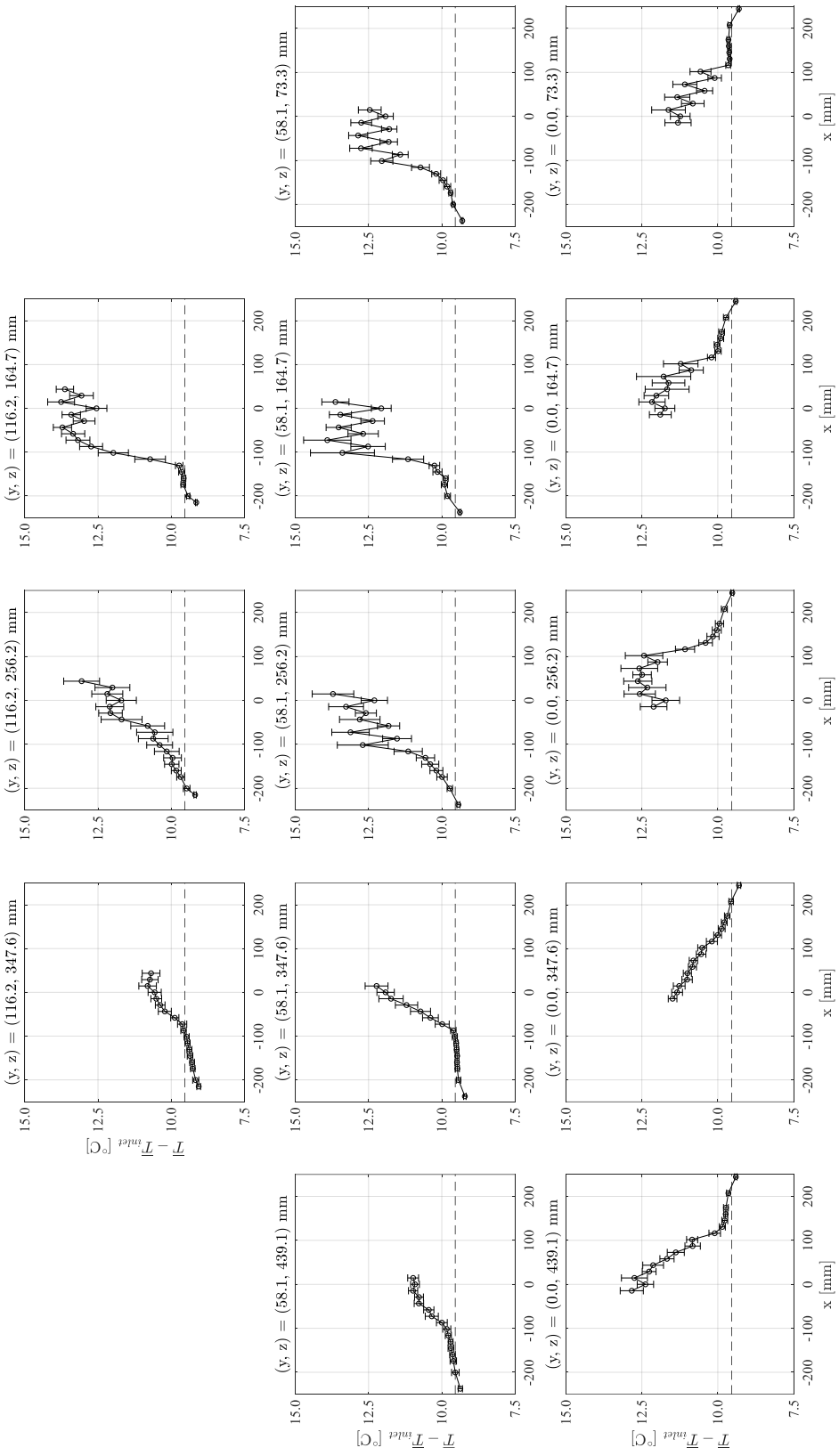

Figure E-5: Time-averaged temperature measurement map for test ID 0823-00 (P_e = 19.77 kW, Q = 29.8 L/min, T_{inlet} = 26.8 °C, ΔT = 9.5 °C, Ar = 0.00353). The dashed line corresponds to outlet conditions and error bars correspond to s_T

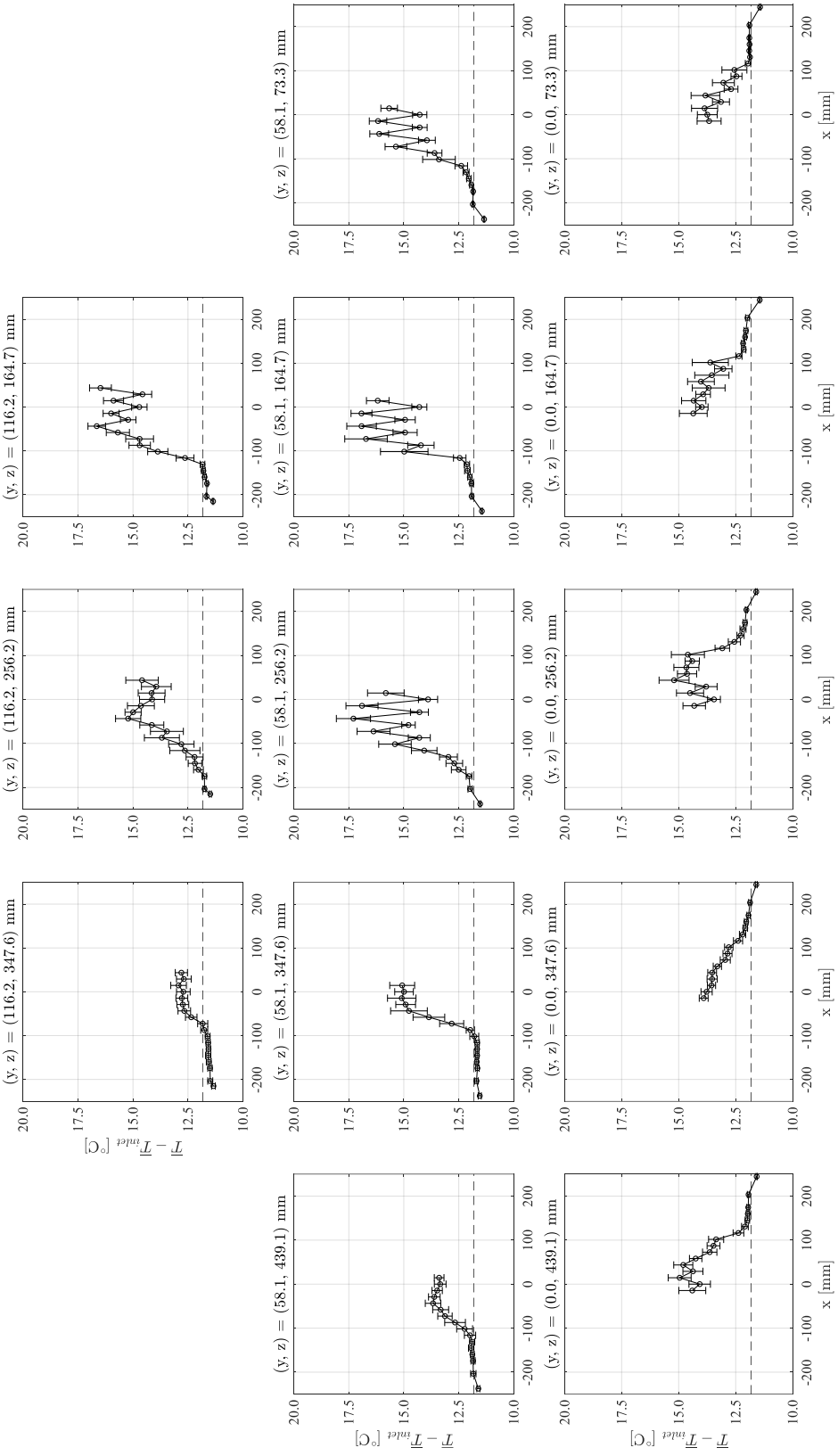

Figure E-6: Time-averaged temperature measurement map for test ID 0831-00 (P_e = 19.77 kW, Q = 24.0 L/min, T_{inlet} = 27.3 °C, ΔT = 11.8 °C, Ar = 0.00705). The dashed line corresponds to outlet conditions and error bars correspond to s_T

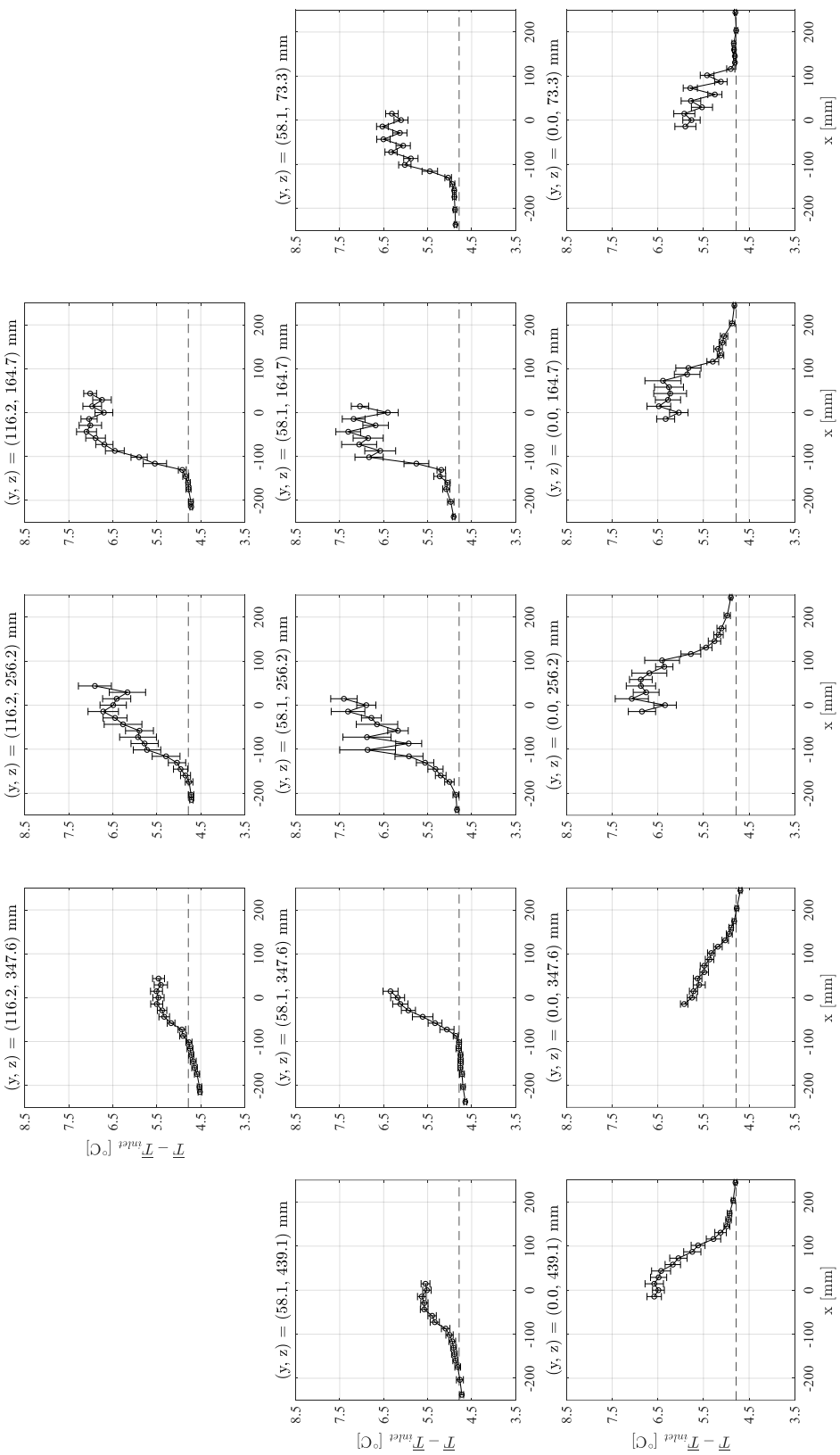

Figure E-7: Time-averaged temperature measurement map for test ID 0908-00 (P_e = 9.85 kW, Q = 30.1 L/min, T_{inlet} = 20.0 °C, ΔT = 4.8 °C, Ar = 0.00128). The dashed line corresponds to outlet conditions and error bars correspond to s_T

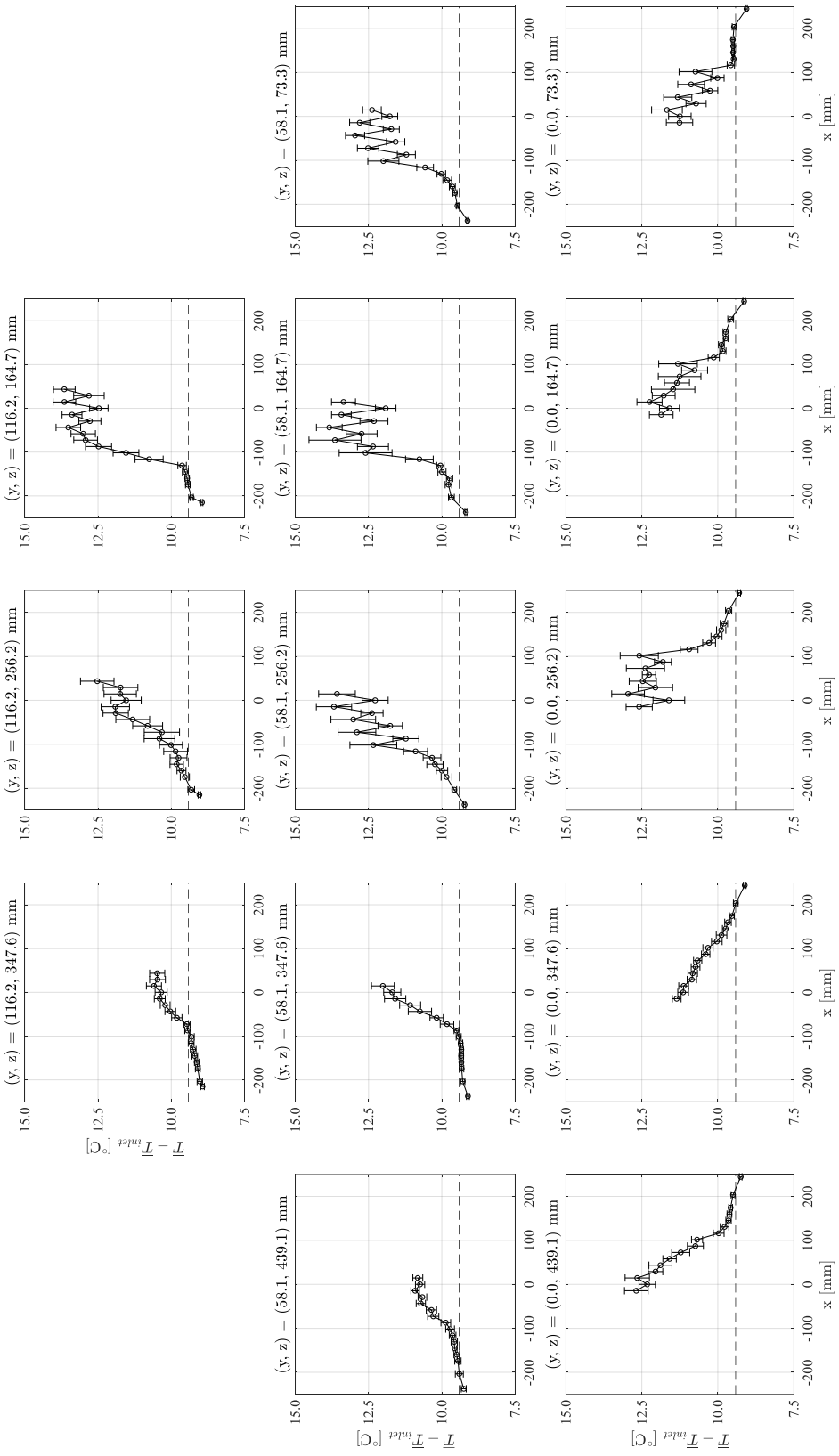

Figure E-8: Time-averaged temperature measurement map for test ID 0915-01 (P_e = 19.76 kW, Q = 30.1 L/min, T_{inlet} = 28.6 °C, ΔT = 9.5 °C, Ar = 0.00363). The dashed line corresponds to outlet conditions and error bars correspond to s_T

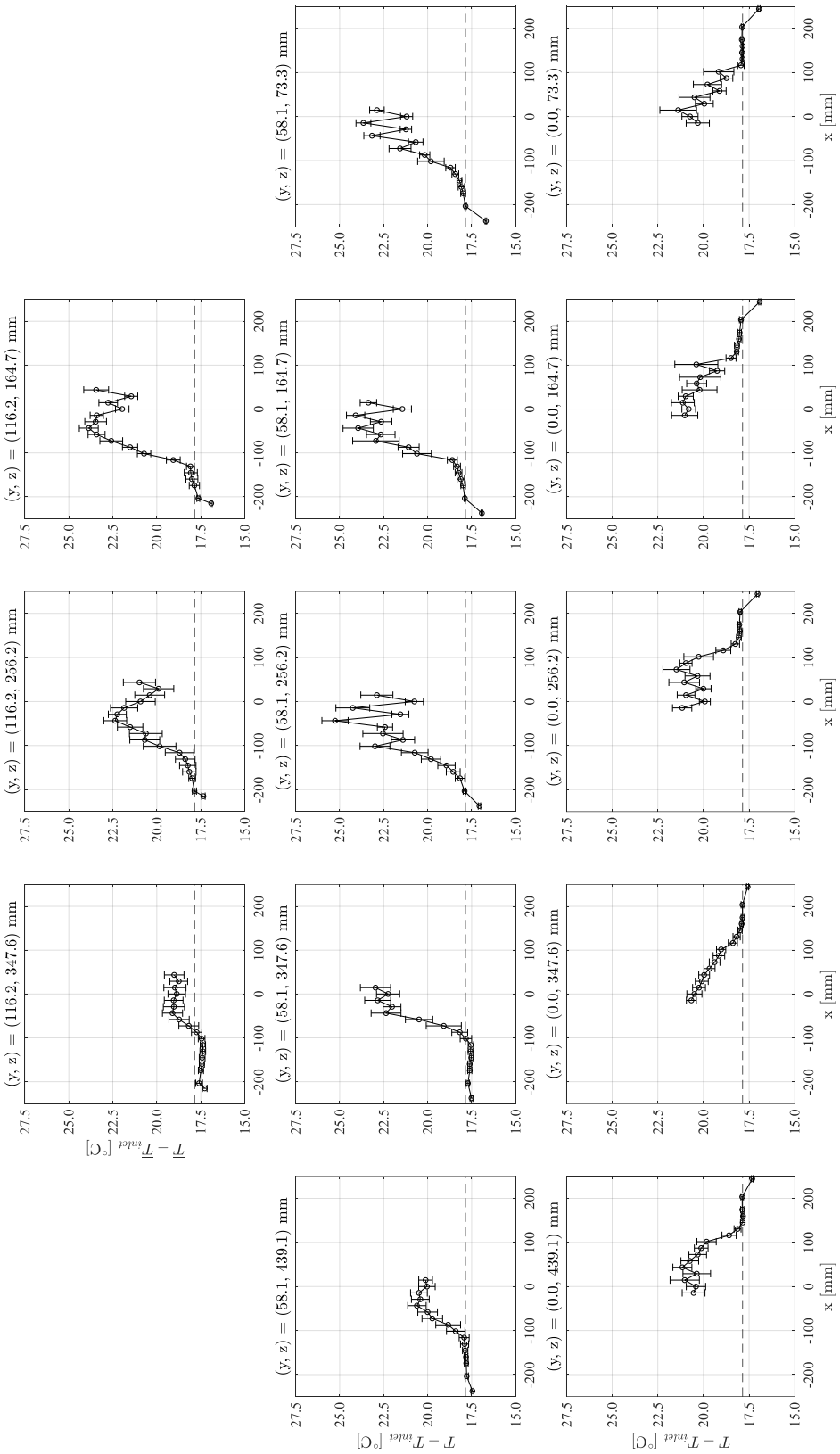

Figure E-9: Time-averaged temperature measurement map for test ID 0922-00 (P_e = 37.58 kW, Q = 30.0 L/min, T_{inlet} = 40.8 °C, ΔT = 17.9 °C, Ar = 0.00943). The dashed line corresponds to outlet conditions and error bars correspond to s_T

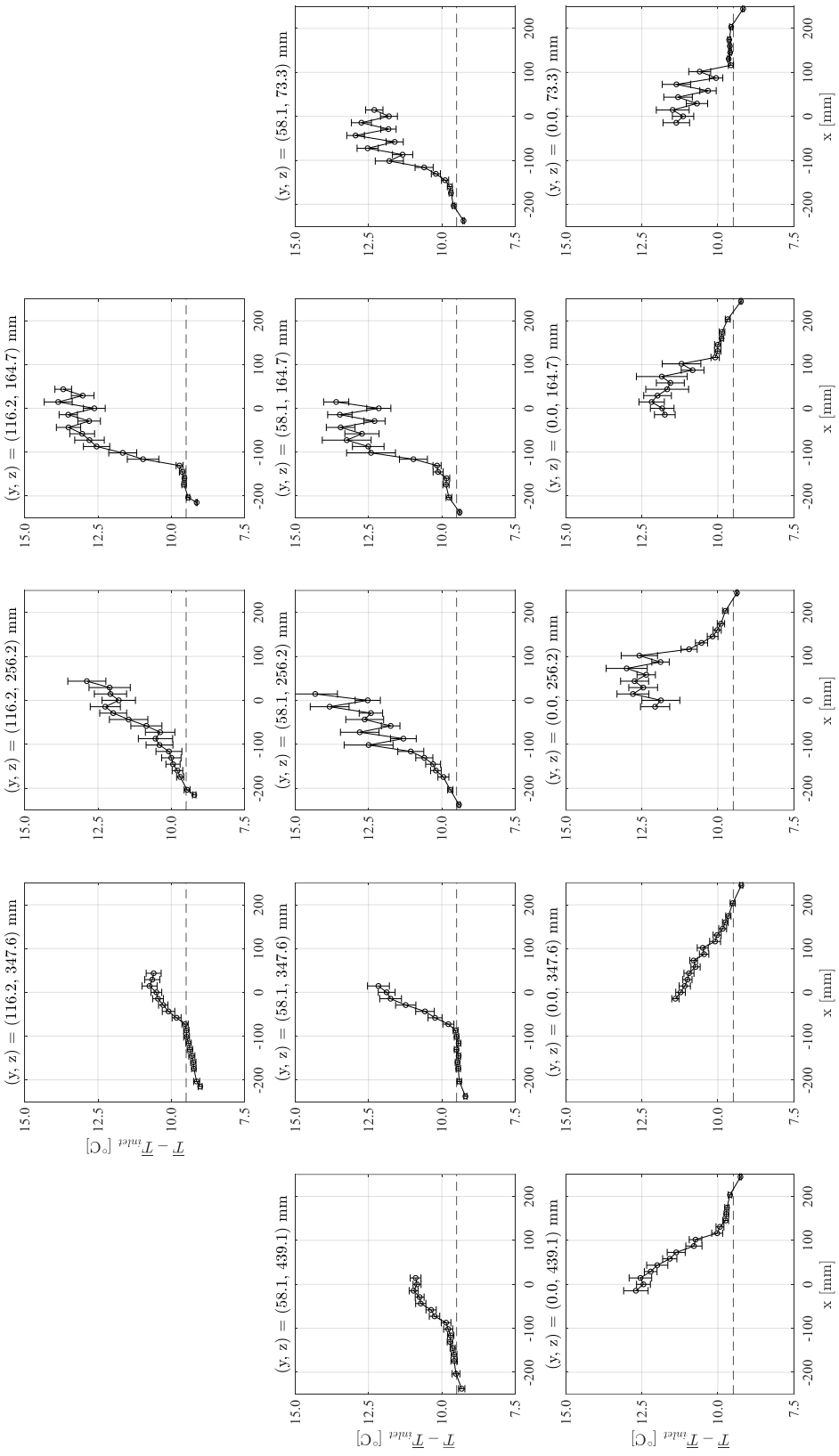

Figure E-10: Time-averaged temperature measurement map for test ID 1011-00 (P_e = 19.81 kW, Q = 30.0 L/min, T_{inlet} = 26.2 °C, ΔT = 9.5 °C, Ar = 0.00343). The dashed line corresponds to outlet conditions and error bars correspond to s_T

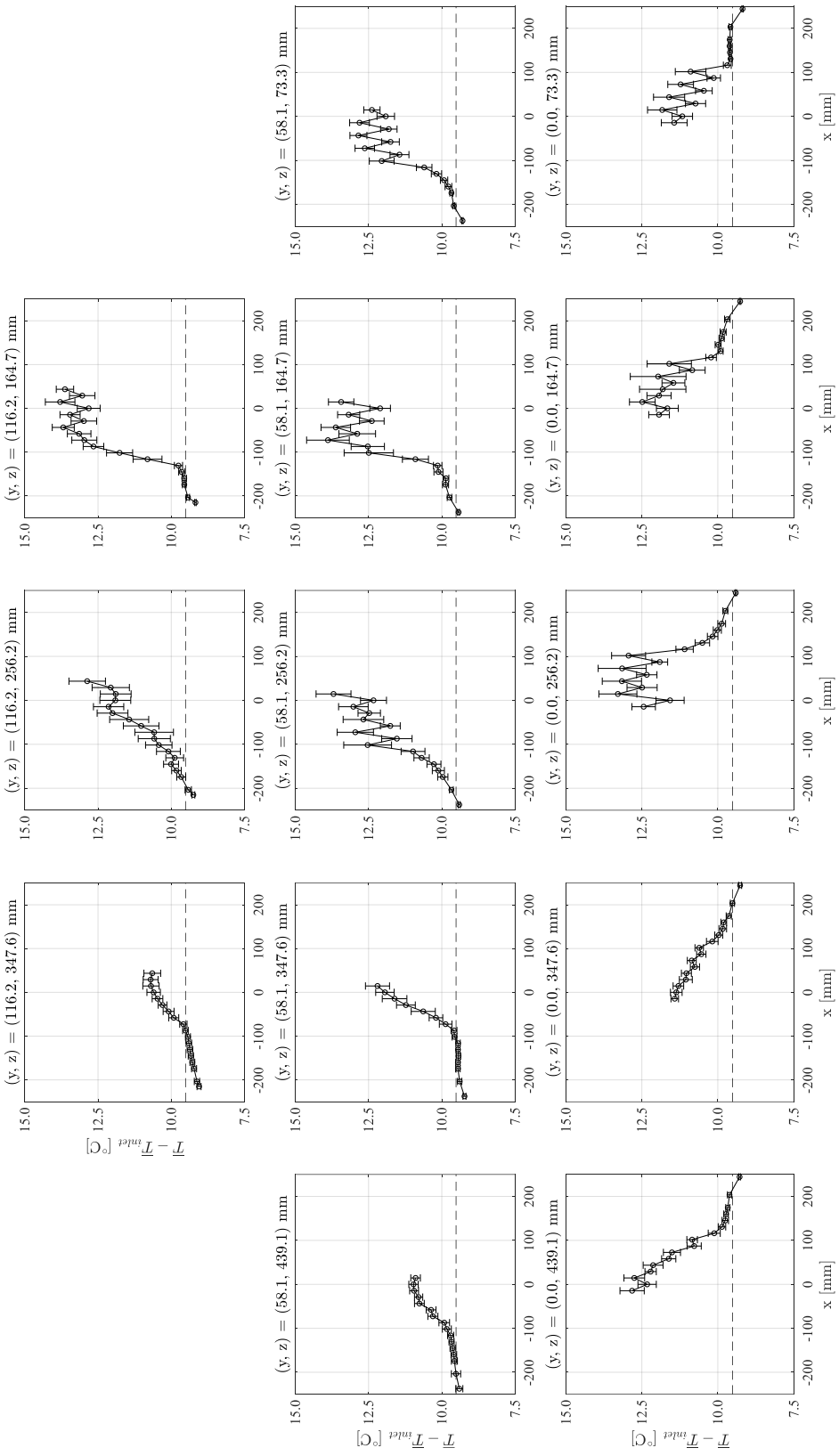

Figure E-11: Time-averaged temperature measurement map for test ID 1011-01 (P_e = 19.79 kW, Q = 29.9 L/min, T_{inlet} = 26.1 °C, ΔT = 9.5 °C, Ar = 0.00344). The dashed line corresponds to outlet conditions and error bars correspond to s_T

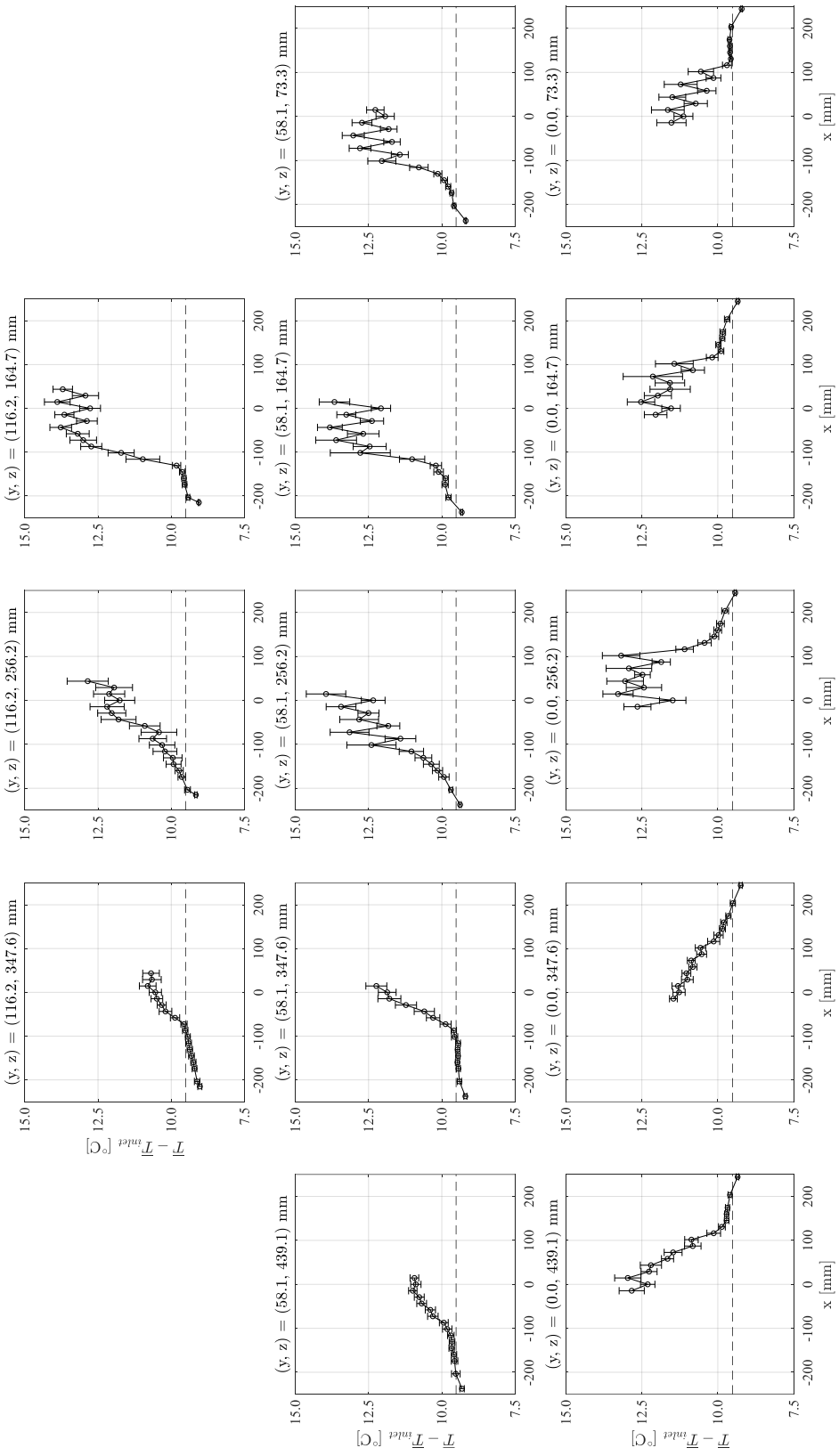

Figure E-12: Time-averaged temperature measurement map for test ID 1011-02 (P_e = 19.78 kW, Q = 29.9 L/min, T_{inlet} = 26.2 °C, ΔT = 9.5 °C, Ar = 0.00345). The dashed line corresponds to outlet conditions and error bars correspond to s_T

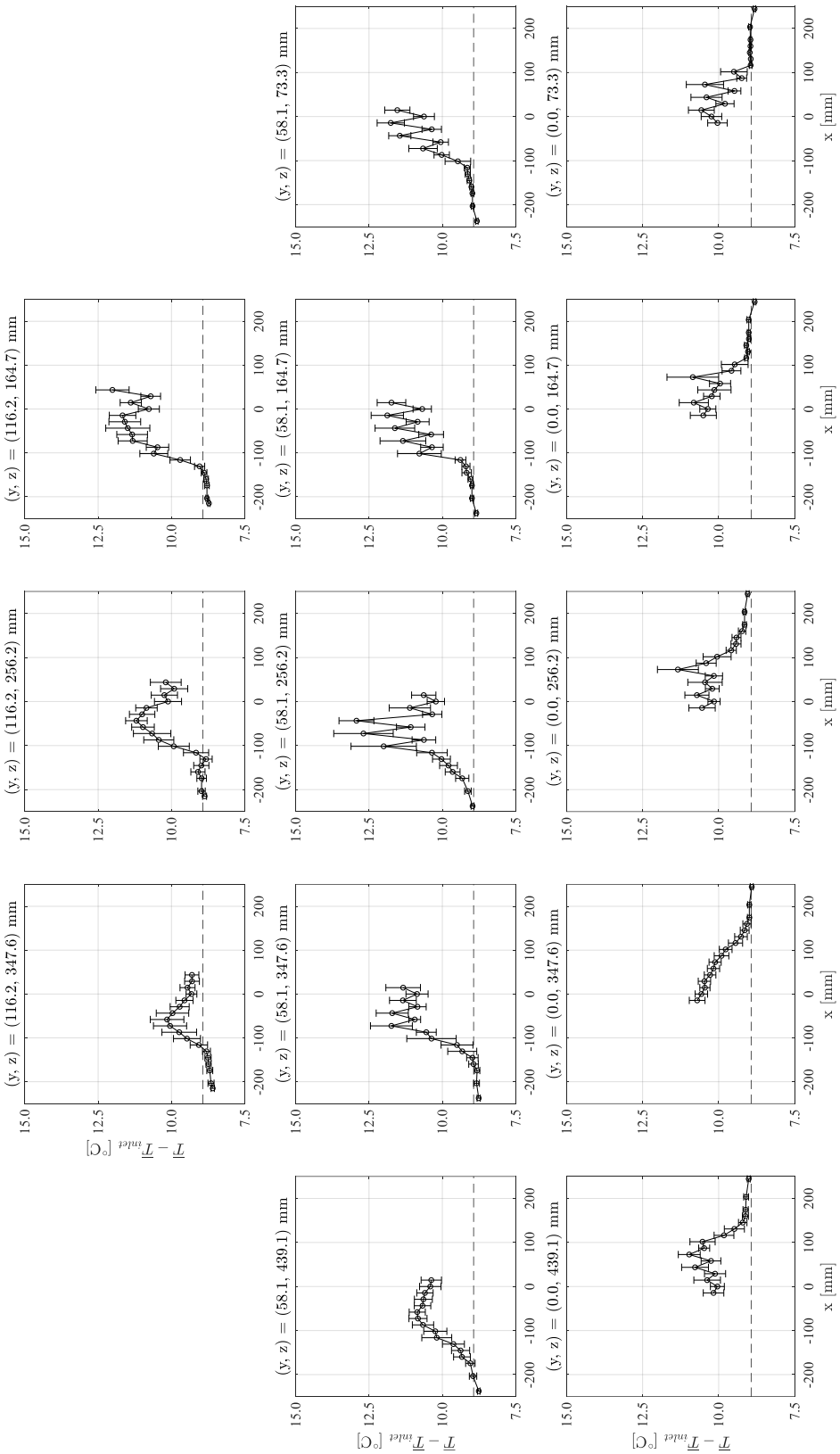

Figure E-13: Time-averaged temperature measurement map for test ID 1017-01 (P_e = 9.35 kW, Q = 15.1 L/min, T_{inlet} = 19.8 °C, ΔT = 8.9 °C, Ar = 0.0102). The dashed line corresponds to outlet conditions and error bars correspond to s_T

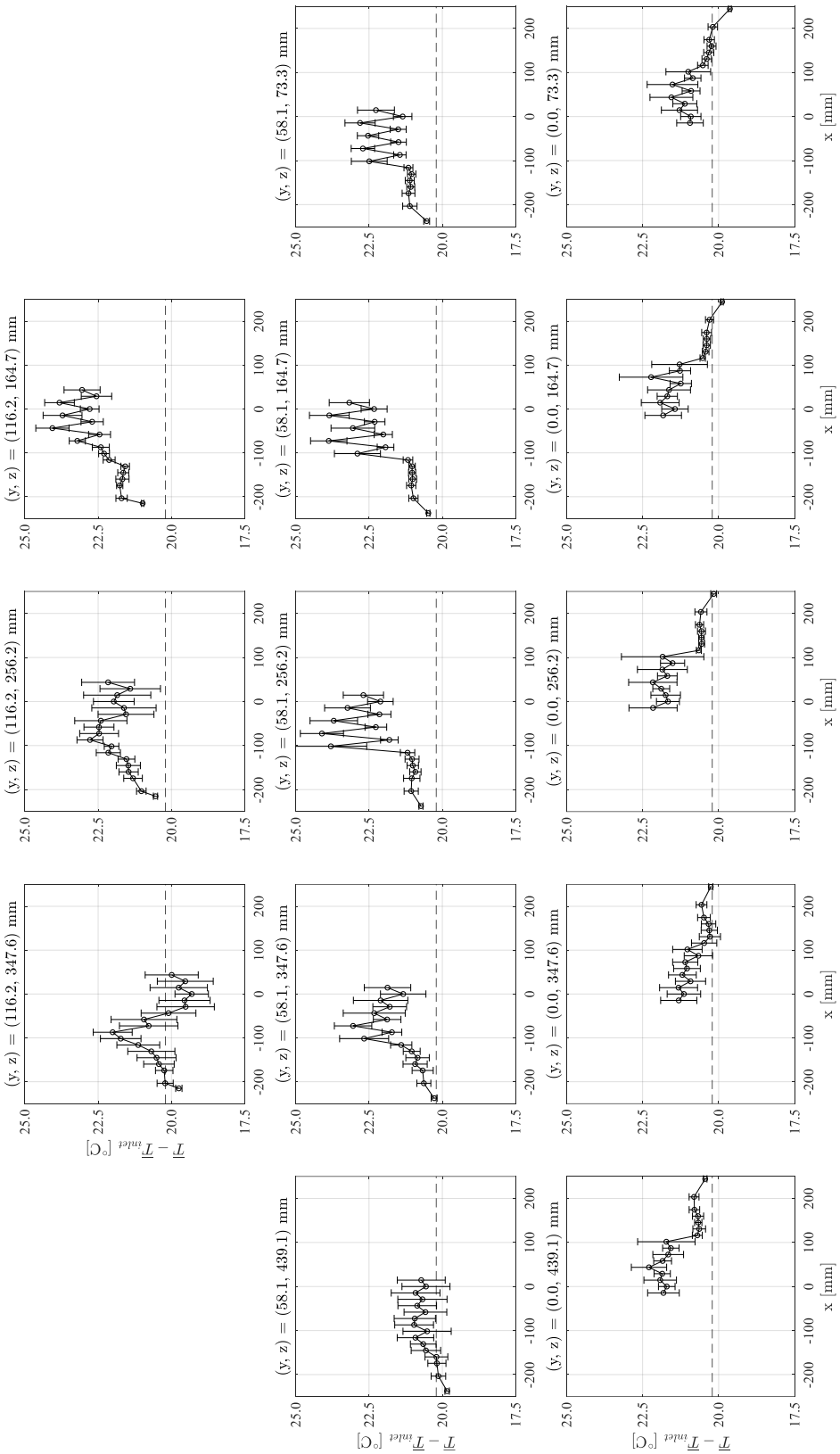

Figure E-14: Time-averaged temperature measurement map for test ID 1018-00 (P_e = 11.87 kW, Q = 8.2 L/min, T_{inlet} = 23.1 °C, ΔT = 20.2 °C, Ar = 0.103). The dashed line corresponds to outlet conditions and error bars correspond to s_T

E.3 Temperature Measurement Repeatability Data

Several repeat tests for the 20-kW power and 30 L/min inlet flow rate conditions were performed, corresponding to test ID numbers 0823-00, 0915-01, 1011-00, 1011-01, 1011-02. Tests were performed across separate days with temperature measurements gathered at the same coordinates within the test section for each test. The latter three tests were performed at separate times on the same day and were included to further test the repeatability of locating the positions of the thermocouples within the test section.

Temperature profile plots showing comparisons between the time-averaged measurements and standard deviations for each thermocouple probe locations are shown in Figure E-15 through Figure E-27. In general, the repeat temperature measurements from each separate test corresponded well with each other. In order to quantify the repeatability, an average excess temperature $\bar{T}_{ex}$ and deviation from the average $\delta_{T_{ex_i}}$ was calculated across the five data sets for each measurement location:

$$\bar{T}_{ex}(x,y,z) = \frac{1}{5}\sum_{i=1}^{5} T_{ex_i}(x,y,z)$$

$$\delta_{T_{ex_i}}(x,y,z) = \left|\bar{T}_{ex}(x,y,z) - T_{ex_i}(x,y,z)\right|$$

The standard deviation of the repeat temperature measurements $\sigma_{T_{ex}}$ was calculated as:

$$\sigma_{T_{ex}} = \sqrt{\frac{1}{N-1}\sum\left(\delta_{T_{ex_i}}(x,y,z)\right)^2}$$

The maximum observed deviation from the average was 0.7ºC while the standard deviation was 0.1ºC.

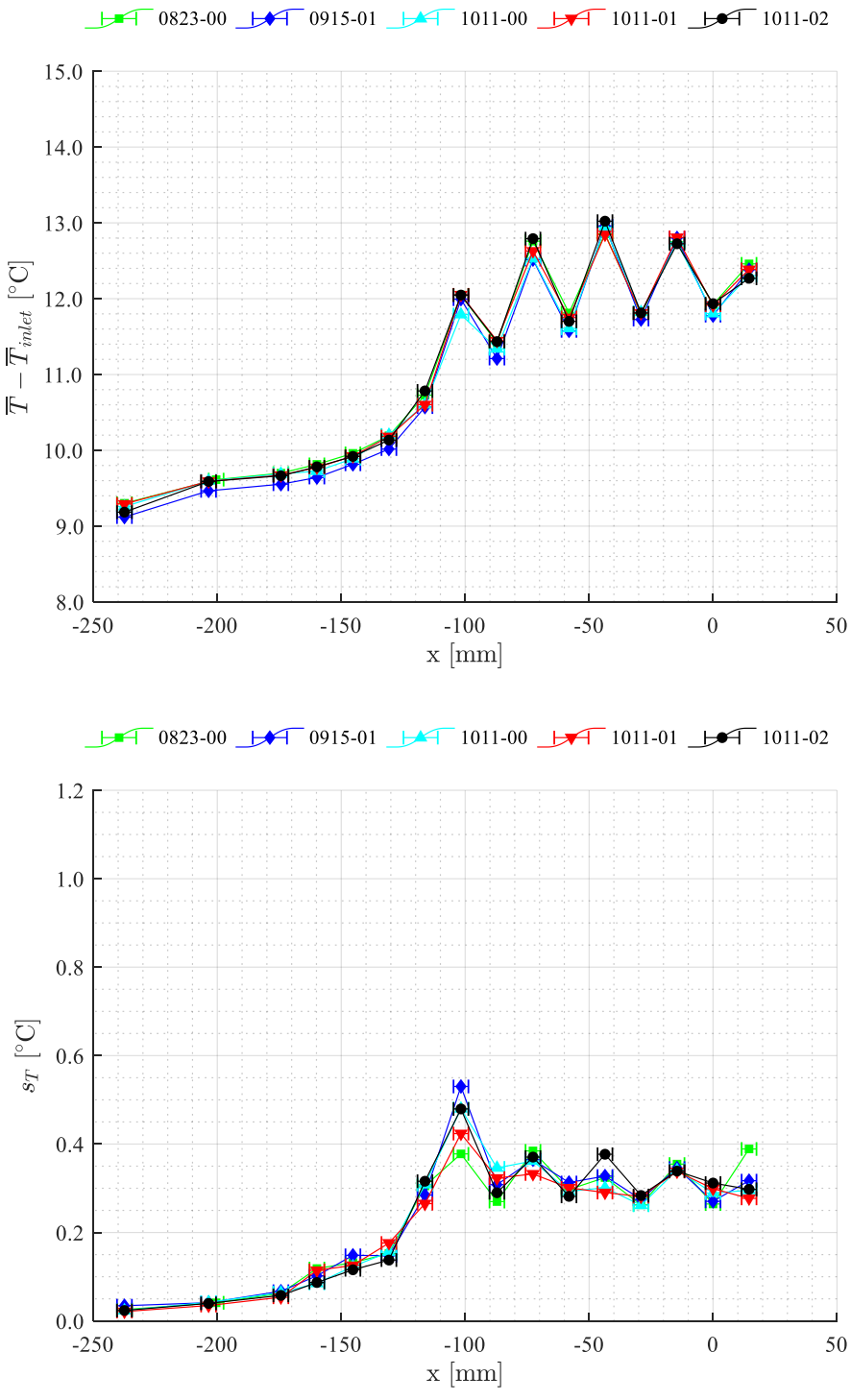

Figure E-15: Average (top) and standard deviation (bottom) repeat temperature measurements for thermocouple TCM1-00 at 20 kW, 30 L/min

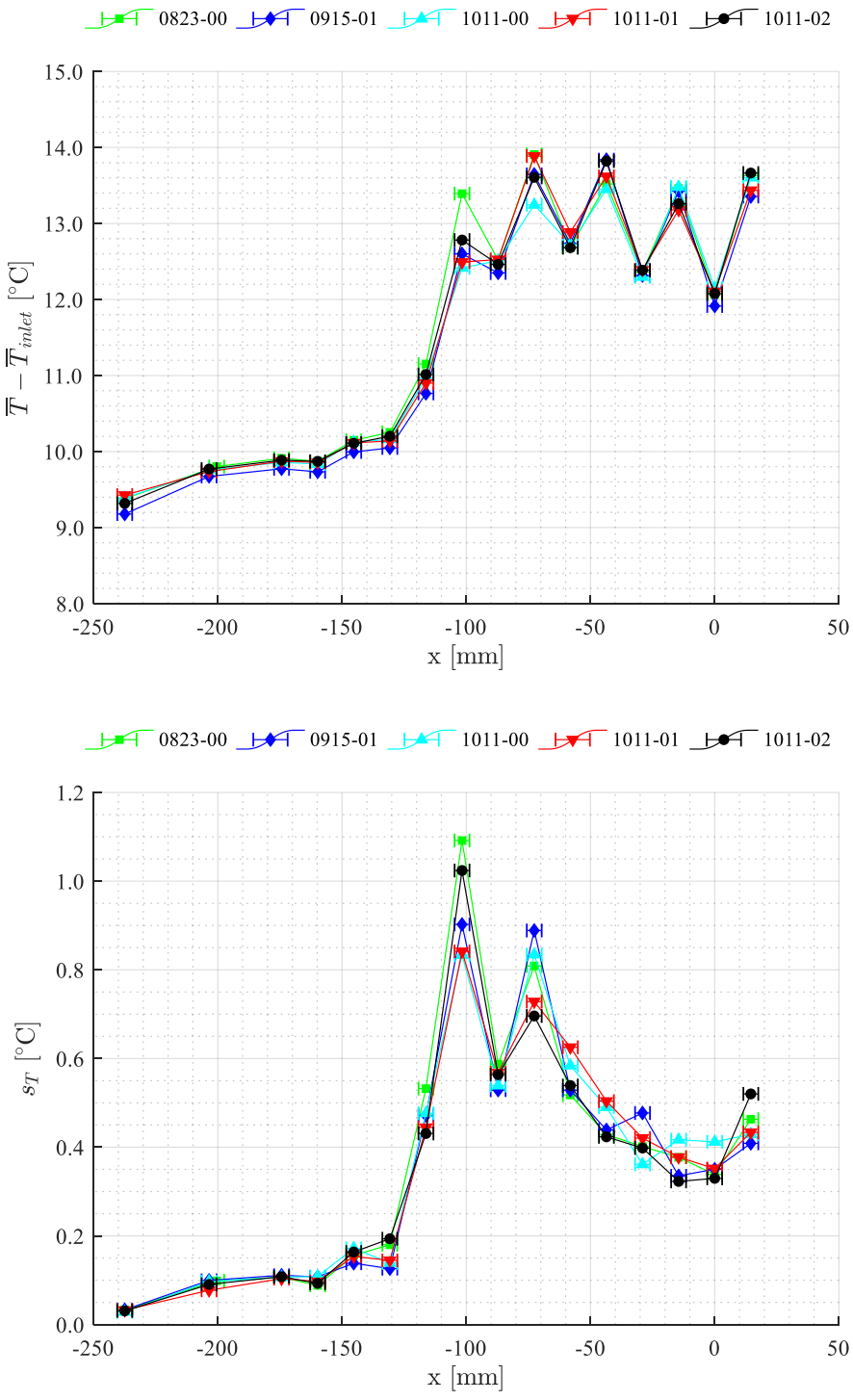

Figure E-16: Average (top) and standard deviation (bottom) repeat temperature measurements for thermocouple TCM1-01 at 20 kW, 30 L/min

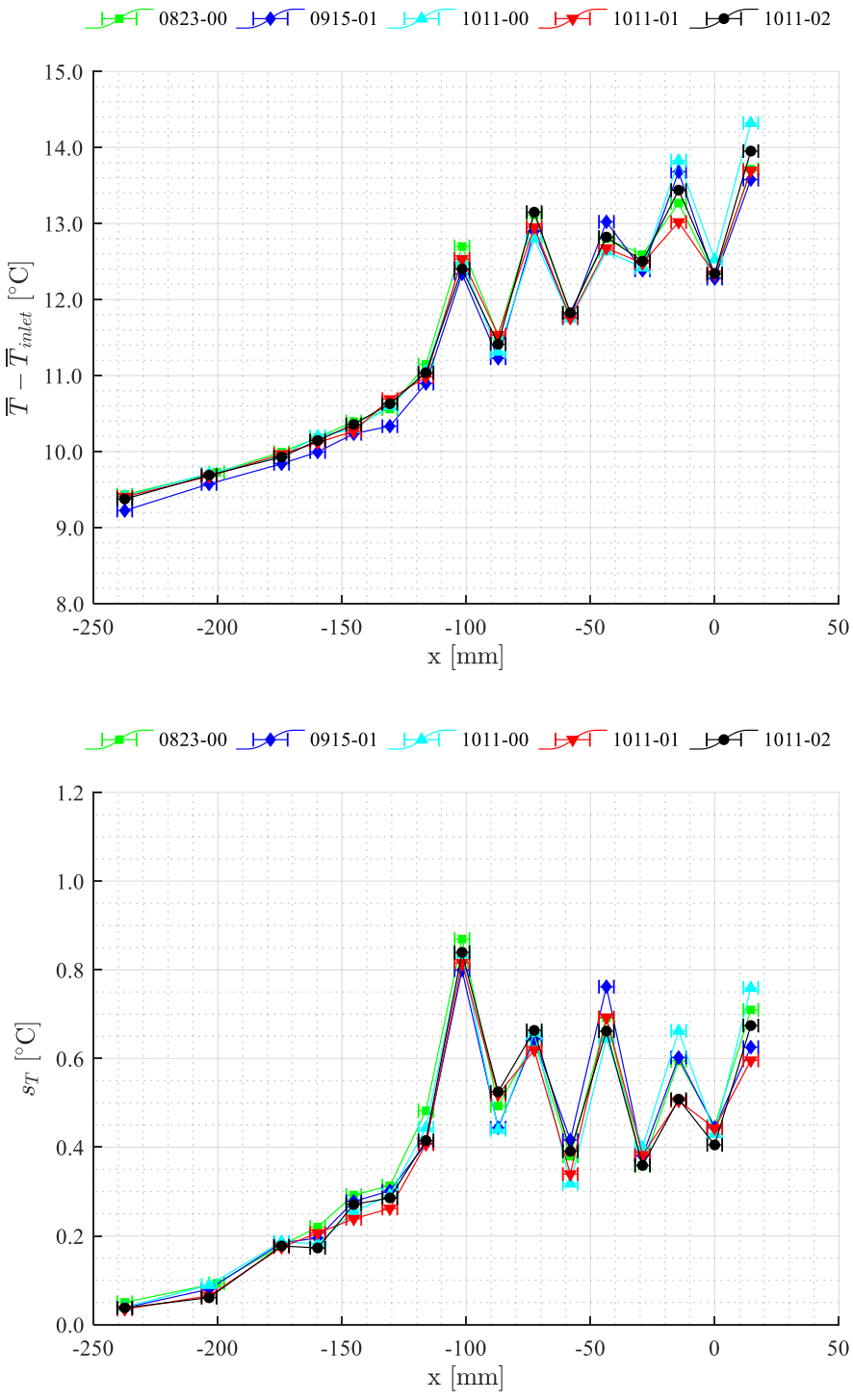

Figure E-17: Average (top) and standard deviation (bottom) repeat temperature measurements for thermocouple TCM1-02 at 20 kW, 30 L/min

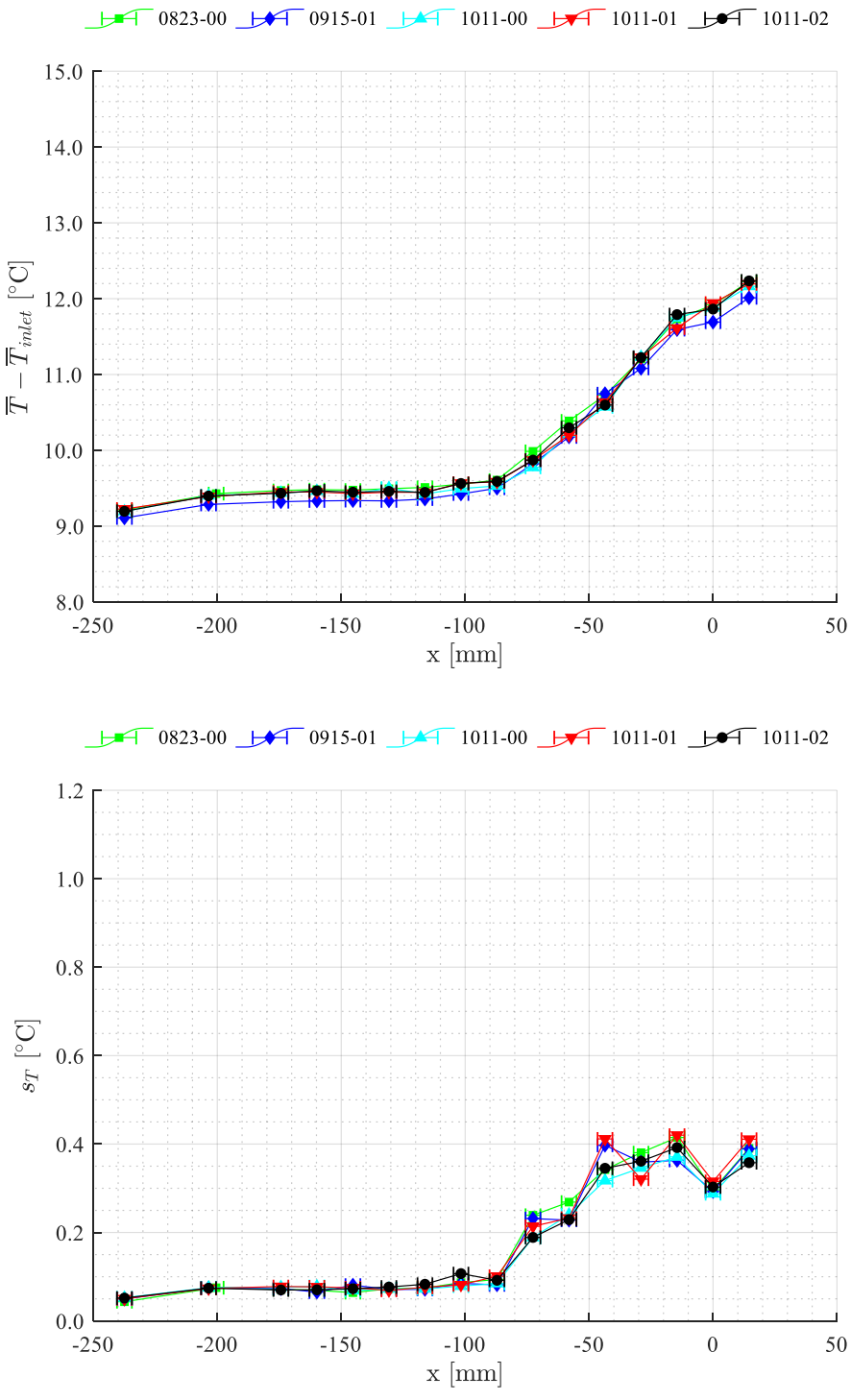

Figure E-18: Average (top) and standard deviation (bottom) repeat temperature measurements for thermocouple TCM1-03 at 20 kW, 30 L/min

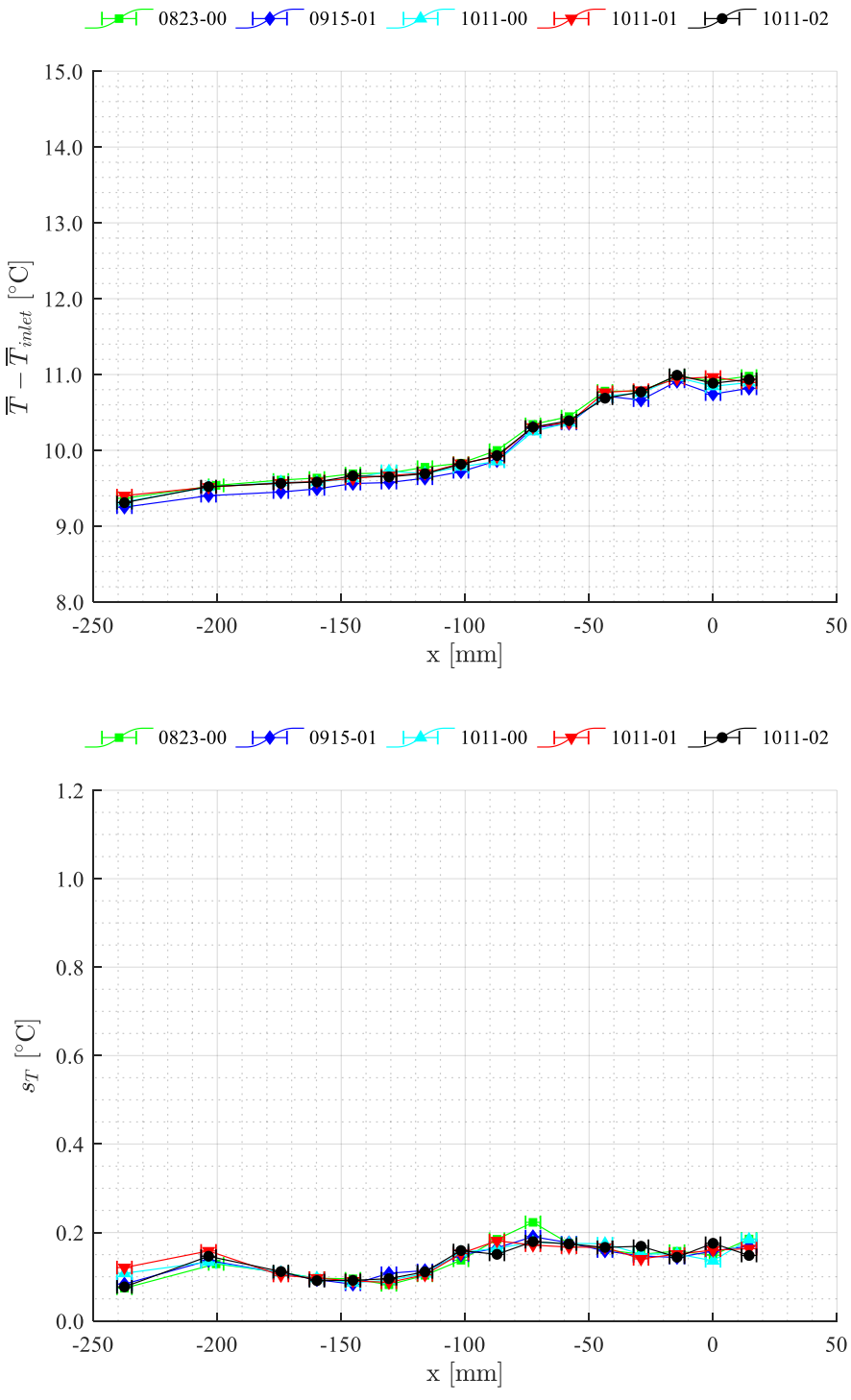

Figure E-19: Average (top) and standard deviation (bottom) repeat temperature measurements for thermocouple TCM1-04 at 20 kW, 30 L/min

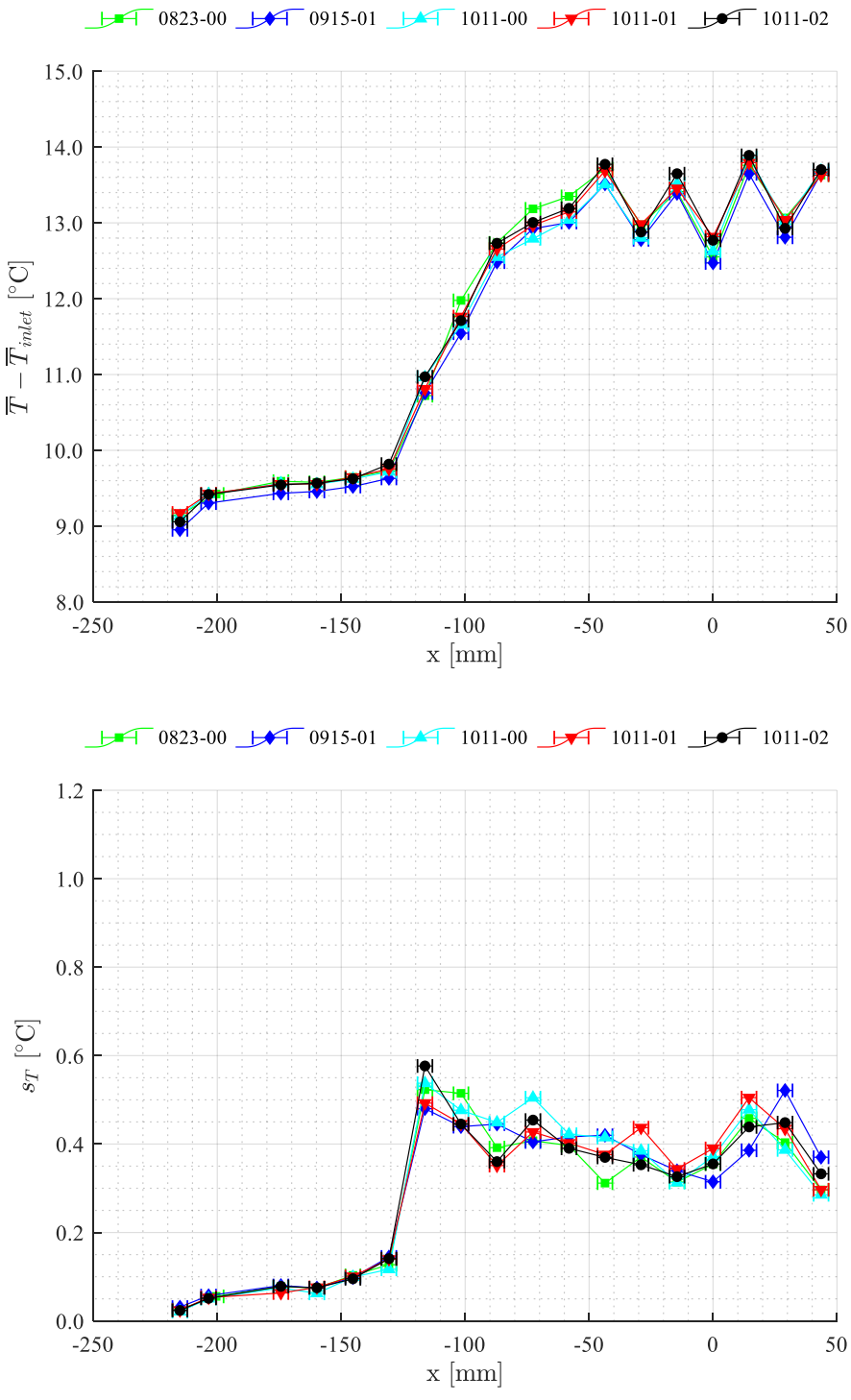

Figure E-20: Average (top) and standard deviation (bottom) repeat temperature measurements for thermocouple TCM1-05 at 20 kW, 30 L/min

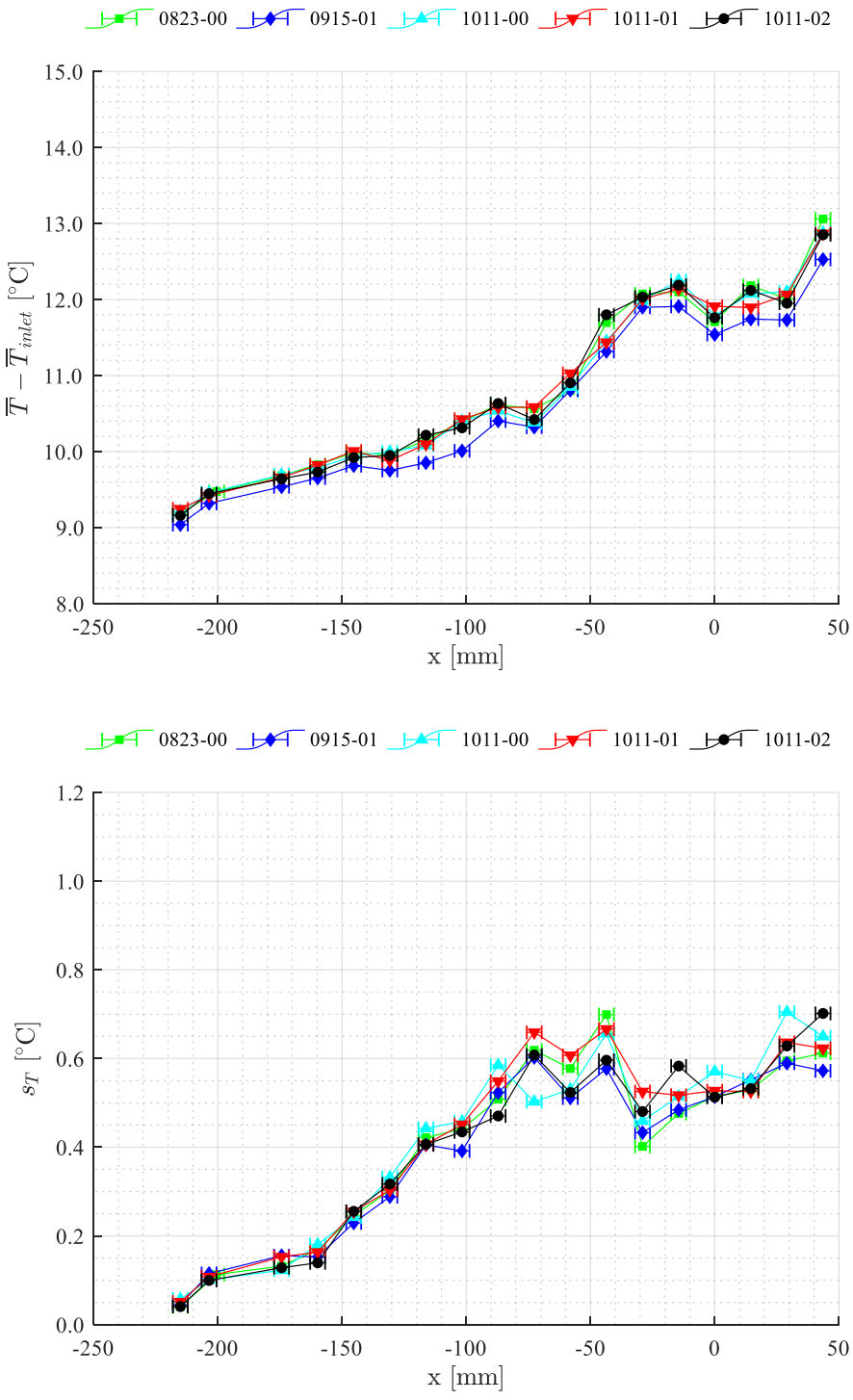

Figure E-21: Average (top) and standard deviation (bottom) repeat temperature measurements for thermocouple TCM1-06 at 20 kW, 30 L/min

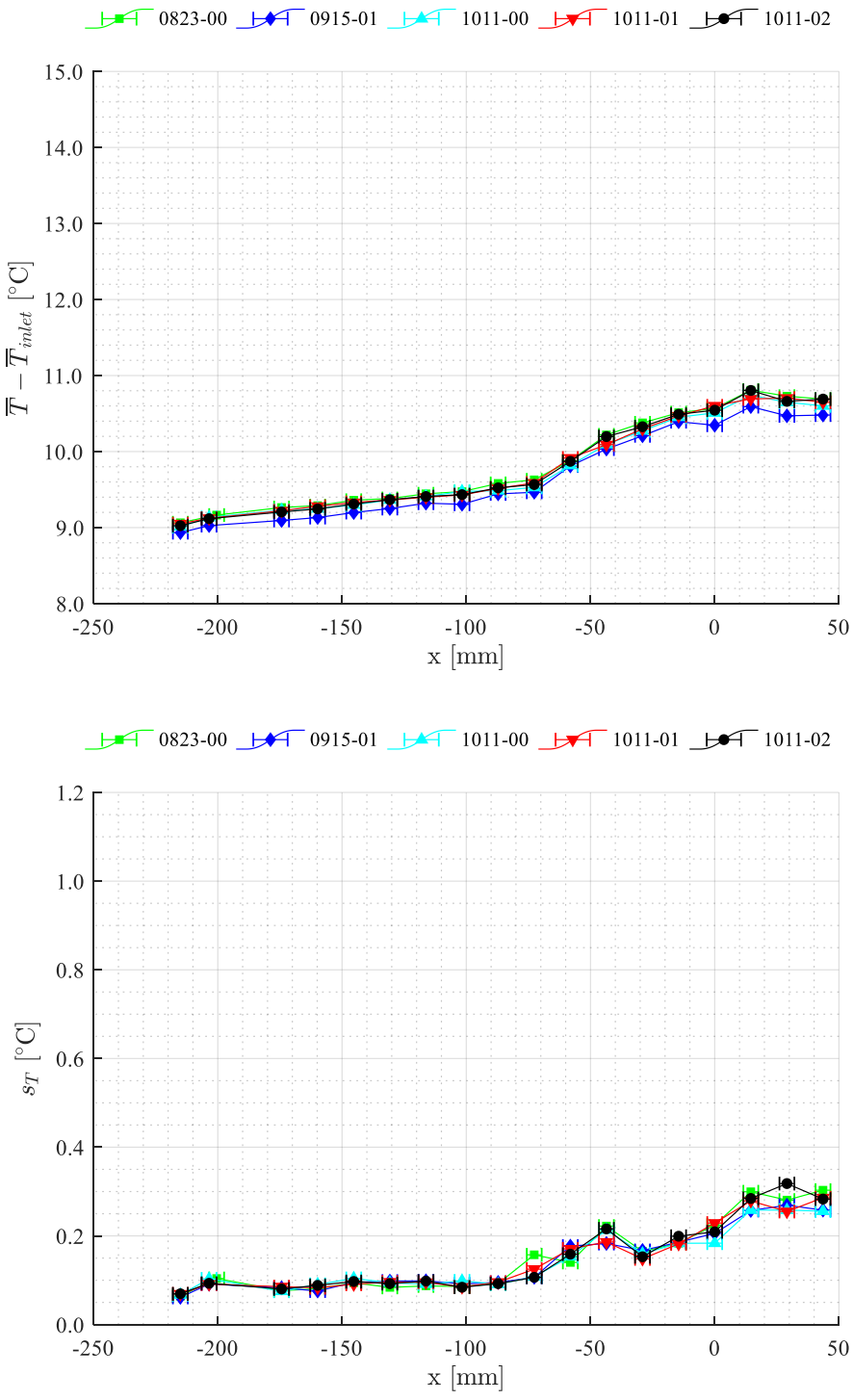

Figure E-22: Average (top) and standard deviation (bottom) repeat temperature measurements for thermocouple TCM1-07 at 20 kW, 30 L/min

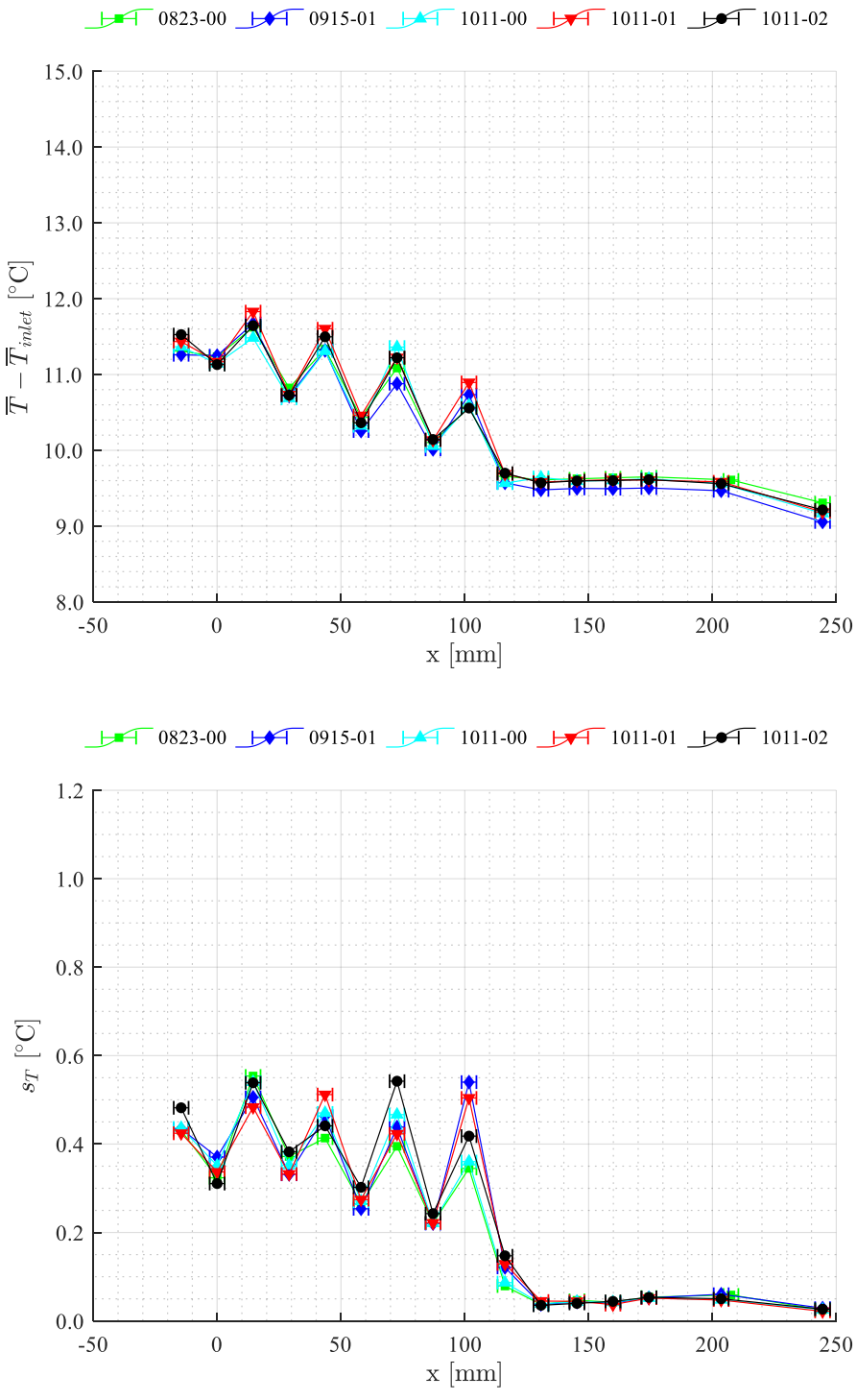

Figure E-23: Average (top) and standard deviation (bottom) repeat temperature measurements for thermocouple TCM1-08 at 20 kW, 30 L/min

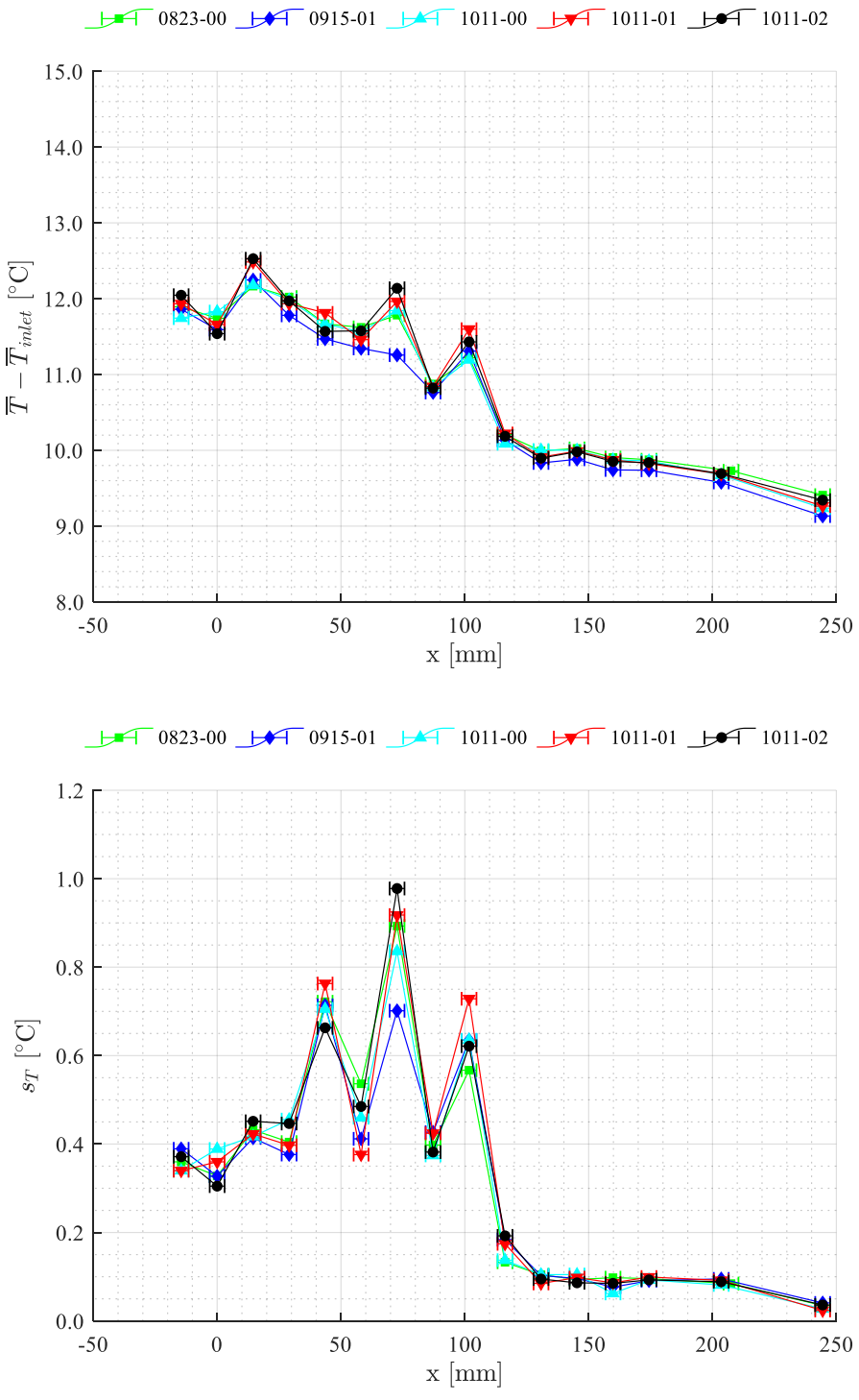

Figure E-24: Average (top) and standard deviation (bottom) repeat temperature measurements for thermocouple TCM1-09 at 20 kW, 30 L/min

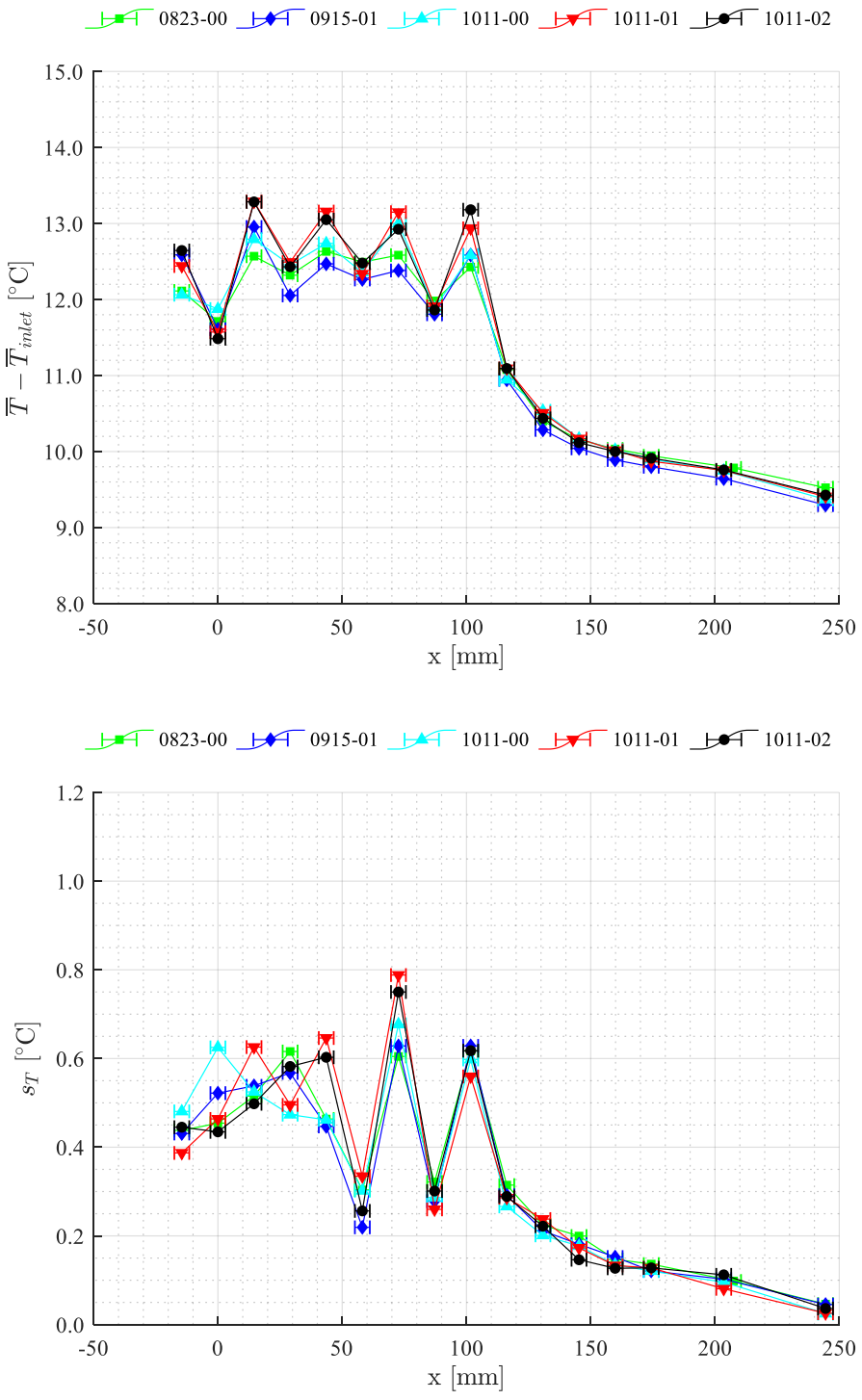

Figure E-25: Average (top) and standard deviation (bottom) repeat temperature measurements for thermocouple TCM1-10 at 20 kW, 30 L/min

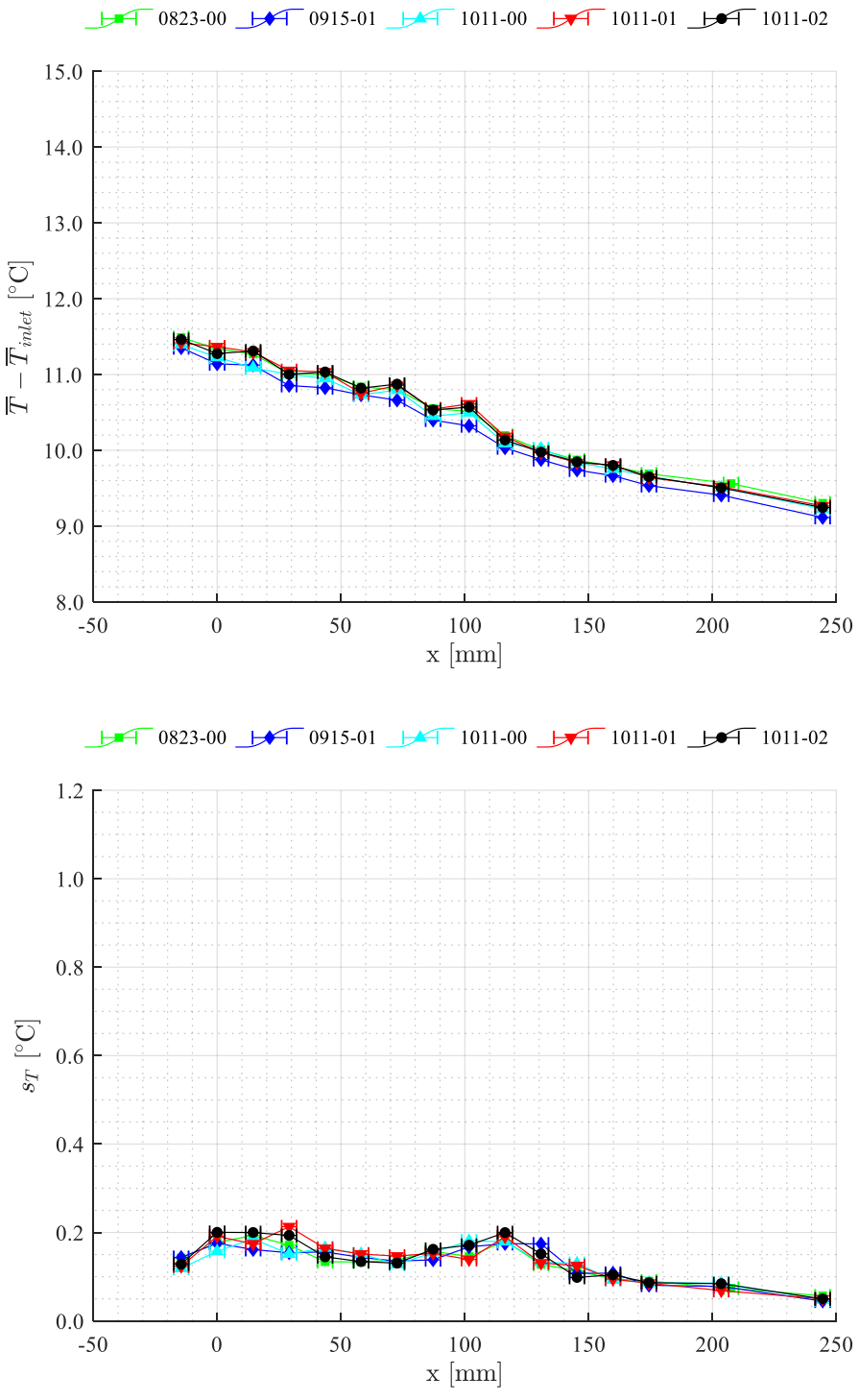

Figure E-26: Average (top) and standard deviation (bottom) repeat temperature measurements for thermocouple TCM1-11 at 20 kW, 30 L/min

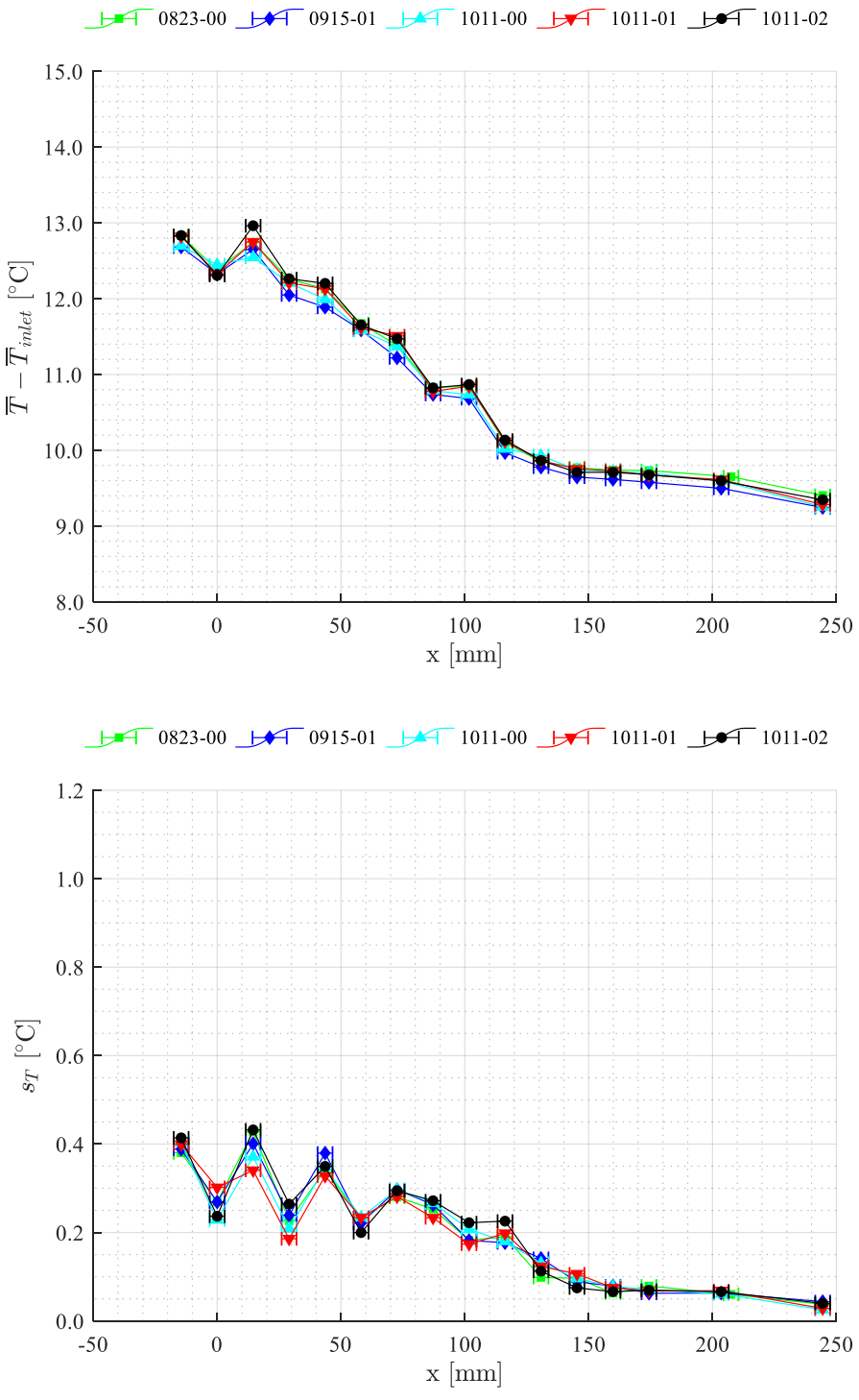

Figure E-27: Average (top) and standard deviation (bottom) repeat temperature measurements for thermocouple TCM1-12 at 20 kW, 30 L/min

E.4 Time-Dependent Temperature Behaviour

This section presents time dependent temperature measurements locations where the maximum instantaneous temperatures were observed for each experimental run. Additionally, the time-dependent temperature measurements are included for the locations where the largest temperature fluctuations were observed (corresponding to the largest recorded of s_T as calculated by Equation E.4). In some instances, these two locations corresponded to each other.

Table E-4: Summary of maximum instantaneous temperatures and largest temperature fluctuations for each experimental test

Test ID	Flow [L/min]	Power [kW]	Inlet T [°C]	Outlet T [°C]	T_{peak} (t) [°C]	Maximum s_T [°C]
0308-00	30.0 ± 0.2	19.93 ± 0.08	22.4 ± 0.5	31.9 ± 0.5	38.3 ± 0.5	1.0
0309-00	30.0 ± 0.2	39.80 ± 0.20	34.3 ± 0.5	53.1 ± 0.5	63.1 ± 0.5	1.5
0823-00	29.8 ± 0.2	19.77 ± 0.08	26.8 ± 0.5	36.3 ± 0.5	43.4 ± 0.5	1.1
0831-00	24.0 ± 0.1	19.77 ± 0.08	27.3 ± 0.5	39.1 ± 0.5	46.4 ± 0.5	1.1
0908-00	30.1 ± 0.2	9.85 ± 0.04	20.0 ± 0.5	24.8 ± 0.5	28.9 ± 0.5	0.6
0915-01	30.1 ± 0.2	19.76 ± 0.08	28.6 ± 0.5	38.1 ± 0.5	44.4 ± 0.5	0.9
0922-00	30.0 ± 0.2	37.58 ± 0.20	40.8 ± 0.5	58.7 ± 0.5	67.9 ± 0.5	1.3
1011-00	30.0 ± 0.2	19.81 ± 0.08	26.2 ± 0.5	35.7 ± 0.5	43.0 ± 0.5	0.8
1011-01	29.9 ± 0.2	19.79 ± 0.08	26.1 ± 0.5	35.6 ± 0.5	42.4 ± 0.5	0.9
1011-02	29.9 ± 0.2	19.78 ± 0.08	26.2 ± 0.5	35.7 ± 0.5	42.2 ± 0.5	1.0
1017-01	15.1 ± 0.1	9.35 ± 0.04	19.8 ± 0.5	28.7 ± 0.5	35.2 ± 0.5	1.1
1018-00	8.2 ± 0.1	11.87 ± 0.05	23.1 ± 0.5	43.3 ± 0.5	49.9 ± 0.5	1.3

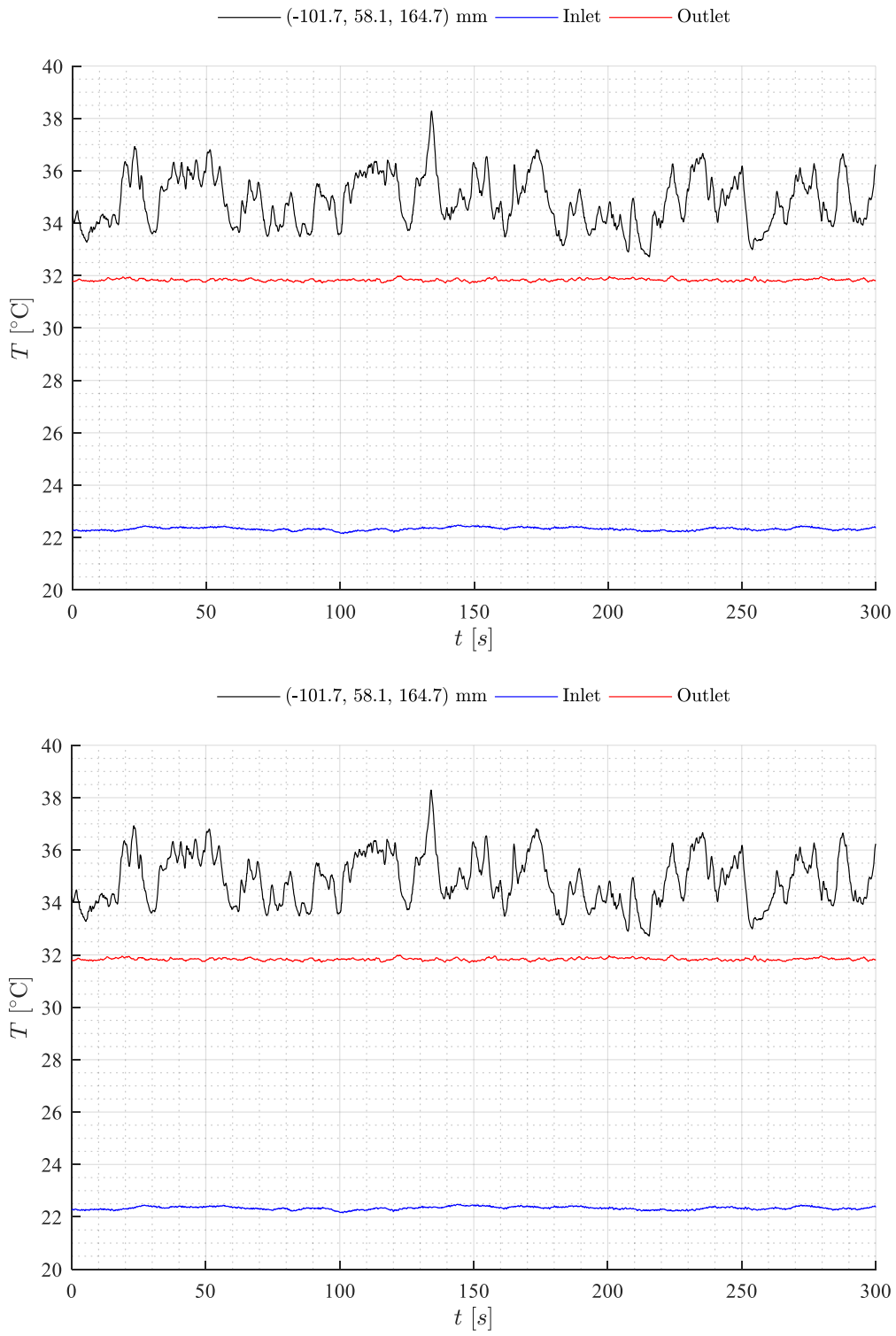

Figure E-28: Temperature measurements for test ID 0308-00 (19.93 kW, 30.0 L/min) at maximum temperature (top) and most unsteady (bottom) locations

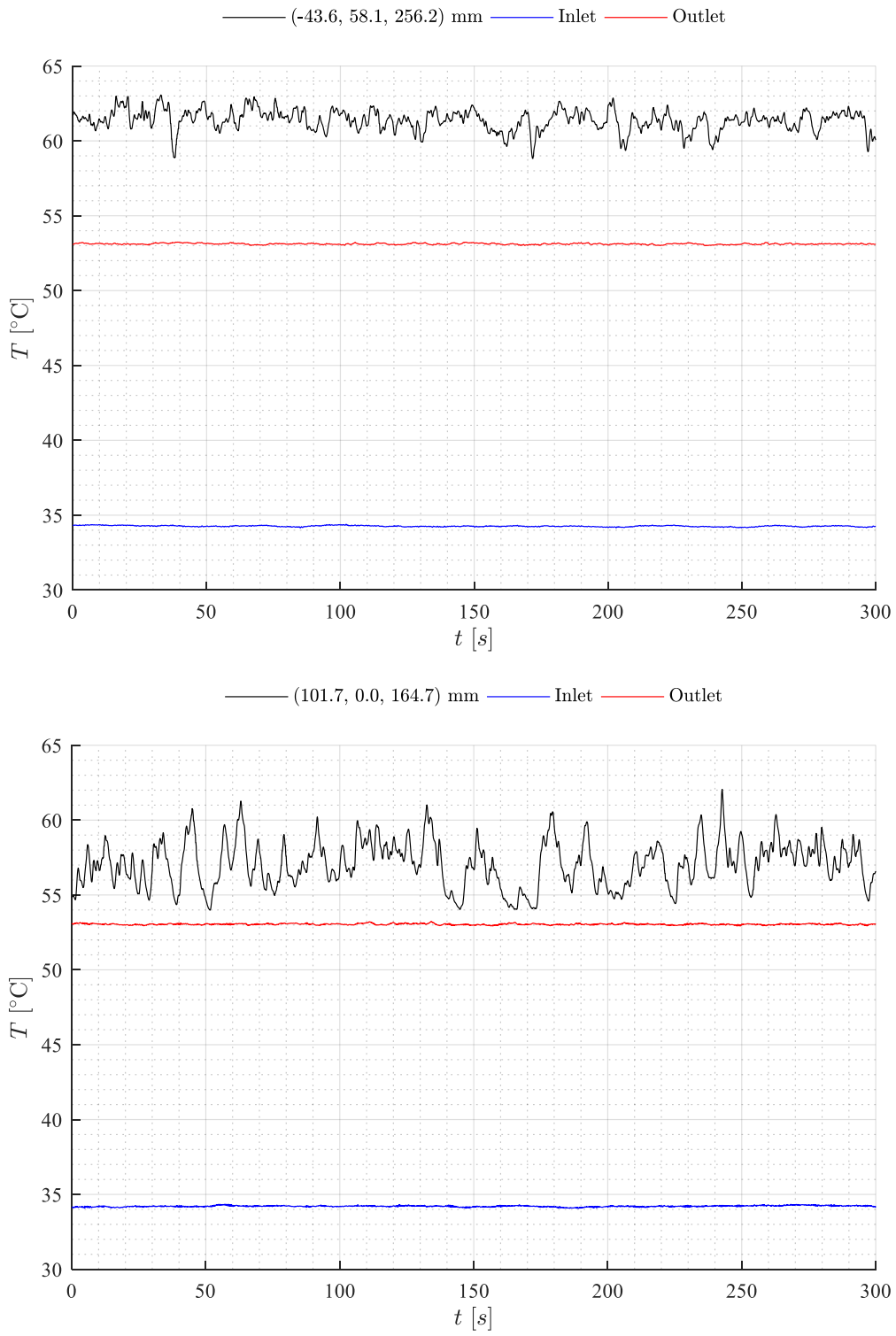

Figure E-29: Temperature measurements for test ID 0309-00 (39.80 kW, 30.0 L/min) at maximum temperature (top) and most unsteady (bottom) locations

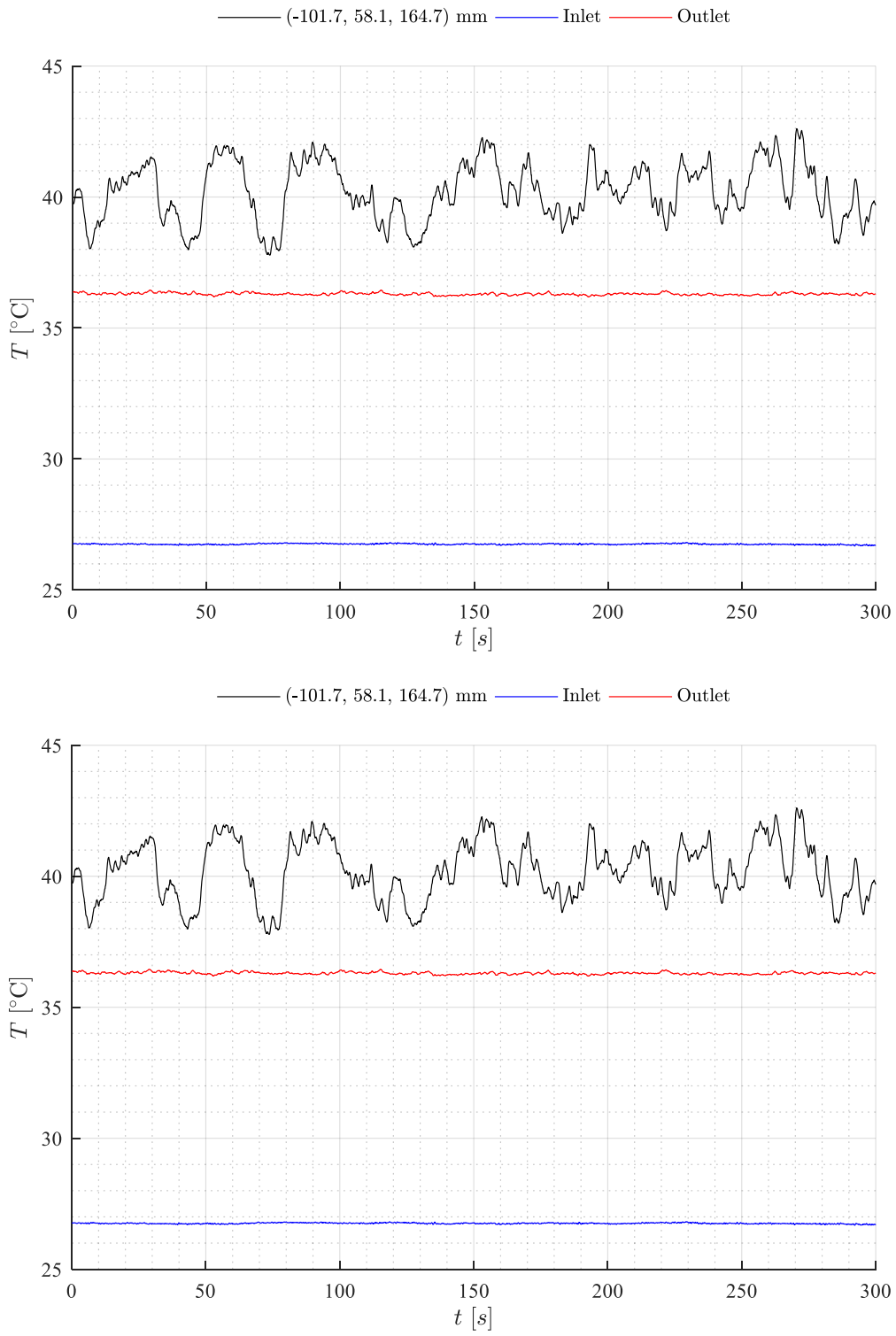

Figure E-30: Temperature measurements for test ID 0823-00 (19.77 kW, 29.8 L/min) at maximum temperature (top) and most unsteady (bottom) locations

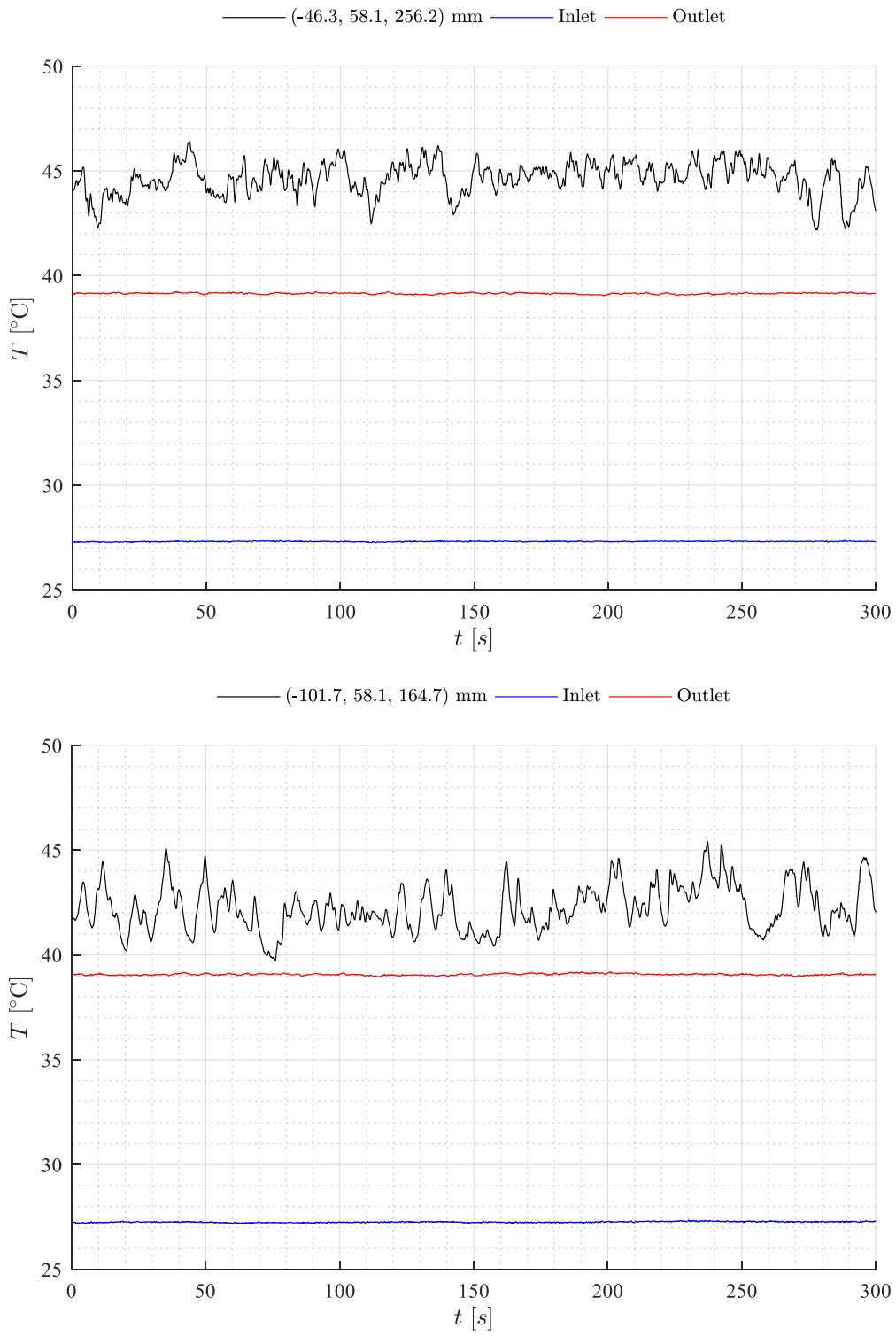

Figure E-31: Temperature measurements for test ID 0831-00 (19.77 kW, 24.0 L/min) at maximum temperature (top) and most unsteady (bottom) locations

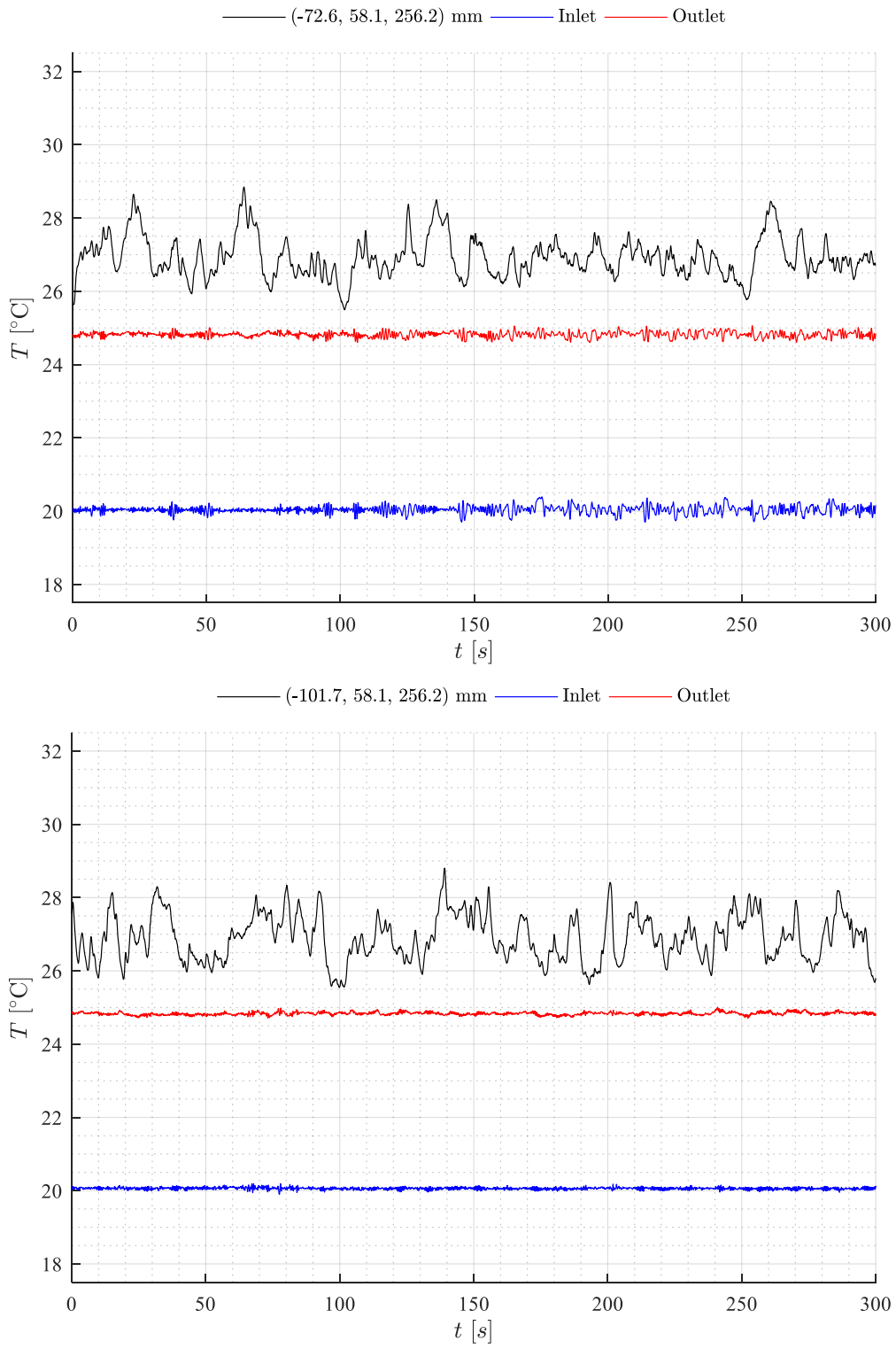

Figure E-32: Temperature measurements for test ID 0908-00 (9.85 kW, 30.1 L/min) at maximum temperature (top) and most unsteady (bottom) locations

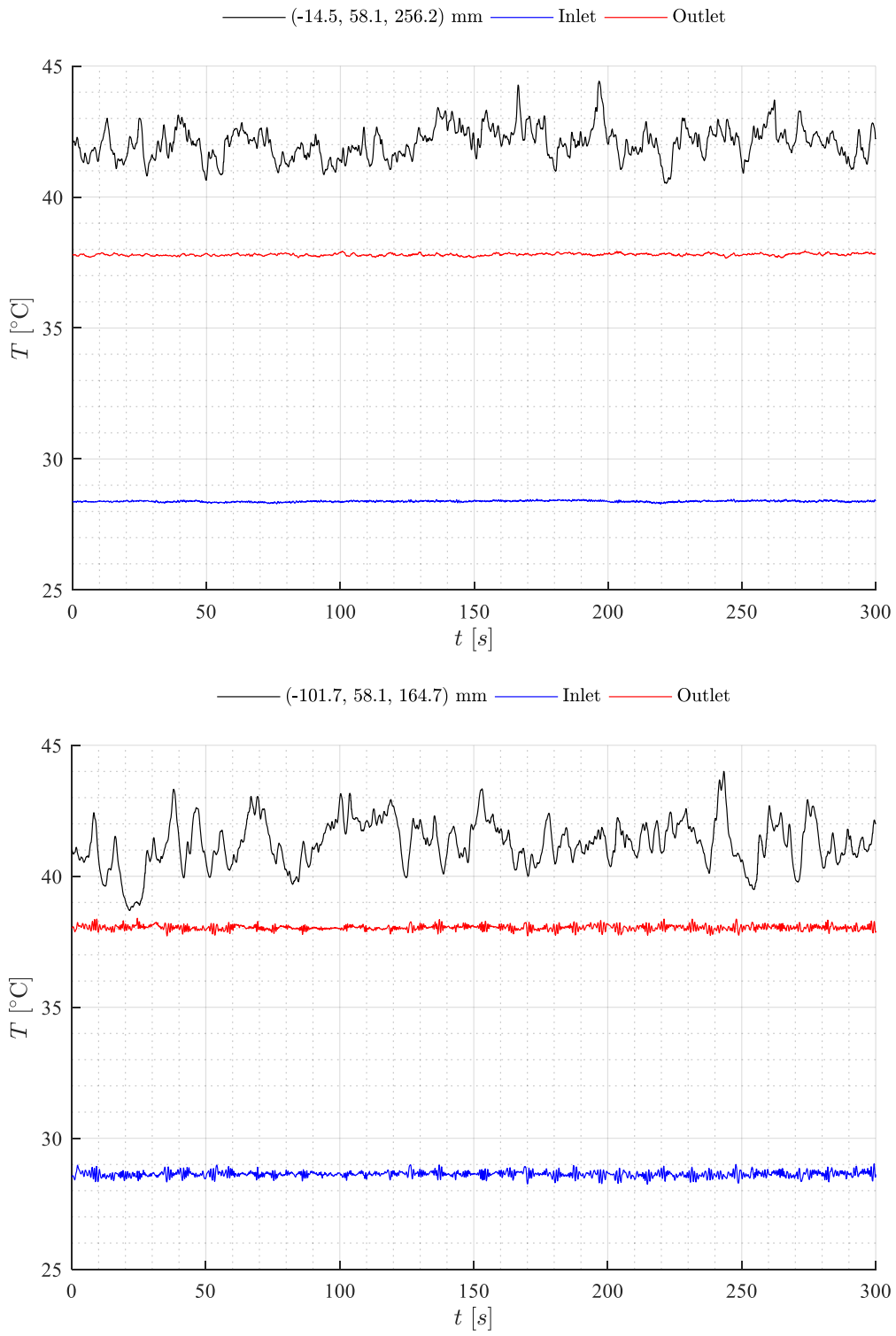

Figure E-33: Temperature measurements for test ID 0915-01 (19.76 kW, 30.1 L/min) at maximum temperature (top) and most unsteady (bottom) locations

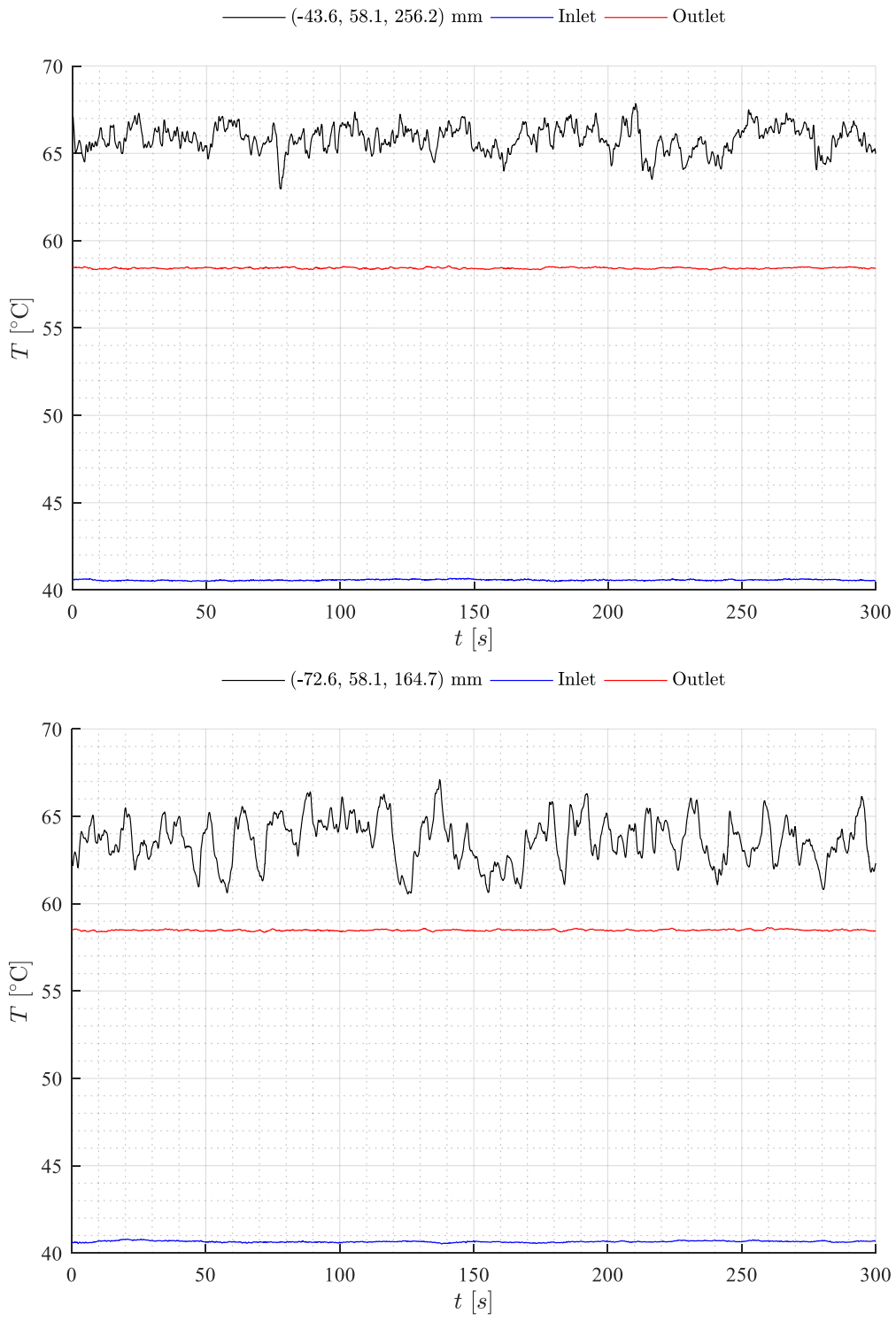

Figure E-34: Temperature measurements for test ID 0922-00 (37.58 kW, 30.0 L/min) at maximum temperature (top) and most unsteady (bottom) locations

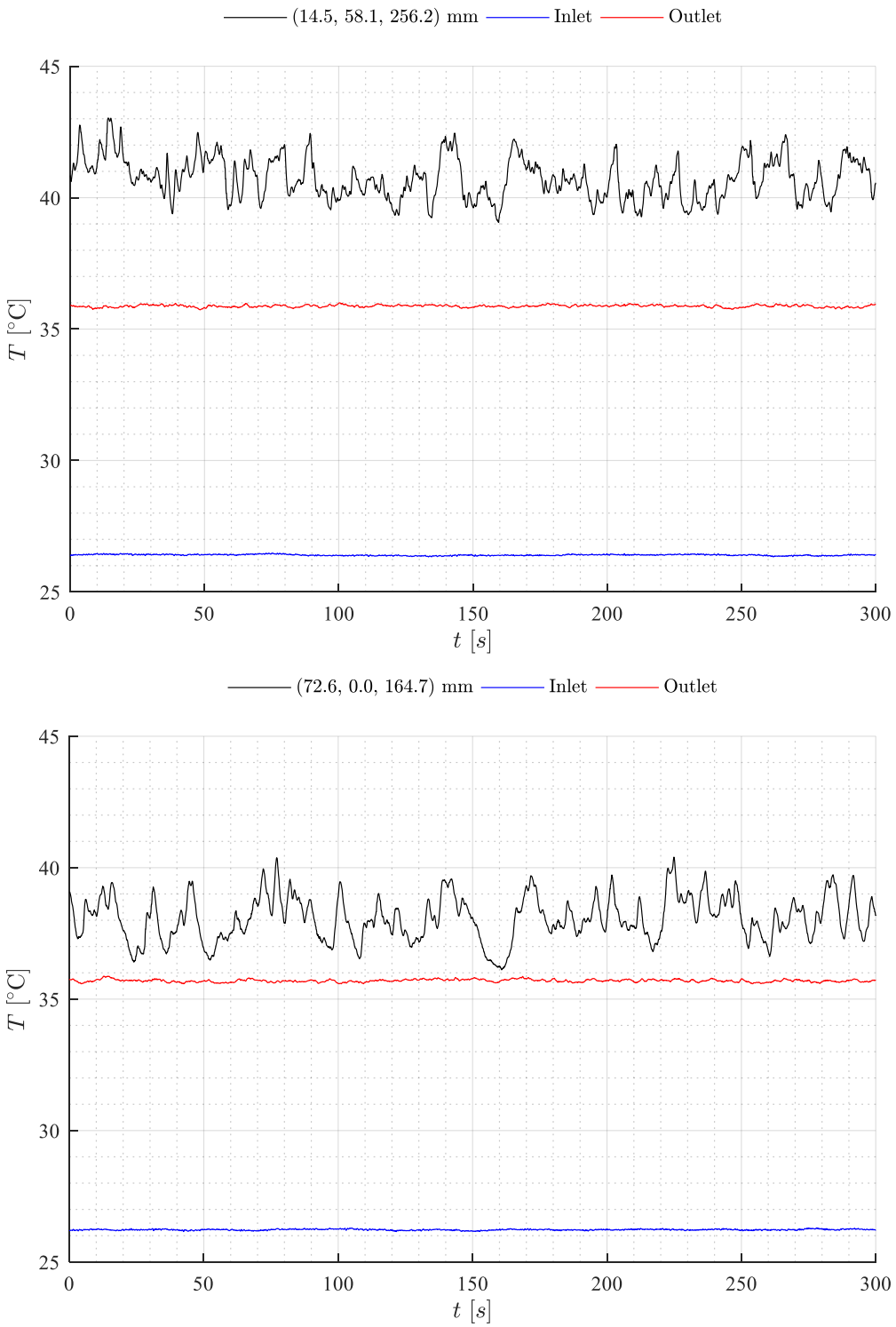

Figure E-35: Temperature measurements for test ID 1011-00 (19.81 kW, 30.0 L/min) at maximum temperature (top) and most unsteady (bottom) locations

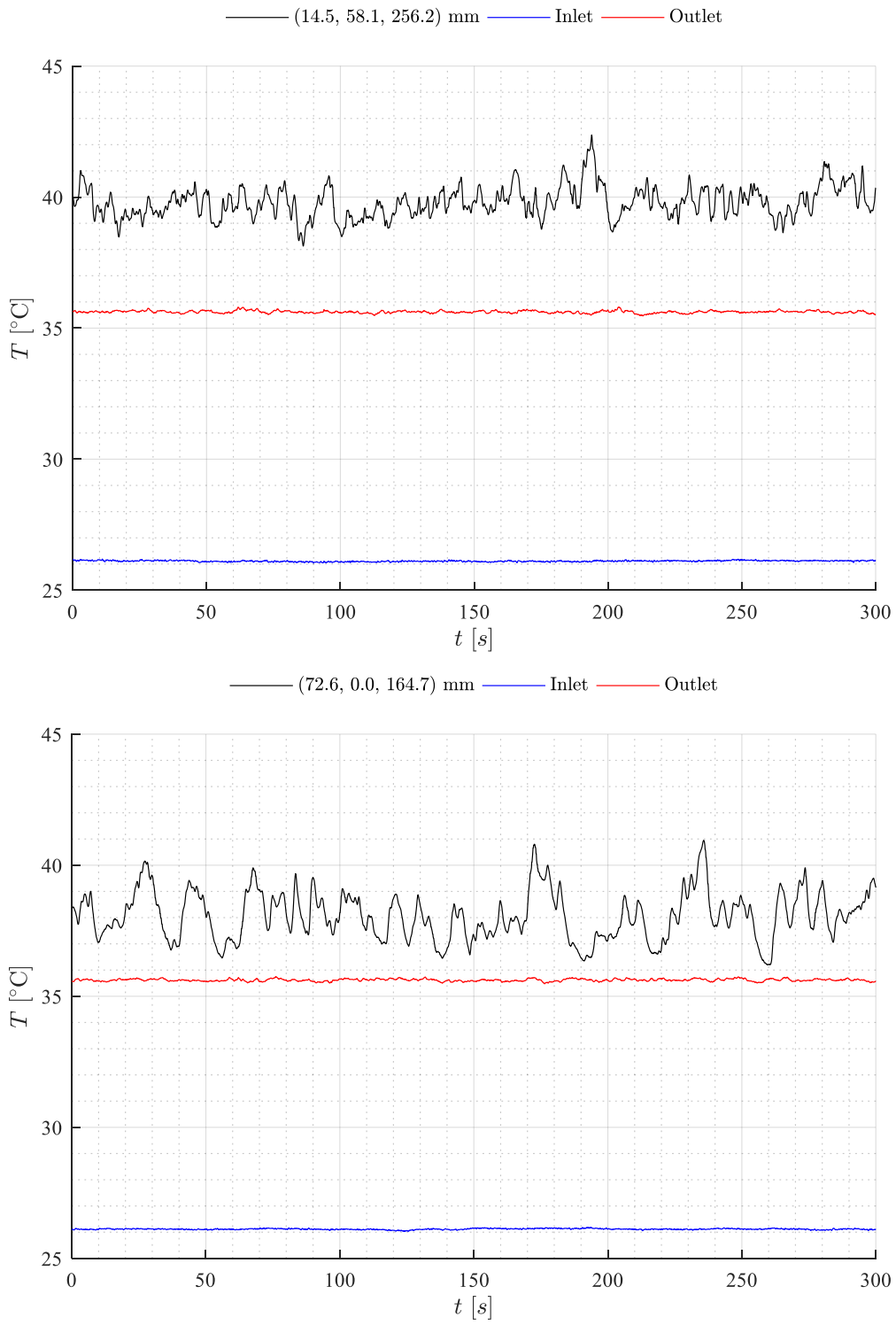

Figure E-36: Temperature measurements for test ID 1011-01 (19.81 kW, 30.0 L/min) at maximum temperature (top) and most unsteady (bottom) locations

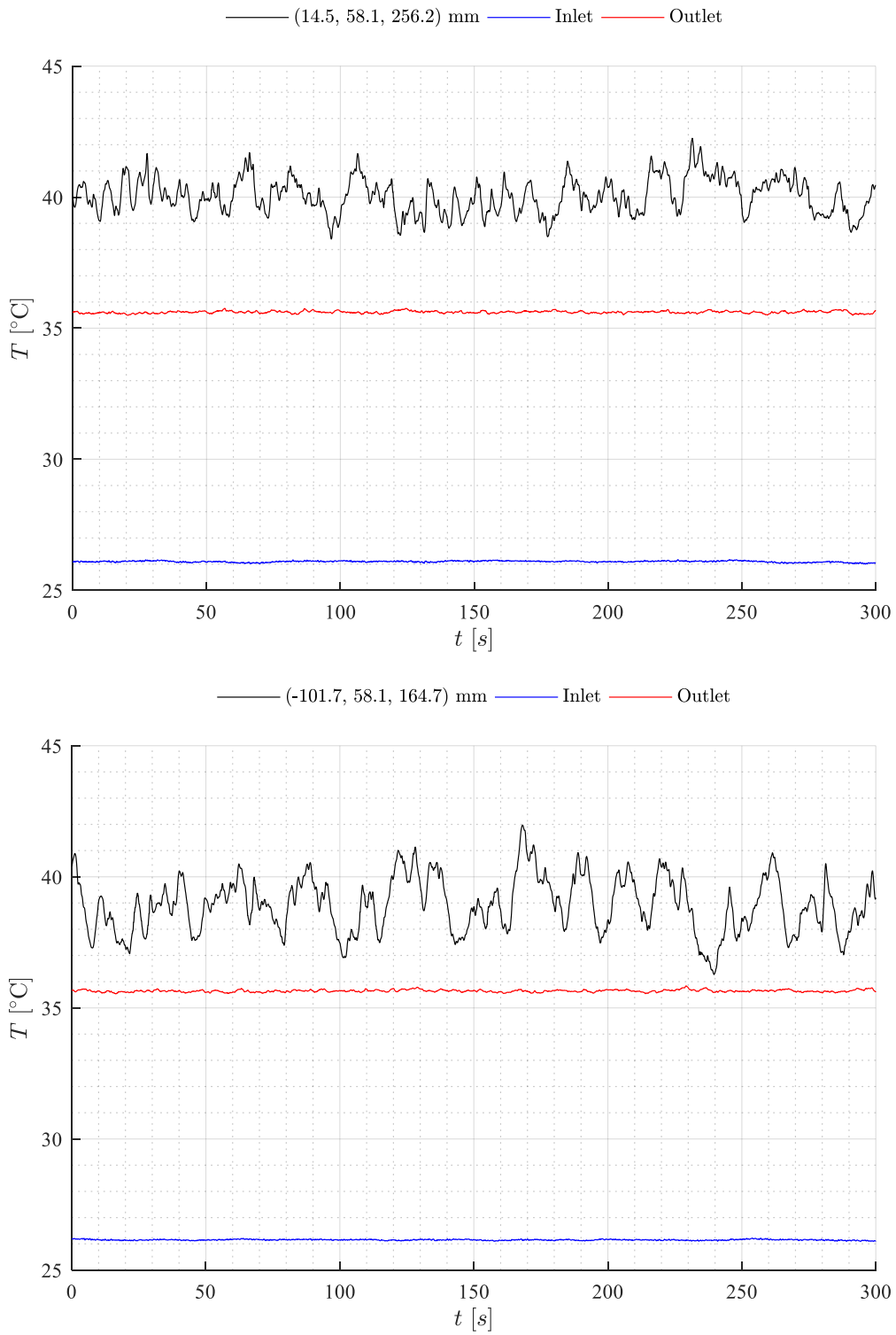

Figure E-37: Temperature measurements for test ID 1011-02 (19.81 kW, 30.0 L/min) at maximum temperature (top) and most unsteady (bottom) locations

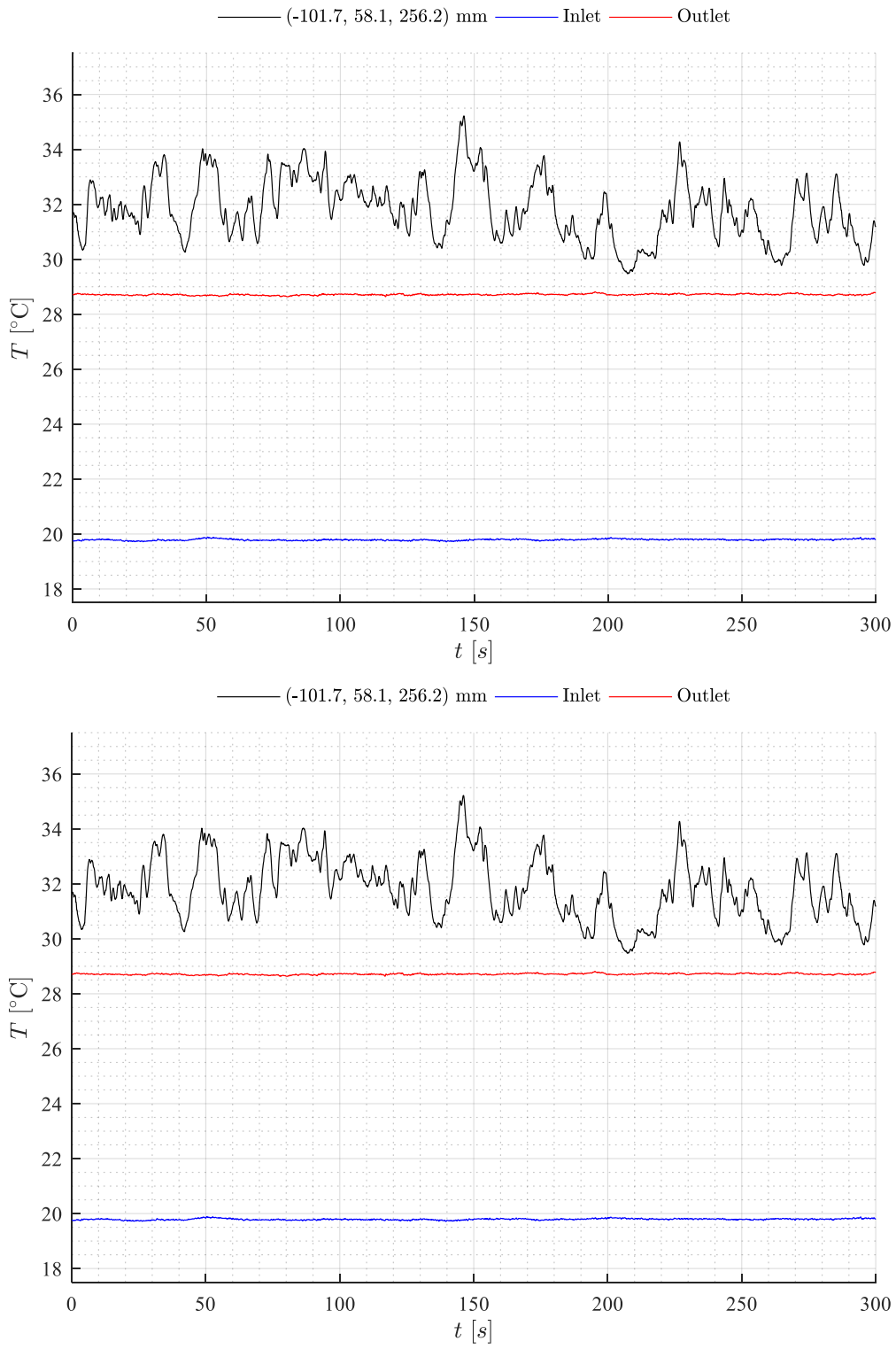

Figure E-38: Temperature measurements for test ID 1017-01 (9.35 kW, 15.1 L/min) at maximum temperature (top) and most unsteady (bottom) locations

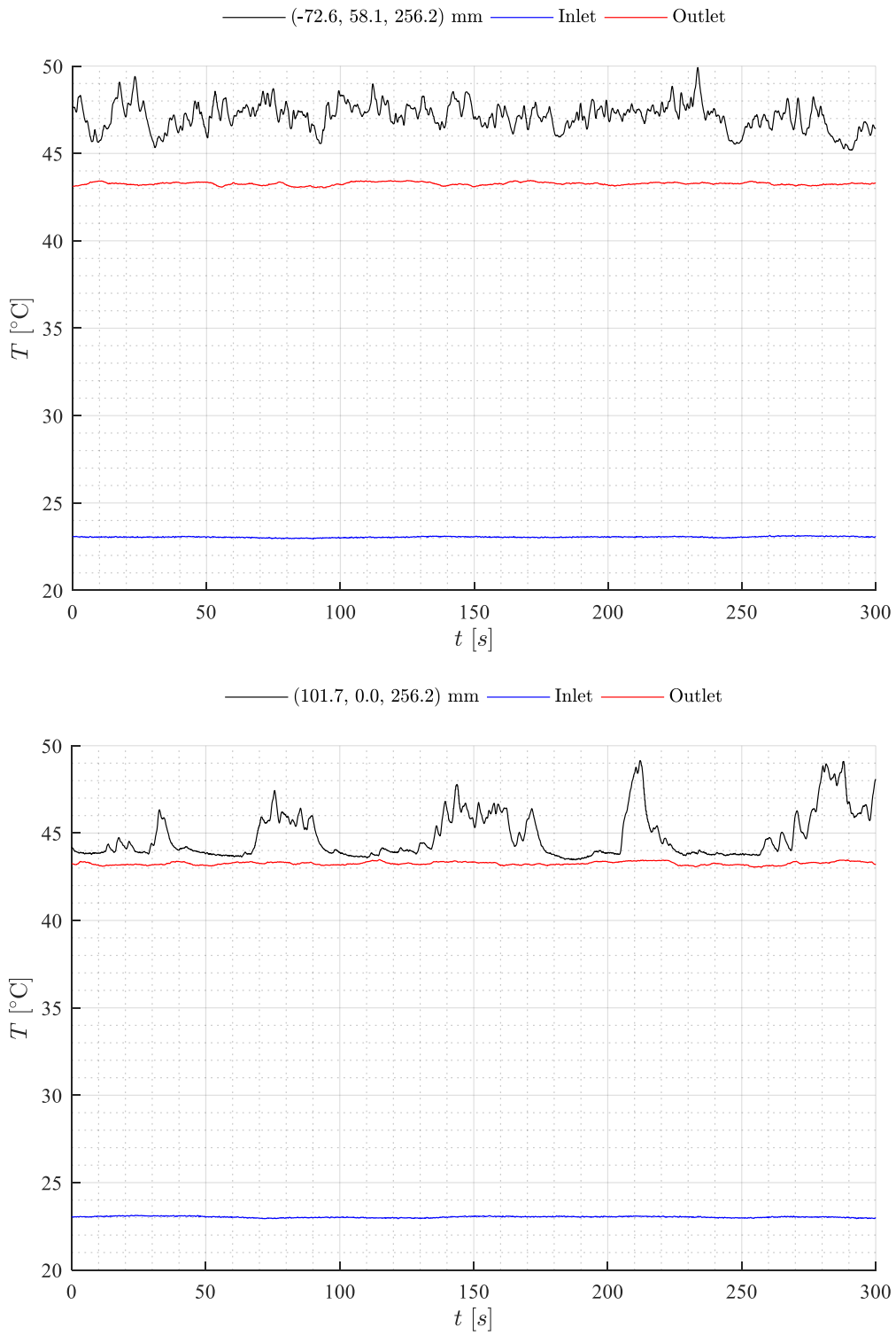

Figure E-39: Temperature measurements for test ID 1018-00 (11.87 kW, 8.2 L/min) at maximum temperature (top) and most unsteady (bottom) locations

Appendix F

Velocity Measurement Data

Velocity measurements using LDV were first obtained for isothermal conditions at both 24 L/min and 30 L/min inlet flow rates. Additionally, velocity measurements were also obtained for a subset of the heated conditions tested for temperature measurements. A full list of measured test section conditions corresponding to each set of velocity measurements is included in section F.3. A subset of the measured velocity contour plots along with comparisons to the simulations are presented in section F.2.

Velocities were collected at predefined *xz* and *yz* planes as depicted in Figure F-2. Due arrangement of the beams on the measurement probe, measurement locations within the tube bank were limited to the centres located between intersection of midplanes between rows and columns, as shown in Figure F-1. LDV data were collected for a fixed 120 second period at each measurement location. Data rates were observed to be higher for lower *z* values (i.e. – at lower measurement depths); this was expected as the attenuation of transmitted and scattered laser light would be greater for larger depths of water. The maximum data rates for a single measurement component were on the order of 250 - 500 Hz at distances close to the front end-shield.

A coincidence window of 500 μs was selected when processing the measured 3-component data. The coincidence window was the window in which a measurement signal must be received simultaneously by all three channels in order to be selected as a valid measurement point. In other words, all three velocity measurement channels would have to measure a particle velocity within 500 μs of each other in order to generate a single 3-D LDV measurement point. The coincidence window should typically be comparable to the transit time of a particle across the LDV measurement volume and should also be an order of magnitude smaller than the average time between data points [71]. Peak velocities on the order of 0.2 m/s were observed in preliminary tests. Referring to Table 3-17 on page 68, the LDV measurement volume was approximately 100 μm, suggesting a transit time on the order of 500 μs. A data rate of 250 Hz suggests that the coincidence window should be an order of magnitude smaller than 4000 μs. Therefore, a coincidence window of 500 μs was deemed appropriate.

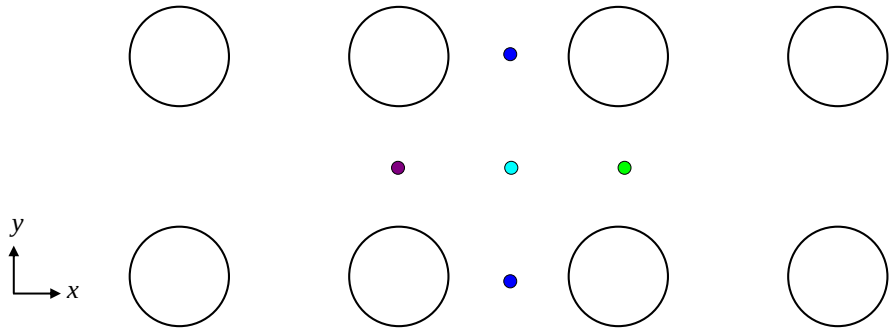

Figure F-1: Example (x, y) location for velocity measurements inside the tube bank. The measurement location corresponds to the central point

Table F-1: Locations and number of measurement points for the velocity measurement planes

Plane	*x* [mm]	*y* [mm]	*z* [mm][17]	Count
E1	-107.7 < *x* < 107.7	*y* = 181.1	20 < *z* < 220	135
E2	-87.2 < *x* < 87.2	*y* = 195.58	20 < *z* < 220	143
X0	*x* = 0.0	-116.2 < *y* < 174.4	20 < *z* < 180	99
X2	*x* = -58.1	-116.2 < *y* < 174.4	20 < *z* < 180	99
X3	*x* = -87.2	-116.2 < *y* < 174.4	20 < *z* < 180	99
R0	*x* = 181.1	-116.2 < *y* < 116.2	20 < *z* < 180	81
R1	*x* = 195.6	-87.2 < *y* < 87.2	20 < *z* < 180	63

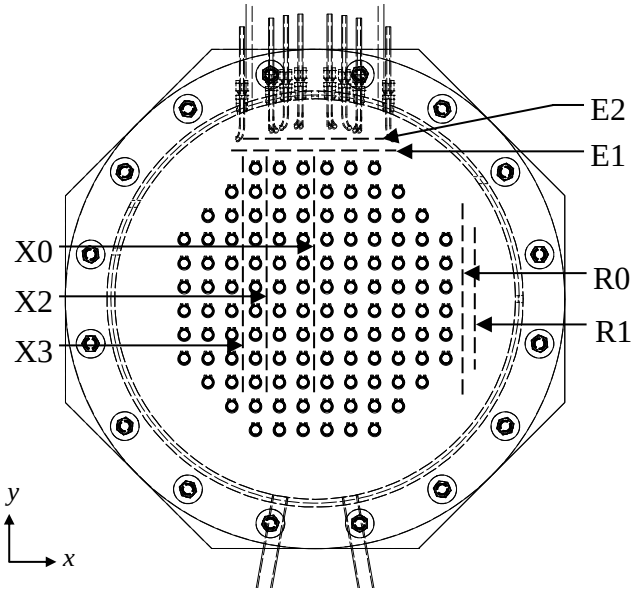

Figure F-2: Front view of test section illustrating the locations of the velocity measurement planes

F.1 Measurement Depth Limitations

For all measured planes, it was observed that the depth of achievable velocity measurements in the *z* direction was reduced for the heated cases compared to the isothermal case. The presence of temperature gradients within the test section proved problematic for LDV measurements since the refractive index of water

[17] Coordinates are presented with respect to the traversing mechanism (in air). The depth *z* coordinate of the presented results is corrected for the refractive index of water as described in Equation 3.2.

varied with temperature [70]. Temperature fluctuations were observed with time and position within the test section, with larger fluctuations corresponding to regions near the heaters. Changes in the refractive index would change the angle of the transmitted beams from the measurement probe. Large enough changes could cause the beams from the measurement probe to uncross, or for scattered light from the measurement volume to be missed by the detector; both would lead to a loss of Doppler signal.

As a result of variations in the refractive index, regions with higher temperature gradients showed lower data rates for heated cases as compared to the isothermal case. This difficulty was further compounded by the cosine power profile of the test section heaters; regions of the tube bank with higher temperature gradients were located further within the vessel where data rates were already reduced due to greater attenuation of light. The depth of achievable velocity measurements in the z direction was further reduced at higher test section power levels, as shown in Figure F-3.

The difficulty with LDV measurements within temperature gradients was evident for the E1 and E2 planes as large temperature gradients would be present the regions where the cool inlet nozzle flow interacts with the warmer test section fluid volume. For the isothermal cases, this region corresponded to $z > 150$ mm. For the heated case, measurements were not achievable at these locations. Additionally, regions for the X0, X2, and X3 measurement planes where LDV measurements were not achievable correspond roughly to the location of the heaters (-116 mm $< y < 116$ mm).

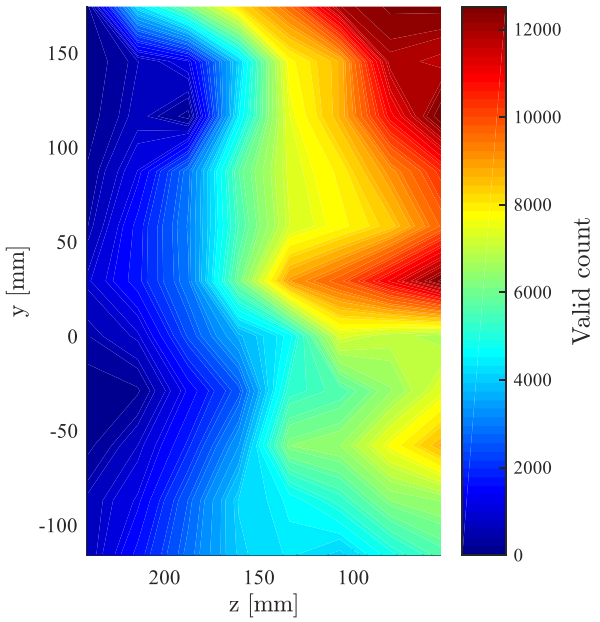

a) Isothermal, 30 L/min (test 0717-00)

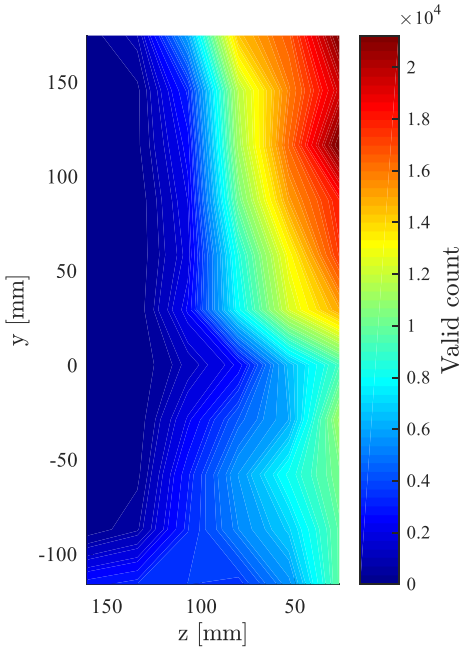

b) 20 kW, 30 L/min (test 0823-02)

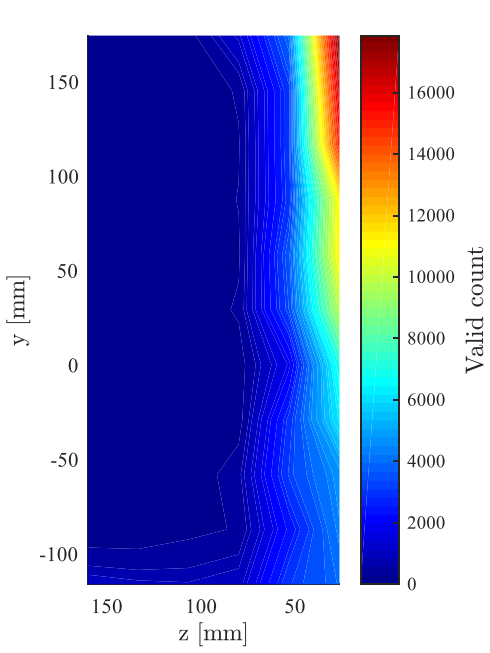

c) 38 kW, 30 L/min (test 0920-00)

Figure F-3: Valid LDV measurement count for the X0 measurement plane at various power levels

F.2 Velocity Contour Plots

This section presents selected time-averaged velocity contour plots on the E1 and R1 measurement planes for isothermal and heated test cases. Similar contour plots for the X0 measurement planes were previously presented in Chapter 5 section 5.1.2. The contour plots are presented alongside a corresponding time-average velocity contour plot from the simulations for comparison. The contour plots for the measurements and the simulations are presented on the same colour-bar scale. All velocity plots include unit length vectors projected onto the selected plane to indicate flow direction; a flow direction perpendicular to the page would result in a zero-length unit vector. Empty areas in the contour plots correspond to regions where fewer than 100 valid LDV measurements were obtained in the 120 second period due to laser light attenuation issues (as described in section F.1).

Contour plots for the E1 measurement region (corresponding to an *xz* plane) include velocity magnitude plots and *v*-velocity component contours. For the *v*-velocity contour plots, positive values correspond to facing upward from the page while negative values correspond to facing inward to the page.

Contour plots for the R1 measurement region (corresponding to an *yz* plane) include velocity magnitude plots and *u*-velocity component contours. For the *u*-velocity contour plots, positive values correspond to facing into to the page while negative values correspond to facing outward from the page.

Contour plots for the X0 measurement region (corresponding to an *yz* plane) include velocity magnitude plots only. Within this region of the tube bank, the average *u*-velocity component was near zero.

F.2.1 E1 Measurement Plane

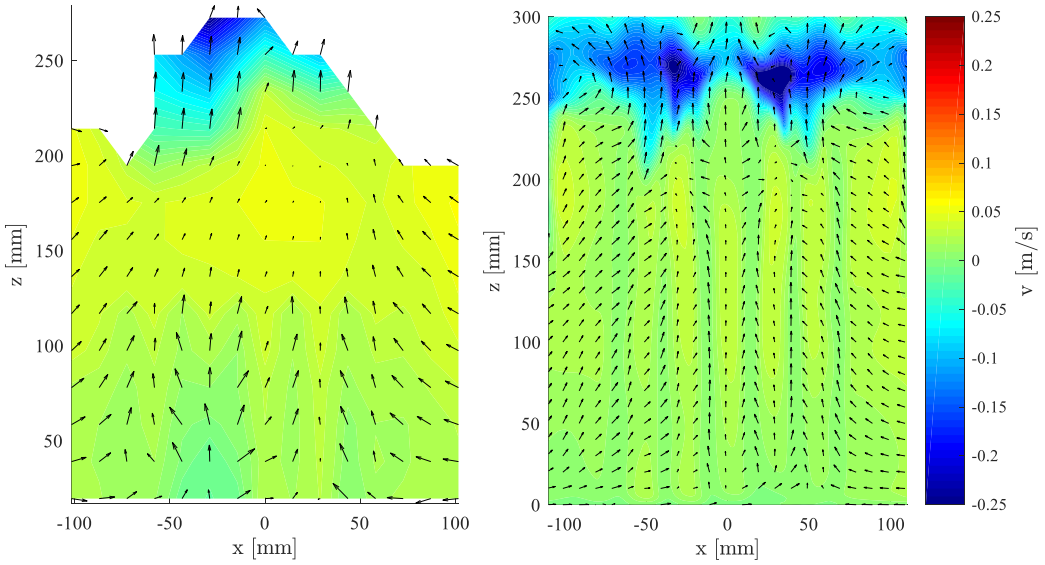

a) Measured (test ID 0716-00) b) Simulated (i30-KEreal-4mm)

Figure F-4: Velocity (*v*-component) contour with unit vectors at the E1 measurement plane (Isothermal, 30 L/min)

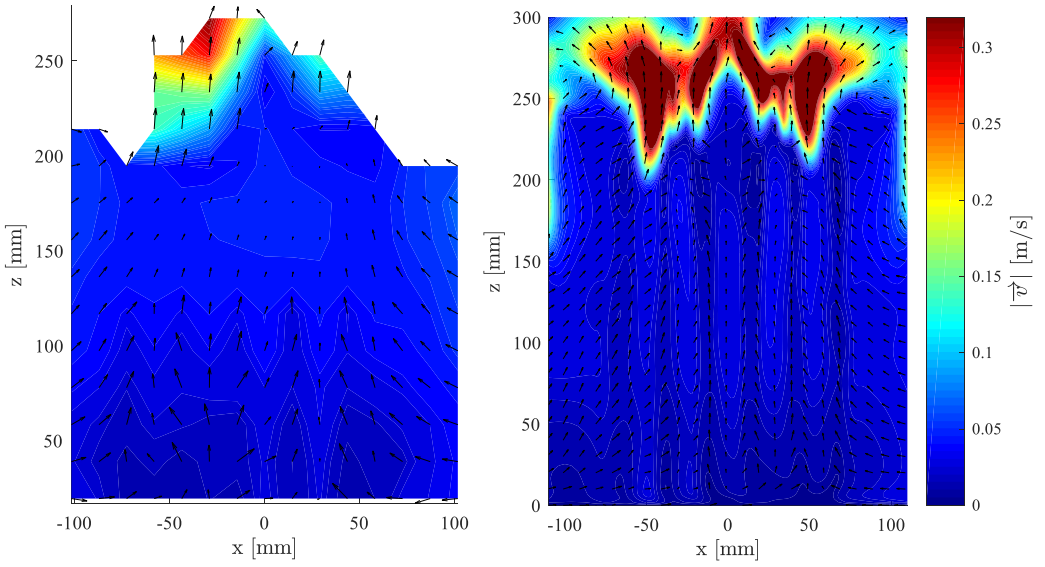

a) Measured (test ID 0716-00) b) Simulated (i30-KEreal-4mm)

Figure F-5: Velocity magnitude contour with unit vectors at the E1 measurement plane (Isothermal, 30 L/min)

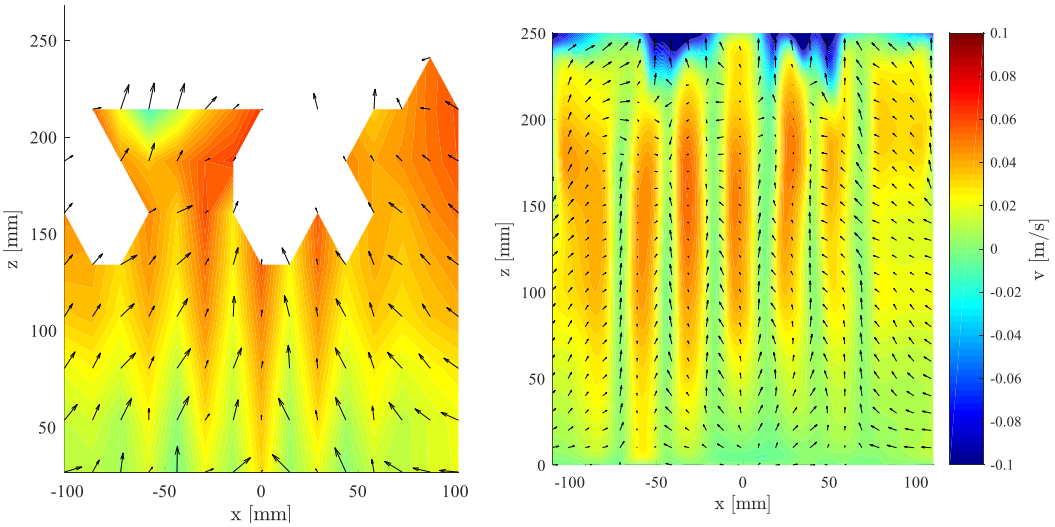

a) Measured (test ID 0906-02) b) Simulated (sim0908-KEreal-4mm)

Figure F-6: Velocity (*v*-component) contour with unit vectors at the E1 measurement plane (10 kW, 30 L/min, Ar ~ 0.0013)

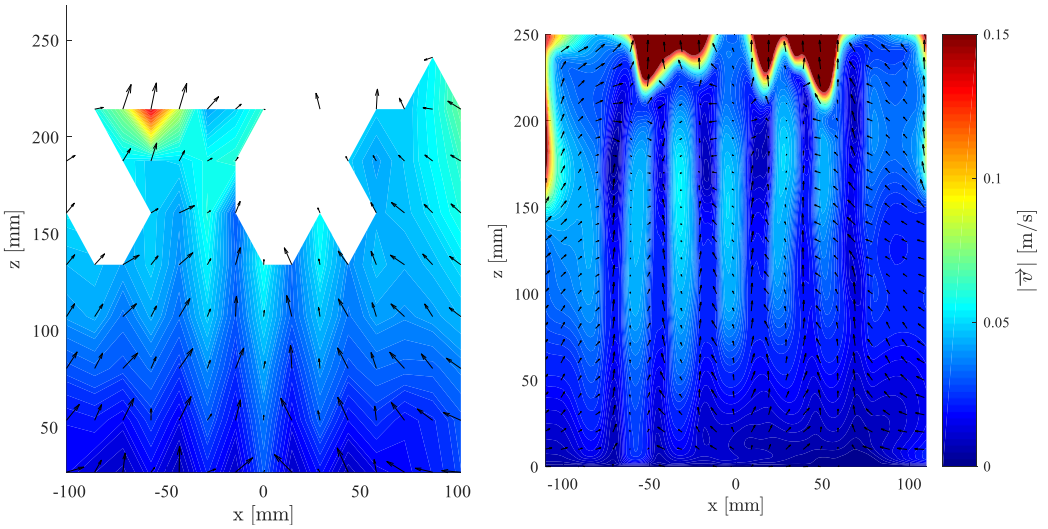

a) Measured (test ID 0906-02) b) Simulated (sim0908-KEreal-4mm)

Figure F-7: Velocity magnitude contour with unit vectors at the E1 measurement plane (10 kW, 30 L/min, Ar ~ 0.0013)

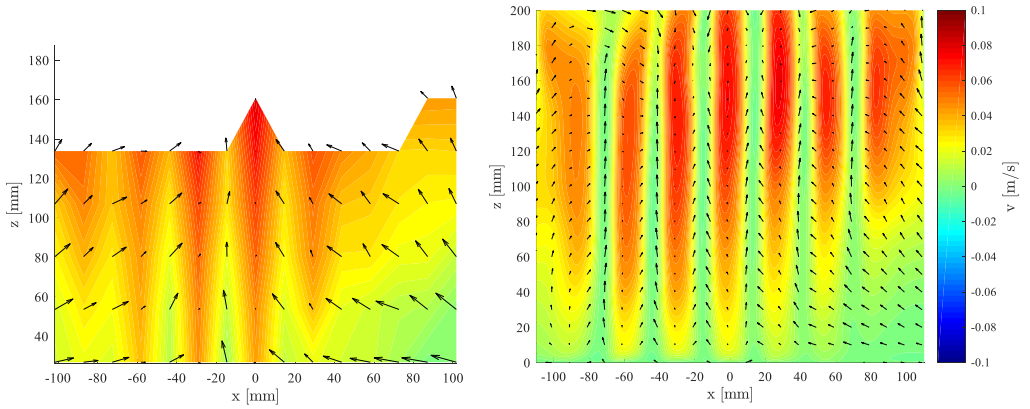

a) Measured (test ID 0825-00) b) Simulated (sim0308-KEreal-4mm)

Figure F-8: Velocity (*v*-component) contour with unit vectors at the E1 measurement plane (20 kW, 30 L/min, Ar ~ 0.0035)

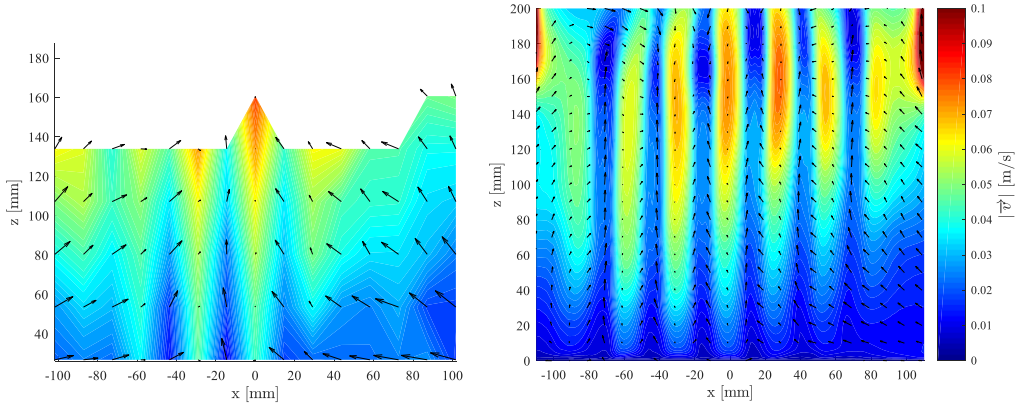

a) Measured (test ID 0825-00) b) Simulated (sim0308-KEreal-4mm)

Figure F-9: Velocity magnitude contour with unit vectors at the E1 measurement plane (20 kW, 30 L/min, Ar ~ 0.0035)

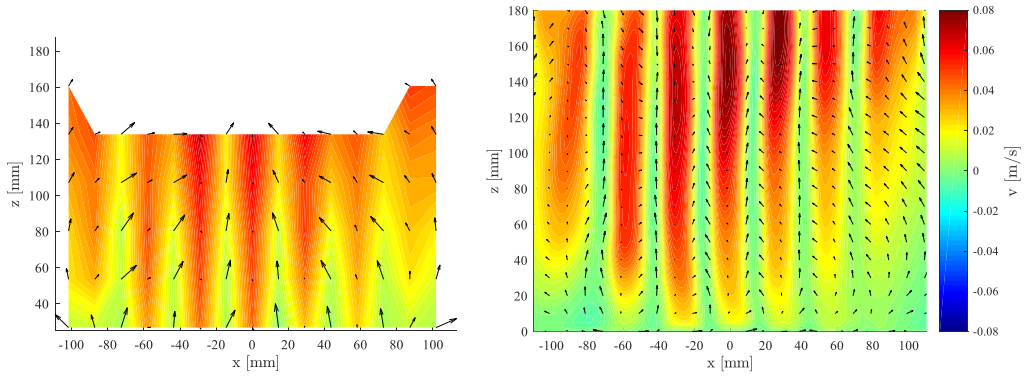

a) Measured (test ID 0831-01) b) Simulated (sim0831-KEreal-4mm)

Figure F-10: Velocity (*v*-component) contour with unit vectors at the E1 measurement plane (20 kW, 24 L/min, Ar ~ 0.0072)

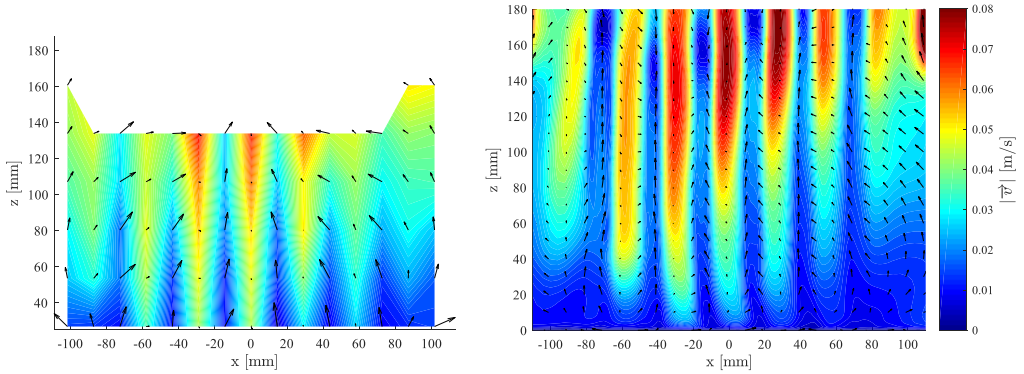

a) Measured (test ID 0831-01) b) Simulated (sim0831-KEreal-4mm)

Figure F-11: Velocity magnitude contour with unit vectors at the E1 measurement plane (20 kW, 24 L/min, Ar ~ 0.0072)

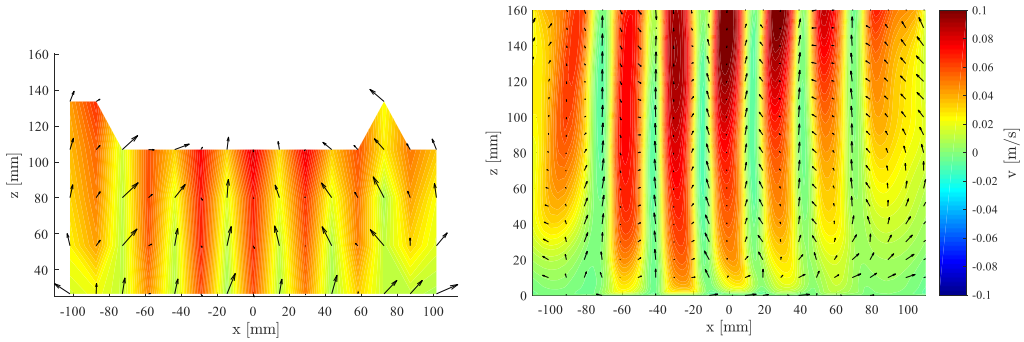

a) Measured (test ID 0925-00) b) Simulated (sim0922-KEreal-4mm)

Figure F-12: Velocity (*v*-component) contour with unit vectors at the E1 measurement plane (38 kW, 30 L/min, Ar ~ 0.0092)

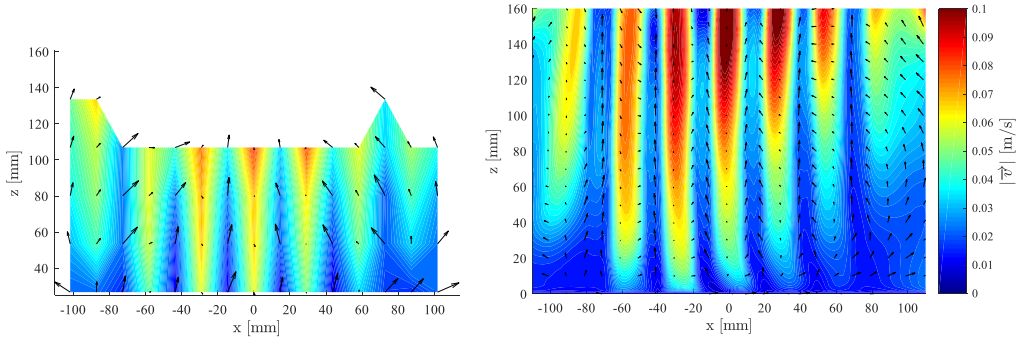

a) Measured (test ID 0925-00) b) Simulated (sim0922-KEreal-4mm)

Figure F-13: Velocity magnitude contour with unit vectors at the E1 measurement plane (38 kW, 30 L/min, Ar ~ 0.0092)

F.2.2 R1 Measurement Plane

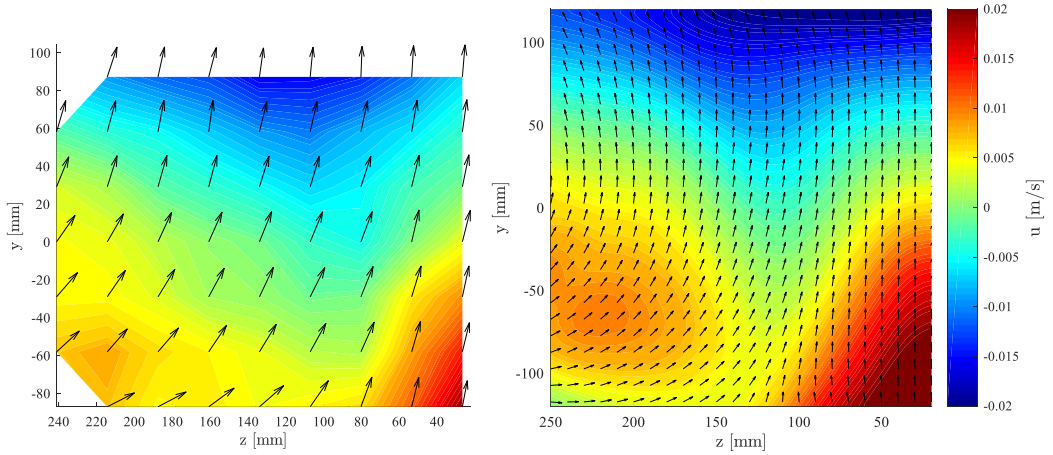

a) Measured (test ID 0720-01) b) Simulated (i30-KEreal-4mm)

Figure F-14: Velocity (*u*-component) contour with unit vectors at the R1 measurement plane (Isothermal, 30 L/min)

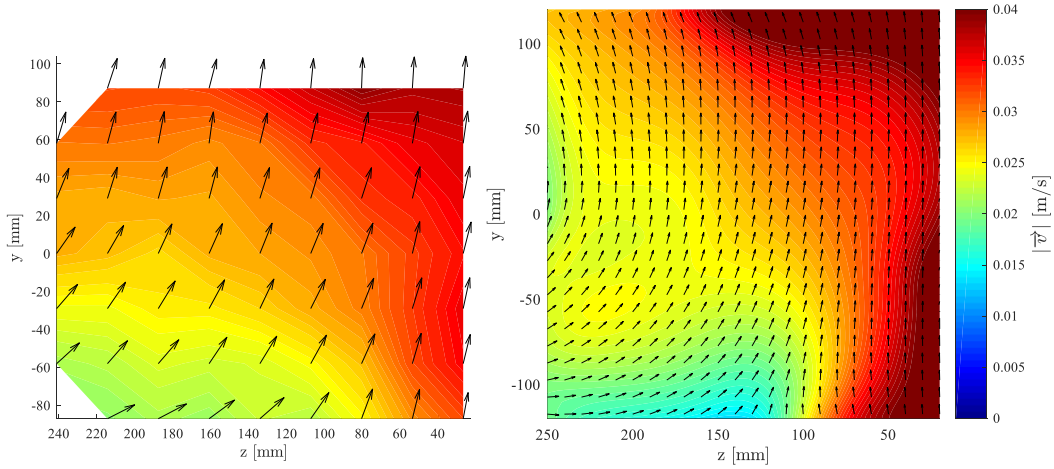

a) Measured (test ID 0720-01) b) Simulated (i30-KEreal-4mm)

Figure F-15: Velocity magnitude contour with unit vectors at the R1 measurement plane (Isothermal, 30 L/min)

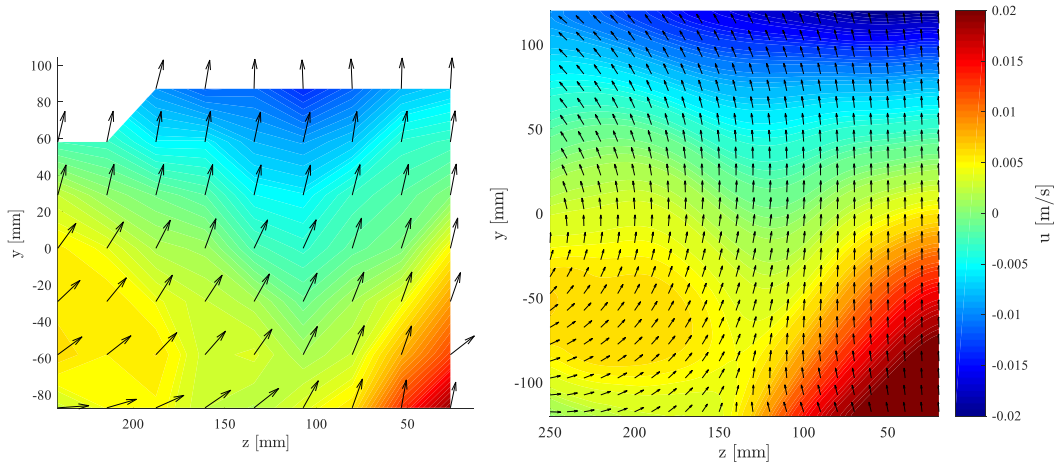

a) Measured (test ID 0906-02) b) Simulated (sim0908-KEreal-4mm)

Figure F-16: Velocity (*u*-component) contour with unit vectors at the R1 measurement plane (10 kW, 30 L/min, Ar ~ 0.0013)

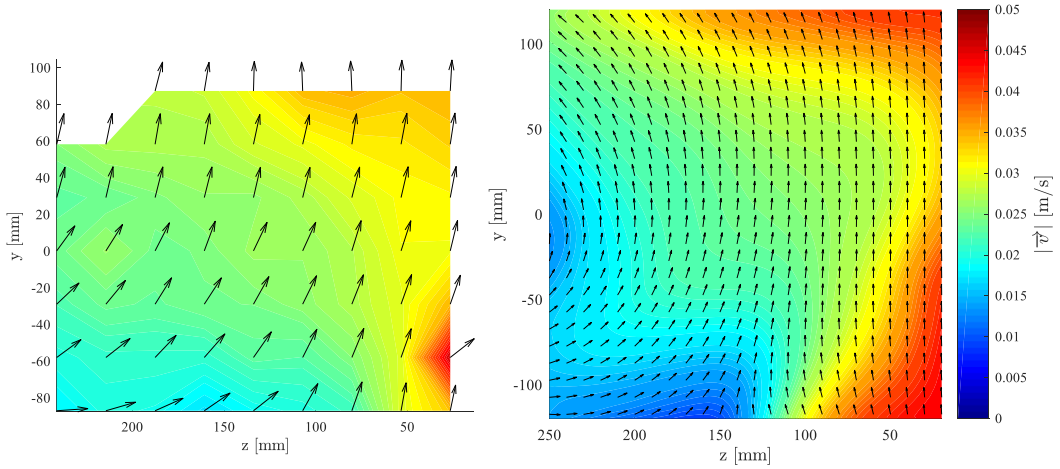

a) Measured (test ID 0906-02) b) Simulated (sim0908-KEreal-4mm)

Figure F-17: Velocity magnitude contour with unit vectors at the R1 measurement plane (10 kW, 30 L/min, Ar ~ 0.0013)

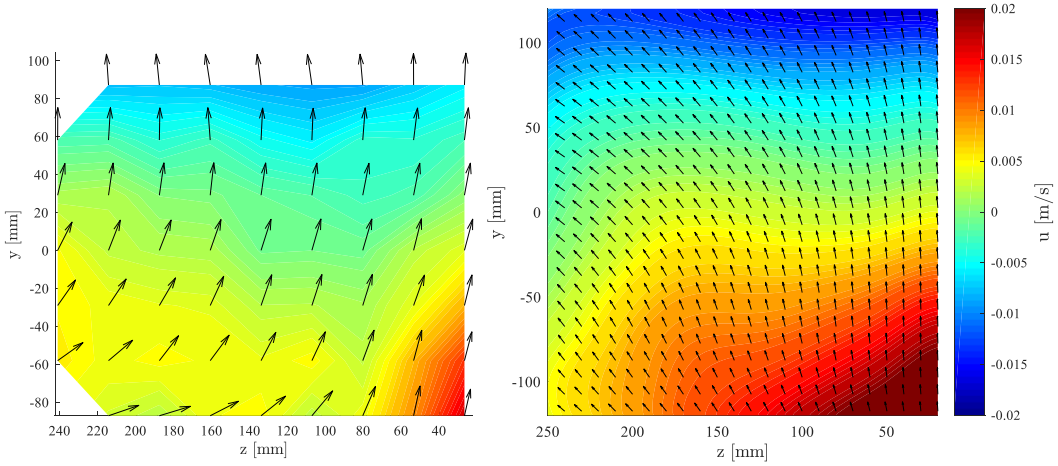

a) Measured (test ID 0821-01) b) Simulated (sim0308-KEreal-4mm)

Figure F-18: Velocity (*u*-component) contour with unit vectors at the R1 measurement plane (20 kW, 30 L/min, Ar ~ 0.0035)

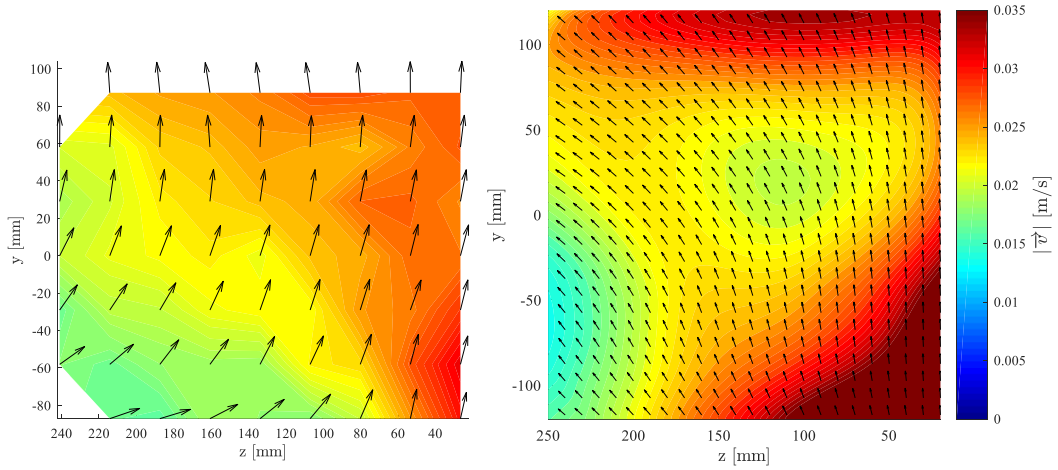

a) Measured (test ID 0821-01) b) Simulated (sim0308-KEreal-4mm)

Figure F-19: Velocity magnitude contour with unit vectors at the R1 measurement plane (20 kW, 30 L/min, Ar ~ 0.0035)

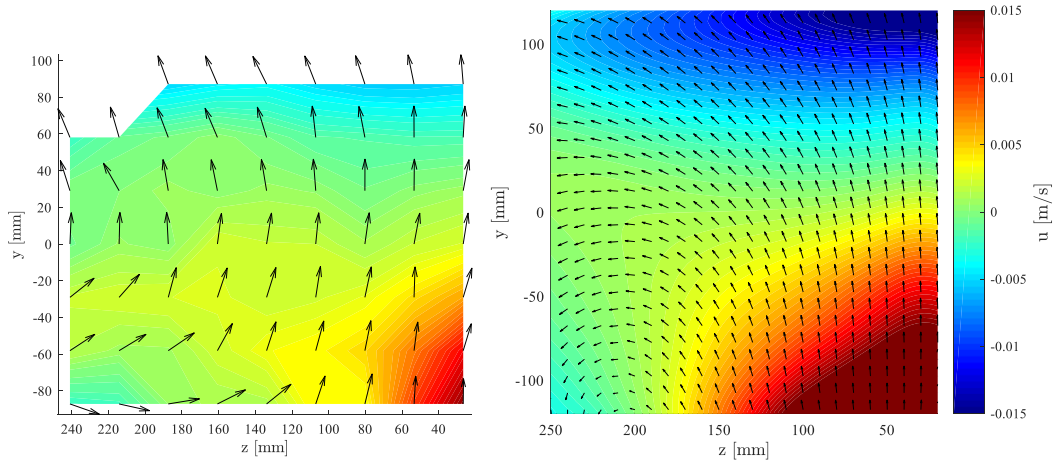

a) Measured (test ID 0830-00) b) Simulated (sim0831-KEreal-4mm)

Figure F-20: Velocity (*u*-component) contour with unit vectors at the R1 measurement plane (20 kW, 24 L/min, Ar ~ 0.0072)

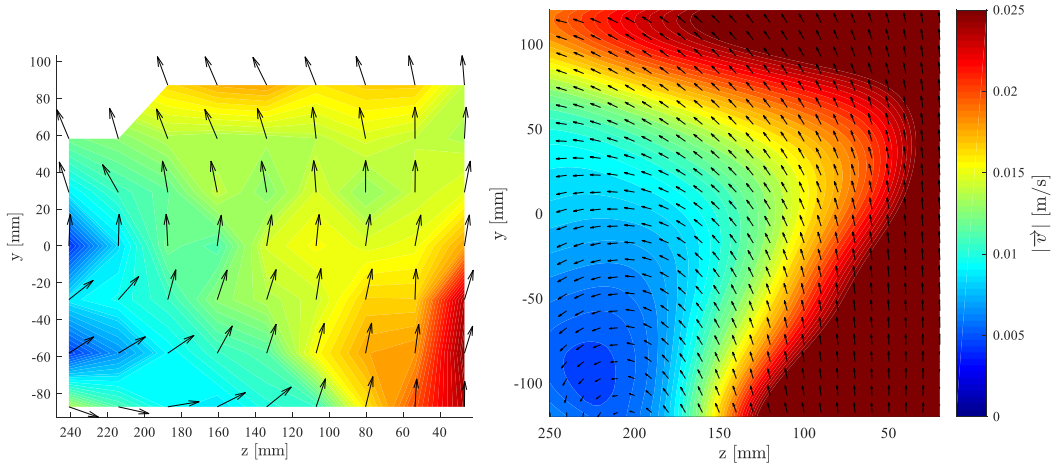

a) Measured (test ID 0830-00) b) Simulated (sim0831-KEreal-4mm)

Figure F-21: Velocity magnitude contour with unit vectors at the R1 measurement plane (20 kW, 24 L/min, Ar ~ 0.0072)

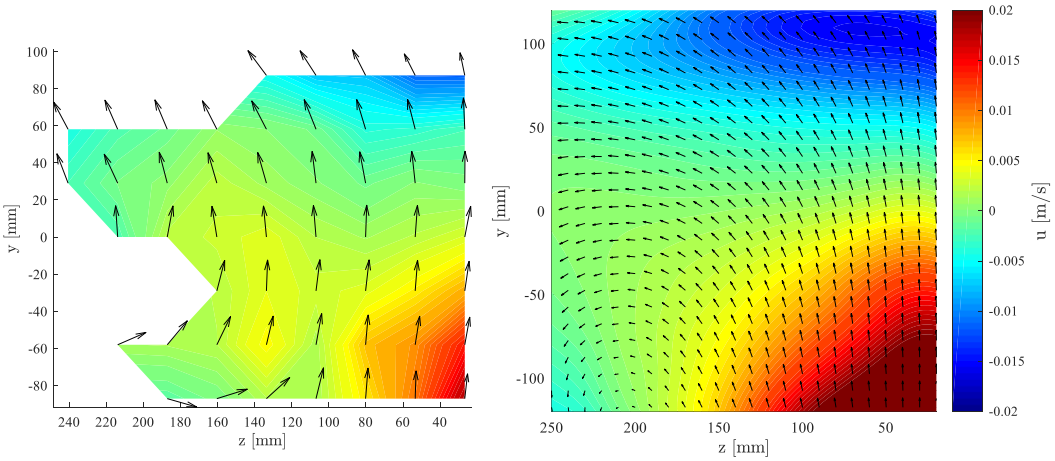

a) Measured (test ID 0830-00) b) Simulated (sim0922-KEreal-4mm)

Figure F-22: Velocity (*u*-component) contour with unit vectors at the R1 measurement plane (38 kW, 30 L/min, Ar ~ 0.0092)

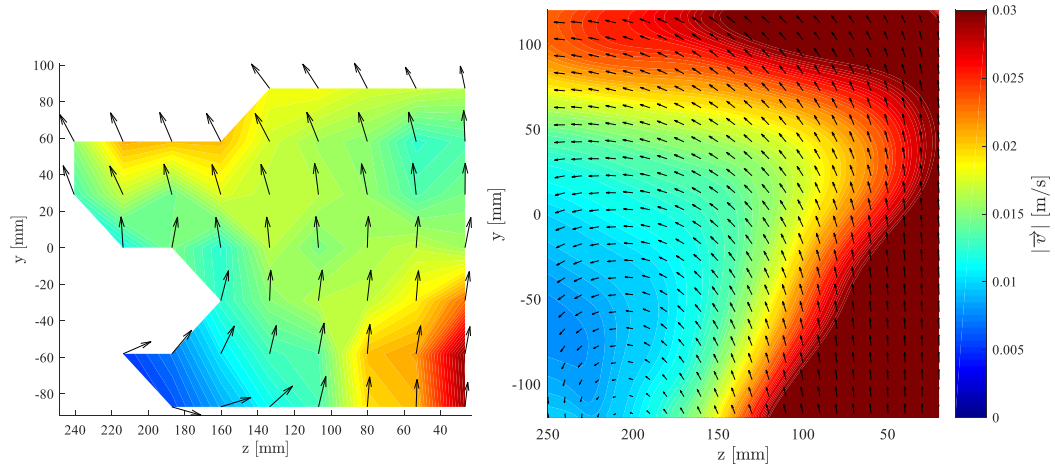

a) Measured (test ID 0830-00) b) Simulated (sim0922-KEreal-4mm)

Figure F-23: Velocity magnitude contour with unit vectors at the R1 measurement plane (38 kW, 30 L/min, Ar ~ 0.0092)

F.3 Experimental Conditions for Velocity Measurements

This section lists the measured flow rate, test section power, inlet temperature, and outlet temperatures for each velocity measurement test.

Table F-2: List of experiment conditions for the velocity measurement tests at isothermal conditions and 30 L/min inlet flow rate

Test ID	Plane	Flow [L/min]	Power [kW]	Inlet T [ºC]	Outlet T [ºC]	*Ar*
0716-00	E1	29.9 ± 0.2	0	27.3 ± 0.8	27.3 ± 0.8	0
0716-01	E2	29.8 ± 0.2	0	26.7 ± 1.0	26.7 ± 1.0	0
0717-00	X0	29.8 ± 0.2	0	28.0 ± 0.5	28.0 ± 0.5	0
0717-01	X2	29.9 ± 0.2	0	28.9 ± 0.5	28.9 ± 0.5	0
0718-00	X3	29.7 ± 0.2	0	27.0 ± 0.5	27.0 ± 0.5	0
0720-00	R0	30.0 ± 0.2	0	26.2 ± 0.5	26.2 ± 0.5	0
0720-01	R1	30.0 ± 0.2	0	27.4 ± 0.5	27.4 ± 0.5	0
0809-00	R0	30.0 ± 0.2	0	28.2 ± 0.5	28.2 ± 0.5	0
0809-01	R1	29.9 ± 0.2	0	28.7 ± 0.5	28.7 ± 0.5	0
0810-00	X0	29.8 ± 0.2	0	27.1 ± 0.5	27.1 ± 0.5	0
0810-01	X2	29.9 ± 0.2	0	28.4 ± 0.5	28.4 ± 0.5	0
0816-00	E1	30.1 ± 0.2	0	27.2 ± 0.6	27.2 ± 0.6	0
0817-00	X3	30.0 ± 0.2	0	27.5 ± 0.5	27.5 ± 0.5	0
0818-00	E2	30.0 ± 0.2	0	27.1 ± 0.5	27.1 ± 0.5	0

Table F-3: List of experiment conditions for the velocity measurement tests at isothermal conditions and 24 L/min inlet flow rate

Test ID	Plane	Flow [L/min]	Power [kW]	Inlet T [ºC]	Outlet T [ºC]	*Ar*
0721-00	R1	24.0 ± 0.1	0	27.7 ± 0.5	27.7 ± 0.5	0
0724-00	R0	23.9 ± 0.1	0	26.0 ± 0.5	26.0 ± 0.5	0
0724-01	X0	23.9 ± 0.1	0	27.5 ± 0.5	27.5 ± 0.5	0
0724-02	X2	23.9 ± 0.1	0	28.3 ± 0.5	28.3 ± 0.5	0
0726-00	X3	23.9 ± 0.1	0	26.4 ± 0.5	26.4 ± 0.5	0
0727-00	E2	23.8 ± 0.1	0	26.9 ± 0.7	26.9 ± 0.7	0
0728-00	E1	23.9 ± 0.1	0	27.4 ± 0.6	27.4 ± 0.6	0

Table F-4: List of experiment conditions for the velocity measurement tests at 10 kW and 30 L/min inlet flow rate

Test ID	Plane	Flow [L/min]	Power [kW]	Inlet T [°C]	Outlet T [°C]	*Ar*
0901-01	X0	29.9 ± 0.2	9.85 ± 0.04	20.7 ± 0.5	25.5 ± 0.5	0.0013
0905-00	X2	30.0 ± 0.2	9.86 ± 0.04	20.0 ± 0.5	24.8 ± 0.5	0.0013
0906-00	X3	29.9 ± 0.2	9.87 ± 0.04	20.2 ± 0.5	25.0 ± 0.5	0.0013
0906-01	R0	29.9 ± 0.2	9.86 ± 0.04	20.1 ± 0.5	24.9 ± 0.5	0.0013
0906-02	R1	30.1 ± 0.2	9.85 ± 0.04	20.1 ± 0.5	24.9 ± 0.5	0.0013
0907-00	E1	30.1 ± 0.2	9.86 ± 0.04	20.2 ± 0.5	25.0 ± 0.5	0.0013
0908-00	E2	29.9 ± 0.2	9.86 ± 0.04	20.4 ± 0.5	25.2 ± 0.5	0.0013

Table F-5: List of experiment conditions for the velocity measurement tests at 20 kW and 30 L/min inlet flow rate

Test ID	Plane	Flow [L/min]	Power [kW]	Inlet T [°C]	Outlet T [°C]	*Ar*
0821-00	R0	29.8 ± 0.2	19.75 ± 0.08	26.6 ± 0.5	36.1 ± 0.5	0.0035
0821-01	R1	30.0 ± 0.2	19.76 ± 0.08	26.5 ± 0.5	36.0 ± 0.5	0.0035
0823-01	E2	29.7 ± 0.2	19.77 ± 0.08	26.8 ± 0.5	36.4 ± 0.5	0.0036
0823-02	X0	29.9 ± 0.2	19.76 ± 0.08	26.8 ± 0.5	36.3 ± 0.5	0.0035
0823-03	X2	29.8 ± 0.2	19.78 ± 0.08	27.2 ± 0.5	36.7 ± 0.5	0.0036
0823-04	X3	30.0 ± 0.2	19.76 ± 0.08	27.4 ± 0.5	36.9 ± 0.5	0.0035
0825-00	E1	29.8 ± 0.2	19.78 ± 0.08	26.7 ± 0.5	36.2 ± 0.5	0.0035
0911-00	E2	30.0 ± 0.2	19.80 ± 0.08	28.6 ± 0.5	38.1 ± 0.5	0.0037
0913-00	E1	29.8 ± 0.2	19.79 ± 0.08	28.2 ± 0.5	37.8 ± 0.5	0.0037
0913-01	X0	29.9 ± 0.2	19.76 ± 0.08	28.1 ± 0.5	37.6 ± 0.5	0.0036
0914-00	X2	29.9 ± 0.2	19.79 ± 0.08	28.0 ± 0.5	37.5 ± 0.5	0.0036
0914-01	X3	29.9 ± 0.2	19.77 ± 0.08	28.1 ± 0.5	37.6 ± 0.5	0.0036
0914-02	R1	30.1 ± 0.2	19.76 ± 0.08	28.5 ± 0.5	38.0 ± 0.5	0.0036
0915-00	R0	30.1 ± 0.2	19.78 ± 0.08	27.8 ± 0.5	37.2 ± 0.5	0.0035

Table F-6: List of experiment conditions for the velocity measurement tests at 20 kW and 24 L/min inlet flow rate

Test ID	Plane	Flow [L/min]	Power [kW]	Inlet T [°C]	Outlet T [°C]	*Ar*
0829-00	R0	23.8 ± 0.1	19.76 ± 0.08	26.6 ± 0.5	38.5 ± 0.5	0.0071
0830-00	R1	23.9 ± 0.1	19.79 ± 0.08	27.2 ± 0.5	39.0 ± 0.5	0.0071
0830-01	X0	23.9 ± 0.1	19.76 ± 0.08	27.3 ± 0.5	39.2 ± 0.5	0.0072
0830-02	X2	24.0 ± 0.1	19.75 ± 0.08	27.3 ± 0.5	39.1 ± 0.5	0.0071
0830-03	X3	24.0 ± 0.1	19.74 ± 0.08	27.4 ± 0.5	39.2 ± 0.5	0.0071
0831-01	E1	23.9 ± 0.1	19.76 ± 0.08	27.4 ± 0.5	39.3 ± 0.5	0.0072
0901-00	E2	24.1 ± 0.1	19.78 ± 0.08	28.0 ± 0.5	39.7 ± 0.5	0.0071

Table F-7: List of experiment conditions for the velocity measurement tests at 38 kW and 30 L/min inlet flow rate

Test ID	Plane	Flow [L/min]	Power [kW]	Inlet T [°C]	Outlet T [°C]	*Ar*
0919-00	R0	30.0 ± 0.2	37.56 ± 0.20	40.0 ± 0.5	57.8 ± 0.5	0.0093
0919-01	R1	29.9 ± 0.2	37.55 ± 0.20	40.3 ± 0.5	58.2 ± 0.5	0.0094
0920-00	X0	30.2 ± 0.2	37.55 ± 0.20	40.8 ± 0.5	58.5 ± 0.5	0.0092
0920-01	X2	30.1 ± 0.2	37.54 ± 0.20	40.5 ± 0.5	58.3 ± 0.5	0.0093
0920-02	X3	30.1 ± 0.2	37.54 ± 0.20	40.5 ± 0.5	58.3 ± 0.5	0.0093
0921-00	E2	30.0 ± 0.2	37.55 ± 0.20	41.2 ± 0.5	59.0 ± 0.5	0.0094
0925-00	E1	30.1 ± 0.2	37.56 ± 0.20	40.3 ± 0.5	58.1 ± 0.5	0.0092